UNIVERSITY OF CALIFORNIA
Los Angeles

Reticulated Foam Materials for the Evaporative Cooling of Hypersonic Vehicles & for Control of Secondary Electron Emission in Space Electric Propulsion

A dissertation submitted in partial satisfaction
of the requirements for the degree
Doctor of Philosophy in Aerospace Engineering

by

Dylan Abraham Dickstein

2022

ABSTRACT OF THE DISSERTATION

Reticulated Foam Materials for the Evaporative Cooling of Hypersonic Vehicles & for Control of Secondary Electron Emission in Space Electric Propulsion

by

Dylan Abraham Dickstein
University of California, Los Angeles, 2022
Professor Nasr M. Ghoniem, Chair

An experimental- and simulation-based approach is used to investigate the fundamentals and applications of aerospace "metamaterials". This dissertation trisects the subject and delves deeply into the following topics: secondary electron yield suppression, controlling transpirant in hypersonic leading edges, and mass loss processes via arc jet testing. All three segments use computer simulations to produce data whereas experiments are incorporated for only the former and latter. In the first topic, secondary electron yield (SEY) is measured in solid copper and copper foam through direct measurements using a high vacuum electron gun chamber at The Aerospace Corporation in El Segundo, CA. These results are compared with ray-tracing Monte Carlo simulations. It is found that the 4.6% volume fraction copper foam has approximately a 20% reduction in yield compared with its solid counterpart. Furthermore, SEY is determined to be inversely proportion to volume fraction. The second focus is investigated by modeling a 5° half-angle leading edge wedge with a semicircular nose tip of 1 mm radius of curvature. The complex method of optimization is used to maximize the cooling effectiveness in a porous leading edge in Mach 6 conditions. We found that by focusing transpirant on regions with the highest incident heat flux, the wedge inherits a 6% increase in cooling effectiveness compared with the isotropic permeability case. In this manner, foam volume fraction is inversely proportional to incident heat flux. The last segment is explored by performing arc jet experiments on lanthanum hexaboride (LaB_6) discs, corroborating results with computer simulations of the setup, and involving such characterization tools as microscopy, spectroscopy, and X-ray diffraction. It was measured that an incident heat flux of 19.5 MW/m^2 causes a LaB_6 surface to recess at 0.11 mm/s. Moreover, the material was determined to have a nearly constant surface recession rate for energy fluence magnitudes exceeding about 400 MJ/m^2.

The dissertation of Dylan Abraham Dickstein is approved.

Y. Sungtaek Ju

Jaime Marian

Timothy S. Fisher

Nasr M. Ghoniem, Committee Chair

University of California, Los Angeles

2022

Dedicated to my parents, David and Mimi Dickstein, for allowing their six-year-old son to amuse himself with rocket propellant.

TABLE OF CONTENTS

LIST OF FIGURES

LIST OF TABLES

ACKNOWLEDGMENTS

This investigation is made possible by Distinguished Professor Nasr Ghoniem. More than an adviser, he is a mentor, expediter, facilitator, and motivator. His real-world insight combined with his analytical prowess is something to revere. He has also been a source of inspiration on the microengineered materials and electron emission fronts. Professors Fisher, Marian, and Ju, of who comprise the remainder of my committee, have provided further guidance on the topics of heat transfer and materials science. Each has played a critical role in the development of my academic maturity. Professor Fisher, commanding the role of UCLA MAE (Mechanical and Aerospace Engineering) Department Chair at the time of writing, spearheaded the DARPA MACH (Defense Advanced Research Projects Agency Materials Architectures and Characterization for Hypersonics) proposal which provided a specific application to benefit from this research. Professor Ju, an expert in micro- and nanoscale thermosciences, maintains a first-principle-based multiscale modeling approach and established a precedent for comprehensive, exact, and meticulous simulations. Professor Marian, dually appointed in UCLA's departments of Materials Science Engineering and MAE, emboldened discussions on crystallography and highlighted novel contributions to phase transformations.

Collaborations are paramount to the development of this body of work. Daily interactions with colleagues in Professor Nasr Ghoniem's lab have unquantifiable, but undeniably vast benefits. Warren Nadvornick, Arian Ghazari, Yue Huang, Edward Gao, Mohammad Alabdullah, Chris Matthes, Giacomo Po, Andrew Yang, Yang Li, Ruggero Forte, and Camile El-Bayar are irreplaceable. Access to neighboring laboratories is also vital. X-ray diffraction and atomic force microscopy were made possible by Professor Mark S. Goorsky and his students Pranav V. Meta and Michael Liao. Scanning electron micropscopy was learned via Professor Sergey Prikhodko and computer tomography scans are credited to the training and acumen of USC's Professor Tea Jashashvili. Furthermore, industrial partnerships with Raytheon, Ultramet, and The Aerospace Corporation have completed the bridge between research ideality and commercial practicality.

The National Science Foundation Graduate Research Fellowship Program (NSF GRFP) has supported me from Fall of 2018 until graduation and sets a standard for transformative research while maintaining a strong sense of scientific communication. Special thanks are also due to the Air Force Office of Scientific Research (AFOSR) for their financial support through Grant No. FA9550-16-1-0444 with UCLA. Additionally, the U.S. Department of Energy, Office of Science, Office of Fusion Energy Sciences provided assistance under award number DE-SC0018410 in our study of effects of cyclic plasma heating on surface damage of micro-porous tungsten.

Encouragement, advice, and backing from family, friends, and mentors cannot be overlooked in a dissertation, and especially in this one. Upon conferral of the Ph.D., if I can be so presumptuous, those three letters would be the first in my family's recent history and yet everyone in on board. Doctors of philosophy aside, I was surrounded by people who value higher education from birth onward and this instilled the values needed to seek a degree of this magnitude. What I did not realize the merit of until long after birth was that of a mentor. My first came in 2015 when I was introduced to Joanne Maguire, former executive Vice President of Lockheed Martin Space Systems. She gave me the platform I had been asking for to show the aerospace community that I belong. In 2017 I also gained the mentorship of George Whitesides, CEO of Virgin Galactic. Fireside chats about the direction of the space industry have been tremendously impactful and inspiring. George introduced me to my newest mentor the following year and the first meeting was anything but mundane. Standing alongside my then girlfriend in Tehachapi, California, I met CJ Sturckow, former commander of the Space Shuttle. We got to know each other in a glider flight over the nearby mountains. When your first time co-piloting an aircraft is with an astronaut, you have no choice but to learn how to fly. CJ urged me to get my private pilot license as soon as I had an opening in my schedule, so I signed up for lessons once I completed the course requirements for this degree.

As the final student in Professor Ghoniem's roster of Ph.D.s, I have seen the MATRIX (Materials Research in Extreme Environments) laboratory dwindle from a dozen. Tagged Ph.D. student number 41, I acknowledge the responsibility to determine the final scratches on a career packed with discoveries. I also recognize the prosperous and foundational academic lineage that I stand upon. Professor Nasr Ghoniem's adviser is Gerald Kulcinski from the University of Wisconsin. His adviser is Charley Maynard, for whose adviser is Nobel laureate Nicolaas Bloembergen. Then it continues Gorter, de Haas, Hamerlingh (another Nobel laureate), Mees, Rees, Moll, and then branches since students previously had up to three advisers. The climax of this geneology is that our research group is directly connected via advisers to both Bernoullis, Euler, Cassini, Ricci, Huygens, Erasmus, Copernicus, Leibniz, and Galileo. Thus, as I "stand on the shoulders of giants" and present the novel research I have compiled, it is from the direct descendant of advisers that I repeat Galileo's words and humbly cite his greatness and the volumes of work that make my trifle contribution possible.

VITA

2014	Aerospace Lab Technician, California Polytechnic State University, San Luis Obispo.
2015	United Launch Alliance, Denver, Colorado.
2015-2016	Teacher Assistant, Aerospace Structural Analysis I and II, California Polytechnic State University, San Luis Obispo.
2016	United Launch Alliance, Cape Canaveral, Florida.
2016	B.S. (Aerospace Engineering), California Polytechnic State University, San Luis Obispo.
2016-Present	Research Assistant, MATRIX Laboratory, University of California, Los Angeles.
2017	M.S. (Aerospace Engineering), University of California, Los Angeles.
2017	Virgin Galactic, Long Beach, California.
2017-2019	The Aerospace Corporation, El Segundo, California.
2018-2022	Awarded NSF GRFP (National Science Foundation Graduate Research Fellowship Program)
2018	SpaceX, Hawthorne, California.
2018-2020	Santa Monica Flyers Student Pilot, Los Angeles, California.
2019-2021	Mars Desert Research Station Astronaut Analog (Crew 245 Commander), Hanksville, Utah.
2020-2022	NASA Astronaut Candidate Quarter Finalist, Houston, Texas.

PUBLICATIONS

Dickstein, D., Chang, H. Y., Marian, J., Feldman, M., Hubble, A., Spektor, R., Ghoniem, N. (2020). Secondary electron emission from reticulated cellular copper surfaces. Journal of Applied Physics, 128(12), 123302.

Ghazari, A., McElfresh, C., **Dickstein, D.**, Marian, J., Ghoniem, N. (2021). Effects of cyclic plasma heating on surface damage of micro-porous tungsten. Physica Scripta, 96(12), 124033.

Dickstein, D., Ko, D., Nadvornick, W., Jain, K., Holdheim, S., Ju, Sungtaek., Ghoniem, N. (2022). Optimized permeability of microporous foam for transpiration cooling in hypersonic leading edge. Journal of Thermophysics and Heat Transfer

Ghazari, A., McElfresh, C., **Dickstein, D.**, Nadvornick, W., Pintsuk, G., Wessel, E., Wirtz, M., Hughes, D., Williams, B., Marian, J., Ghoniem, N. (2022). Intense cyclic heating effects on thermo-fracture and thermal shock of solid tungsten and open-cell tungsten foam. Journal of Nuclear Materials, 153760.

Dickstein, D., Ghazari, A., Nadvornick, W., Liao, M., Carson, B., Ghoniem, N. (In-Progress). Mass loss, sublimation, and surface damage of lanthanum hexaboride in an arc jet plasma.

CHAPTER 1

Introduction and Thesis Objectives

Operation in thin atmosphere at speeds exceeding Mach 5 is a necessary challenge for humanity as it continues to edge closer to existing as an interplanetary species. And well in advance of this eventual leap for sufficiently intelligent life, expeditious travel through Earth's atmosphere via rockets, missiles, experimental aircraft, and reentry vehicles is a multi-billion dollar industry with implications on homeland security, international relations, and even personal travel. Hypersonic vehicles have existed since the late 1940s, at which time design limitations were predominately focused on propulsion. As delta-v became less of a limiting factor for the majority of proposed missions, upper limits of material properties, especially thermal, became the greatest technological burden. Dissipating the extreme heat flux imparted on the structure, principally at the leading edge, is achieved through various methods of cooling. These include evaporation/condensation devices, phase change processes, ablation, electron emission, and others. Combining these cooling processes with the latest materials science and manufacturing methods revitalizes the conversation about what is feasible for the future of hypersonic vehicle designs.

1.1 The Need for Micro-engineered Meta Materials

Largely a synonym for microtechnology, microengineering is the modification of structures on the order of micrometers. While the name microtechnology has predominate association with electronic circuits, it surely applies to the design and manufacturing of materials as well. By modifying the geometry and composition of materials at the microscale, properties can be optimized to fit a particular application more appropriately than elemental or alloyed bulk materials. Another description of this aspect of material fabrication is the term "metamaterial". This word is derived from the Greek word meta (beyond) and the Latin word materia (matter), and describes microengineered materials that have a property that is not found in nature [1]. While the milliscale certainly has room for growth and the nanoscale has numerous research avenues, the order in the middle satisfies the Goldilock's principle. Microscale provides sufficient precision such that electron emission is relevant, but not excessively diminutive to deem design changes impractical for hypersonic vehicles. Within the microscale, the research pertains to a couple of novel material categories. These microengineered materials are metal foams and metal powders. As their names suggest, the former is a reticulated form of a solid metal and the latter is a metal which has been broken into fine particles. Each of their categorical properties, applications, and manufacturing methods are discussed.

Foams, referring to their porous geometry, are lightweight structures which are incompletely characterized and have untapped potential. While foams can be made with ceramics, composites, and polymers, the research presented shall focus on metallic applications. Some examples include energy absorption, thermal management, strain isolation, electrical screening, electrodes, and filters. Metal foams are desirable in these fields due to their relatively large elongation, high thermal conductivity, sizable surface area to volume ratio, and controlled pore size. A key asset to foams is their manufacturing customization.

Metal foams can be built using one of nine methods. (1) Gas can be secreted into a molten metal to create voids. The temperature is then reduced to solidify the structure. (2) A foam facilitator such as a surfactant or a blowing agent is introduced into a molten metal and pressure is managed during cooldown. (3) Metal powders are combined with a foam facilitator and then the temperature is elevated. This releases gas and creates voids similar to the first method. (4) Foams can be developed by passing molten metal or a metal powder slurry into a ceramic mold. This is performed at high pressure and then the contents are sintered. (5) Chemical vapor deposit or electrodeposit the desired metal onto a polymer foam skeleton. Once deposition is complete, then the temperature is raised to burn out the interior skeleton. The product is a foam with hollow ligaments. (6) Another method to create pores is by hot isostatic pressing (HIP) powders prior to volume expansion at elevated temperatures. (7) Metal-oxide or hydride pellets can be sintered and dehydrated onto polymer spheres to create pores. Vapor deposition and reduction are viable variations to dehydration. (8) A reticulated skeleton can result from applying pressure to a metal powder and leachable powder slurry. (9) A gas can be dissolved in a high-pressure, liquid-phase metal to infiltrate bubbles during solidification. These bubbles can be released in a controlled manner which enables void density to be predetermined and varied [2].

Foam geometry can be specified with three independent characteristics: volume fraction, VF, pore density, ρ_p, and mean ligament thickness, LT_m. Volume fraction is the percentage of material relative to its fully dense analog. It follows that $0\% < VF < 100\%$ for foams and the solid version is defined as $VF = 100\%$. Pore density refers to the number of cells or windows visible per unit length. The accepted unit is pores-per-inch (PPI). Commercial applications which incorporate foams tend to design for pore densities on the order of 10 or 100 PPI. A few examples of different pore densities are illustrated in Figure 1.

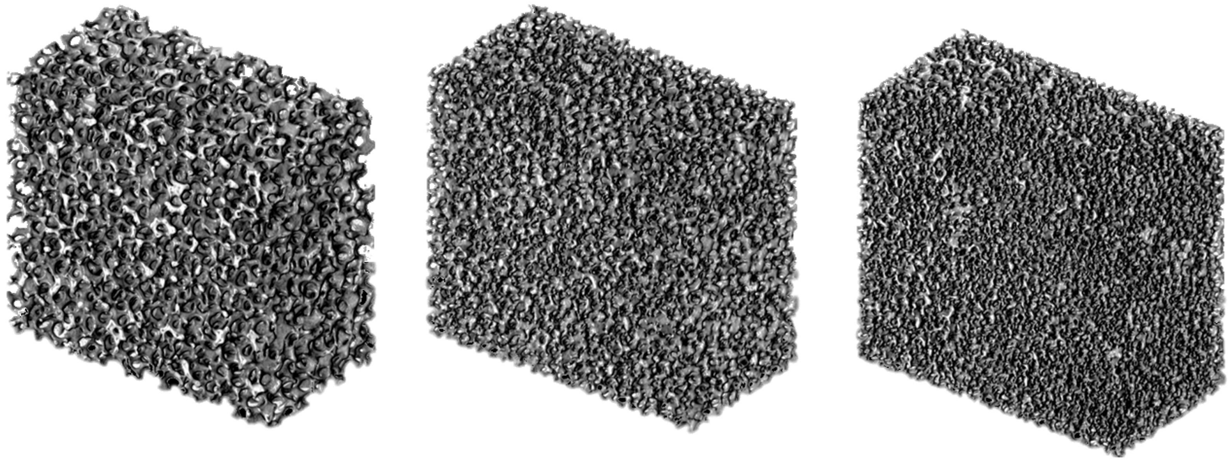

Figure 1: Pore density comparison in foams. From the left, $\rho_p = (20,\ 30,\ 45)\ PPI$ [3]

Segments of a foam are connected via ligaments in a three-dimensional and nearly isotropic web. While most cross-sections vary from a deltoid curve to a Releaux triangle, the diameter is reported as a mean value across the specimen to account for inherent irregularities and partial hollowness in certain specimens. Together, the three foam parameters define a foam's theoretical geometry. Since the three variables are independent, there can exist a low or high volume fraction foam with either small or large ligaments, and few or numerous pores. The theoretical limits depend on the overall dimensions. In practice, however, manufacturing constraints force a narrower range of possibilities. These limitations pertain to foam parameter accuracy, property consistency, and local irregularities. Relative to solid metals, foams have lower thermal conductivity and increased brittleness. This is due to the thin ligaments being more prone to crushing and creating narrower pathways for heat to transfer. Still, the effective properties, or those that consider the reduced volume of material, illustrate improved characteristics. The incomplete characterization of foams results in knockdowns being applied to structural and thermal properties in foam. This knowledge gap is an opening for which this novel research puts forth effort to fill.

Microengineering *metamaterials* can also be achieved with microscale constituents, namely powders. Their high surface-area-to-volume ratios, good workability, and versatility make metals in this form a powerful design asset. Metal powders can be considered on their own or as part of a master alloy. Many powders are produced through either plasma, gas, liquid, or centrifugal atomization. The hydride-dehydride process is a lower cost option as well. SEM images of Ti-6Al-4V with four of these powder production techniques are shown in Figure 2. A benefit of liquid atomization is the rapid cooling of molten metal droplets produces quasi-spherical, smooth, and denser granules.

Powders are combined to create larger metallic products using a variety of manufacturing methods categorized under the title of powder metallurgy. These include two types of sintering (electric current assisted and selective laser) as well as HIP and powder forging. Less commonly, metal injection molding and selective laser melting are employed.

Metal powders are applicable in numerous industries from aerospace and defense to electrical and electronics. This variety can be attributed to novel metal powder designs having preferred properties for thermal management, filters, and sintered components. It is worth noting that these applications largely overlap with metal foams. When considering additive manufacturing the two microengineered material categories also have production parallels. That is, metal powders can be selectively sintered to produce complex geometries. When

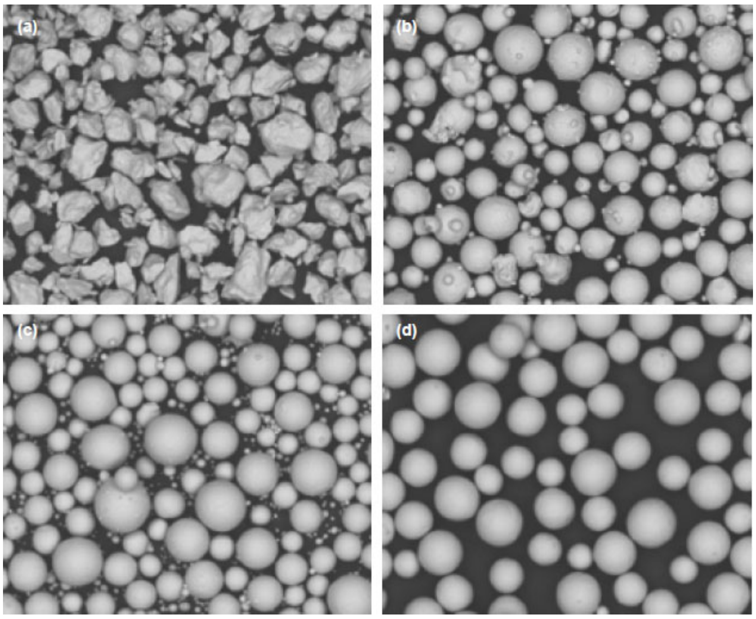

Figure 2: SEM images of Ti-6Al-4V powder. (a) Hydride-dehydride process, (b) gas atomization, (c) plasma atomization, and (d) plasma rotating electrode process [4].

all foam parameters (volume fraction, mean ligament thickness, and pore density) and material composition are satisfied, then the product is identically a metal foam. Limitations of powders are less drastic than with foams, but difficulties with material selection scaling exist. Only certain elements and alloys are workable as powders and their microscale deems large structures made from them impractical. Limits are where novel research begins and thus this work aims to extend them.

1.2 Review of Electron Emission Physics

1.2.1 Thermionic Emission

Considering the electron energy distribution, which is defined as the product of the density of states and the Fermi-Dirac probability distribution function, thermionic emission is the discharge of those electrons which travel approximately perpendicular to the surface. A quantum mechanical effect must be considered as well since reflection is possible due to uncertainty surrounding momentum caused by the width of the barrier. It follows that electrons emitted thermionically have energies slightly greater than the vacuum level. This energy, akin to the emission's namesake, is garnered with elevated temperatures. Mathematically detailed in later sections, the current density at a cathode ejecting such electrons is also dependent on the emitter's work function and the reflection coefficient [5].

Electron emission is an exothermic process. That is, the release of high energy electrons gives way for those with lower energies and thus the system cools. Two related methods are differentiated. Thermionic (TI) cooling involves thermionic emission over a potential barrier. When an electron is emitted thermionically, other electrons move to populate higher energy states to restore equilibrium. This step absorbs heat from the crystal lattice and thus cools the region before the emitter-barrier junction. The other phenomenon is thermoelectric (TE) cooling, where carrier transport is considered diffusive and joule heating is part of the heat balance. This contrasts from TI cooling for which the transport mechanism and joule heating are ballistic and none, respectively. Considering applications, TI devices typically operate in the nonlinear regime with large drain bias whereas the linear regime and small voltage differences are more common for TI devices [6].

1.2.2 Cold Field Emission

A cathode submerged in a strong electric field discharges electrons more easily as the emitting tip is made increasingly narrow. The constricted electron emitter has a reduced energy barrier and thus gives off electrons via Fowler-Nordheim tunneling at lower temperatures. Called cold-field-emission (CFE) for this reason, the design results in a beam with approximately 1,000 times higher electron density than that produced by a tungsten filament via thermionic emission [7]. A visualization of the energy barrier as it relates to emitter sharpness is provided in Figure 3.

Most CFE electons leave by Fowler-Nordheim tunneling since the electron needs a longitudinal energy close the emitter Fermi level. Internal electron states in bulk crystalline materials can be described using Fowler-Nordheim-type equations. CFE is also applicable for the Schottky emission regime, whereby electrons escape with energies exceeding the emitter

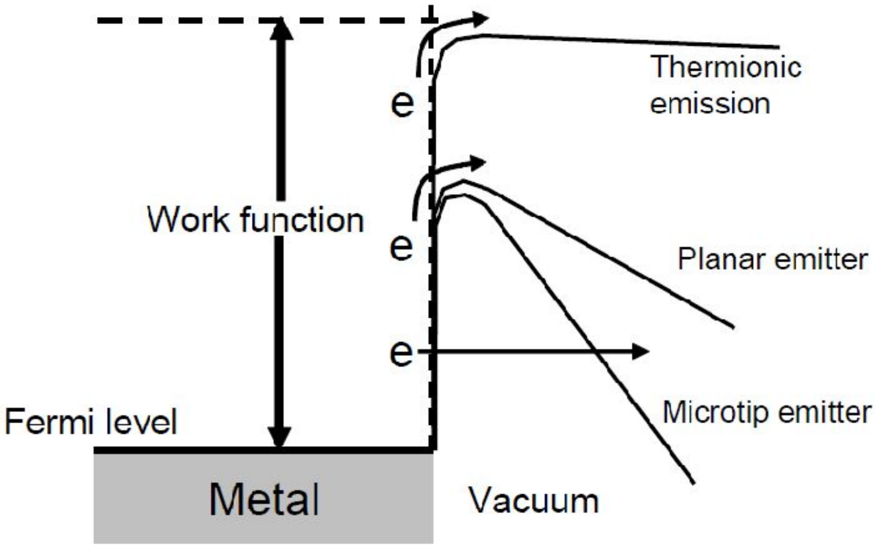

Figure 3: Field emission barrier schematic [8].

Fermi level [9].

1.2.3 Surface Photo-Electron Emission

Coupling of incident photons into surface plasmon (surface electromagnetic wave) oscillations causes increased electron emission for rough surfaces. Resulting in achievement of the 1921 Nobel Prize, Einstein gave a groundbreaking explanation of nonenhanced photoeffect. Various mechanical and chemical surface treatments alter the barrier to emission. Scattering in an oxide layer reduces electron current and layer thickness is inversely proportional to yield [10].

1.2.4 Secondary Electron Emission

When a beam of energetic primary electrons (PEs) impinges upon the surface of a solid, a sequence of collisions near the material's surface is initiated and the emission of electrons from the solid may be observed. This phenomenon, termed secondary electron emission (SEE), was first discovered by Austin and Strake in 1902. While studying the reflection of electrons by metals, they observed that more electrons were emitted than were incident. This indicated that the bombarding PEs can liberate electrons from the solid and opened the field to researchers and inventors alike.

SEE can be best understood by parsing the event into a few of its possible paths. A common scenario is a knock-on collision during which a portion of the PE beam is elastically reflected and the remainder penetrates into the solid. Energy from the penetrating PE beam is transferred to free electrons in the solid. This is followed by a collision cascade process during which the secondaries diffuse through the solid. As they penetrate deeper, they multiply and lose energy until they either rejoin the sea of conduction electrons or reach the surface with sufficient energy to emerge as true SEs. Another potential path is for a PE to lose some of its energy inside the solid, return to the surface, and escape as a result of Rutherford scattering; such electrons are called inelastically reflected primaries. Although it is common to employ the term SEs with reference to all electrons which escape from the surface and are collected by a positive collector electrode, the above remarks help distinguish three categories of electrons leaving the surface: (1) elastically reflected primaries, (2) inelastically reflected primaries, and (3) true SEs. These categories as well as all others included in the electron interaction volume are shown in Figure 4.

Secondary electron yield (SEY), δ, is the total number of SEs produced per incident PE, and is thus a measure of SE production. Generally, SEY curves can be described by the so-called universal curve, i.e., a hump which monotonically increases before the hump's maximum value and monotonically decreases after the peak. Unity on an SEY curve, or $\delta = 1$, means on average that for every incident primary electron, one secondary electron is emitted. An SEY less than unity means fewer secondaries are created than incident electrons are impinged. The inverse of this statement is also true [12]. A δ greater than unity suggests there exists an inherent risk for an electron avalanche, or a chain reaction of electrons separating from their positive ions by a potential gradient. Electron avalanches can result in arcing and other discharges, all of which are potentially fatal to spacecraft. This fact alone provides strong impetus to reduce SEY where possible and ideally keep yield below unity.

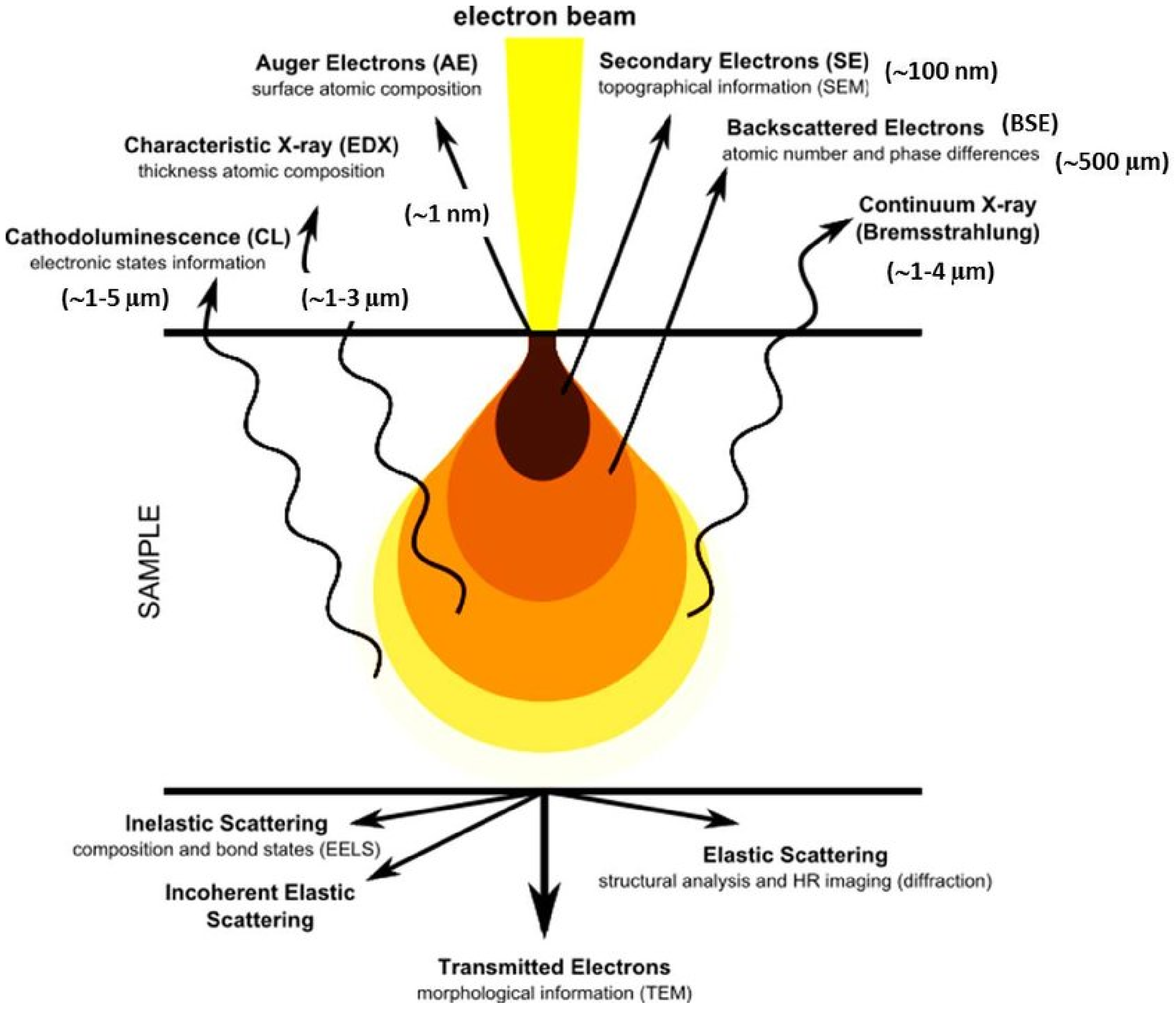

Figure 4: Electron beam interaction volume schematic [11].

At high energies, the SEE yield is low due to the fact that most of the SE production occurs too far below the surface to escape and it increases as energy decreases. A broad peak is reached eventually, corresponding to the condition where the incident PE penetration depth is comparable with the SE escape distance. At still lower energies, the yield again falls because of the lower energy input from the PE beam.

Applications of SEs are diverse. The quantity and state of SEs is relevant in scanning electron microscopes (SEMs), particle accelerators, plasma TV displays, waveguides, and satellites. Within these developments, it is critical to understand how SEs impact design performance and lifetime in concert with identifying measures to control yield. For most applications this condenses to keeping SEY at a minimum, though notable exceptions are Everhart-Thornley detectors in SEMs, for which the objective is the opposite.

1.3 Hypersonic Vehicle Environments

1.3.1 Flow Characteristics

Gas particles interact with hypersonic objects in vastly different ways depending on the attributes of the flow and the properties of the moving object itself. The fluid impacting the ram-facing side can be understood as a series of layers. These include the shock layer, entropy layer, and boundary layer. For hypersonic bodies, especially those with a wedge-like shape, the space between the shock and the object is diminished since the oblique shock angle is inversely proportion to Mach number. Considering Reynolds number as well, low values can result in a fully viscous shock layer while a high value can create nearly inviscid conditions. Shock waves, or energy carrying supersonic disturbance fronts, are categorized as normal, oblique, and bow. The fluid properties ahead of and behind a shock front are nearly discontinuous and the process is irreversible.

Considering practical application of shock theory, leading edges do not come to a point as they do in a perfect wedge. Commensurate with Figure 5, they are rounded for structural and thermal considerations. This curvature changes the angle of the oblique shock from one that is nearly normal at the tip to one that is significantly shallower along the body. It follows that the greatest change in entropy occurs at the tip and decreases with falling shock angle. Thus, a gradient exists and comprises the entropy layer. Residing inside this region is the boundary layer, for which the freestream velocity slows to a no-slip condition at the surface. Surface roughness and changing entropy adds vorticity to the flow. The boundary layer thickens with increasing Mach and decreasing Reynolds numbers. Thus, high speed flows tend to have a sufficiently far-reaching boundary layer such that viscous interactions occur with the normally inviscid region relatively far from the surface.

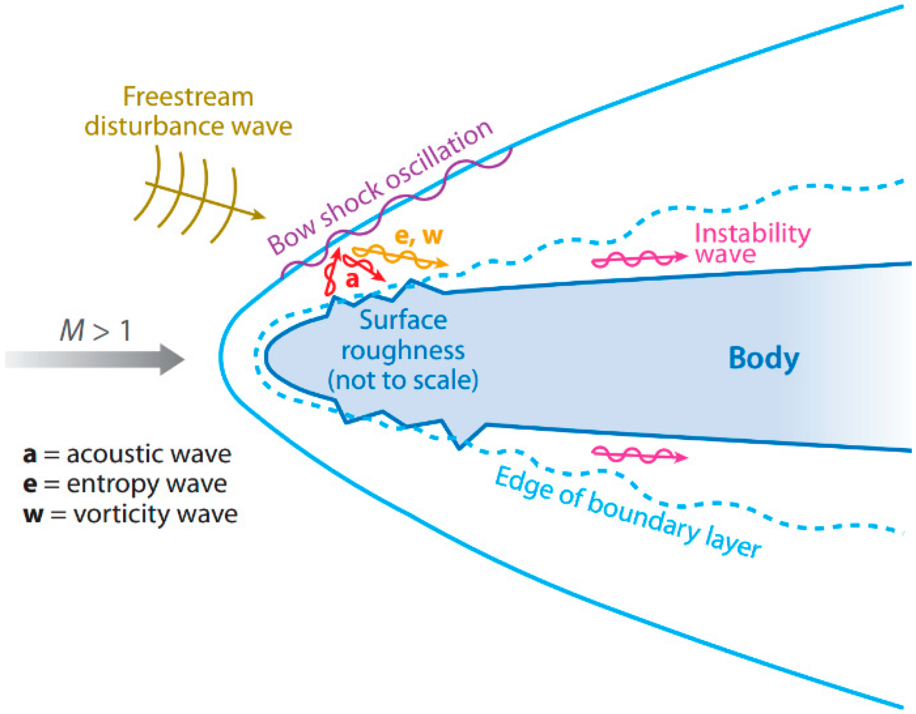

Figure 5: Super- and hypersonic flow layers.

Other relevant topics worth introducing are aerodynamic heating and the breakdown of continuum assumptions. Table 1 describes the chemical changes in air at heightened temperatures. A vehicle traveling through a working fluid that dissociates oxygen molecules, synthesizes nitrogen or nitrogen monoxide, or ionizes oxygen or nitrogen atoms is traveling through a chemically reacting boundary layer and should be modeled as such.

Temperature [K]	Chemical Change
800	Molecular Vibration
2,000	O_2 Molecules Dissociate
4,000	N_2, NO Forms
9,000	O_2, N_2 Atoms Ionize

Table 1: Elevated Temperature Chemical Changes in Air

Since hypersonic vehicles can operate in low density fluid environments, it is prudent to recognize the free-molecule flow situation and how it differs from continuum mechanics.

Atoms interact with the moving object and not with each other. Friction is negligible so the flow velocity at the object's surface is nonzero. Moreover, the temperature of the surface and the neighboring gas particles are not necessarily equal. The latter two conditions are named velocity slip and temperature slip, respectively [13].

1.3.2 Flow Regimes

Building on the understanding that the flow state alters assumptions needed to accurately model hypersonic flight, one can sort conditions into a series of regimes. Commencing this discussion with the fastest traveling vehicles (those exceeding speeds of approximately 12 km/s), the heat transfer between the body and the adjacent flow is dominated by radiation. Within this regime, the gas is either optically thin or thick, referring to whether the transmittance is sufficient to consider reabsorption. Freestream flows between 10 and 12 km/s are most accurately modeled as non-radiating plasmas. This regime is characterized by the significant population of ionized electrons in the stagnated flow. For this reason, the gas temperature is best modeled as separate from that of the electrons. Slightly slower flows tend to experience molecular dissociation as they interact with the body's bow shock. Temperature of the flow in this category for Earthbound hypersonic vehicles is about 2,000 to 4,000 K. Flows with temperatures of roughly 1,000 K have sufficient energy that the vibrational and rotational temperatures should be parsed. The flow is still considered an ideal gas, but requires a two-temperature model. The least energetic hypersonic flows can be modeled as ideal gases since temperatures are not sufficiently high to cause substantial dissociation, formation, or ionization of air molecules [14].

1.3.3 Vehicle Designs

Design criteria for hypersonic vehicles must take into account the extreme heat flux encountered by the body at such high speeds. Efficient transfer of heat is paramount for mission success. This is highlighted by the failure mode for the first vehicle to exceed Mach 5. The two-stage Bumper rocket launched in February 1949 but burned and disintegrated on re-entry. The particular geometry of the vehicle is dependent on the altitude and speed of operation. Rockets momentarily pass through the atmosphere at hypersonic speeds before traveling within the near vacuum of space. This fact, along with their purpose to transport cargo and/or humans gives the ram-direction an ogive, parabolic, or conical shape. Another key form determiner is the need or lack thereof to produce lift. Missiles, despite operating primarily within the atmosphere, tend to have a rounded nose like a rocket since they often carry a warhead payload. Secondly, they are designed to avoid lift production in an effort to minimize drag. Re-entry vehicles are similar to gliders in that they produce lift, but differ in their design purpose and preferred geometry. These vehicles use a blunt surface to steadily fall through the atmosphere with an optimal amount of aerobraking.

Recent hypersonic vehicle requirements focus on reducing the size of vehicles, increasing their operating speeds, and raising their lifespan. Ram- and scramjet propelled vehicles as well as hypersonic gliders have been researched and developed. A scramjet aircraft in development at the time of writing is named the Hypersonic Technology Demonstrator Vehicle (HSTDV). Headed by the the Indian Defense and Development Organization, the vehicle is designed to fly autonomously for 20 seconds under the power of a scramjet engine and reach Mach 6.5 at 20 miles in altitude [15]. A recent ramjet program called Blackswift was funded through the DARPA Falcon Project until 2014. The HTV-2 vehicle, incorporating an aeroshell prototype and a carbon-carbon manufacturing approach, briefly reached Mach 22 during a critical flight test but ended in a catastrophic anomaly [16].

With the upswing of United States private space companies, a variety of architectures are being pursued to return humans from the International Space Station (ISS) as well as to land them on other atmospheric celestial bodies; Mars, Europa, and Titan are among the most promising. The future of human spaceflight could include Boeing's CST-100 Starliner, SpaceX's Crew Dragon and Starship, Blue Origin's New Glenn, and NASA's Orion Multi-Purpose Crew Vehicle. To ground this research in practicality, it is worth discussing some relevant design decisions that have gone into one of these architectures. Given its significant public disclosure relative to the other vehicles, the Crew Module in the Orion spacecraft shall be the example.

As illustrated in the exploded view presented in Figure 6, Orion is the assembly of three sections: From left to right these include the service module, crew module, and Launch Abort System. The discussion is directed at the center portion since the crew module is what endures aerodynamic heating upon atmospheric entry.

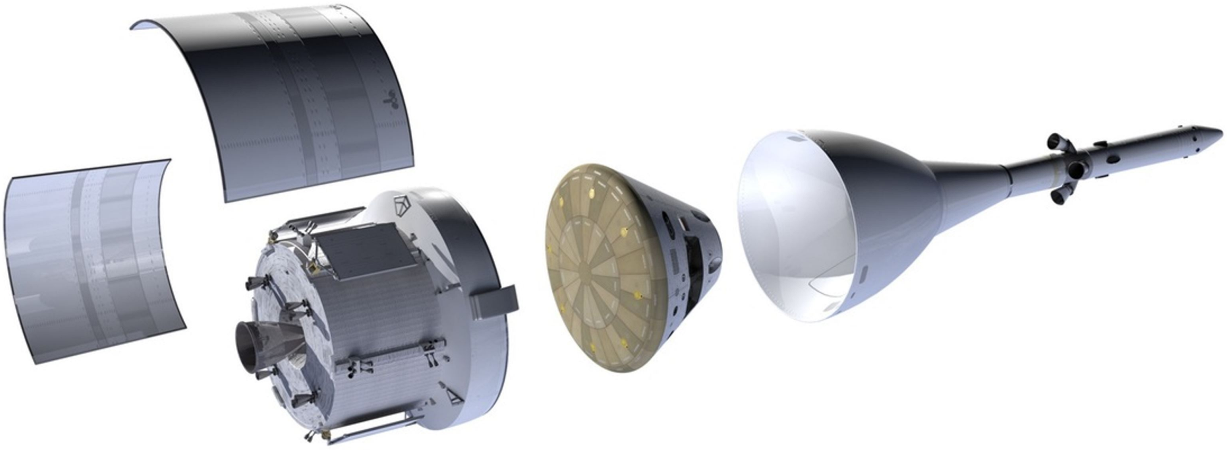

Figure 6: Orion Multi-Purpose Crew Vehicle [17].

The body is a 3.3 m tall, 57.5° frustrum, and concludes in a 5.02 m heat shield base. Able to withstand temperatures of 3,070 K, the shield is made with a titanium structure and AVCOAT ablative panels [17]. The design is a response to expected Mars entry heat rates peaking around 125 W/cm^2 and resulting in surface temperatures of 2,770 K [18]. AVCOAT was chosen over PICA to reduce gaps, decrease the number of unique pieces, and leverage heritage from the Apollo program. A dedicated schematic of the crew module is shown in Figure 7.

The other modern re-entry vehicle architectures follow similar guidelines with the exception of SpaceX's Starship. This particular design emphasizes reusability and simplicity. One vehicle is responsible for entry, descent, and landing (EDL) as well as Martian ascent. The gives the vehicle an overall appearance between the Space Shuttle and the Mercury Atlas rocket. Ram- and scramjet propelled vehicles as well as hypersonic gliders have different requirements from re-entry vehicles and thus have contrasting design criteria. The aforementioned Blackswift project by DARPA laid the groundwork for modern hypersonic

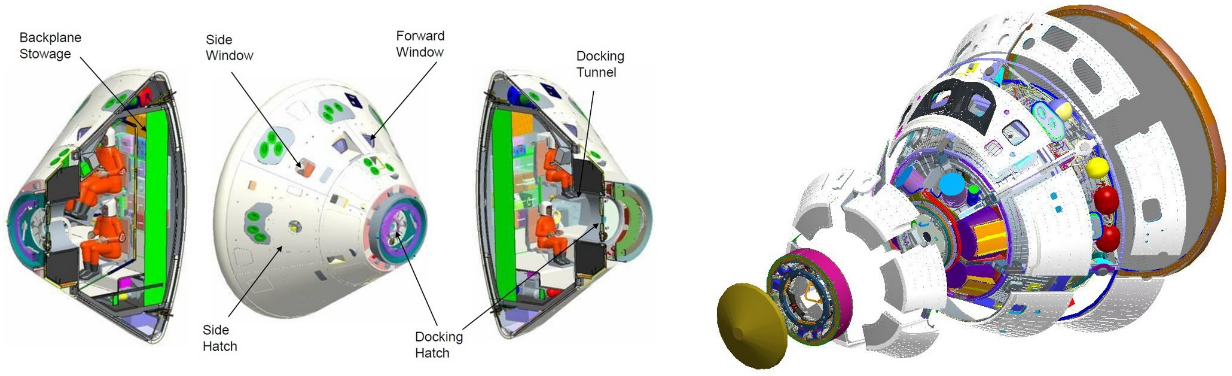

Figure 7: Orion crew module [17].

vehicles, but was itself canceled in October 2008. In place of Blackswift came the Boeing X-51 Waverider. Illustrated in Figure 8, this 7.62 m long vehicle cruises at Mach 5 and operates at 21,000 m. The hydrocarbon-fueled scramjet engine at the vehicle's aft is produced by Pratt and Whitney and is designated SJX61.

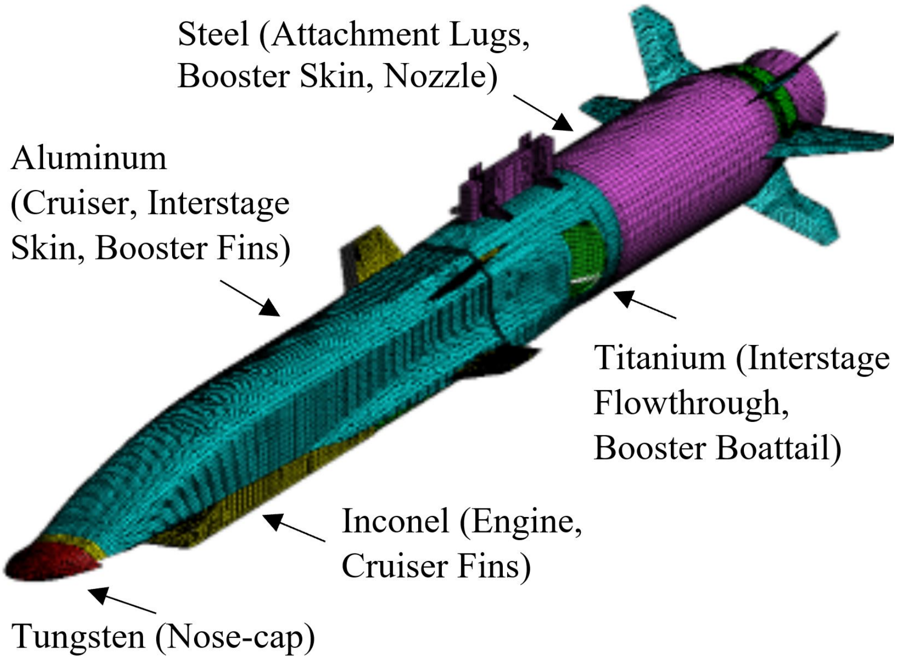

Figure 8: X-51 hypersonic test vehicle.

The leading edge is made with tungsten and the remainder of the vehicle incorporates Inconel, aluminum, steel, and titanium. Thermal protection materials are included for additional temperature control. Light-weight ablators, both sprayed-on and honeycomb reinforced, are part of the design. Boeing proprietary reusable insulation tiles are also installed on the vehicle's underside [19]. The X-51 set duration and distance records for continuous air-breathing hypersonic flight, but at 230 nautical miles is too short for long-range reconnaissance or space travel. Thus, the US Air Force is using the knowledge gained from the program toward its High Speed Strike Weapon (HSSW). The program is expected to cost nearly a billion dollars and is motivated by current Russian and Chinese national hypersonic initiatives [20].

1.4 Space Electric Propulsion Environments

1.4.1 Environmental Conditions

Vehicles which operate in space are exposed to a variety of conditions which can impair nominal performance. The primary concerns are related to micrometeroids and orbital debris (MMOD), upper atmospheric drag, spacecraft electrostatic charging, and cosmic radiation. MMOD is clearly a combination of natural and artificial causes. Micrometeroids, or small rock particles in space which typically have a mass of under 1 gram, contribute on the order of 10 million tons of cosmic material to the Earth's surface every year [21]. In their path to Earth, these numerous particles are hurtling past, and occasionally crashing into, spacecraft in all orbits. Responses to this type of orbital debris are largely defensive in nature. That is, structural additions such as Whipple shields and armor-like multilayer insulation coverings, aim to protect the spacecraft from the debris rather than stop the rocks from colliding in the first place.

The other type of debris is fragments of, or dead, spacecraft. While the same structural defenses are employed to guard against the sporadic interception of “space junk”, more active approaches are being put in place to limit the addition of such artificial MMOD and reduce the number of existing pieces in orbit. Regulations are becoming stricter for new vehicles to be designed with an end-of-life disposal operation. Disposal can involve propulsion to a less crowded orbit or reducing speed as to initiate a deorbit. Passivation and design-for-demise are related efforts whereby all fuel is depleted at the end of a spacecraft's mission and vehicles are designed in a way that an uncontrolled reentry would result in minimal environmental impact. Between the two types of debris that encompass MMOD, the potential of impact is significant. Figure 9 depicts the estimated impact flux on the Sentinel-1 spacecraft. The sun-synchronous satellite endures more than 70 hits per square meter over the course of a year on some of the most exposed components. Certainly the magnitude is dependent on a spacecraft's particular orbit, but with the majority of debris impacting at roughly 15 km/s, even micro-scale debris can cause significant damage [22].

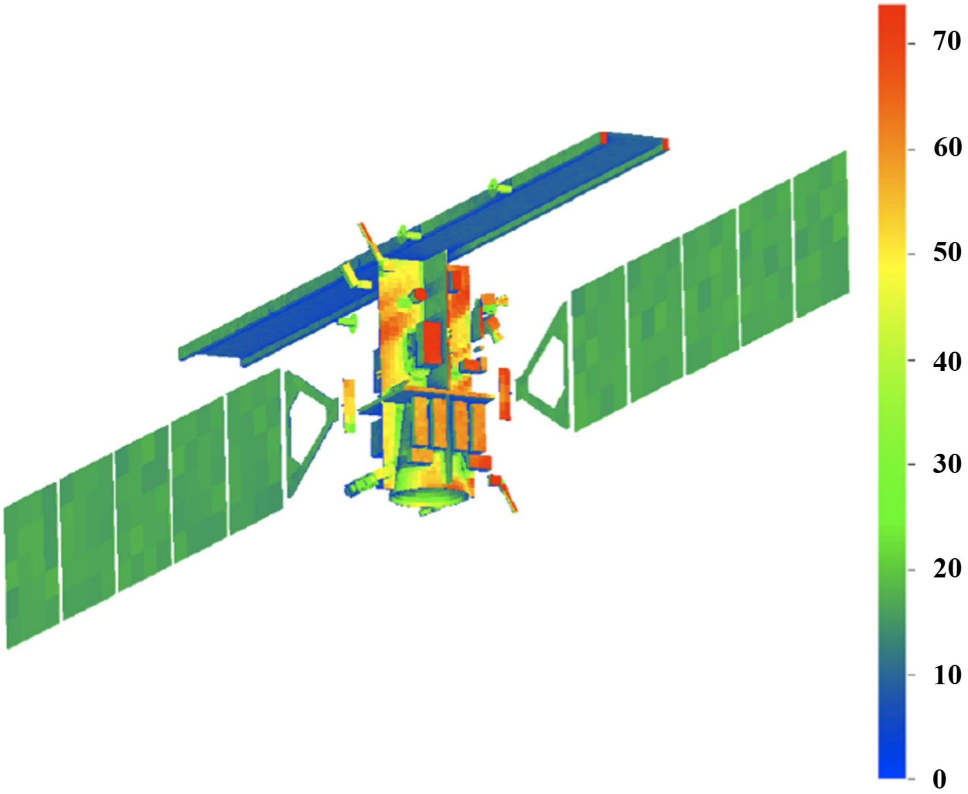

Figure 9: MMOD impact flux model for the Sentinel-1 spacecraft. Flux magnitudes have units of $1/\mathrm{m}^2/\mathrm{yr}$. Adapted from [22].

Upper atmospheric drag is another space environments factor which most spacecraft architectural designs must consider. While the atmospheric density in space is insignificant when compared with that at Earth's sea level, it is still consequential even at high altitudes.

The reason for this is that while Earth may not normally have a substantial atmospheric density above low Earth orbit (lowest 2,000 km of altitude), the Sun adds energy to the atmosphere and can cause satellites in middle Earth orbit (2,000 km to 35,786 km) to periodically experience increased drag.

The third major concern for spacecraft is electrostatic charging. This phenomenon is most pronounced in the magnetosphere as it has a relatively high plasma density. The near-Earth region of space is differentiated into the ionosphere, the plasmasphere, and the plasmasheet. The first subregion extends to roughly 1,000 km above the Earth's surface and contains a high proportion of neutral atoms. Thermal energies here are cold (generally only a few tenths of a volt). The plasmasphere is a roughly toroidal region above the ionosphere and is bounded by the closed geomagnetic field lines at about Earth's 60° magnetic latitude. Thermal energies are similar to the lower subregion, but the electron density is reduced by over an order of magnitude at the plasmapause. The plasmasheet subregion, however, continues along the magnetotail and contains substantially higher electron energies at 1 keV. It is worth noting that these subregions, and their corresponding plasma properties, are often disturbed by magnetospheric substorms. These storms result from disruptions to the solar wind and the magnetic field and can be accompanies by several tens of keV electron energies. Such changes to the plasma environment can damage spacecraft if vehicle designs do no properly protect against such events.

Spacecraft in Earth-orbit gain an electrostatic charge by way of the plasma flux, secondary emission and backscattered electrons, and photoemission. Each of these mechanisms delivers electron and ion currents to the spacecraft in different proportions. The plasma flux predominately delivers current though electrons and depends on the spacecraft potential and the characteristics of the local plasma. Secondary emission and backscattered electrons are correlated with the incident plasma energy, the materials on the spacecraft's surface, and the spacecraft potential. Photoemission also is impacted by the surface material and spacecraft potential, but differs in that it also depends on the the amount of surface illumination through solar ultraviolet light [23].

The last space environment condition we will discuss is cosmic radiation. The energies of primary cosmic rays are exceptionally high and range from 1×10^{9} to 1×10^{20} eV [24, 25]. The majority are at the lower end of this range, but even those are highly energetic. Cosmic rays are composed primarily of bare nuclei of hydrogen and helium. Nuclei of heavier elements exist as well, but with far lower frequency. Additionally, a small percentage of cosmic rays are stable particles of antimatter, such as positrons and antiprotons. Cosmic rays can be dangerous to satellites since the high-energy particles can damage electronic integrated circuits. For instance, cosmic rays can corrupt data and cause improper performance by central processing units. A historical example is the Voyager 2 spacecraft which experienced a single bit flip in 2010 and subsequently malfunctioned due to a cosmic ray.

While this discussion has largely pertained to uncrewed missions, it is worth mentioning that cosmic radiation is a significant concern for human payloads as well. The dose absorbed by an astronaut in a year on the International Space Station (ISS) is roughly eight times the maximum allowed dose by a Department of Energy radiation worker in the same period. Furthermore, a two-way transit between Earth and Mars could cause astronauts to take roughly four times the dose of the astronauts who spend a year on the ISS [26]. This does not even account for the time that an astronaut would stay on Mars. It is clear that space is a hostile environment, but now we have a better sense for how to prepare. MMOD, upper atmospheric drag, spacecraft electrostatic charging, and cosmic radiation are significant space environments issues and proper precautions are needed to avoid damaging hardware and jeopardizing human life.

1.4.2 Propulsive Designs

Whether a spacecraft needs to maintain its altitude (known as station keeping), raise its orbit, and/or produce a delta-v with low thrust requirements, electric propulsion is an efficient alternative to chemical propulsion. Three categories of electric propulsion devices include electrostatic, electrothermal, and electromagnetic. Electrostatic devices are characterized as those which use a static electric field in the direction of the acceleration. The main types in this category include gridded ion thrusters and Hall-effect thrusters. As we will do for the other two major electric propulsion categories as well, we will briefly discuss the design architectures of each type.

Gridded ion thrusters have been in use since the NASA SERT-1 (Space Electric Rocket Test) launch in 1964. Since then, integral programs have included NSTAR (NASA Solar Technology Application Readiness), XIPS (Xenon Ion Propulsion System) and NEXT (NASA Evolutionary Xenon Thruster). The fundamental concept employed in gridded ion thrusters is biasing metallic plates to create a voltage potential and flowing positive ions through openings in the plates. A significant voltage potential across the grids will cause the ions to flow across them at high speed, and thus produce thrust. These positive ions are originally neutral propellant atoms, but they are forced to interact with electrons supplied by an electron gun causing them to become ionized. Finally, the positive ions are neutralized by an externally mounted electron gun which supplies negative charge to the exiting flow. Figure 10 illustrates the various components in a Kaufman configuration of a gridded ion thruster. This version maximizes ionization efficiency with the use of solenoids.

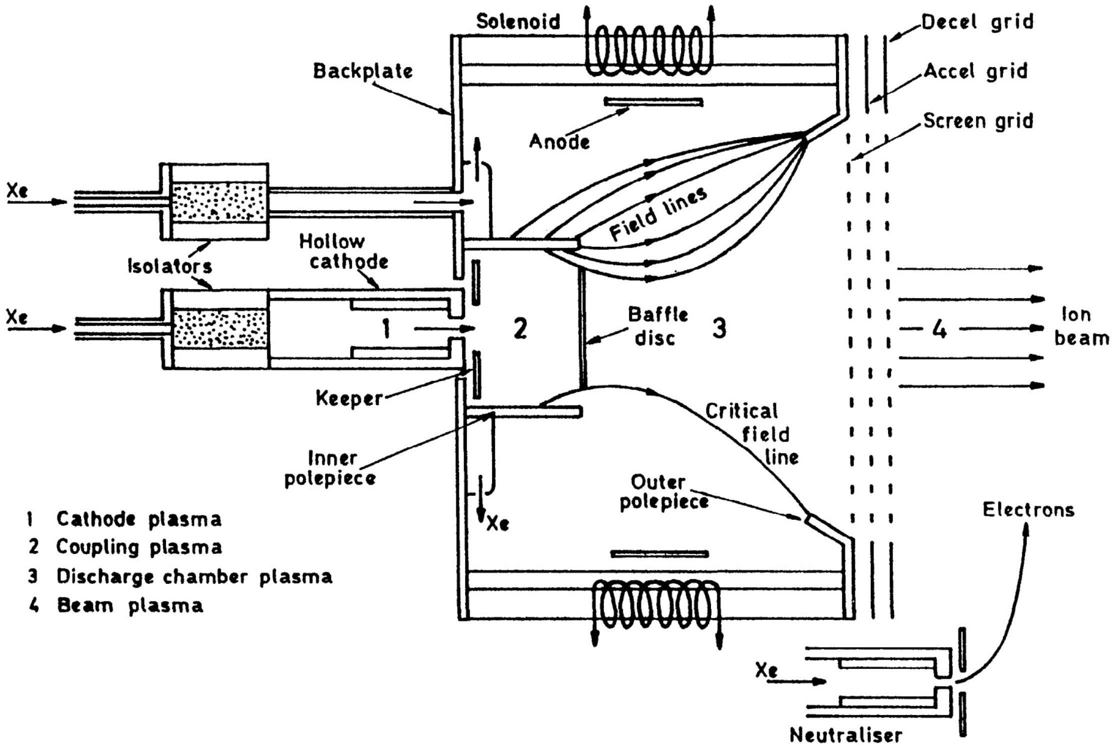

Figure 10: Schematic of the Kaufman version of a gridded ion thruster. Borrowed from [27].

While the United States was focused on gridded ion thrusters in the 1960s, the Soviet Union turned their attention to Hall thrusters during that time. A weather observation satellite was the first to carry a thruster of this kind. An SPT-50 (Stationary Plasma Thruster) flew on a Soviet Meteor Spacecraft for the purpose of orbit stabilization. Thrust on the SPT-50 was limited to 20 mN. The Aerojet BPT-4000 was the first American Hall thruster to be operational in space. It launched on a geosynchronous orbit satellite called AEHF (Advanced Extremely High Frequency) in August of 2010. Most recently, each satellite in the SpaceX Starlink constellation has been equipped with Hall thrusters which ionize krypton gas to manuever, stationkeep, and guide the spacecraft during end-of-life atmospheric re-entry operations.

Rather than accelerating ionized propellant atoms with biased grids, a Hall thruster uses a set of solenoids to create a radially directed magnetic field and a cathode and anode to create an axial electric field with a low-pressure direct current discharge. Similar to gridded ion thrusters, the anode is the gas injector and the cathode provides electrons to neutralize the flow. Figure 11 illustrates the generic Hall thruster design. The propellant is often selected to be xenon because of its high atomic mass and low ionization energy, though krypton is sometimes chosen instead to reduce the cost of propellant. While single channel Hall thrusters peak around 50 kW of power, there are nested Hall thruster versions which output 100 kW. Nested Hall thrusters have concentric channels and share a central cathode. One of the most promising experimental 100 kW Hall thrusters is known as the X3. It produced 5.4 N of thrust using a 400 V discharge voltage and xenon propellant. Furthermore, it produced a specific impulse of about 2,400 s and has been determined to be as high as 2,650 s under lower thrust operating conditions [28].

Another category of electric propulsion devices is electrothermal. Whereas electrostatic designs produce acceleration mostly by the Coulomb force, these machines use electromagnetic fields to create a plasma which energizes the propellant. More similar to chemical propulsion, electrothermal devices typically flow propellant through a nozzle. The most prevalent types of thrusters in this category include resistojets and arcjets. The name resistojet derives from the working principle that a resistor, often a coiled wire heating element,

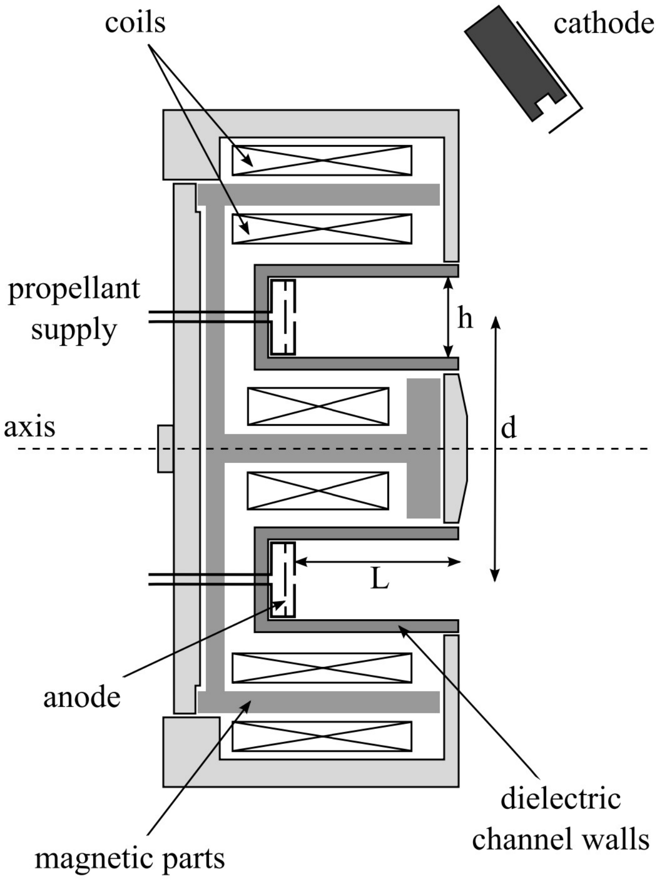

Figure 11: Schematic of a single channel Hall-effect thruster. The required power and thrust are partially dependent on the depth of the channel, L, the diameter of the channel, d, and the channel gap distance, h. Borrowed from [29].

is used to elevate the temperature of the propellant prior to it being flowed through a nozzle. This process causes the propellant to expand and exit with a higher specific impulse. While the design is less efficient than that of most other electric propulsion devices, its simplicity helped it to be chosen for attitude control on the the Iridium satellite constellation, among others. Examples of resistojet thrusters include the Aerojet Rocketdyne MR-501/MR-502 series. In terms of performance, the MR-501B uses hydrazine and produces up to 0.37 N of thrust with a specific impulse of approximately 300 s.

The main difference between a resistojet and an arcjet is the latter induces electrical breakdown in the propellant prior to the the atoms exiting through a nozzle. Arcjet thrusters typically flow hydrazine or ammonia. Peak thrust is often somewhat lower than resistojets.

Specific impulse, however, is generally higher. Aerojet Rocketdyne won a contract from Lockheed Martin in 2015 to deliver MR-510 arcjet thrusters for two updated A2100 satellites. The MR-510 is a hydrazine propelled arcjet thruster which outputs about 250 mN of thrust at a specific impulse of roughly 600 s. Low-power arcjets have also been developed, though they are most often used in laboratory settings on solid ground rather than in space. Changes in nozzle geometry are made along with incorporating different internal materials (e.g., boron nitride, molybdenum, and graphite foil) to better suit propellants such as hydrogren and argon. An advantage of arc jet thrusters created for this purpose is that they are modular, meaning they are easy to disassemble and reassemble [30].

The third category of electric propulsion devices we will discuss is electromagnetic thrusters. They typically use a combination of electric and magnetic forces to accelerate propellant and produce thrust. An important type of device in this category is the pulsed plasma thruster. Used for momentum management and pitch control, these devices electrically ignite solid propellant and exhaust it supersonically. This is achieved by charging a capacitor and sparking it with an igniter to produce a plasma. Creating plasma in this manner causes the surface of the solid propellant to ablate and ionize. These atoms are then accelerated toward the outlet by the Lorentz force. Some pulsed plasma designs include a spring to push the unused propellant forward and continually provide a fresh surface to sustain the process. This type of thruster was first used in space by the Soviet Zond 2 spacecraft in 1964. More recently, the EO-1 (Earth Observing 1) spacecraft used a dual-axis variant which produced 860 μN of thrust. While this magnitude is insufficient for most delta-v operations, it is useful for precise adjustments. Additionally, it only consumes 70 W making it favorable for most power budgets. Clearly there are a variety of methods to create propulsion with electricity. Still, they share some common themes. Thrust is typically low, but operation can be sustained for hours or even weeks. Propellant is typically gaseous, though a few burn solids. Finally, power consumption and scalability are important issues that will guide the future of electric propulsion designs.

1.4.3 Device Lifetime Considerations

The amount of time that electric propulsion devices can operate nominally is greatly impacted by two concepts that were introduced earlier, secondary electron emission and thermionic emission. A key component that is impacted by thermionic emission is the orificed hollow cathode since it is a plasma source of electrons. Thermionic emission, first discussed in Section 1.2.1 is related to the quantity of electrons being emitted from the cathode whereas secondary electron emission, initially examined in Section 1.2.4, is associated with the lifetime of the electrons in the discharge [31]. Hollow cathodes are used to neutralize the positively charged flows which exit such electric propulsion devices as gridded ion thrusters and Hall thrusters. A schematic of this critical component is provided in Figure 12. Partly due to the tendency of low work function emitter materials to have a more robust thermionic emission, tungsten infiltrated with barium oxide (BaO-W) and lanthanum hexaboride (LaB_6) are commonly used.

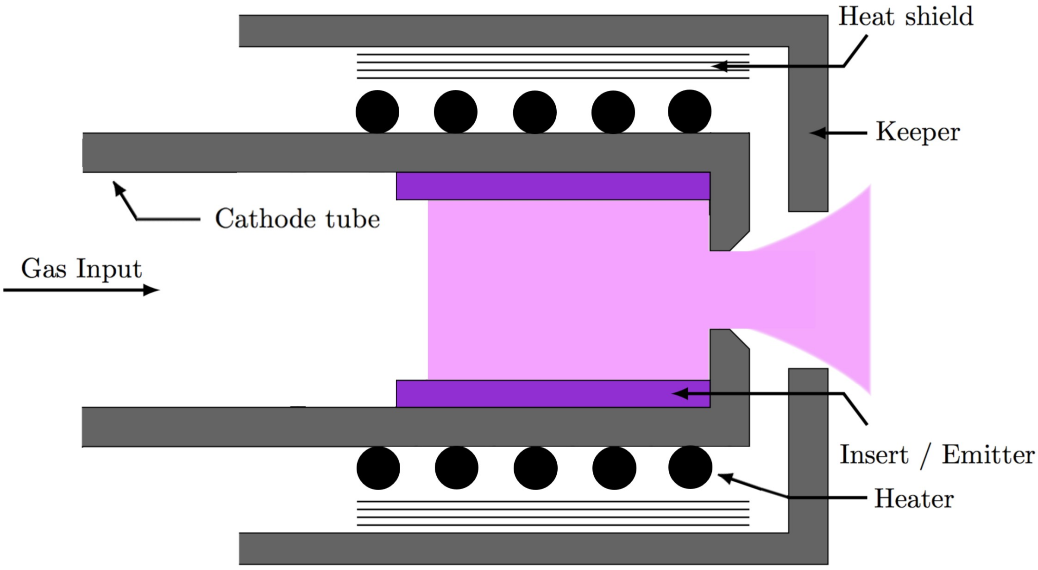

Figure 12: Schematic of a hollow cathode. Adapted from [32].

Hollow cathodes have significant risks of failure that can be mitigated by understanding the mechanisms by which the device can become damaged. Since thermionic emission is highly dependent on temperature, a heater is incorporated into the design. While necessary for efficient electron emission, this exposes neighboring materials to high temperatures. Furthermore, since the operation of electric propulsion devices can be intermittent, the heated materials are frequently cycled through cold and hot temperatures. Though these cycles are ameliorated with the use of heat shields, as illustrated in Figure 12, the cathode tube and the keeper tube are still susceptible to thermal stresses and fatigue.

Electrospray thrusters, or colloid thrusters, are particularly sensitive to secondary electron emission. These electrostatic devices, which produce micronewton level thrust using ionic liquid, are related to gridded ion thrusters and Hall effect thrusters. Interactions between ions and molecules at the walls and extractor grids, among other components, limit and degrade the lifetime, thrust, and efficiency of these devices. Similarly, secondary electrons can neutralize and decay the propellant as some backflow into the emitter and cause the plume potential profile to deviate from nominal [33]. Backstreaming secondary electrons may also cause neutral mass loss via Ohmic dissipation [34].

1.5 Thesis Objectives

Electron emission is a common phenomenon that can severely influence the magnitude of surface heat flux in space electric propulsion devices as well as the leading edge of hypersonic aircraft. Metamaterials that are fabricated from reticulated metallic foams can be designed to control electron emission and also to cool leading edges by transpiration cooling. This work seeks to achieve the following objectives:

1. Experimentally quantify SEY for copper foam relative to flat copper, and understand the relationship between the micro-geometry of the foam and its SEY.

2. Use Monte-Carlo simulations to unravel the physical mechanisms that control SEY in reticulated foam materials.

3. Generalize findings to elements and micro-architectured materials other than flat and copper foam.

4. Determine the optimal distribution of tungsten foam micro-geometry as to achieve maximum evaporative cooling of a hypersonic leading edge wedge.
5. Deduce the feasibility of using W-foam infiltrated with LaB_6 for mass evaporation and thermionic emission as cooling mechanisms for hypersonic vehicles.

CHAPTER 2

Research Background

2.1 Thermal Energy Transport for the Leading Edge of Hypersonic Vehicles

2.1.1 Heating Modes

Heat flux at the leading edge of hypersonic vehicles, q_w, is the summation of the heat flux from the gas to the wall, q_{gw}, and the radiative heat transfer, q_r. This summation is written simply as

$$q_w = q_{gw} + q_r \tag{1}$$

Figure 13 illustrates the general idea. Typically a curved surface, the leading edge endures stagnated flow and the surrounding regions are aeroheated by the energetic flow impacting these areas. The body shall be analyzed in two parts, the curved frontal section and the flat portion which trails the curved segment. The boundary is considered adiabatic and the direction of flight is to the left such that the leading edge faces the ram direction. Note that the symbol s, specifying the position along the surface, shall be exchanged for the variable x in the proceeding derivations.

The heat balance of the hypersonic leading edge can be analyzed by discussing compressible boundary-layer theory. Robust viscous dissipation causes the flow to be chemically reacting and high temperature. The gas is assumed to be calorically perfect, that is the specific heat capacity, c_p, is considered constant ($h = c_pT$) and the gas is ideal ($p = \rho RT$). Note that h is enthalpy and R is the gas constant. One involves the Navier-Stokes equations and reduces them to apply to the boundary layer. For which u is the speed of the gas in the

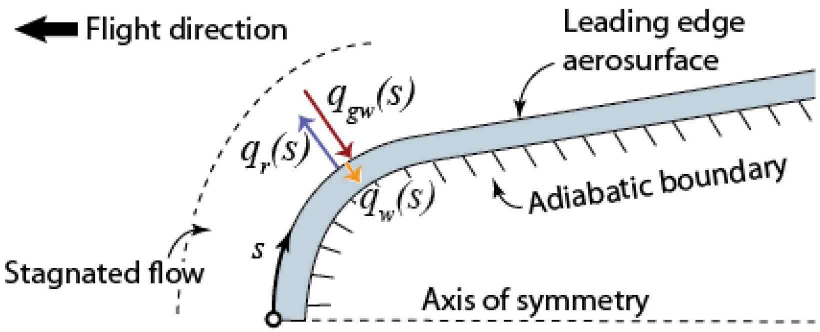

Figure 13: Heat flux balance schematic for leading edge [35].

direction of flow and v is the speed normal to it, continuity can be written as

$$\frac{\partial(\rho u)}{\partial x} + \frac{\partial(\rho v)}{\partial y} = 0 \tag{2}$$

With p_e defined as the pressure at the outer edge and μ being the flow viscosity, momentum in the x-direction is written as

$$\rho u \frac{\partial u}{\partial x} + \rho v \frac{\partial u}{\partial y} = -\frac{dp_e}{dx} + \frac{\partial}{\partial y}\left(\mu \frac{\partial u}{\partial y}\right) \tag{3}$$

The pressure is assumed constant in the normal direction to the flow. This is accurate for all but exceptionally large Mach numbers. The trivial expression is simply

$$\frac{\partial p}{\partial y} = 0 \tag{4}$$

Lastly, the equation which describes the energy balance is

$$\rho u \frac{\partial h}{\partial x} + \rho v \frac{\partial h}{\partial y} = \frac{\partial}{\partial y}\left(k \frac{\partial T}{\partial y}\right) + u \frac{dp_e}{dx} + \mu \left(\frac{\partial u}{\partial y}\right)^2 \tag{5}$$

In terms of boundary conditions, the velocity and height are zero ($u = v = y = 0$) and the temperature is that of the wall ($T = T_w$). Furthermore the wall is considered adiabatic, so the temperature gradient $\left(\frac{\partial T}{\partial n}\right)_w = 0$. n is defined as the coordinate normal to the wall. Concerning the boundary-layer edge, the thickness is unbounded ($y \to \infty$), and the flow velocity and temperature are defined at the edge ($u \to u_e$, $T \to T_e$)

To find the heat flux around the leading edge of hypersonic vehicles, one can use self-similar boundary layers to obtain self-similar solutions. This involves a transformation from

(x, y) to (ξ, η) named the Lees-Dorodnitsyn transformation. A beneficial property is the flow field does not depend on the location along the surface. The first coordinate, ξ, is defined as

$$\xi = \int_0^x \rho_e u_e \mu_e dx \tag{6}$$

and the second coordinate, η, as

$$\eta = \frac{u_e}{\sqrt{2\xi}} \int_0^y \rho dy \tag{7}$$

Applying the transformation to the momentum and energy balance equation, one gets equivalent forms that are more amenable to practical applications. Defining the Chapman-Rubesin factor, $C = \rho\mu/\rho_e\mu_e$ and $f' = \frac{\partial f}{\partial \eta} = \frac{u}{u_e}$, momentum in the x-direction for two-dimensional compressible flow is written as

$$(Cf'')' + ff'' = \frac{2\xi}{u_e}\left[(f')^2 - \frac{\rho_e}{\rho}\right]\frac{du_e}{d\xi} + 2\xi\left(f'\frac{\partial f'}{\partial \xi} - \frac{\partial f}{\partial \xi}f''\right) \tag{8}$$

Momentum in the y-direction simply becomes

$$\frac{\partial p}{\partial \eta} = 0 \tag{9}$$

Assigning a nondimensional static enthalpy, $g = g(\xi, \eta) = \frac{h}{h_e}$ and involving the Prandtl number, $Pr = \mu c_p/k$, where k is the thermal conductivity, the transformed energy balance is written as

$$\left(\frac{C}{Pr}g'\right)' + fg' = 2\xi\left[f'\frac{\partial g}{\partial \xi} + \frac{f'g}{h_e}\frac{\partial h_e}{\partial \xi} - g'\frac{\partial f}{\partial \xi} + \frac{\rho_e u_e}{\rho h_e}f'\frac{du_e}{d\xi}\right] - C\frac{u_e^2}{h_e}(f'')^2 \tag{10}$$

From the previous self-similar solutions, the governing equations for a compressible stagnation point boundary layer are

$$(Cf'')' + ff'' = (f)^2 - g \tag{11}$$

and

$$\left(\frac{C}{Pr}g'\right)' + fg' = 0 \tag{12}$$

The results to these governing differential equations are given and used in Section 4.3.

2.1.2 Thermionic Cooling

Sir Owen Willans Richardson earned the Nobel Prize in Physics in 1928 for his fundamental work on thermionic emission. Taking a similar form to the Arrhenius equation, he derived a mathematical statement relating emitter temperature to emission current. Current density, J is a function of a constant defined as A_G, temperature, T, work function, W, and Boltzmann constant, k. $A_G = \lambda_B(1-\bar{r})A_0$ where λ_B is a correction that is material-specific and $A_0 = \frac{4\pi mk^2 q_e}{h^3}$. m is electron mass, $-q_e$ is the elemenatary charge, and h is Planck's constant. Sir Owen's name is attached to the relation, and thus Richardson's law is written as

$$J = A_G T^2 e^{-W/kT} \tag{13}$$

Summarizing the derivation, one starts with the Fermi-Dirac distribution function to account for the probability of certain energy levels being occupied. With E_f defined as the Fermi energy, the Fermi function is

$$f(E) = \frac{1}{1+e^{(E-E_f)/kT}} \tag{14}$$

where E is the energy of the moving electron and is solely kinetic. Thus, $E = \frac{1}{2}m(v_x^2 + v_y^2 + v_z^2)$. Considering a differential volume of the electron and its associated component-wise momentum, one must know the number density of electrons occupying quantum states to know its current density. Recalling that each state can hold two spin directions ($+\frac{1}{2}$ and $-\frac{1}{2}$), the differential number density in the momentum interval is stated as

$$dn = \frac{2}{h^3} f(E) dp_x dp_y dp_z \tag{15}$$

Taking the x-axis to be the emitting direction, one writes the differential current density as

$$dJ_x = q_e v_x dn \tag{16}$$

Integrating the differential current density over the volume and noting $v_x = p_x/m$, the total emission current is shown to be

$$J_x = \frac{2q_e}{mh^3} \int_{p_x'}^{\infty} \int_{-\infty}^{\infty} \int_{-\infty}^{\infty} f(E) p_x dp_x dp_y dp_z \tag{17}$$

Substituting the Fermi function $f(E)$ and working through the triple integration gives Richardson's law. Calculus and arithmetic details in the derivation can be found in Dushman's book on the matter [36]. Further work showed that a fraction of outward electrons would be reflected near the emitter surface, so the current density is less than initially derived. More recently, Antonis Modinos made a case for how the band structure in clean metal surfaces effects the current density. Accounting for these updates, the constant A_G is written as $A_G = \lambda_B(1 - r_{av})A_0$ where λ_B is the modified correction factor and r_{av} is the average value of reflected outgoing electrons.

Until this point, the discussion has pertained to surfaces with negligible electric field strength. When this condition no longer holds, then the Schottky effect must be considered. For uniform metallic surfaces, the image force, F, or the attraction to a charge's electric image, equals $\frac{-q_e^2}{16\pi\varepsilon_0 x^2}$. This derives from the Coulomb force given by the image charge at a distance x from the metal surface. The potential energy is the force integrated over this distance. The equation for the potential is thus

$$U = \int_{\infty}^{x} \mathbf{F} \cdot \mathbf{dx} \tag{18}$$

Assuming a constant electric field, E_m, and writing the electrostatic potential, ϕ, the reduced potential energy due to the depletion region is

$$U_{total}(x) = q\phi(x) = \frac{-q_e^2}{16\pi\varepsilon_0 x} - q_e E_m x \tag{19}$$

Taking a derivative with respect to position, solving for the critical value, and plugging into the total potential energy equation above, one finds that the Schottky barrier lowering is electric field dependent and is written as

$$\Delta W = q_e \Delta\phi = \sqrt{\frac{q_e^3 E_m}{4\pi\varepsilon_0}} \tag{20}$$

One can then conclude the modified Richardson equation takes the form

$$J = A_G T^2 e^{-(W-\Delta W)/kT} \tag{21}$$

It is also of interest to discuss the extent to which entropy is convected by an electric current. Irreversible Joulean heating and reversible linear Peltier or Thomson heat results from inhomogeneous temperature or composition profiles. An outline for the derivation of change in entropy as a result of these effects is provided. Introducing the Thomson coefficient, σ, the entropy converted per unit current is shown to be

$$C = \int_0^T (\sigma/T)dT \tag{22}$$

Evaporation is a cooling process which takes several forms in nature. Humans exude sweat through pores in the skin to maintain appropriate internal body temperature. Water evaporates and condenses into clouds which allows for its distribution on land as precipitation. Prudent to this derivation, this exothermic process also applies to electron evaporation from the surface of a conductor. With the end goal of measuring the heat loss per emitted electron at saturation conditions, l_{sat}, quasistatic conditions are first considered to obtain l_{quas}. The necessary adjustments are then applied to achieve l_{sat}.

Given a bounded and uniform emitting surface with slowly increasing volume, one can start by finding the useful work in the quasistatic thermodynamic system. For this, we use the Helmholtz free energy equation which contains variables F for free energy, U as internal energy, and S for entropy. The equation is simply $F = U - TS$. The differential, dF, is the fundamental thermodynamic relation and is shown to be

$$dF = -SdT - pdV + \bar{\mu}dn \tag{23}$$

where p is pressure, V is volume, $\bar{\mu}$ is the electrochemical potential, and n is the number of moles of electrons transferred in the reaction. The maximum reversible work is of interest, so one involves Gibbs function. The Gibbs free energy, G, is written as

$$G = U + pV - TS \tag{24}$$

By substituting Helmholtz free energy, Gibbs equation equates to the sum $F + pV$. It follows that the differential form, dG, becomes

$$dG = -SdT + Vdp + \bar{\mu}dn \tag{25}$$

For a simultaneously isobaric and isothermal quasistatic process, the electrochemical potential can then be isolated and Gibbs energy differentiated such that

$$\bar{\mu} = \left(\frac{\partial G}{\partial n}\right)_{T,\ p} = \left(\frac{\partial U}{\partial n}\right)_{T,\ p} + \left(\frac{\partial (pV)}{\partial n}\right)_{T,\ p} - T\left(\frac{\partial S}{\partial n}\right)_{T,\ p} \tag{26}$$

The gas can be treated as perfect and the potential can be assumed constant. Recalling the ideal gas relation $pV = nkT$ and noting the three degrees of freedom and the effect of the work function, it is shown that

$$\left(\frac{\partial U}{\partial n}\right)_{T,\ p} = \frac{3}{2}kT - q_e\Phi_v, \quad \left(\frac{\partial (pV)}{\partial n}\right)_{T,\ p} = kT \tag{27}$$

where Φ_v is the electrostatic potential in the vapor region. Noting that the work function is $W = -q_e\Phi_v - \bar{\mu}$ and solving for the entropy per electron in quasistatic conditions, one finds

$$\left(\frac{\partial S}{\partial n}\right)_{T,\ p\ (quas)} = \frac{W}{T} + \frac{5}{2}k \tag{28}$$

This term is substituted into the final relation. The heat loss per emitted electron at quasistatic conditions is

$$l_{quas} = T\left[\left(\frac{\partial S}{\partial n}\right)_{T,\ p\ (quas)} + q_e C\right] \tag{29}$$

Transcribing this quasistatic result to saturated conditions, the electron velocity should be reconsidered as having a Maxwellian distribution. In doing so, it is found that the average kinetic energy of each electron is $2kT$ rather than $\frac{5}{2}kT$. Generalizing to include cases with nonzero field emission, a strong collecting field, E, is included in the final relation. The heat loss per electron at saturated conditions is shown explicitly as

$$l_{sat} = W - q_e^{3/2}E^{1/2} + 2kT + q_e T\int_0^T (\sigma/T)dT \tag{30}$$

2.1.2.1 Complex Geometries

Non-uniformity of emission can be a result of patches, or crystal grains having different work functions. The work function of each patch is a combination the bulk material and the surface double layer. The particular arrangement of atoms at the surface causes asymmetric charge distributions. This, in turn, leads to different moments from the double layer of neighboring grains, and thus non-uniform emission properties. Another cause of variability is forbidden reflections per Bragg's law. Crystallographic features in each lattice type cause certain reflections to be omitted. This reduces emission when corresponding energies are sampled. It is worth noting that the formation of double layers is a surface effect whereas forbidden reflections is a volume effect. It follows that geometries which have a high surface area to volume ratio are more greatly impacted by the former. The inverse of this conditional is also true. Letting f be the fraction of surface covered by the ith patch, $\bar{r}_i$, be defined as the average reflection coefficient of that patch, and the product $q_e\phi_i$ being equitable to the true work function, W, for that patch, Richardson's Law can be modified to become the weighted summation of all patches. The equation is discretized such that

$$J = \sum f_i J_i = \lambda_B A_0 T^2 \sum f_i (1 - r_i) e^{[-q_e(\phi_i - (q_e E)^{1/2})]/kT}$$
$$\Rightarrow J = \lambda_B A_0 T^2 \sum f_i (1 - r_i) e^{-(W_i - \Delta W_i)/kT} \quad (31)$$

Defining ϕ_i^* as the zero field work apparent work function of the ith kind of path and w_i as the portion of the total zero field emission current from that patch variety, one can sum across all patch types to give the zero field apparent work function, ϕ^{**}. Mathematically, this is expressed as $\phi^{**} = \sum w_i \phi_i^*$. The cooling effect detailed in the previous section can also be considered in terms of a summation of patches. The zero field heat loss per electron of the ith patch type is represented as $l_{sat}^{(i)}$ to avoid subscript confusion. Taking a similar form to the previous expression, this quantity is written as

$$l_{sat}^{**} = \sum w_i l_{sat} \quad (32)$$

Keeping consistent notation, W^{**} is the zero field true work function that is summed across all patch types. Recalling previous results, this equation is expressed as

$$W^{**} = q_e\phi^{**} = l_{sat}^{**} - \sum T w_i \frac{dl_{sat}^{(i)}}{dT} + q_e \sigma T \quad (33)$$

2.1.2.2 Material Selection for Thermionic Cooling

Thermionic emission constants depend on the atomic structure of a material as well the particular crystallographic plane in question. From a practical standpoint, a low work function is desirable for emitter applications since it requires less energy for the material to discharge electrons. For this reason, refractory metals including tungsten, rhenium, and tantalum are commonly used to produce filaments. Alkaline earth metal oxides including barium oxide, strontium oxide, calcium oxide, aluminum oxide, and thorium oxide, are effective coatings for cathodes. Lanthanum hexaboride and cerium hexaboride have beneficial properties for thermionic emission as well. Tungsten's apparent work function and Richardson's constant, both expressed at zero field emission current conditions, are shown in Table 2.

Miller Indices	ϕ^{**} (eV)	A_G^{**} $\left(\frac{A}{cm^2K^2}\right)$
111	4.39	35
112	4.69	125
116	4.39	53
001	4.56	117
110	4.68	15

Table 2: Thermionic constants for various crystallographic planes of tungsten.

Note how the Richardson's constant for the same materials can vary by more than an order of magnitude. This can be attributed predominately to different reflection coefficients for each crystal face. Contrast this with the work function at each face which varies by no greater than 7%. The work function of tungsten can also be predicted by simply knowing its electronegativity. Figure 14 illustrates the correlation between work function and electronegativity, χ. Named after physicists Walter Gordy and W. J. Orville Thomas, the Gordy and Thomas equation is a linear regression curve which has the form $\phi = 2.3\chi + 0.34$. Tungsten has coordinates $(2.1, 4.5)$ which corresponds well with the mean of the work functions provided in the previous table.

Yamamoto, Susa, and Kawabe continue this work for binary compounds. Figure 15

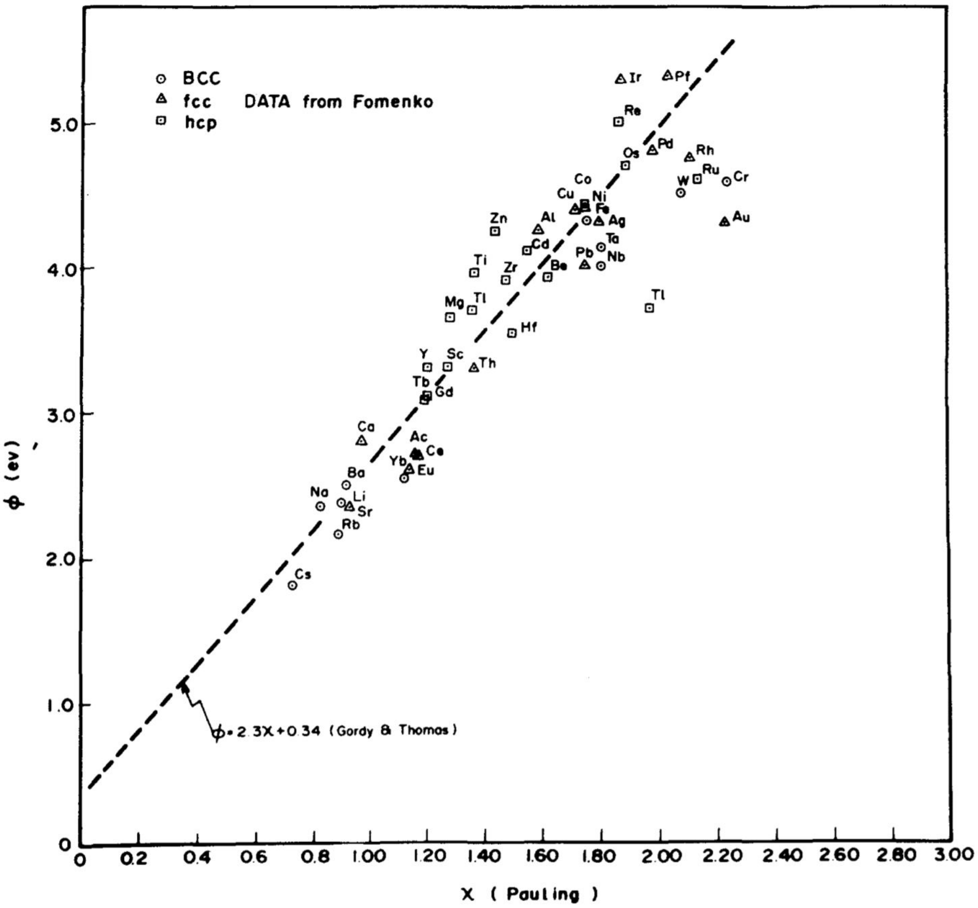

Figure 14: Relationship between work function and electronegativity for select elements [37].

illustrates the work function for select compounds as they relate to the electronegativity of the element with the smaller work function. The Gordy and Thomas equation is included and fairly well represents the trend. Note the position of the most commonly used emitter materials. A few are located in the bottom left (e.g. LaB_6) where the lowest work functions are, but some (e.g. HfC) have substantially higher ϕ. Given two elements that can combine to make a binary compound, the element with a lower work function is denoted as A and the other is identified as B. Using empirical results, a simple rule of mixtures, and the bond length, d, one can estimate the work function for the compound [37]. This equations is written as

$$\phi_{AB} = \phi_A + \frac{1.41}{d_A}\left(\frac{2\phi_A - \phi_B - 0.34}{\phi_A + \phi_B - 0.68}\right) \tag{34}$$

By inspection of Richardson's law, it is clear that the constant A_G should be maxi-

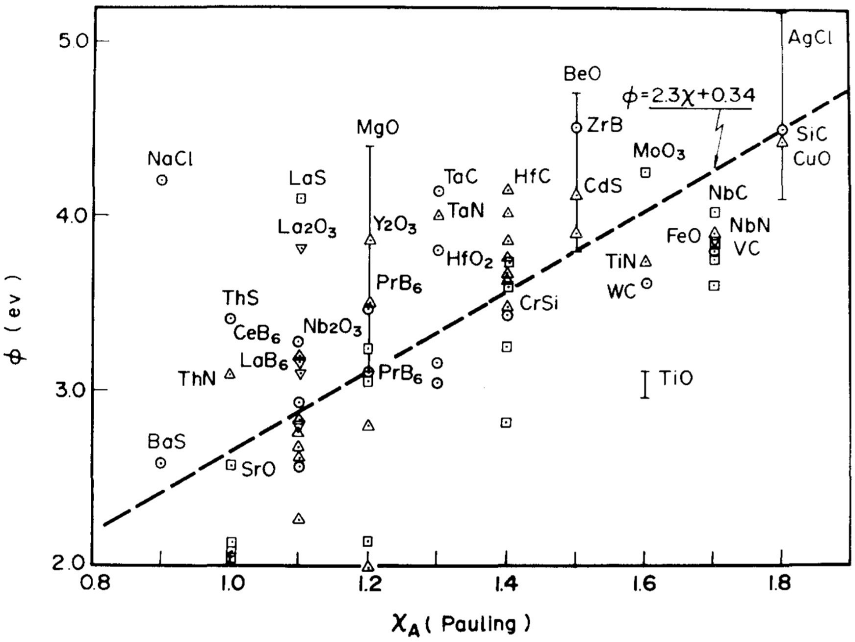

Figure 15: Relationship between work function and electronegativity for select binary compounds [37].

mized to achieve the highest current density. As prefaced earlier, correction factors are material dependent as a result of varying band structure and reflections. Table 3 presents the Richardson's constant for select elements, coatings, and the popular emitter compound $\mathrm{LaB_6}$. Recall that $A_G = \lambda_B(1-\bar{r})A_0$ and $A_0 = \frac{4\pi m k^2 q_e}{h^3}$. In consistent units with the following table, $A_0 = 120.2\left(\frac{A}{cm^2K^2}\right)$. This theoretical value is equal to A_G while, but not limited to, the correction constant is unity and reflections are none.

Richardson's constant has substantial variability, especially for complex compositions and geometries. While the mechanisms that cause this variability are fairly well understood, the confidence interval is inadequately defined and excessively broad for designers to pinpoint current density for their respective applications. This knowledge gap leaves room for advances in this area. This research strives to answer specific questions including a) how Richardson's constant correlates with surface area and b) the variability of Richardson's constant while a material is near its melting point.

Material	A_G $\left(\frac{A}{cm^2K^2}\right)$	Material	A_G $\left(\frac{A}{cm^2K^2}\right)$
Molybdenum (Mo)	55	Iridium (Ir)	170
Nickel (Ni)	30	Platinum (Pt)	32
Tantalum (Ta)	60	Rhenium (Re)	100
Tungsten (W)	60	Ba on W	1.5
Barium (Ba)	60	Cs on W	3.2
Cesium (Cs)	160	LaB_6	29

Table 3: Richardson's constant for select materials [38].

2.1.3 Radiation Cooling

As a body moves through thin atmosphere at speeds exceeding Mach 5, the body inevitably heats. A natural cooling is the heat transfer mode of radiation. That is, a temperature gradient between the vehicle and the surrounding space causes an outward heat flux, q_{rad}. With ϵ defined as the material emissivity and σ symbolizing the Stefan-Boltzmann constant, the well known heat transfer equation is written as

$$q_{rad} = \sigma \epsilon T^4 \tag{35}$$

As introduced earlier, elevated temperatures can cause electrons to be emitted and cause a cooling effect. This process, called thermionic emission, is a mode of heat transfer analogous to the evaporation of a liquid. The heat flux resulting from thermionic emission, q_{therm}, is expressed as

$$q_{therm} = \frac{J_e}{q_e}\left(W + 2kT\right) \tag{36}$$

where J_e is the same current density found in Richardson's law. The subscript e, meaning electron, is added to distinguish it from other current density terms introduced in the following discussion. Kyle Hanquist and Iain Boyd compared the effectiveness of these two heat transfer modes. This ratio of heat fluxes, $q_{rat} = q_{therm}/q_{rad}$ is plotted against surface temperature for various work functions in Figure 16. For simplicity, blackbody radiation conditions are used, so $\epsilon = 1$. Low work functions and high temperatures are the conditions that cause thermionic emission to be the most effective. Thermionic emission provided a greater outward heat flux for materials which simultaneously have temperatures above 1,000 K and a work function exceeding about 1.5 eV. That temperature cutoff rises to 2,900 K for $W = 4$ eV.

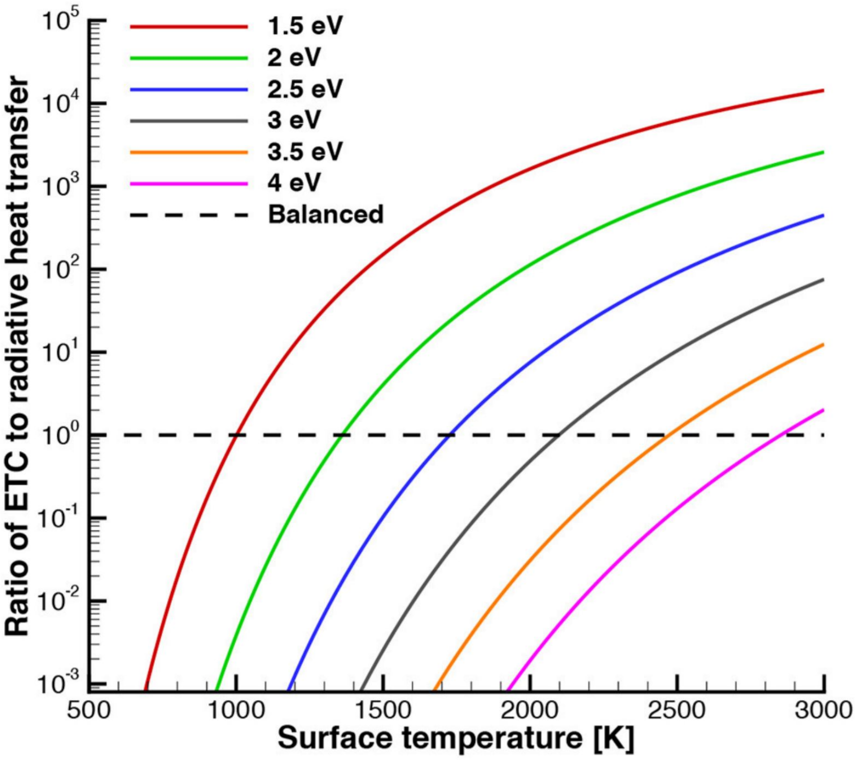

Figure 16: Cooling effectiveness comparison between thermionic emission and radiation for several work functions [39].

Near the wall of an electron emitting hypersonic vehicle, a plasma sheath forms naturally from the high mobility electrons leaving more stagnant ions. A positive charge near the wall results in a negative potential difference in this region. The surface can either have floating potential or a biased potential. The former means the material is electrically insulated, so there is zero net current through the sheath, whereas the latter refers to a negative bias which allows a net current to pass through the sheath edge. We continue to use the subscript e for electrons and i shall also be used to reference ions. The current density on a floating surface is the difference between the current density of the flow field ions, $J_{i,f}$, and flow field electrons, $J_{e,f}$. This statement is simply

$$J_e = J_{i,f} - J_{e,f} \tag{37}$$

Figure 17 illustrates an example of the alternate case whereby the surface becomes biased. In the depicted scenario, electrons are heated at the leading edge and are emitted. These electrons cool and are redeposited further aft. If a current exists, then the electrons can flow back to the emitter surface to complete the circuit. Touching on some relevant equations, the normalized sheath potential is written as

$$\Phi_w = \frac{q_e \phi_w}{T} \tag{38}$$

where ϕ_w is the voltage drop, or sheath potential, between the plasma and the material's surface. The sheath potential is the combined potentials from the floating potential, ϕ_{float} and any other applied bias, ϕ_{app}. This summation is simply

$$\phi_w = \phi_{float} + \phi_{app} \tag{39}$$

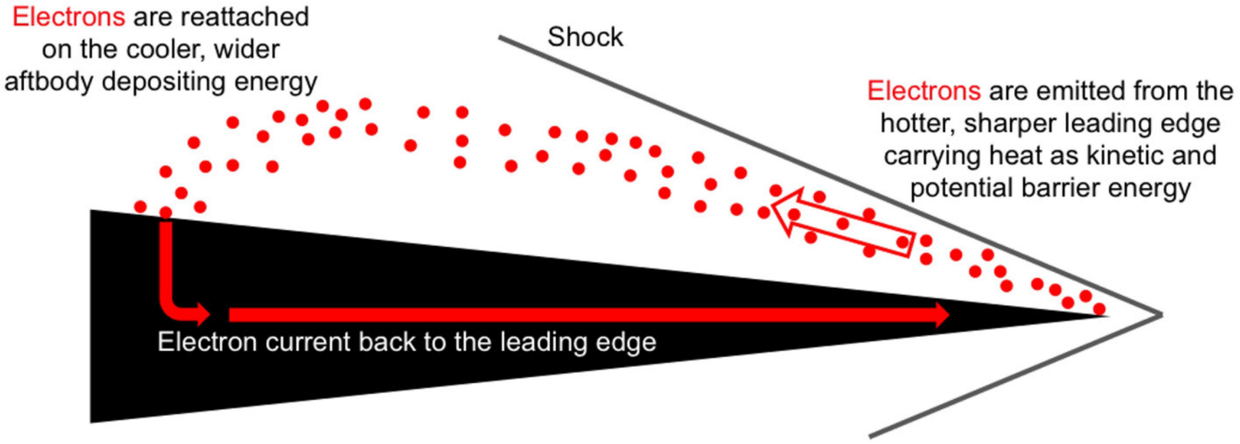

Figure 17: Thermionic emission cooling cycle schematic [39].

Since the extent to which thermionic emission is effective is proportional to the amount of emission, it is worth noting the maximum emission from a biased surface is

$$\lim_{\Phi_w \to -\infty} \frac{J_{e,sc}}{J_i} = \gamma = \sqrt{\frac{m_i}{m_e}} \tag{40}$$

for which the subscript sc stands for space charge. M_i and M_e are the mass of the ions and electrons, respectively. To compare the effectiveness of thermionic emission for charged and ideal conditions, researchers at the University of Michigan applied a CFD model to predict the heat flux and temperature profiles along the surface of the NASA Stardust Return Capsule during the reentry phase of flight. Figure 18 plots the temperature and heat transfer magnitudes along the surface. T-limited refers the ideal current density case and SC-limited used the reduced charge density due to space charge effects. ETC stands for electron transpiration cooling and is the process whereby thermionic emission results in heat removal. The trajectory point analyzed has a freestream velocity of 12.4 km/s, an ambient temperature of 218 K, and an air density of 1.27E-14 kg/m^3. It is worth highlighting that the ETC case with work function 3 eV creates a greater heat flux away from the surface than radiation does. The reason for the T-limited and SC-limited cases having the same surface temperature is because space-charge limits are not reached. Thus, the saturated ETC cases equal the sheath effect examples.

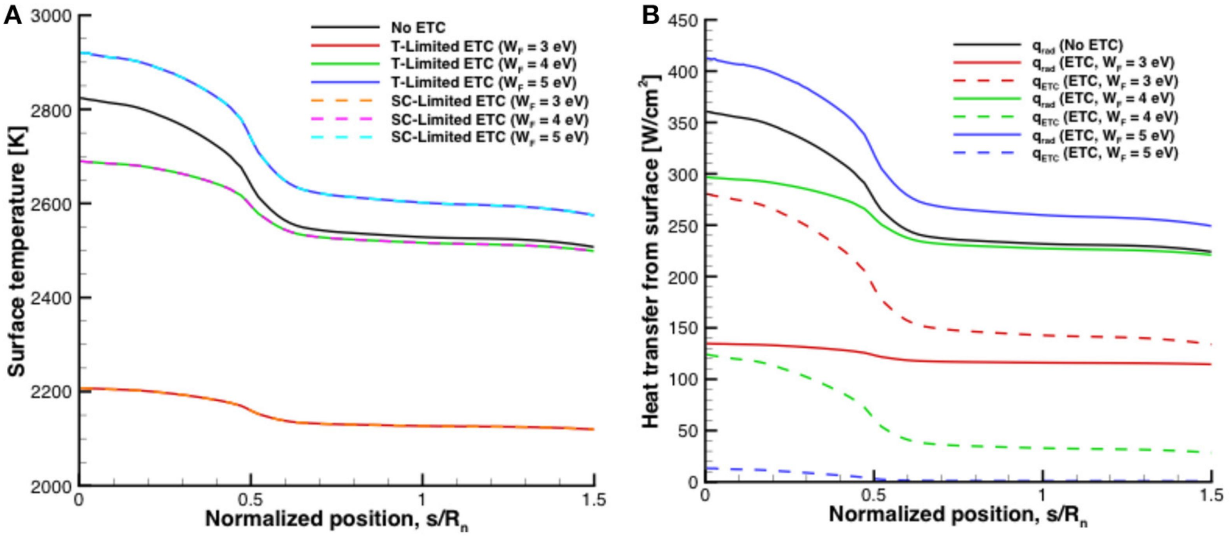

Figure 18: Comparing (A) temperature and (B) heat transfer profiles along surface of Stardust reentry vehicle for different thermionic emission conditions [39].

2.1.4 Evaporative Cooling & the Wicking Process

A benefit to porous media such as foam metals is their ability to wick. In other words, their hollowness makes possible the transport of liquids through them. In the context of hypersonic vehicles, these liquids can be molten metals. Heat pipes have been designed into hypersonic vehicles to make use of wicking in this manner. These devices passively cause evaporation of the chosen liquid in the regions nearest the leading edge. Condensation occurs more aft where the aeroheating is less intense. While such designs have been considered in academic and industrial settings, few contributions have been made to the scenario of simultaneous wicking and thermionic emission. This section briefly introduces the physical mechanisms associated with wicking and a potential design is discussed in Section 5.1.

Considering metal foams which have pores with diameters on the order of micrometers, surface tension and adhesion are inherent. These forces are caused by cohesion in the liquid and forces between the liquid and wall materials. The resulting propulsion is called capillary action. The Young-Laplace equation determines the pressure differential across the fluid interface, Δp. The Laplace pressure is a function of the surface tension, γ, and the radii of the menisci, R_1 and R_2. Where $\hat{n}$ is the unit normal pointing away from the surface, θ is the wetting angle, and a is the tube radius, the equation for the pressure differential is written as

$$\begin{aligned} \Delta p &= -\gamma \nabla \cdot \hat{n} \\ &= 2\gamma \left(\frac{1}{R_1} + \frac{1}{R_2} \right) \end{aligned} \tag{41}$$

where $R_n = a / \cos\theta_n$. Figure 19 illustrates the capillary effect for a generic thin tube. Note that the displayed meniscus is concave, but a convex meniscus, whereby $\theta > 90°$, is possible under certain conditions. The flow rate, or amount of liquid being transferred per unit time, is the integration of Darcy's law over the wick cross-sectional area, A. A form of Darcy's law gives the liquid velocity, $\vec{u}$, as a function of material permeability, k, viscosity, μ, and the pressure differential. The velocity vector is stated as

$$\vec{u} = \frac{k}{\mu} \Delta p \tag{42}$$

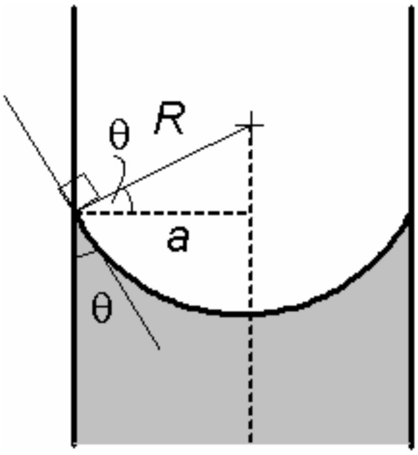

Figure 19: Capillary effect with spherical meniscus of wetting angle θ [40].

After integrating over A and defining the tube length as L, the flow rate takes the similar form

$$Q = \frac{k}{\mu}\left(\frac{A}{L}\right)\Delta p \tag{43}$$

For anisotropic geometries such as metal foams, a value $(\mathrm{A/L})_{eff}$ can be substituted to give an effective capillary length to the overall structure.

2.2 Secondary Electron Emission in Space Electric Propulsion

2.2.1 Early Work

Since opening at the turn of the 20th century, the field of secondary electron emission (SEE) has grown alongside advancements in sample manufacturing and computing power. During its infancy, previous to experimentation with complex material geometries and Monte Carlo simulations, the field gained a platform of ideas and observations upon which further work could firmly stand. This pedestal of foundational breakthroughs belongs to Baltruschat, Starke, and Farnsworth who realized increased incident angles correspond with heightened secondary emission. While their conclusion has since been overwhelmingly supported, this dissertation nonexempt, opposing data made it to publication during this time. In light of Tate and Tingwaldt asserting alternative findings which illustrate an invariance between incident angle and secondary emission, competing research helped the field gain intrigue and ushered in a new generation of researchers.

The basis that secondary emission had been shown to change with beam incident angle and sample topography laid the footing for the developing field. These data, in combination with an ambiguity regarding responsible physical phenomena led to subsequent work into improving yield prediction accuracy and differentiating electrons as a function of their total energy. Baroody drew upon Whiddington's law which predicts the loss of primary energy, E, with penetration depth, x. A is a constant that differs for each material. Whiddington's law is written as

$$\frac{dE}{dx} = -\frac{A}{E(x)} \tag{44}$$

Baroody describes a set of assumptions that draws a normalized secondary electron yield (SEY) curve which is independent of a solid sample's geometric or material parameters. The SEY relative to its maximum value, δ/δ_m, versus the primary energy relative to its value at peak yield, E_{0s}/E_{0sm}, was found to give a *universal* SEY curve. This equation is

$$\frac{\delta}{\delta_m} = \frac{1}{F(.92)} F\left(\frac{0.92E_0}{E_{0m}}\right) \tag{45}$$

where $F(r)$ is the function of the effective range of the secondaries for the specific material under investigation and is shown as

$$F\left(r\right) = e^{-r^2} \int_0^r e^{y^2} dy \tag{46}$$

In response to poor agreement between Baroody's theoretical curve and experimental data for metallic samples at beam energies greater than that at maximum yield, δ_m, Lye and Dekker improved upon this derivation with their "power law" formulation. This elementary theory of secondary electrons (SEs) starts with a subtle but prevailing addition to Whiddington's law shown previously in Equation 46. Raising the penetration energy to a fitted power, n, results in SEY curves which more closely match experimental results. Following a similar derivation to Baroody, the updated expression for the universal reduced yield curve became

$$\frac{\delta}{\delta_m} = \frac{1}{G_n(r_m)} G\left(\frac{r_m E_0}{E_{0m}}\right) \tag{47}$$

where r_m is the value of r for which the maximum range of the secondaries occurs and is evaluated as

$$G_n\left(r\right) = e^{-r^{n+1}} \int_0^r e^{y^{n+1}} dy \tag{48}$$

2.2.2 Incident Angle Dependence

Refinements in SEE analytics have been paired with decades of revising and augmenting direct measurements. One of the foundational experiments for polycrystalline copper was performed by Koshikawa and Shimizu [41]. The team aimed an electron gun at a flat copper specimen inside of a vacuum chamber and gathered data using a spherical retarding field analyzer. With this apparatus the team quantified SEY as a function of primary energy and beam incident angle. The former was tested between 0.5 and 10.0 keV and the latter from 0 to 70°. The two most relevant conclusions Koshikawa and Shimizu make are that polycrystalline copper has a δ = 1.43 at 500 eV and SEY increases monotonically with incident angle. Applying a polynomial trend line to δ vs. θ at this beam energy and increasing the order until the coefficient of determination is above 0.99, the resulting third order polynomial is found to be $\delta = 0.0058E_0^3$ - $0.0461E_0^2 + 0.1453E_0 + 1.3129$. Bruining expressed the relationship of SEY and beam incident angle as

$$\ln\frac{\delta(\theta)}{\delta(0)} = A(1 - \cos(\theta)) \tag{49}$$

where A is a constant [42]. Closeness of fit to this equation along with our original results are presented in Section 3.5.

Scholtz from Philips Research Laboratories proposed a universal secondary electron curve based on the maximum yield, δ_m, and the energy at which it occurs, E_m. A Gaussian distribution is applied to $\ln\left(\frac{E_0}{E_{0m}}\right)$. With the standard deviation, σ, found to be 1.6, the Scholtz model is written as

$$\delta(E_0, \theta) = \delta_m(\theta)\exp\left[-\left(\frac{\ln\left[E_0/E_{0m}(\theta)\right]}{\sqrt{2}\sigma}\right)^2\right] \tag{50}$$

and is applicable for flat surfaces. Note that while this empirical model accurately describes SEY data across a wide range of incident energies, it has no physical basis [43].

2.2.3 Surface Phenomena Effects

It is important to note that SEY is sensitive to surface phenomena. This includes contaminants such as oxide layers, carbon films, and water content as well as differences in geometry at the nano- and microscale. This point has two implications, one theoretical and one practical. Respectfully, (1) in-depth material characterization is necessary to pinpoint SEY and (2) practically, SEY has a range of values that should be expected. Davies and Dennison performed experiments quantifying the range of values to be expected after contaminating a sample with outgassed polytetrafluoroethylene, commonly referred to as Teflon. As testing continued in the ultrahigh vacuum environment, the sample experienced an approximate doubling in oxide presence. Electron stimulated absorption was found to result in a 30% decrease to SEY after a couple minutes of continuous electron bombardment. Further reduction in SEY, up to an additional 25% after several hours, can be attributed to the deposition of disordered carbon [44].

2.2.4 Monte Carlo Simulations

Monte Carlo algorithms have been developed to predict SEY for various materials including copper. Among other assumptions, Furman and Pivi incorporate in their model that (1) secondary electrons are generated instantaneously when a primary electron hits a surface, (2) the energy of an emitted electron is no greater than the incident energy, and (3) emission angles of the secondary electrons are independent of incident angle as well as beam and emission energy. The team at Lawrence Berkeley National Laboratory is able to reproduce the experimental data for polycrystalline copper with a handful of fitting parameters. Extra attention is paid to SEY at incident energies below 20 eV since their model assumes only backscattered electrons are emitted at zero beam energy [45]. This contrasts from a few previous analytical conclusions which say $\delta(0) \sim 0.07$. Furthermore, experimental data is understood to become increasingly sensitive as beam energy is lowered to only a few eV.

The Monte Carlo method has been applied to predict the SEY for general foam surfaces. Charles Swanson and Igor D. Kaganovich conducted numerical simulations to estimate the yield reduction effect of reticulated geometries. The team from Princeton Plasma Physics Laboratory used the aforementioned Scholtz model to estimate the yield for analogous flat surfaces. They simulate foams by using a collection of whiskers and sum the secondaries created at the top, bottom, and sides. From their simulations, the team concludes that foams reduce yield by up to 30% [46].

CHAPTER 3

Secondary Electron Emission from Reticulated Cellular Copper Surfaces

3.1 Introduction & Objectives

When a beam of energetic primary electrons (PEs) impinges upon the surface of a solid, a sequence of collisions near the material's surface is initiated and the emission of electrons from the solid may be observed. This phenomenon, termed secondary electron emission (SEE), was first discovered by Austin and Starke in 1902 [47]. Since then, experimental [48, 49, 50], theoretical [51, 46, 52] and computational [53, 54] studies have contributed to an ever-increasing database on the SEE phenomenon for numerous materials. SEE measurements associated with statistical scatter notwithstanding, systematic studies on the relationship between surface architecture (e.g. micro-geometry) and SEE are lacking.

Energetic primary electron knock-on collisions initiate cascades of momentum transfer events with the free electron gas within the solid. A fraction of the primary incident electrons is elastically reflected and the remainder penetrate and share their energy with the free electron system, thus creating energetic *secondary* electrons that further transport through additional collisions. As they penetrate deeper, they multiply and lose energy until they either rejoin the sea of conduction electrons or reach the surface with sufficient energy to emerge as true secondary electrons (SEs). PEs can also lose a portion of their energy inside a solid which can cause them to dissipate energy, resurface, and escape via Rutherford scattering. Such electrons are called inelastically reflected primaries. Although it is common to employ the term SEs with reference to all electrons which escape from the surface and are collected by a positive collector electrode, one must distinguish between three categories of electrons leaving the surface: (1) elastically reflected primaries, (2) inelastically reflected primaries, and (3) true secondary electrons.

Unstable erosion of material surfaces, multipactor discharge, and electron cloud effects (ECE) are phenomena in which SEE plays an important role. Such phenomena have direct impact on the lifetime and effectiveness of scanning electron microscopes (SEMs), particle accelerators, plasma TV displays, waveguides, and satellites. It is thus critical to understand how SEs impact design performance and lifetime in concert with identifying measures to control yield. For most applications this condenses to keeping SEY at a minimum, though notable exceptions are Everhart-Thornley detectors in SEMs, for which the objective is the opposite. An understanding of the energy- and angular distributions of SEs for common materials such as elemental copper would allow more accurate models of spacecraft charging in the presence of charge-induced electrostatic fields and ambient magnetic fields.

The secondary electron yield (SEY), symbolically stated as δ, is the total number of SEs produced per incident PE and thus the measure of SE production. The SEY is generally a function of the primary electron energy and angle of incidence. The energy dependence is described by the so-called universal curve, which is characterized by a single asymmetric broad peak [12]. A value of δ greater than unity suggests a potential risk for an electron avalanche or a chain reaction that can result in voltage breakdown in devices with a potential gradient or an oscillating electric field. Electron avalanches can result in arcing and other discharges, all of which are potentially fatal to spacecraft or satellite RF-tubes. This fact alone provides strong impetus to find mechanisms that suppress SEY. At high energies, the SEY is comparatively low due to the fact that most of the SE production occurs too deep below the surface to readily escape. The broad peak corresponds with the condition in which the incident PE penetration depth is comparable with the SE escape distance. At still lower energies, the yield again falls because of the lower energy input to the free electron system from the incident PE beam.

The relationship between the SEY and incident electron angle has been investigated first by [55], and [56], who realized that as the PE incident angle gets steeper (approaches grazing) secondary emission increases. However, Tingwaldt asserted alternative findings which illustrate an invariance between incident angle and secondary emission [57]. Since then, it has been appreciated that secondary emission depends on *both* beam incident angle and surface topography. These data, in combination with an ambiguity regarding responsible physical phenomena led to subsequent work toward improving yield prediction accuracy and differentiating electrons as a function of their total energy.

The SEY is sensitive to surface composition and structure, including contaminants such as oxide layers, carbon films, and water content, as well as differences in geometry at the nano- and microscale. For example, Davies and Dennison performed experiments to measure SEY after contaminating a sample with outgassed polytetrafluoroethylene, commonly referred to as Teflon. As testing continued in the ultrahigh vacuum environment, the sample experienced an approximate doubling in oxide presence. Electron stimulated adsorption was found to result in a 30% decrease to SEY after a couple of minutes of continuous electron bombardment. Further reduction in SEY, up to an additional 25% after several hours, was attributed to the deposition of disordered carbon [58]. While solid materials have a substantial research history in SEE, complex geometries, and particularly those with reticulated structures, have comparably sparse available data. The present work aims at bridging this gap by experimentally measuring foam SEY data, and by performing computer simulations to understand the experimental results. In this manner, SEY sensitivity to differences in the surface micro-architecture and composition of the material are accounted for and analyzed relative to the reference conditions of a solid material (Cu) with a well-characterized and nearly flat surface.

Recent results on the influence of the surface structure on the SEY have been reported by [59] who showed a sharp reduction in the SEY from grooved surfaces. Suppression of the SEY when primary electrons interact with a micro-porous arrayed surface was also examined by [60]. The impact on electron emission from fuzz was investigated by Patino *et al.*[61] and further studied by Huerta *et al.*[62]. The secondary electron yield from high aspect ratio carbon velvet surfaces was studied by Jin, Ottaviano, and Raitses[50] and later modeled by Swanson and Kaganovich [52]. Additionally, experiments which tested surface roughness as it relates to electron yield were performed by Bundaleski *et al.*[63]

We present here experimental measurements for the energy and angular dependence of the SEY in micro-engineered materials, specifically in copper foam, where primary electrons can penetrate deep into the sample before they release secondary electrons. The study seeks to achieve the following objectives: (a) experimentally quantify the change in SEY for foam copper relative to solid copper with a flat surface, (b) predict SEY for copper foam and flat copper using our recently-developed ray-tracing Monte Carlo simulations [64, 65], and finally (c) compare experimental to computational results so as to identify the mechanisms leading to inherent differences. The paper is organized as follows. First, we review the theoretical background behind the physics of SEY and briefly discuss the history of this area in Section 3.2. A description of our ray-tracing Monte Carlo methods is given in Section 3.3, where we briefly present the basic equations for elastic scattering (Subsection 3.3.1), inelastic scattering (Subsection 3.3.2), and the computational algorithm (Subsection 3.3.3). Our experimental approach is then detailed in Section 3.4, where we outline sample characterization (Subsection 3.4.1), experimental approach (Subsection 3.4.2), apparatus (Subsection 3.4.3), and measurements (Subsection 3.4.2). Results of the study, and a comparison between measurements and computer simulations are also presented in Section 3.5. Finally, conclusions of the present study are given in Section 3.6.

3.2 Theoretical Background

The theory of SEE was developed by [66] on the basis of the Sommerfeld free-electron model. The theoretical development was built on the work of [67], who showed that metals with the largest work functions have the highest SEY. When a fast primary electron with momentum p_0 collides with an electron in the metal, momentum is transferred in the amount of $\Delta p = 2e^2/Vd$, where e is the electron charge, V the incident electron velocity, and d the distance of closest approach. Metal electrons at a distance d will experience a shift of their momentum-space sphere by the amount of Δp. The volume of the displaced sphere which lies outside a sphere of radius μp_0 in momentum space was calculated by Baroody. When this is multiplied by the density in momentum space of $2/h^3$, where h is Planck's constant, and then integrated over all possible closest approach distances d, an expression for the number of secondaries per unit primary path length, $N(\mu)$ with momentum exceeding μp_0 was found to be: $N(\mu) = B\sqrt{E_F}/E_0(\mu^2 - 1)$, where E_F is the Fermi energy, E_0 the kinetic energy of the primary electron, and B is a constant. μ represents a dimensionless momentum in units of the incident momentum p_0. To determine the SEY, Baroody considered two extreme cases: (1) a singly scattered electron that escapes the surface, and (2) multiply-scattered electron. The two cases are based on whether the scattering mean free path (mfp) l is greater (case 1), or much less (case 2) than the adsorption characteristic length λ. For the first case, the probability that this collision takes place at a distance between r and $r + dr$ is simply $\exp(-\sigma r)dr/l$, where σ is the inverse mfp. One can integrate over r and assume isotropic scattering. This allows for the scattering probability per unit solid angle to be $\frac{1}{4\pi\sigma l}$. The team also defines q as the cosine of the angle with the outwardly directed normal to the surface. The probability of scattering into any range dq is found to be $dq/2l\sigma$. Letting $n(q, z)$ be the number of secondaries produced per unit length at depth z with sufficient energy to escape at the angle $\cos^{-1} q$, the number of secondaries that escape the surface was given by

$$\delta_1 = (2l\sigma)^{-1} \int_0^1 \int_0^\infty n(q, z) \exp(-\sigma z/q) dz dq \tag{51}$$

In Eqn. 51, $n(q, z) = N\left(\frac{\mu_0}{q}, z\right) = \frac{B\sqrt{E_F}q^2}{E_0(\mu_0^2 - q^2)}$, with $\mu_0^2 = (E_F + \Phi)/E_F$ corresponds to the minimum electron energy to escape the surface, and Φ is the metal's work function. The dependence of SEY on z is through the energy dependence E_0 on z, which must be assumed. It is customary to assume that the energy loss of the primary is inversely proportional to its energy, i.e. $-dE_0/dz \propto E_0^{-1}$, giving $E_0^2 = E_{0s}^2 - az$, where a is a constant and E_{0s} is the incident energy at $z = 0$. The z-integral was calculated with the help of the functions $F(x) = e^{-x^2} \int_0^x \exp(t^2)dt$ and $\omega = q^{-1/2}$. The SEY was found to be

$$\delta_1 = \frac{2B\sqrt{E_F}}{l\sigma^{3/2}a^{1/2}} F(H) \int_0^\infty \frac{d\omega}{(\mu_0^2\omega^4 - 1)\omega^4} \tag{52}$$

The energy dependence of the SEY is given by the function $F(H)$, where $H = \sqrt{E_{0s}^2\sigma/a}$, and has a maximum at $H = 0.92$ [68]. The SEY relative to its maximum value, δ/δ_m, versus the primary energy relative to its value at peak yield, E_{0s}/E_{0sm}, was found to give a *universal*

SEY curve, given by

$$\frac{\delta}{\delta_m} = \frac{1}{F(.92)} F\left(\frac{0.92 E_{0s}}{E_{0sm}}\right) \tag{53}$$

For the case of multiple primary electron collisions, where $l << \lambda$, the SEY was obtained by a double integral over the dimensionless momentum μ and the penetration depth z. It is also assumed the primary electron current decays exponentially with depth. The dependence on the primary energy was found to be described by the same function $F\left(\sqrt{E_{0s}^2/aL}\right)$, where now L is the electron diffusion length. Baroody's theory provided a beneficial template from which further refinements could be readily made. This model, however, had inadequate agreement with experimental measurements at high primary electron energies such that the theory consistently underestimated experimental results in this region.

To combat these inaccuracies, Lye and Dekker introduced a "power law" formulation [69]. Their theory of SEY assumes that the penetration energy dependence on depth is not simply quadratic, as used by Baroody, but is fitted to a power, n. Following a similar derivation to Baroody, the expression for the universal reduced yield curve became

$$\frac{\delta}{\delta_m} = \frac{1}{G_n(r_m)} G\left(\frac{r_m E_{0s}}{E_{0sm}}\right) \tag{54}$$

where r_m is the value of r for which the maximum range of the secondaries occurs, and is evaluated as $G_n\left(r\right) = e^{-r^{n+1}} \int_0^r e^{y^{n+1}} dy$.

More recent modeling efforts have focused on the development of Monte Carlo algorithms to predict SEY for various materials, including copper. Furman and Pivi made the following assumptions in their MC model: (1) Secondary electrons are generated instantaneously when a primary electron strikes a surface, (2) the energy of an emitted electron is no greater than the incident electron energy, and (3) emission angles of the secondary electrons are independent of the incident angle as well as beam and emission energy. The computer simulations reproduced the experimental data for polycrystalline copper with a number of fitting parameters. Extra attention was paid to SEY at incident energies below 20 eV since the model assumes only backscattered electrons are emitted at zero beam energy. Note that this contrasts from a few previous analytical findings; one says $\delta(0) \sim 0.07$ [45]. Furthermore, experimental SEY data becomes increasingly sensitive as beam energy is lowered to only a few eV. Most recently, our group developed a ray-tracing MC algorithm for simulating the secondary electron yield in various micro-engineered materials [64, 70, 65]. We will summarize this method in Section 3.3 and then show how it compares to our experimental results.

3.3 Monte Carlo Simulations of SEY

Our ray-tracing MC model is based on the use of Mott's elastic scattering cross-section and Penn's dielectric function approach to electron inelastic scattering, as detailed in our previous publications [64, 65]. For the sake of completeness, we give a brief description of the methods here before we apply it to the present study of SEE from copper with reticulated open-cell structure. The control study will be on copper with a flat planar surface.

3.3.1 Elastic Scattering

The significant disparity in mass between electrons and atomic nuclei results in electron-atom collisions being approximated as perfectly elastic. A commonly used elastic scattering cross-section is that of Rutherford. Moreover, the analytical expression is readily adaptable to Monte Carlo calculations. This equation does have shortcomings, however. The screened Rutherford cross-section applies strictly to high-energy electrons and solids with low atomic number. For this reason, the relativistic partial wave expansion method (RPWEM) of the Mott scattering cross-section is the superior choice for modeling copper SEY from 20 eV to 570 eV. In the Mott theory [71], the differential elastic scattering cross-section (DESCS) can be calculated as

$$\frac{d\sigma_{el}}{d\Omega} = |f(\theta)|^2 + |g(\theta)|^2$$

where $|f(\theta)|$ and $|g(\theta)|$ are the direct and indirect scattering amplitudes, respectively. The atomic differential cross-sections for elastic scattering are extracted from the NIST Electron

Elastic-Scattering Cross-Section Database [72] for angles which range from 0° to 180° and for 16 incident energies between 50 eV and 600 eV (in increments of 10 eV from 50 to 100 eV and 50 eV from 100 eV to 600 eV, respectively) and put into a tabulated data file. The elastic differential cross-sections for energies and angles other than those in the table can be calculated by linear interpolation accurate to two decimal places. The total elastic scattering cross-section for electron-molecule interaction can then be calculated by

$$\sigma_{el}(E_0) = \frac{\lambda_{el}^{-1}}{N} = 2\pi \int_0^{\pi} \frac{d\sigma_{el}(E_0, \vartheta)}{d\Omega} \sin\vartheta d\vartheta$$

where N is the number of molecules per unit volume in the target and λ_{el} is the elastic mean free path.

3.3.2 Inelastic Scattering

The energy loss function (ELF), which characterizes the inelastic scattering process, is defined as $\mathrm{Im}\left[-\frac{1}{\varepsilon(\mathbf{q},\Delta E)}\right]$ and is a function of momentum transfer, $\mathbf{q}$, and energy loss, ΔE. The dielectric function $\varepsilon(\mathbf{q}, \Delta E)$ in the ELF reflects the response of a solid to an external electromagnetic perturbation. As it is impractical to determine the $\mathbf{q}$-dependent ELF experimentally, Ritchie and Howie [73] suggested deriving an approximate $\mathbf{q}$-dependent ELF from the optical dielectric constants. By fitting the measured optical data into a finite sum of Drude-Lindhard model functions in the optical limit ($\mathbf{q} = 0$), one can extend the explicit formula to the required $\mathrm{Im}\left[-\frac{1}{\varepsilon(0,\Delta E)}\right]$ for finite $\mathbf{q}$-values.

To perform this calculation, the ELF of the material is parametrized in terms of an expansion of Drude-Lindhard-type oscillators at the optical limit with an N-term analytic form. These terms are obtained directly from the features observed in the reflection electron energy loss spectroscopy (REELS) spectrum:

$$\mathrm{Im}\left[-\frac{1}{\varepsilon(\mathbf{q}, \Delta E)}\right] = \sum_{i=1}^{n} \frac{A_i \gamma_i \Delta E}{((\hbar\omega_{0i\mathbf{q}})^2 - \Delta E^2)^2 + \gamma_i^2 \Delta E^2} \times \theta(\Delta E - E_g),$$

where

$$\hbar\omega_{0i\mathbf{q}} = \hbar\omega_{0i} + \zeta \frac{\hbar^2 \mathbf{q}^2}{2m}.$$

The $3n$ parameters A_i, γ_i, and $\hbar\omega_{0i\mathbf{q}}$, are the oscillator strength, the damping coefficient, and the excitation energy of the ith oscillator, respectively. The step function $\theta(\Delta E - E_g)$ simulates a band gap for the case of semiconductors and insulators such that $\theta(\Delta E - E_g) = 0$ if $\Delta E < E_g$ and $\theta(\Delta E - E_g) = 1$ if $\Delta E > E_g$. With the dependence of $\hbar\omega_{0i\mathbf{q}}$ on $\mathbf{q}$ being little understood, the previous equation is written with the addition of an adjustable parameter, ζ. The parameter's value is related to the effective mass of the electrons; $\zeta = 1$ for free electrons and $\zeta = 0$ for insulators with flat bands. A variety of pure elements and oxides have calculated fitting parameters for the ELF in an online database [74, 75].

An algorithm for determining the ELF($\mathbf{q}$,ΔE) from the ELF(0,ΔE) is required to continue the computation. According to Ashley's model [76], the electron differential inelastic scattering cross-section can be written as

$$\frac{d\sigma_{inel}(E_0, \Delta E)}{d\Delta E} = \frac{me^2}{2\pi\hbar^2 N E_0} \operatorname{Im}\left[-\frac{1}{\varepsilon(0, \Delta E)}\right] S\left(\frac{\Delta E}{E_0}\right)$$

where m is the electron mass, e the electron charge, N the number of molecules per unit volume in the target, E_0 the electron energy, and ΔE is the energy transfer. The function

$$S(x) = (1 - x)\ln\frac{4}{x} - \frac{7}{4}x + x^{3/2} - \frac{33}{32}x^2$$

so the inelastic scattering cross-section $\sigma_{inel}(E_0)$ for the electron-electron interactions is given by

$$\begin{aligned}\sigma_{inel}(E_0) &= \int_{W_{min}}^{W_{max}} \frac{d\sigma_{inel}(E_0, \Delta E)}{d\Delta E} d\Delta E = \frac{\lambda_{inel}^{-1}}{N} \\ &= \frac{me^2}{2\pi\hbar^2 N E_0} \int_{W_{min}}^{W_{max}} \operatorname{Im}\left[-\frac{1}{\varepsilon(0, \Delta E)}\right] S\left(\frac{\Delta E}{E_0}\right) d\Delta E\end{aligned}$$

for which W_{min} is set to zero for conductors and is equated to the band gap energy for semiconductors and insulating materials; $W_{max} = E_0/2$ is the maximum energy transfer.

3.3.3 Computational Algorithm

The angle of electron scattering at a certain step can be expressed by a random number

$$R = P_{el}(E_0, \theta) = \frac{1}{\sigma_{el}} \int_0^\theta \frac{d\sigma_{el}}{d\Omega} 2\pi \sin\vartheta d\vartheta.$$

The azimuthal angle, ϕ, takes any value in the range 0 to 2π which is selected by a random number, R, uniformly distributed in that range. This is written as

$$\phi = 2\pi(R)$$

The total elastic scattering cross-section in turn defines elastic mean free path and is given by the formula

$$\lambda_{el} = \frac{1}{N\sigma_{el}} = \frac{A}{N_a \rho \sigma_{el}}$$

where N is the atomic number density. The path-length distribution is assumed to follow a Poisson-type law. The step length, Δs, is given by

$$\Delta s = -\lambda_{el} \log R$$

where R is a random number uniformly distributed in the range [0,1].

To find the energy loss of an inelastic collision, W, from an incident electron with kinetic energy, E_0, it is necessary to calculate the function $P_{inel}(W, E_0)$. This value is accurate provided the fraction of electrons losing energy is less than or equal to W.

$$R = P_{inel}(W, E_0) = \frac{1}{\sigma_{inel}} \int_0^W \frac{d\sigma_{inel}}{d\Delta E} d\Delta E$$

for which R is a random number uniformly distributed in the range (0,1).

The probability of a given scattering event occurring is proportional to its cross-section. Thus, the cross-section specified for a given reaction is a proxy for asserting the probability that a given scattering process will occur. The stochastic process for multiple scattering events is assumed to follow Poisson statistics. If R is a random number uniformly distributed in the interval $(0, 1]$, the step length Δs is given by

$$\Delta s = -\lambda_T \ln R, \tag{55}$$

where λ_T is the electron mean free path and is given by

$$\frac{1}{\lambda_T} = \frac{1}{\lambda_{el}} + \frac{1}{\lambda_{inel}}. \tag{56}$$

The logic for determining elastic collisions of subsequent samples is defined as

$$\begin{aligned} &0 < R \leq \frac{1/\lambda_{el}}{1/\lambda_T} \Longrightarrow \text{elastic scattering} \\ &\frac{1/\lambda_{el}}{1/\lambda_T} < R \leq 1\Big(\equiv \frac{1/\lambda_{el} + 1/\lambda_{inel}}{1/\lambda_T}\Big) \\ &\Longrightarrow \text{inelastic scattering} \end{aligned} \tag{57}$$

In this manner, events are sequentially sampled, executed, and followed as effective trajectories. These paths are tracked until an electron reaches the surface with an energy larger than the work function or until it is thermalized inside the material. Electrons that escape the surface are tallied and the net yields are computed as the ratio of escaped electrons to the number of primary trajectories generated.

3.4 Experimental Approach

Since we expect that the SEY is sensitive to surface composition and structure, we outline here our experimental approach that will enable us to determine the specific effects of surface micro-architecture on the emission's energy and angular dependence.

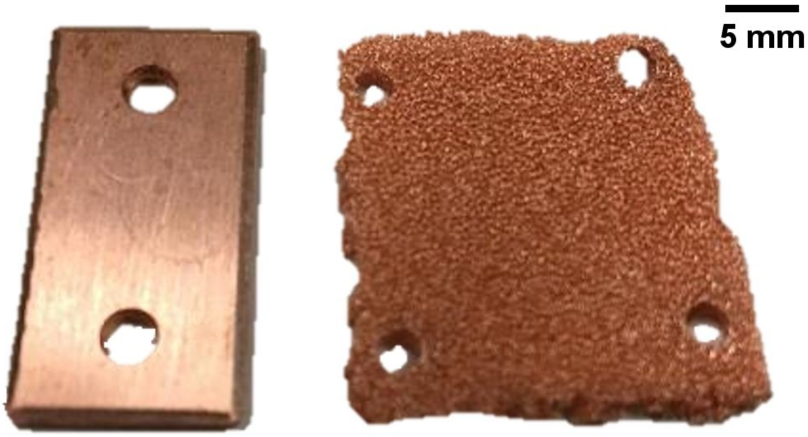

Figure 20: Solid copper (left) and copper foam (right) samples prepared for SEY measurements. Holes are created for mounting to sample holder.

3.4.1 Specimen Characterization

The team analyzed two copper specimens, one with a solid flat surface and the second with a surface composed of a reticulated open-cell structure with interconnected porosity. To thoroughly characterize the specimens we used a wide variety of material characterization tools. The geometric structure of the foam was analyzed with a high resolution CT scanner, and then re-created from a stack of 2-D images using computed tomography software. Scanning electron microscopy (SEM) is involved to provide additional geometric information along with qualitative data on tilt and composition. Surface roughness and texture of the solid copper sample were examined with atomic force microscopy (AFM). Energy-dispersive spectroscopy (EDS) was also used on both samples to quantify surface composition. Finally, X-ray diffraction (XRD) provided supplementary composition information and crystal structure. The two samples that have been characterized are shown in Figure 20.

A foam material can be simply described by any two of the three parameters: volume fraction, mean ligament thickness, and pore density. The values of these parameters, as given by the supplier and cross-checked using CT scans, are shown in Table 4. While reticulated metals can be manufactured with a wide range of parameters, the experiment required small and dense features such that the 1 mm diameter electron beam would always be incident on a representative ligament cluster.

Table 4: Copper foam parameters.

Attribute	Symbol	Unit	Copper Foam
Volume Fraction	VF	-	4.6%
Mean Ligament Thickness	LT_m	μm	45
Linear Pore Density	ρ_p	PPI[a]	100

Given the complex geometry of reticulated structures, computed tomography helps with visualization and analysis by scanning high-resolution slices of the specimen and combining them to create a three-dimensional rendering. CT slices were obtained using the GE Phoenix Nanotom M (University of Southern California Molecular Imaging Center) and combined computationally to create the images in Figure 21. The machine outputs 15 W of power from a nanofocus X-ray tube and resolves details down to 200 nm for optimally small and reflective samples. The examined piece of copper foam resulted in CT scans with 2 μm resolution; this is sufficiently detailed for individual ligaments to be presented with considerable detail.

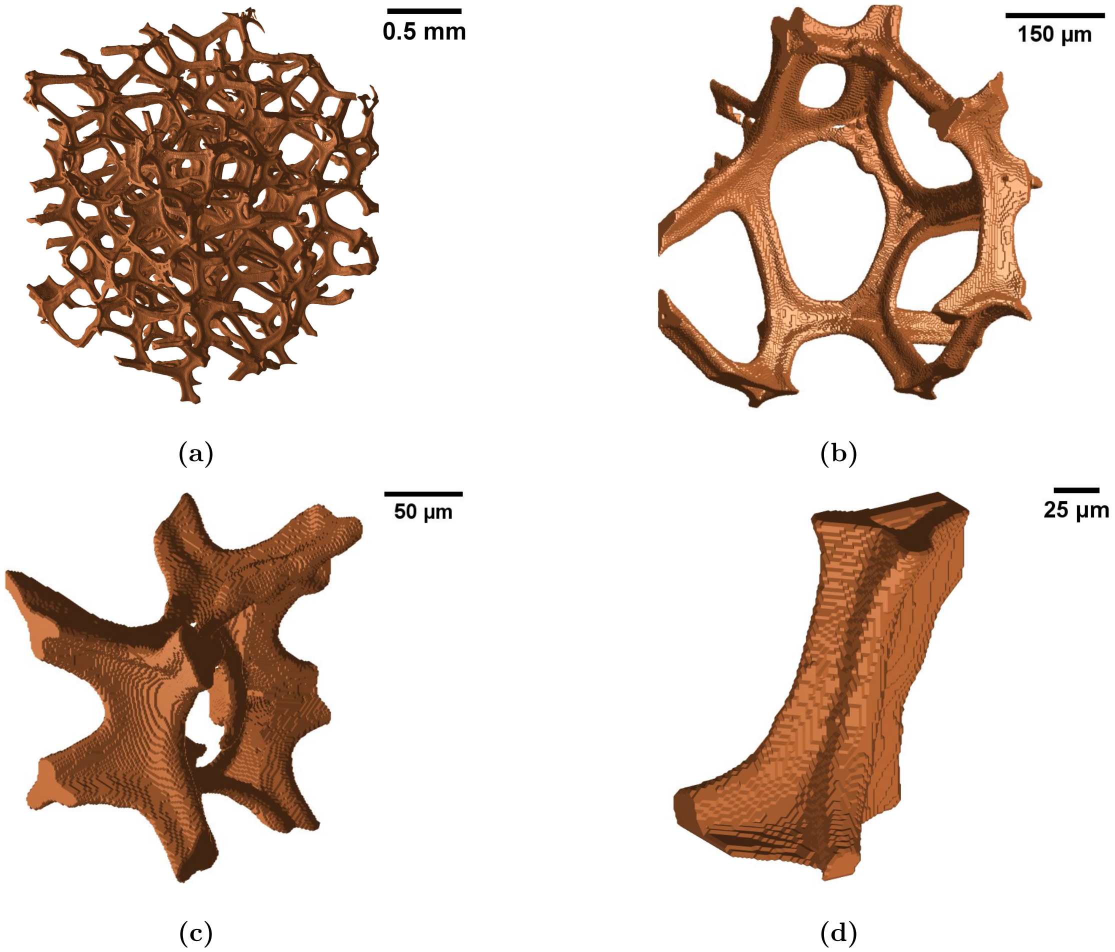

(a) **(b)**

(c) **(d)**

Figure 21: CT renderings of the copper foam's (a) general foam structure, (b) ligament cluster, (c) ligament root, and a (d) single ligament.

Four length scales fully illustrate foam specimens. These include the general foam structure, a ligament cluster, a ligament root, and a single ligament. The actual length of each scale is a function of the foam parameters with the general foam structure being mostly reliant on pore density. In this instance, the 100 PPI specimen shows indicative homogeneity for a general foam structure in approximately 2.5 mm. A ligament cluster is characterized by a central pore with ligaments extending outwardly. There is clear loss of homogeneity, but a gain in radial symmetry. It follows that a ligament root is an intersection of ligaments. At this scale, a ligament's cross-sectional geometry can be ascertained. In the case of the copper foam specimen, each ligament has a cross-section comparable to a concave equilateral triangle, or geometrically similar to a tricuspoid. Figure 21d displays a CT rendering of a single ligament. Severed from its root, this sample clearly shows hollowing along the ligament's length.

Complementary to CT renderings of the copper foam are analogous images using SEM. The machine used is the NOVA 230 NanoSEM which employs a Schottky field emission gun. The four previously mentioned length scales are achieved with magnifications of 125x, 400x, 1,000x, and 2,500x, respectively. An Everhart-Thornley detector, 5.0 spot size, and 10.0 keV accelerating voltage are consistent across the four images.

It is understood that brightness in SEM imagery indicates heavier elements, higher tilt angles, or both simultaneously. Since the copper foam sample is unielemental and nearly void of microscale contaminants, areas of higher brightness are solely indicative of tilt. Inspection of 22a validates the manufacturer's 100 PPI designation. To one significant figure, this suggests the copper foam exhibits four pores per millimeter. It follows that there are approximately two pores per scale bar length in the SEM image. The upper right SEM image shows a ligament cluster. Once again the central pore is clearly visible with ligaments extending outwardly. Figure 22c zooms into the root visible at the center of Figure 22b. At the ligament root length scale for this specimen, SEM provides resolution the CT scanner cannot. Dimples and microscale pores are identifiable, especially near the center-line of each ligament. These features, along with local surface roughness, are clearly visible at 2,500x magnification.

Since this experiment aims to compare secondary electron yield between copper foam and solid copper, geometric and composition differences between the specimens must be known. Thus, SEM images of the solid copper are provided in Figure 23. Note that the detector type, spot size, accelerating voltage, and magnifications are identical between these images and the corresponding ones in Figure 22. Rather than discussing general foam structure, ligament clusters, ligament roots, and single ligaments, respective magnifications give general

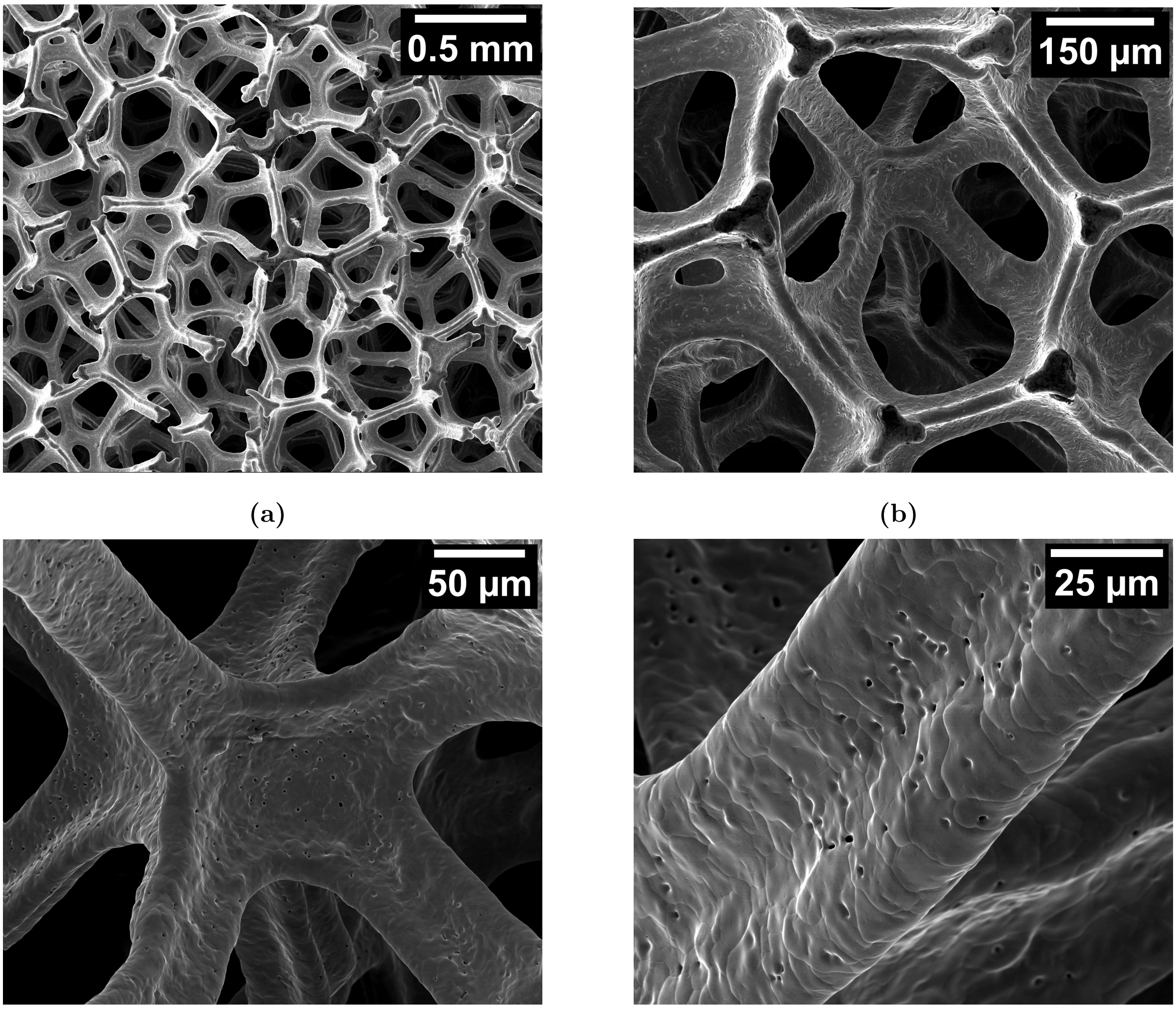

(a) **(b)** **(c)** **(d)**

Figure 22: SEM images of the copper foam's (a) general structure, (b) ligament cluster, (c) ligament root, and a (d) single ligament. Note the scale in each figure.

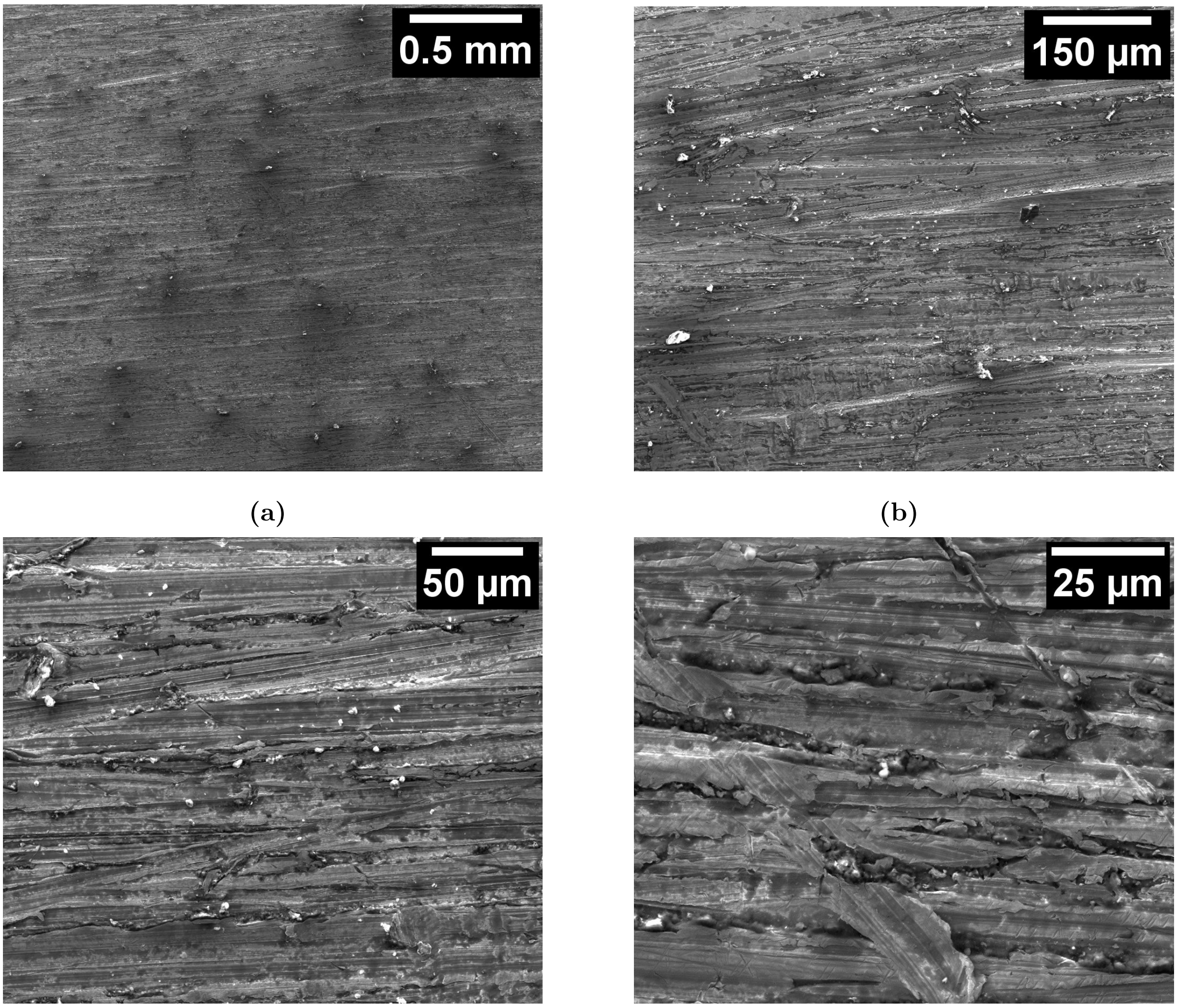

(a)

(b)

(c)

(d)

Figure 23: SEM images of the solid copper's (a) general texture, (b) general microstructure, (c) detailed microstructure, and (d) scratch striations.

texture, general microstructure, detailed microstructure, and scratch striations. As with the copper foam, this specimen is nearly void of microscale contaminants.

While the copper foam's reticulated geometry makes CT scans feasible and informative, the solid copper's relatively smooth and uniform surface makes it a strong candidate for AFM. In the device, a piezoelectic cantilever is oscillated using an alternating voltage. Recording the amplitude of subsequent contractions and expansions allows the scanner to map a three-dimensional profile of the material's topography. Figure 24 displays a 40 μm by 34 μm section of the solid copper as measured by a Quesant Q-Scope 350. As evident from the legend, the height range in the segment is 2.4 μm. The majority of the segment, however, is substantially smoother. The median difference in height across the scanned piece is 1.07 μm. In terms of roughness standards, this puts the solid copper at an N7 ISO level.

The localized areas of peaking brightness in the SEM representation, and thus high tilt, exist in the AFM illustration as orange and brown crests. These towers stand approximately 1 μm above the median plane of the specimen. The valley that cuts diagonally across the scanned portion is a topographic visual of a scratch striation. It is noteworthy that grain boundary widths are on the order of 2 nm [77], so such a feature is not resolute at these scales. The scratch shown has a width of approximately 4 μm and a maximum depth about 1 μm below the median plane.

CT, SEM, and AFM together provide a holistic picture of the geometric features of the two copper specimens, but regarding composition the information garnered from these tools is predominately qualifiable. Energy-dispersive X-ray spectroscopy (EDS) helps with composition quantification. A spectrometer inside the NOVA 230 NanoSEM counts the discrete energies emitted from the specimens. This provides compositional information since these X-rays are characteristic, and thus point to particular emissions. Nearly all X-rays measured from the two samples are electrons returning to the L and K shells of copper. The only measurable elements besides copper are trace amounts of carbon and oxygen on the solid sample (0.04% and 0.03% by weight, respectively). No measurable contaminants were found on the foam specimen. These minuscule amounts are shown to have negligible impacts on SEY. While the EDS results are trivial, they affirm the specimens' composition

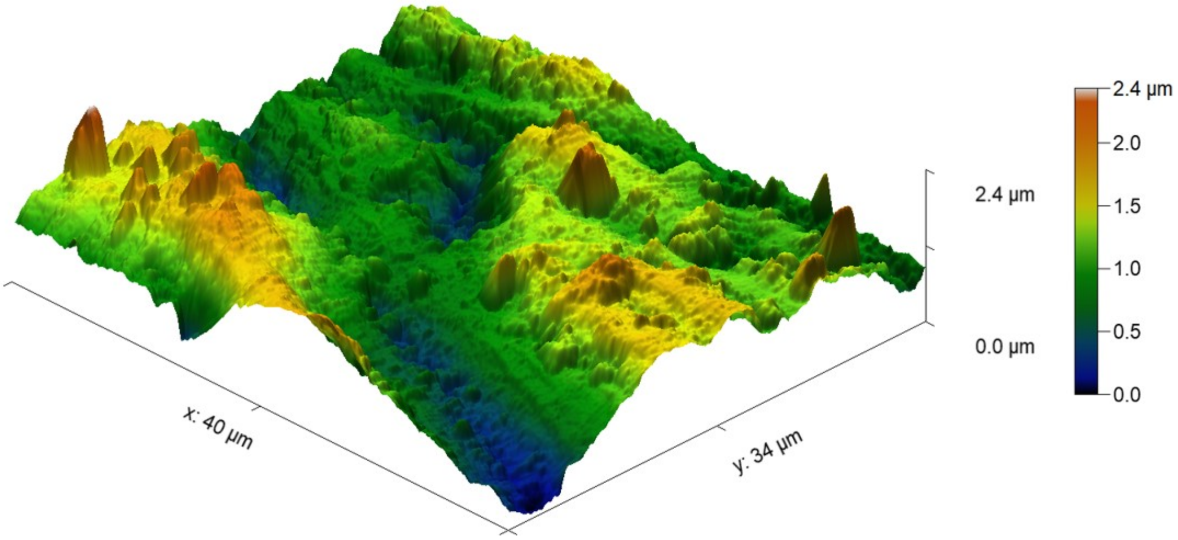

Figure 24: AFM measurements on solid copper. The roughness scale is indicated on the color bar.

and decisively eradicate ambiguity regarding potentially confounding alloying, oxidation, or hydration.

The final form of material characterization in this experiment is X-ray diffraction (XRD). The method provides phase identification of crystalline materials and lattice strain. The instrument used is the BEDE D1 and is equipped with a 2.2 kW sealed tube X-ray generator, a goniometer with 0.16 inch resolution in θ and ω, and a high dynamic range scintillation detector. Similar to EDS, XRD plots show peaks of highest intensity according to characteristic energies. These energies, however, satisfy the Bragg Equation, whereby constructive interference reaches a local maximum. An X-ray diffractometer rotates the sample such that 2θ represents the angle between incident rays and the detector. This differs from ω which is the angle between incident rays and the sample surface. Figure 25 overlays the XRD scans for the two copper specimens. Five coinciding peaks are prominent in each data set. These represent the (111), (200), (220), (311), and (222) crystallographic planes of copper. This supports the EDS results which suggest negligible contaminants and impurities are present in the samples. Analyzing the intensities of respective peaks, one can involve the Scherrer and Williamson Hall equations to determine the lattice strain in each sample. One can conclude these values are 850 μ for the solid copper and 375 μ for the copper foam.

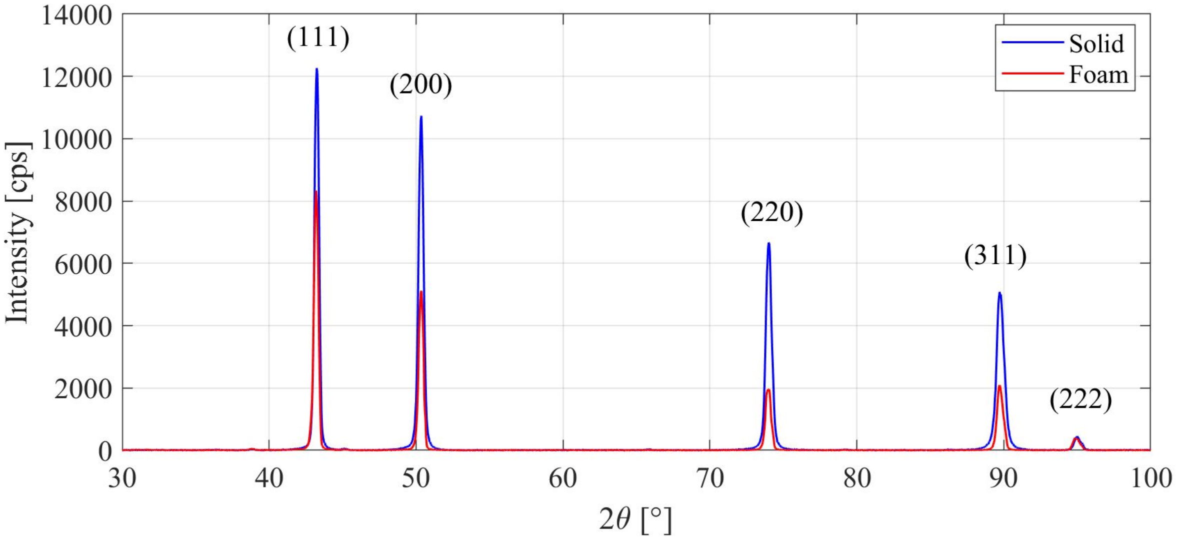

Figure 25: XRD measurements for solid and foam copper specimens.

The comprehensive techniques of material characterization allow one to conclude that the two specimens, copper foam and solid copper, differ by the existence of geometric reticulation only. That is, confounding variables such as subtle differences in composition are negligible. It was also discussed that the foam parameters in the reticulated sample are chosen to pair well with the secondary electron chamber. 4.6% volume fraction with 45 μm mean ligament thickness and 100 pores per inch maintain that the 1 mm diameter electron beam is sufficiently large relative to a ligament cluster. The proceeding discussion delves into the components that comprise the experimental apparatus and the process by which SEY data is acquired from the two copper specimens.

3.4.2 Measurements of SEY

SEY is fundamentally the average number of emitted secondary electrons for a given incident electron. It follows that one must have a method to count or measure the number of electrons both entering and leaving the test specimen. Since electrons carry elementary charge, current, or the rate of charging, is a straightforward quantity that can be measured directly. Thus, SEY is the quotient of current produced from secondary electrons, I_{SE}, and current from primary electrons, I_p. Assigning SEY to the character δ, one can write this relation as $\delta = \frac{I_{SE}}{I_p}$. Since the number of secondary electrons is the difference in primary electrons and electrons remaining on the specimen, one can involve the sample current, I_s, and write $\delta = \frac{I_p - I_s}{I_p}$. This easily simplifies to the sample method's final expression

$$\delta = 1 - \frac{I_s}{I_p} \tag{58}$$

Rather than using the current of the sample, another technique to calculate SEY is by direct measurement of electrons given off as secondaries. Provided a strong enough voltage to collect the secondary electrons, the current of the collected electrons, I_c, can be compared with the primary current to achieve the same result. Closely related to Equation 58, this quotient which is referred to as the collector method, is written as

$$\delta = \frac{I_c}{I_p} \tag{59}$$

Both of these equations are experimentally valid for calculating SEY and the choice to use one over the other is based on the particular apparatus. It is previously mentioned that SEY is also a function of incident angle, θ. As θ is increased, PEs penetrate the material within a shallow region and SEs produced must traverse shorter distances to reach the surface.

3.4.3 Apparatus

As previously introduced, specimens receive primary electrons at a range of incident angles and at a variety of primary energies. This is achieved with a field-emission source, namely a thermionic electron emitter made of tungsten filament. The sample and emitter are located inside of a high vacuum chamber to maintain the specimen conditions across the test duration as well as to minimize interference from gas phase scattering while beam energy is low.

Sample current, I_s, is measured using wires that are electrically connected to the specimen via a conductive plate. A vacuum-jacketed port in the chamber allows the current to be read externally. Also inside the chamber is a Faraday cup which is used to collect the primary current, I_p. This is identified in Figure 26. The Faraday cup is positioned directly below the electron beam during this measurement and is moved into place by the translating and rotating rod. Three components in the experimental apparatus control voltage potential: the source-meter, battery supply, and the grids. A potential of 72 V is found to be sufficiently strong to collect and accurately measure secondary electrons. Thus, the two batteries in series output 72 V and, for the appropriate setup, the source-meter is prescribed to output the same potential. The collector grids are mounted collinearly to the electron gun and provide both a voltage potential and a housing for the SEs such that a current measurement can be attained. The secondaries are accelerated toward the grids during the collector method procedure. The SEs terminate in a BNC connector which attaches directly to the grids and allows for the charge to be captured.

The electron beam can be steady-state or pulsed. An oscilloscope makes the latter feasible and also provides a second method to record current measurements; the first method is direct measurement from the source-meter. Both beam styles are viable using either the collector current or the sample current method. This gives rise to four ways of acquiring data. For instance, with a steady-state electron beam and using the collector current method, the source-meter is set to output 0 V and grids are biased to 72 V with a pair of batteries in series. The source-meter is connected by wires to the negative terminal of the second battery. With a steady-state electron beam using the sample current method, the source-meter and grids are biased the same as before, but the source-meter is connected to the sample itself. With a pulsed electron beam using the collector method, the setup is the same as the previous one, but an oscilloscope is connected to the negative terminal of the second battery. This allows the currents during each pulse to be measured digitally. The fourth method is a pulsed electron beam using the sample method. For this configuration the source-meter is set to output 72 V and is connected directly to the grids. The sample is wired to the oscilloscope to digitally record the measurements during each pulse. Present experimental data in Figures 27-30 use the configuration for a steady-state electron beam with the collector method.

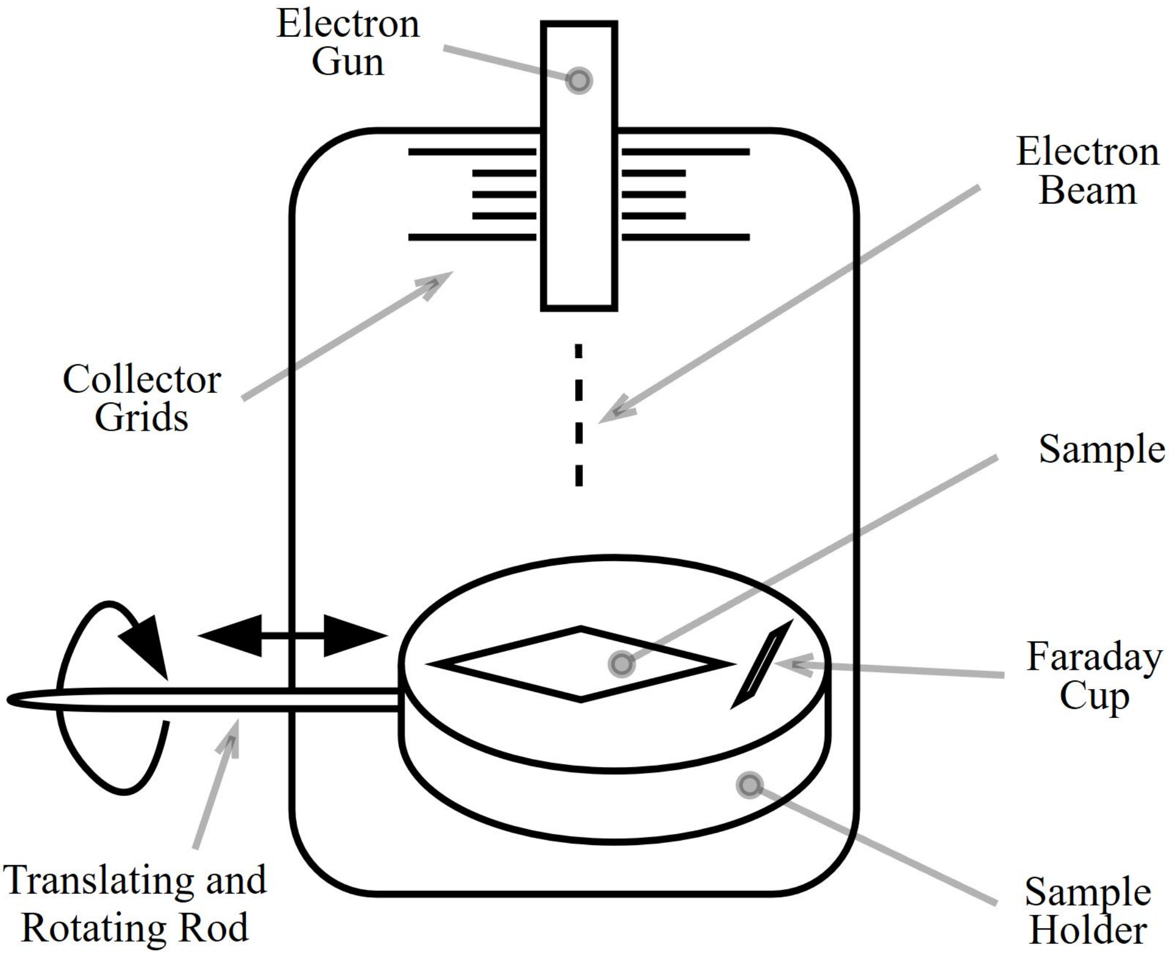

Figure 26: Vacuum chamber schematic with major internal components. Sample holder degrees of freedom also illustrated. Translation is for switching between the Faraday cup and the sample whereas rotation is for prescribing different incident angles, θ.

3.4.4 Procedure

One of the copper specimens is mounted onto the sample holder via nonconducting screws. The holder is then attached to a single-axis rod which articulates to test incident angles. Accuracy of θ is within 0.5°. And though the rod can rotate over 90°, the projected length of the electron beam onto the sample is cosinusoidal with incident angle. This sets an upper limit of $\theta = 75°$. The sample holder is placed inside the vacuum chamber, of which is brought to a pressure below 5e-6 Torr. At this point the electron gun is turned on and the beam is focused to a spot size of 1 mm. The apparatus is then configured according to one of the four wiring configurations described. A particular beam energy, E_0, and incident angle, θ, are set and a data point can be recorded. E_0 and θ are updated until each combination of vectors $\theta = [0, 10, 30, 45, 60, 75]^\circ$ and $E_0 = [20, 80, 200, 400, 570]$ eV is complete. After the chamber is vented, the procedure repeats with the other copper sample.

3.5 Results

One of the early experiments on polycrystalline copper was performed by [54], who aimed an electron gun at a flat copper specimen inside of a vacuum chamber and gathered data using a spherical retarding-field analyzer. Using this apparatus, researchers quantified the SEY as a function of the primary energy and beam incident angle. The former was tested between 0.5 and 10.0 keV and the latter from 0 to 70°. The two most relevant conclusions Koshikawa and Shimizu made are that polycrystalline copper has a $\delta = 1.43$ at 500 eV and that the SEY increases monotonically with incident angle. Applying a polynomial fitting function to δ vs. θ at this beam energy, the resulting third order polynomial is found to be $\delta = 0.0058E_0^3 - 0.0461E_0^2 + 0.1453E_0 + 1.3129$. Other experiments on copper have been reported. [78, 79, 80, 60]

The angular dependence of the SEY was also refined. Bruining expressed the relationship of SEY and beam incident angle as [68]

$$\ln \frac{\delta(\theta)}{\delta(0)} = A(1 - \cos(\theta)) \tag{60}$$

where A is a constant [42]. Scholtz proposed a universal secondary electron curve based on the maximum yield, δ_m and the energy at which it occurs, E_m. A Gaussian distribution is applied to $\ln\left(\frac{E_0}{E_{0m}}\right)$. With the standard deviation, σ, found to be 1.6, the Scholtz model is written as [81]

$$\delta(E_0, \theta) = \delta_m(\theta) \exp\left[-\left(\frac{\ln\left[E_0/E_{0m}(\theta)\right]}{\sqrt{2}\sigma}\right)^2\right] \tag{61}$$

and is applicable for flat surfaces. Note that while this empirical model accurately describes SEY data across a wide range of incident energies, it has no physical basis.

Data presented describes the SEY for solid and foam copper as a function of beam energy and incident angle. These results are obtained experimentally per the aforementioned apparatus and procedure as well as computationally via the described Monte Carlo method. Comparing against existing literature for as-is solid copper δ collected using a normally-incident electron beam, it is evident per Figure 27 that the present experimental data aligns well. Together, these five sets of data are used to produce a 95% confidence interval, a 95% prediction interval, and a nonlinear regression curve. With the present data entirely within the prediction interval, the experimental data for solid copper is statistically valid.

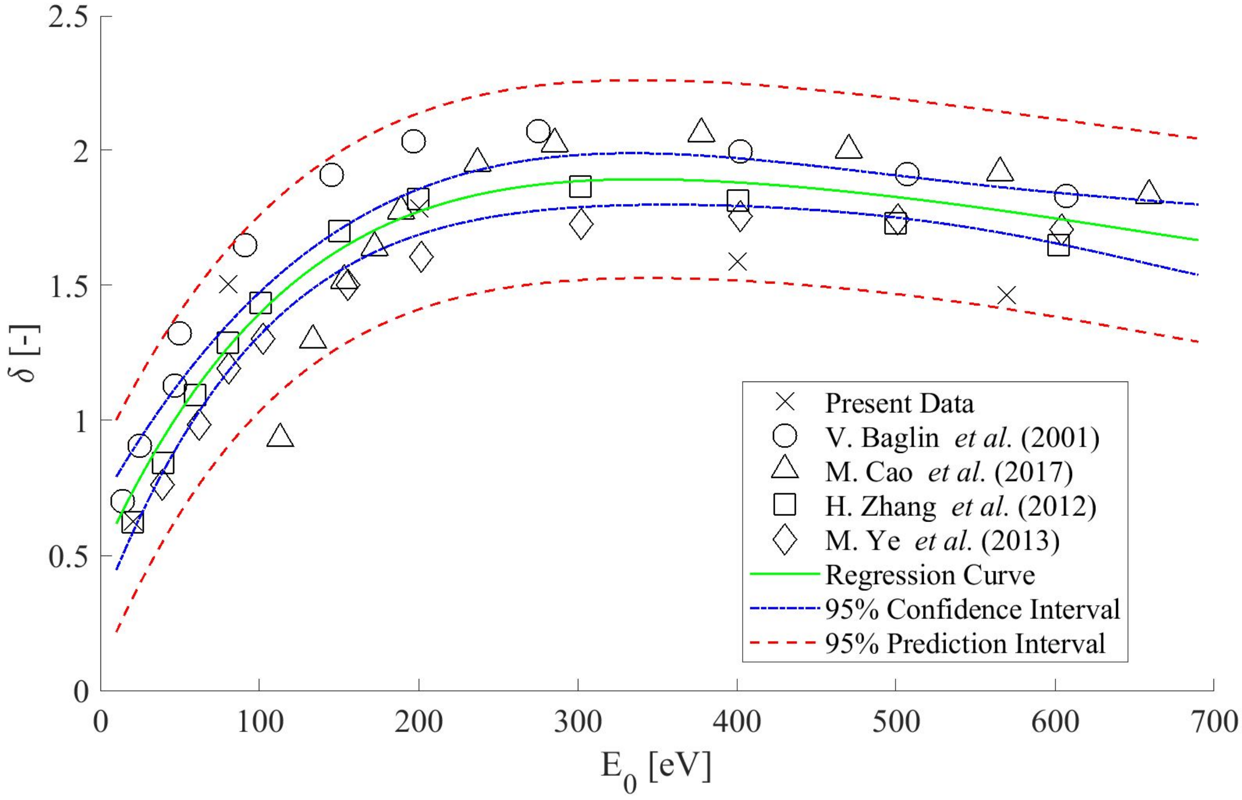

Figure 27: Comparison of present experimental solid copper normal-incidence SEY results with comparable literature data. [78, 79, 80, 60]

A range of δ are to be expected for as-is solid copper specimens due to subtle differences in surface charging, contaminants, and hydration. The 95% prediction interval approximates this range and provides evidence for a proposed data point's appropriateness in the existing collection of data. The nonlinear regression is defined using the polynomial model $\delta = (\theta_1 + \theta_2 E_0)/(1 + \theta_3 E_0 + \theta_4 E_0^2)$. Minimizing the residual gives the coefficients $\theta = [0.48, 0.15, 3.5\text{e-}3, 6.4\text{e-}6]$. The results shown in Figure 27 validate the control. Solid copper δ has been experimentally calculated by several independent teams and is predominately shown for purposes of validation and direct comparison. Since the present data aligns well, novel results can be confidently presented.

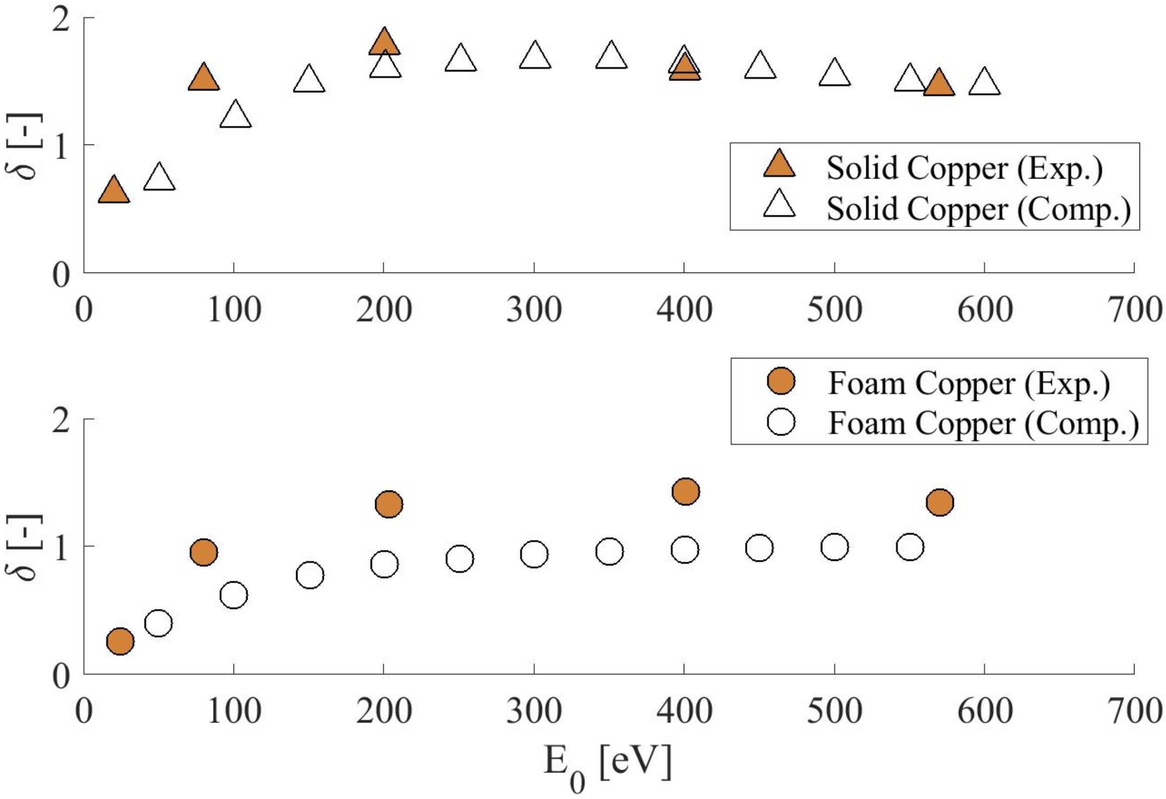

Figure 28: Comparison of solid copper (top) and copper foam (bottom) between empirical and computational results for normal incidence.

The next set of results is for all normally-incident data. The comparisons that can be drawn are between experimental and computational data and between solid copper and copper foam data. Filled markers in Figure 28 represent experimentally-obtained data and the empty markers are from the computer simulations. The upper plot illustrates strong agreement between simulation and experiment for solid copper. Both curves quantify δ_m at approximately 1.8 and locate the peak at about $E_0 = 300$ eV. The copper foam simulation matches the shape of the respective experimental yield curve, but slightly under-predicts the quantity of secondaries to primaries. Reasons for this are discussed later. The copper foam reaches a δ_m of about 1.4 and occurs at about $E_0 = 500$ eV. This is a substantial and undeniably valuable reduction in secondary electron production. The yield saturates and remains nearly unchanged at energies higher than 400 eV. Minimal deviation is found in the tested range. This contrasts from solid copper which gradually produces fewer secondaries for a given primary electron as energies are tested above E_{0m}.

Maintaining the filled and empty marker distinction for experimental and computational results, respectively, Figure 29 displays the SEY curves for solid copper at $\theta = [0, 30, 45, 60, 75]°$. The curves in Figure 29a and 29b both illustrate an increase in δ_m with a rise in incident angle. At $\theta = 75°$ the solid copper plots report a δ_m of 2.5 and 2.2, respectively. This is a considerable increase in secondary electron production relative to the lower incident angles. Recall that normal incidence is calculated to have a δ_m of 1.8. Regarding differences between experimental and computational data, the simulations predict shallower breakdowns than the experiment calculates. Visually, SEY curves in Figure 29a appear to diverge more noticeably at higher beam energies than the simulations suggest.

Quantifying the SEY reduction experienced by the foam sample is best shown in Figure 30 where the solid and foam SEY curves for normal and 45° incidence are illustrated on the same plot. SEY data for the solid material consistently lies above that for the foam data. Overall, the copper foam sample experiences an approximate 20% reduction in SE yield relative to its solid counterpart. This suggests a systematic entrapment of secondary electrons in the reticulated geometry. The greatest difference is seen at δ_m. It is remarkable to notice that the energy dependence of the SEY in the foam samples is quite insensitive to the primary electron energy, especially for energies above approximately 200 eV. By contrast, the decrease in SEY for the solid material in this region is clear. This is consistent with the theoretical models, whereby the electron energy decreases substantially as it penetrates into the solid. This is a signature of a different transport mechanism in the reticulated foam, where ligament shadowing effects determine how deep electrons can penetrate before they generate secondaries.[64, 70]

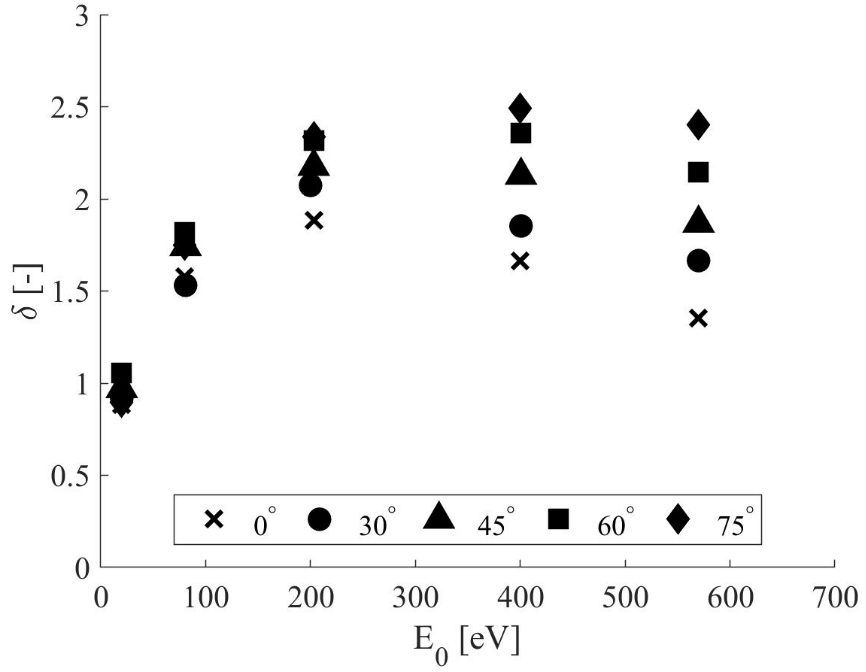

(a)

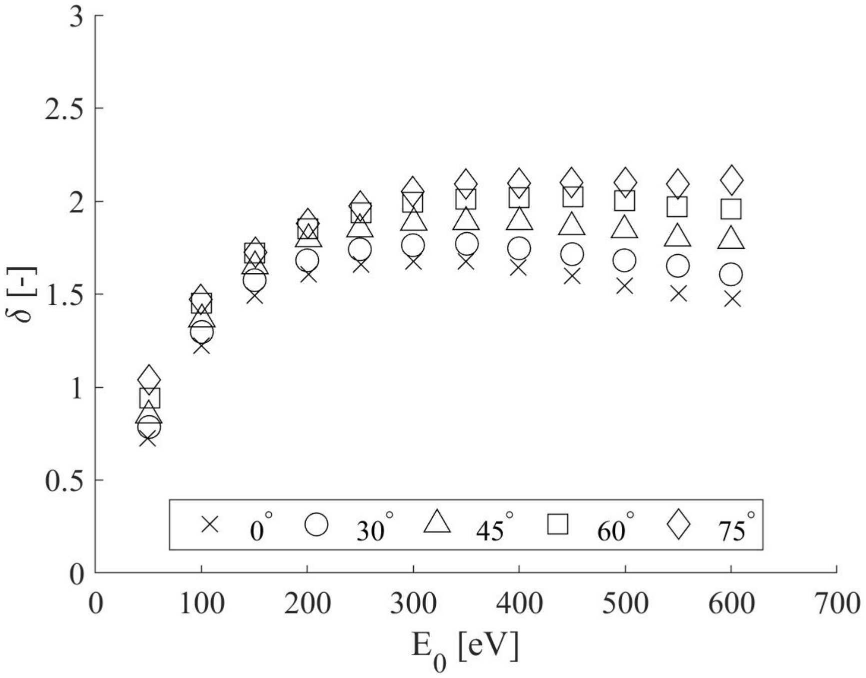

(b)

Figure 29: Solid copper data for different incident angles. (a) Experimental data and (b) computational data.

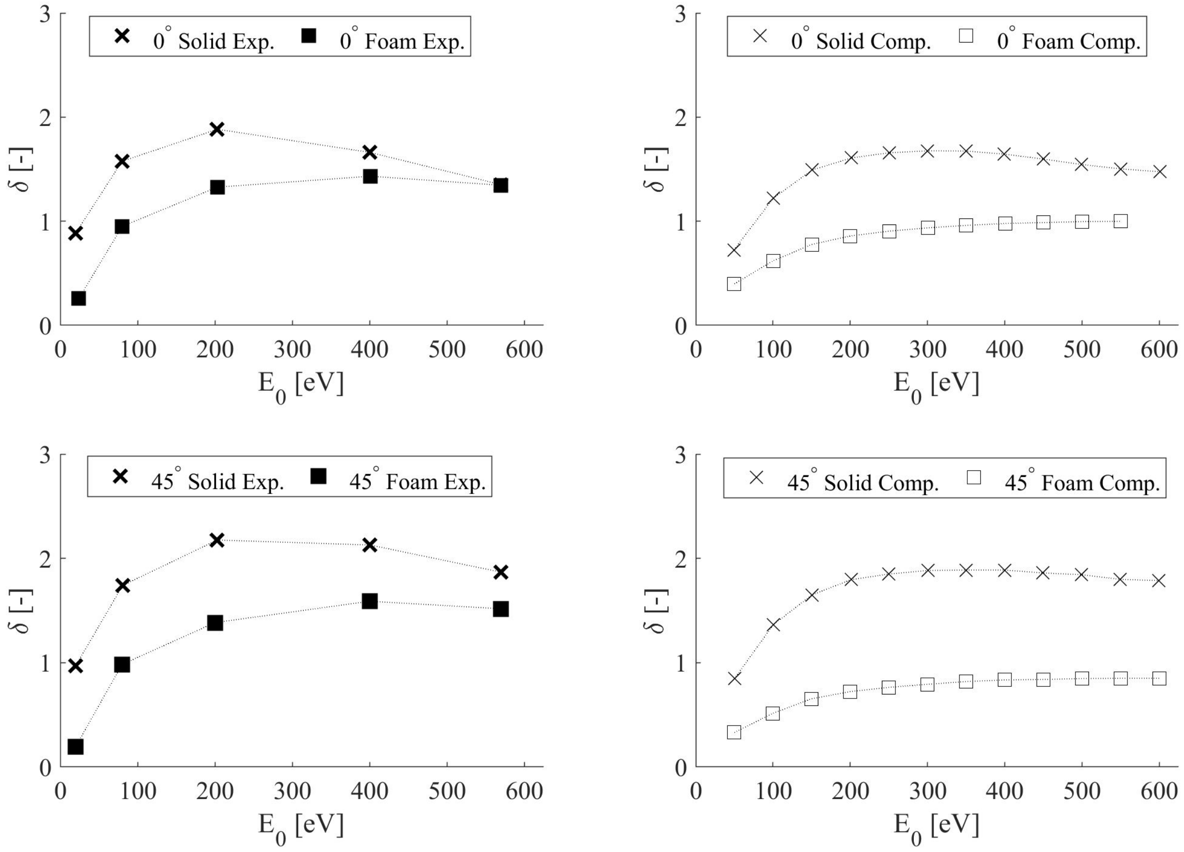

Figure 30: SEY comparison between the solid and foam samples at normal incidence (top) and 45° incidence (bottom). Experimental data is illustrated on the left with computational on the right.

3.6 Summary & Conclusions

In comparing results for SEY between thoroughly characterized copper specimens, it is clear that reticulation in foam geometries decreases yield since the pores trap secondary electrons. One can also conclude that SEY monotonically increases with the incident angle for the solid copper specimen while SEY is less dependent on incident angle for the foam copper specimen since a smaller increase is exhibited. Higher incident angles cause SEs to be generated near the surface, and thus traverse shorter distances to reach the surface. This reduction in collisions prior to reaching the surface gives these electrons a higher likelihood of maintaining sufficient energy to exceed the work function and escape the material. The reticulation in the foam diminishes this overall effect such that an electron's prospect of escaping, and thus the depth of SE generation, is less dependent on incident angle than it is for its solid counterpart. The Monte Carlo simulation results slightly underpredict the experimental data, but these differences are likely attributable to tolerances in the experimental apparatus components and details of the computer simulation that do not perfectly reflect the physical environment. These include the treatment of electrons as point particles and the simplification of the surrounding space to a perfect vacuum.

Data agrees particularly well for incident angles between 30° and 60° whereas the simulations somewhat over-predict the experiments at low incident angles and slightly under-predict at the highest incident angles. Still, agreement is good between the two approaches such that the results further validate the general conclusion that foam materials have lower SEY than their solid counterparts. Generalizations can also be made about other volume fraction foams. That is to say, the reduction in yield is an extensive property of the foam. Qualitatively, had a copper foam with higher volume fraction been tested, the SEY reduction relative to solid copper would be less. Our MC simulations show this general trend. It follows that increasingly reticulated foams shall emit fewer SEs for each PE introduced to the specimen and result in consistent SEY reductions in excess of 20%.

CHAPTER 4

Optimized Permeability of Microporous Foam for Transpiration Cooling in Hypersonic Leading Edge

4.1 Introduction

Recent research on hypersonic vehicles indicates that the key limiting factor in continued progress is the ability for structural materials in the leading edge (LE) to withstand the extreme heat generated by aerofriction while the vehicle moves at hypersonic speeds. Various cooling concepts have been proposed for the dissipation of the extreme heat flux imparted on the LE. These include evaporation/condensation devices, phase change processes, ablation, electron emission, film cooling, etc. [82, 83, 84, 85, 86] The survival of the LE structure in the harsh thermal environment is fundamental to the success of any of these cooling concepts. While advancement in hypersonic vehicles requires a cooling method to be implemented with manufacturability in mind, we focus on presenting the optimal computational results. Still, the present work recognizes that the greatest practical benefits are predicated on fabrication successfully replicating the results of the computer models in its study of the evaporative transpiration cooling mechanism.

Open-cell reticulated foams are porous counterparts to solid materials and have tailored properties which are different from the parent solid form. For this reason, they are considered a class of *metamaterials* that may offer unique advantages for applications in hypersonic vehicles. Foam geometries can be specified with any two of following three characteristics: the volume fraction, VF, the pore density, ρ_p, and the mean ligament thickness, LT_m. The volume fraction is the ratio of the volume occupied by the solid material to the total volume. The pore density refers to the number of cells visible per unit length on a two-dimensional micro-graph, with a typical unit of pores-per-inch (PPI). The ligament thickness is simply the average width of the ligaments which comprise the reticulated foam structure.

Currently, two methods are used to fabricate metallic foams of spatially-varying porosity. These are chemical vapor deposition (CVD) and 3D printing. CVD is a physical process in which gaseous metal halides are applied to heated surfaces to create a uniform coating. In the case of open-cell foams, the gas infiltrates the pores of the foam substrate and coats the ligaments until a desired porosity is achieved [87]. Note that 3D printing is commonly used for building micro-architectured materials with regular (i.e., non-stochastic) cells and is distinct from the CVD/computational-CVD process.

LEs of hypersonic aircraft experience intense heat flux due to aerofriction. Moreover, shock-shock and shock-boundary layer interactions are often culpable for extreme temperatures by aerothermal heating [88]. An interesting question arises, then, regarding the relationship between the spatial variation in foam porosity and its effectiveness in cooling non-uniform incident heat flux. Recently, Du *et al.* [89] demonstrated that the thermal efficiency of concentrating solar power (CSP) receivers can be increased by around 4% by spatially controlling the porosity of 3D printed nickel superalloys. CSPs are devices which focus the sun's energy, often with the use of mirrors. Similar to the receivers of CSP, the spatial distribution of the incident heat flux on the LE can exhibit a single central peak. This aspect brings out the possibility that by proper distribution of porosity, one may be able to achieve substantial benefits by enhancing the cooling rate of the LE. Advantages for hypersonic vehicles with an optimized permeability leading edge could include increased range, heightened Mach capability, and improved reusability. One downside, however, is the added difficulty in the fabrication of spatially-varying porosity, but this can be achieved by 3D printing or by CVD.

Since transpiration cooling requires a continuous supply of the coolant from within the foam, it is important to understand the role of its self-pumping through capillary forces. We note that self-pumping is in direct contrast to active pumping, which requires additional forces to make the fluid flow. Since active pumping necessitates another pumping mechanism, it typically increases the intricacy and weight of the design. In either case, capillary forces may be opposed by dynamic vehicle acceleration forces. Thus, we need to determine the influence of vehicle dynamics on the ability of the structural foam to continuously supply the coolant and not experience “dry-out”. In a transpiration cooling application of a structural foam, a fluid is required to flow through its complex network structure in a tortuous path created by the different orientations and shapes of foam ligaments before it finally evaporates upon exiting the foam’s outer surface. As the fluid, or transpirant, travels through the foam, it is self-pumped by capillary action created by surface tension forces. However, flow is resisted by viscous interaction between the fluid and the complex geometry of the porous structure [90]. It follows that the geometric characterization of the foam is highly significant in determining the way a fluid travels through it, and hence the overall cooling effectiveness. For instance, flow through the interior of fractures can be modeled using a form of Darcy’s law [91] whereas variably saturated porous media are better handled by Richards’ equation [92]. A third approach to modeling flow in porous media is described by the Brinkman equation [93]. These models generally account for the kinetic potential from fluid velocity, pressure and gravitational potential, and the dissipation of kinetic energy by viscous shear.

The objective of this work is to develop a computational method which determines an optimized foam structure for LEs in hypersonic aircrafts and to determine the significance of vehicle acceleration on potential dry-out of the cooling liquid within the foam. We aim to find the optimal spatial distribution of the foam pore density such that more effective transpiration cooling can be realized. To achieve this overarching goal, we address the following: 1) Heat flux distribution along a hypersonic LE for various Mach numbers; 2) Permeability of the structural foam as a function of its volume fraction; 3) Foam topology optimization for transpiration cooling effectiveness; 4) Flow velocity of isotropic and optimized foam models; 5) Influence of vehicle acceleration on passive pumping by capillary action.

The paper is organized as follows. First, research background is given in Section 4.2. Next, in Section 4.3, we introduce the equations used in finding the heat flux along the leading edge as well as practical considerations and relevant schematics. Results for the angular distribution of the heat flux around a semicircular nose tip are also given. Then we discuss fluid flow in porous media in Section 4.4. The theory is detailed along with the methods for developing a permeability model. The section also includes illustrations of flow through porous media of varying porosity and comprises associated quantitative results. The intermediate results contained in Sections 4.3 and 4.4 are leveraged to develop a transpiration optimization model in Section 4.5. The methodology is presented in Section 4.5.1. An isotropic permeability case is provided in Section 4.5.2 as a benchmark for Section 4.5.3 which details the results from the optimized permeability model. Building on the outcomes from this study, we consider the concept of passive pumping. Critical accelerations for passive pumping are found and presented in Section 4.5.4. Finally, conclusions of the present study are summarized in Section 4.6.

4.2 Research Background and Motivation

With increasing aircraft speeds, excessive aerodynamic heating of the nose tip quickly became a significant issue, for which creative cooling strategies have been devised over many years. The growth in computational methods has led to greater understanding of heat flux distributions in millimeter-length LEs [94], validation of heat pipe designs within the inner boundary adjacent to and including the stagnation point [95], and verification of transpirant injection efficiency [96]. A well-regarded and relevant numerical study was performed by Meyer *et al.* [97]. They developed a time-marching Navier-Stokes code to simulate air injection into the stagnation point of the LE and ultimately qualify cooling effects. For a vehicle traveling at Mach 6.5 and an altitude of 30 km, the team found that the forward-facing jet lowered wave drag by up to 55%, which aided in reducing heat transfer rates. More recently, a team from the German Aerospace Center fabricated a porous LE test article from Procelit 170 (91% alumina and 9% silicon dioxide) to advance this idea of injecting transpirant into the flowfield, but now with the injector commanding a greater role in the design. Namely, the transpirant flowed through the porous domain which doubled as the structure. Water was pumped from a reservoir to the stagnation point at a rate of 2×10^{-4} kg/s and 1.7 kPa of gauge pressure was applied to the stagnation point to combat a peak heat flux of 2.8 MW/m^2. It was found that water cooled the test specimen from 2,000 K to under 300 K

[98].

Analyses of fluid flow and heat transfer in porous media, and hypersonic LEs in particular, have seen an increase in model detail and experimental precision [99, 100, 101, 102, 84, 103, 104, 105, 106]. As alluded to earlier, computer-based optimization studies of the LE geometry aimed at minimizing heat flux [107, 108, 109, 110, 111, 112, 113, 114, 115, 116] and maximizing transpirant cooling effectiveness [117, 118, 119] have been performed. Additionally, phase change [120] and self-pumping cooling concepts have incorporated porous media at the front of hypersonic LEs. These efforts concluded that foams could passively pump transpirants into the stagnation region by capillary action. Moreover, it was pointed out that non-uniform porosity can increase coolant effectiveness due to differences in permeability [121]. However, the optimal spatial distribution of pore density (and hence permeability) as well as the influence of vehicle acceleration on self-pumping were not considered. The present investigation seeks to determine how greatly an optimal spatial porosity distribution can lead to more effective evaporative transpiration cooling. Furthermore, the team builds upon this newfound knowledge to understand the influence of vehicle acceleration on self-pumping through the porous LE.

4.3 Heat Flux Distribution Along the Leading Edge

Optimization of the foam structure requires knowledge of the spatial distribution of the incident heat flux on the LE. This heat flux can be determined by boundary layer theory. We utilize a procedure described in Anderson [122] to compute the heat flux distribution. We assume that the velocity components are zero ($u = v = 0$) and the temperature is that of the wall ($T = T_w$) on the leading edge surface ($y = 0$). The thickness is given for arbitrarily large y (i.e. $y \to \infty$) for the boundary layer of the LE, and the flow velocity and temperature are defined at the edge ($u \to u_e$, $T \to T_e$). The subscript e refers to “edge” throughout the paper, while edge velocity is set to zero at the stagnation point. Figure 31 is provided to aid in visualization. It represents a two-dimensional cylindrical body which extends infinitely out of the page. R is the radius of curvature at the stagnation point and x is the distance along the surface.

Utilizing the boundary layer theory gives the heat flux at the stagnation point of cylindrical hypersonic leading edges. This can be accomplished by the "shooting method" where one solves the boundary value problem as an initial value problem and iterates. With this approach, the heat flux near the stagnation point can be written as the rate of convective heat transfer driven by the difference in enthalpy and is given as [123]

$$q_{\mathrm{gw},0} = 0.57 Pr^{-0.6} (\rho_0 \mu_0)^{1/2} \sqrt{\frac{du_0}{dx}} (h_{0,\mathrm{aw}} - h_{\mathrm{w}}) \tag{62}$$

for which the subscript *aw* is an acronym for "adiabatic wall", *gw* is short for "from the gas to the wall", and the subscript 0 indicates the measure is taken at the stagnation point. The edge velocity at the stagnation point is differentiated as a function of position. This term is defined as follows: $\frac{du_0}{dx} = \frac{1}{R_{\mathrm{LE}}} \sqrt{\frac{2(P_0 - P_\infty)}{\rho_0}}$. The stagnation point adiabatic wall enthalpy can be calculated from values in standard atmosphere tables at a defined altitude [124]. $h_{0,\mathrm{aw}}$ for different Mach numbers, along with other pertinent variables, are provided in Table 5. The wall enthalpy can be calculated with the help of the same table and its equation is written as $h_{\mathrm{w}} = C_{p_\infty} T_\infty + \frac{u_\infty^2}{2}$.

With the dynamic pressure maintained at 48 kPa and a particular Mach number prescribed, one can obtain the altitude, free-stream temperature (T_∞), temperature at the stagnation point (T_0), free-stream pressure (P_∞), free-stream air density (ρ_∞), free-stream velocity (u_∞), and adiabatic wall enthalpy at the stagnation point ($h_{0,\mathrm{aw}}$). Recall that 48 kPa is chosen for its practical application to typical flight profiles among hypersonic vehicles. Higher dynamic pressure would lower the corresponding altitude and vice versa. Similarly, nonstandard conditions would further alter the values provided in Table 5. Note that a constant dynamic pressure was used throughout the study since it represents the optimal climb path, and thus the flight trajectory that the LE must be able to survive to be viable.

The heat flux is at its peak at this point since the energy in the flow is entirely potential and internal. As the flow continues around the leading edge and thus away from the stagnation point, the flow trades a portion of this potential for kinetic energy. This, in turn, reduces the heat flux and can be represented as a portion of the maximum value at the

Table 5: Calculated stagnation and free-stream conditions for select Mach numbers at 48 kPa dynamic pressure

M_∞ [-]	Alt. [km]	T_∞ [K]	T_0 [K]	P_∞ [Pa]	ρ_∞ [kg/m^3]	u_∞ [m/s]	$h_{0,aw}$ [MJ/kg]
5	24.4	221.0	1,282	2,746	0.0433	1,490	1.33
6	26.8	225.4	1,790	1,910	0.0295	1,806	1.86
7	28.8	230.0	2,408	1,397	0.0212	2,128	2.49
8	30.6	234.0	3,133	1,063	0.0160	2,453	3.24

stagnation point. Since the free-stream stagnation enthalpy can be thought of as the sum of the free-stream static enthalpy and the free-stream kinetic energy, the extent to which the kinetic energy of the flow is converted to thermal energy dictates the quantity of heat flux a particular point on the LE experiences. Namely, the regions in the post-shock zone away from the stagnation point retain some kinetic energy while the stagnation point itself does not. The heat flux along an extruded semicircular leading edge takes the symbol $q_{\mathrm{gw,cur}}$ and the position along the edge is defined as $\theta = x/R$. The angular distribution, shown in Fig. 32 is given by [125]. The magnitudes are normalized by the stagnation point heat flux for the Mach 6 case. These relative values are also used in Figures 34 and 43 to contextualize the magnitudes presented. A work which modeled a wedge of similar geometry and composition, and simulated it in a like environment, reported a Mach 6 peak heat flux of 4.4 MW/m^2 [126]. Note that the borrowed magnitude is from a wedge with a R = 6.5 mm radius of curvature whereas the present wedge contains a nose tip with R = 1 mm. From the cited reference, we can extrapolate a Mach 6 peak heat flux of about 7 MW/m^2 for the sharper wedge. The ratio of heat flux along this frontal section to that of the stagnation point is given as

$$\frac{q_{\mathrm{gw,cur}}}{q_{\mathrm{gw,0}}} = 2\theta \sin\theta \left[\left(1 - \frac{1}{\gamma M_\infty^2}\right) \cos^2\theta + \frac{1}{\gamma M_\infty^2} \right] G^{-1/2} \tag{63}$$

for which

$$\begin{aligned} G = &\left(1 - \frac{1}{\gamma M_\infty^2}\right) \left[\theta^2 - \frac{\theta}{2} \sin 4\theta + \frac{1 - \cos 4\theta}{8} \right] \\ &+ \frac{4}{\gamma M_\infty^2} \left[\theta^2 - \theta \sin 2\theta + \frac{1 - \cos 2\theta}{2} \right] \end{aligned} \tag{64}$$

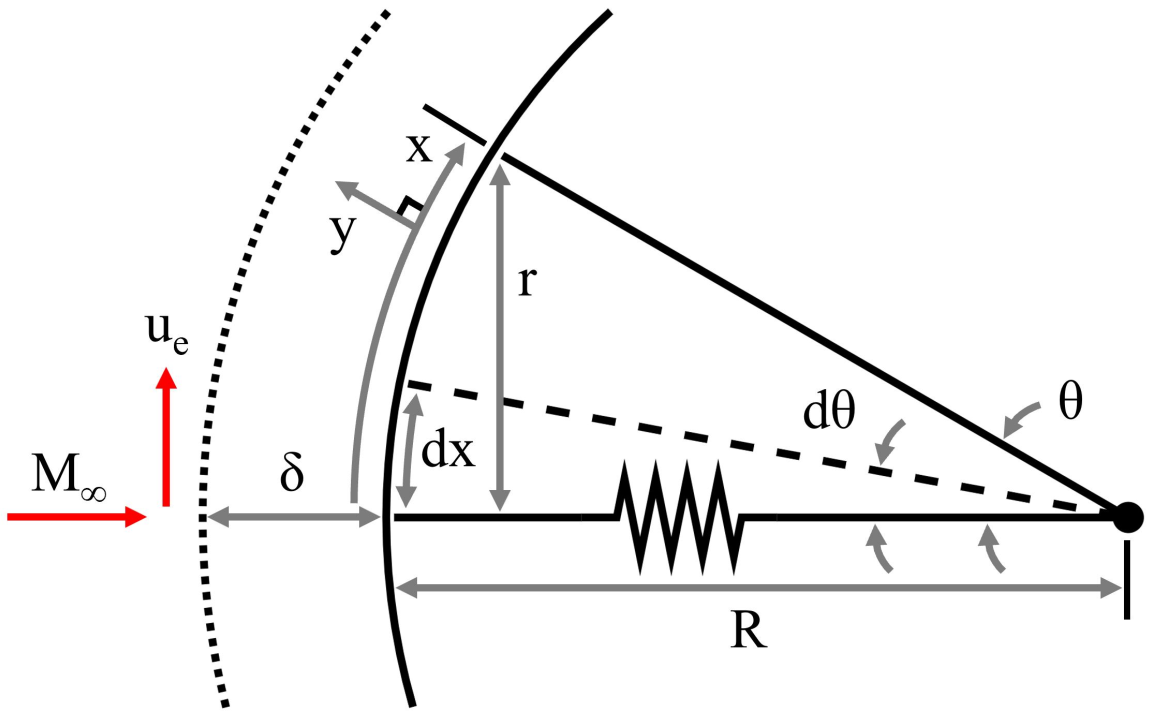

Figure 31: Stagnation region schematic. The dashed line designates the bow shock and M_∞ refers to the pre-shock Mach number.

The flat boundary of the LE is analyzed in a similar manner to a flat plate in high enthalpy flow conditions. Where C_H is the Stanton number and $h_{e,\text{aw}}$ is the adiabatic wall enthalpy, heat flux imparted from the gas to the flat walls, $q_{\text{gw,flat}}$, is given by

$$q_{\text{gw,flat}} = C_H \rho_e u_e \left(h_{e,\text{aw}} - h_w\right) \tag{65}$$

C_H is the ratio of the heat transfer into the fluid to the thermal capacity of the fluid. The adiabatic wall enthalpy is calculated from the equation $h_{e,\text{aw}} = C_{p_\infty} T_e + \frac{u_e^2 \sqrt{\text{Pr}}}{2}$. The only other parameters involved are the fluid density and flow velocity along the leading edge, ρ_e and u_e, respectively.

The radiative heat transfer, q_r, takes the same form for the curved and flat sections, but is integrated over different limits. Where σ is the Stefan-Boltzmann constant and ϵ_r is the material's emissivity, the familiar expression is written as

$$q_r = -\sigma \epsilon_r T^4 \tag{66}$$

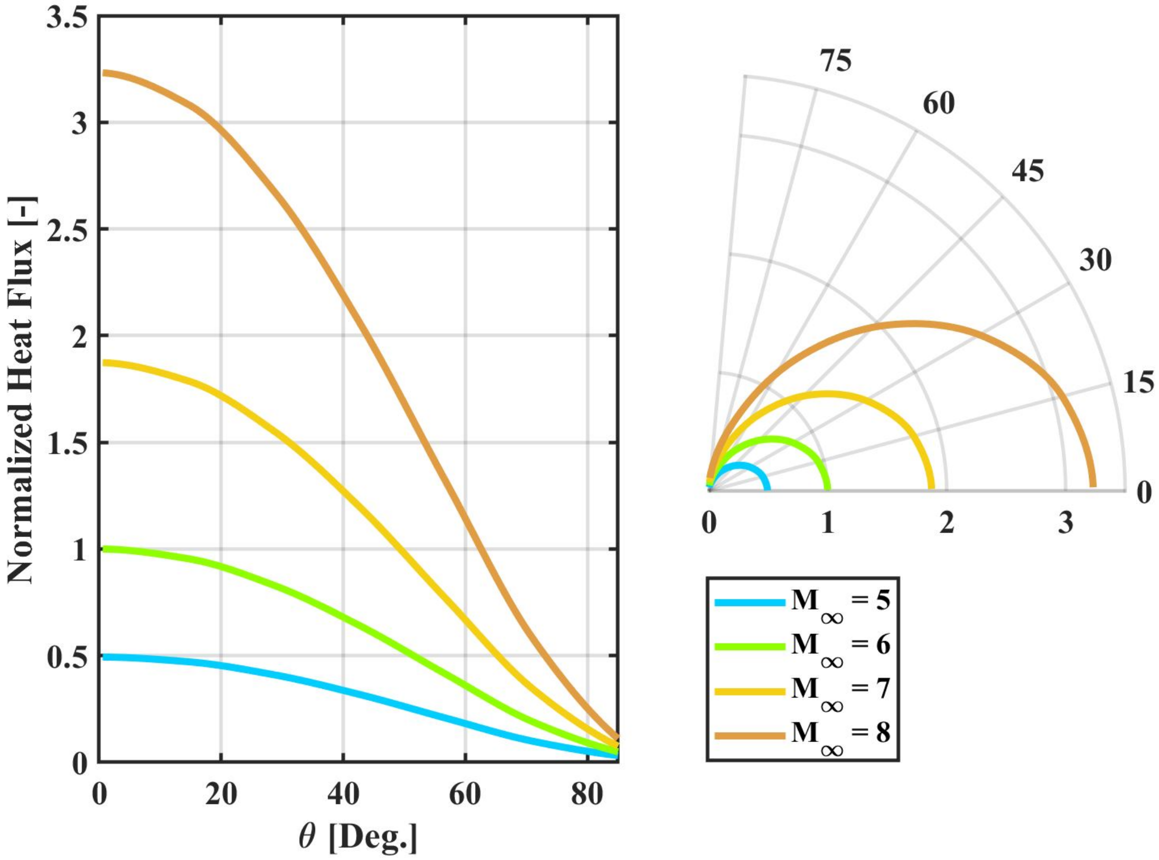

Figure 32: Angular distribution of the incident heat flux along the curved section of the LE for select Mach numbers. Rectangular (left) and polar coordinates (right) are shown. Heat fluxes are normalized by the stagnation point heat flux for the Mach 6 case. The angular distribution is calculated per Equations 63 and 64.

Recall that these heat flux expressions are per unit area. The heat flux balance between that imparted on the walls and that outgoing as radiation is the integration of these two terms along the curved and flat sections. A steady-state heat balance can be applied for the case of isothermal walls. Considering the curved and flat section on one side of the axis of symmetry and acknowledging that x is the direction along the curved surface and y is the vertical projection of the flat portion, one writes

$$\int_0^{R\theta_0} (q_{\text{gw,cur}} + q_r)\, dx + \int_{R\tan\theta_0}^{L_{\text{flat}}+R\tan\theta_0} (q_{\text{gw,flat}} + q_r)\, dy = 0 \tag{67}$$

where the angle defining the border between the semicircular segment and the flat side is $\theta_0 = \pi/2 - \phi$, L_{flat} is the length of the flat side, and $R\tan\theta_0$ is the distance from the leading edge tip to the beginning of the flat surface. The analysis is based on a steady-state energy balance between the heat transferred from the flow stream to the wall, q_{gw}, and the thermal radiation from the wall, q_r. A boundary condition used in this analysis to help derive a solution is [35, 127]: the radiation-adiabatic wall limit, whereby thermal radiation is equal in magnitude but opposite in sign to the flow stream heat flux ($q_r = -q_{\mathrm{gw}}$) and the net heat flux into the wall is zero.

The following assumptions are made to analyze the heat flux impinging on the vehicle as a function of the inviscid flow field properties: 1) The vehicle is undergoing steady, level flight; 2) No ionization reactions occur in the gas; 3) We assume local thermal equilibrium in the boundary layer; 4) We assume a binary gas model consisting of only atomic and diatomic air molecules; 5) There is only weak viscous interaction between the boundary layer and inviscid flow, so that any influence in the inviscid flow results in negligible feedback on the boundary layer; 6) The boundary layer flow is laminar; 7) The flow is modeled as a perfect gas; 8) A "no-slip" condition is imposed at the wall (i.e. all fluid velocity components are zero at the wall); 9) The model initially assumes a uniform wall temperature on the vehicle's surface. A moderate Reynolds number and a low blowing ratio on the order of 0.01 are what give us confidence the boundary layer downstream is laminar [128]. It is worth noting that had the model considered additional species, we would expect slightly decreased temperatures near the wall which would cause a lowered viscosity and a subtly higher density. These, in turn, would result in a higher Reynolds number. We acknowledge that turbulence for nonequilibrium flows is more complicated due to the multitude of finite rate processes taking place [129]. In the present work we analyze the LE with nose tip radius $R = 1$ mm and a wedge half angle of $\phi = 5°$. The geometry of the LE is illustrated in Fig. 33. The total length of the LE is 50 mm. Various points along the structure are identified in a normalized fashion to this total length. That is, 50 mm behind the nose tip is designated "1" and the nose tip itself is "0". The heat flux distribution, q_{gw}, is shown in Fig. 34. Conditions for the optimization study are provided in the figure as well and are discussed further in Section 4.5.

The team analyzed the mesh and found the assumptions to be satisfied in the model. The

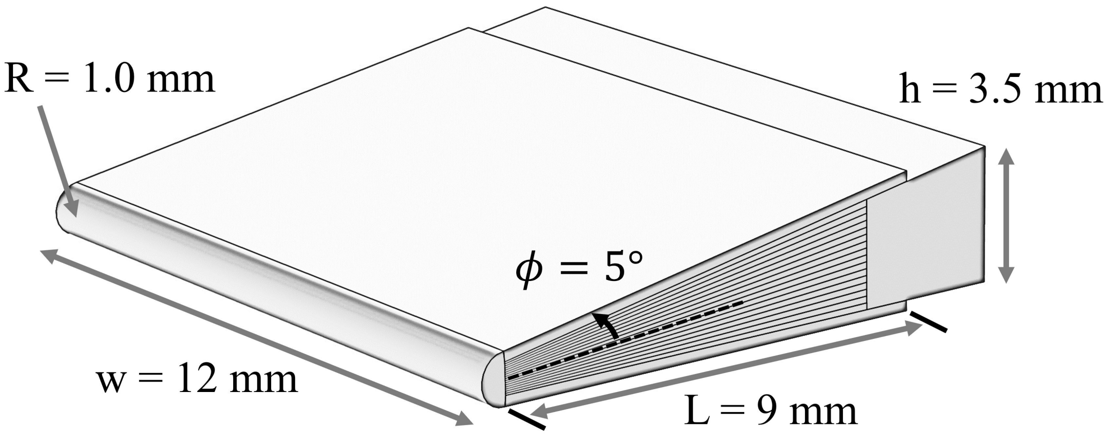

(a) Three-dimensional view of the LE with dimensions

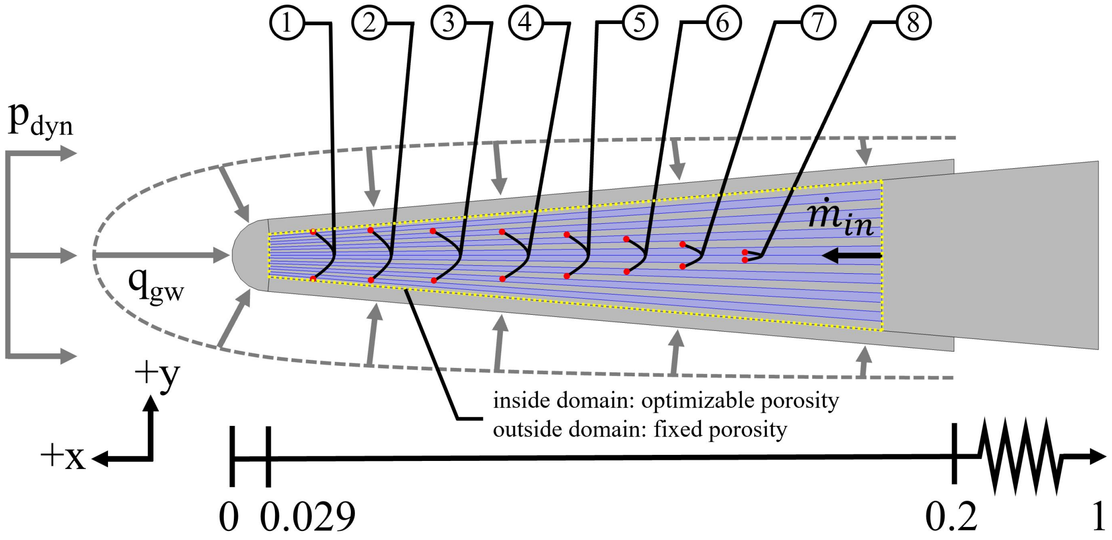

(b) Side view with conditions. Numbered bubbles illustrate the layers for which each independent variable in the optimization study is responsible. Normalized horizontal position along the leading edge is denoted. 0.029 is the intersection of the semicircular front section and the flat sides. The region to the right of 0.2 continues the flat sides with $\phi = 5°$, but does not include transpiration through porous media.

Figure 33: Leading edge model schematics.

steady, level flight assumption simplified the mesh since it could be roughly symmetric about the midplane of the wedge. Ignoring ionization reactions is satisfactory for Mach numbers not far greater than Mach 5. This contributed to us restricting the study to Mach 5 to 8. The high altitudes considered make the weakly viscous interaction reasonable as well. Similarly, a laminar boundary layer would be expected at the frontal part of an LE. Certainly, if the back portion of a hypersonic vehicle were considered, a turbulent boundary layer (i.e., one that includes jetties and other forms of flow separation) would likely need to be investigated. A no-slip condition is reasonable as well given the viscosities considered. Finally, a uniform wall temperature is initially assumed and this is complemented by the roughly symmetric mesh and the fact that the LE wedge is sufficiently small. Care was taken to make sure the wedge had small enough and sufficiently well-behaving mesh elements such that no sharp corners were jutting from the surface and potentially disturbing the heat flux distribution.

To determine the heat flux distribution along the surface of the LE, the magnitude at the stagnation point was first calculated as a reference (Equation 62), from which the values along the remainder of the semicircular tip can be calculated using Equations 63 and 64. The flux along the sides is calculated as a flat plate in high enthalpy flow conditions per Equation 65. Results from these calculations are shown for various Mach numbers in Fig. 34.

The isothermal wall temperature was iteratively solved to obtain accurate terms for each Mach number in Equations 62-67. For simplicity, we assume only radiative and aerodynamic heat transfer to solve for the wall temperature as done in [122]. We acknowledge the temperatures found are higher than those that would be obtained after involving evaporative cooling. The solver used a numerical integration method with 10,000 steps. The flat portion integral bands are related to the virtual tip. Using a reference starting temperature the isothermal temperatures for Mach numbers $M = [5, 6, 7, 8]$ are determined to be $T = [1208, 1381, 1568, 1762]$ K. This array is used to calculate the overall heat flux profile. An emissivity of 0.95 [130] was used for evaluating heat flux radiated away from the vehicle surface as part of the wall temperature calculations.

Considering typical operating altitudes for hydrocarbon-fueled scramjet engines, the heat

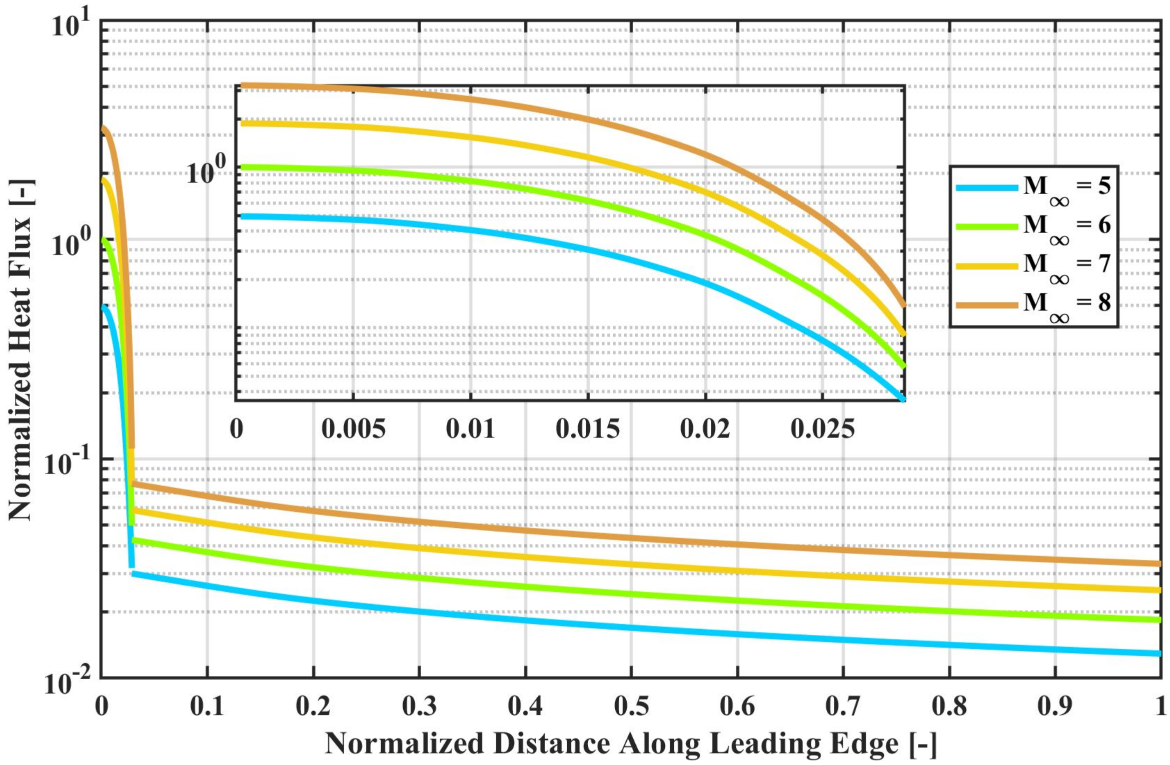

Figure 34: Heat flux along a normalized length of the leading edge for select Mach numbers. Semicircular segment enlarged for clarity. Heat fluxes are normalized by the stagnation point heat flux for the Mach 6 case.

flux profiles correspond to a specified external dynamic pressure of 48 kPa. Hence, each Mach number has a particular altitude to maintain the dynamic pressure condition. Standard atmosphere conditions are implemented for each altitude. Regarding angle of attack, the angle between the relative wind and the vehicle is maintained at zero.

The normalized heat flux distribution along the semicircular LE segment and the flat sides is shown in Fig. 34 on a semi-log scale. As expected, the stagnation point experiences the maximum heat flux and the magnitude decreases precipitously away from the stagnation point. We also note that the heat flux magnitude remains extreme on the curved part of the LE. This transition is evident from the slope discontinuity at a normalized distance of 0.029 on the horizontal axis. The farthest point on the LE experiences a slightly lower incident heat flux than the semicircular tip-flat plate interface primarily from the change in the Reynolds number due to the increasing distance from the virtual tip.

4.4 Fluid Flow in a Porous LE

Active transpiration cooling of a LE involves discharging fluid at the surface to absorb and block severe aerodynamic heating. The cooling effectiveness of the LE increases as the mass flow rate of a coolant increases. However, an increase in inlet or chamber pressure is needed to increase the mass flow rate. The magnitude of the pressure head through porous media is governed by viscous and inertial forces on the liquid as it travels through tortuous paths. The pressure drop through a porous material is described by the generalized Darcy's law in Equation 68.

$$\nabla p = \frac{\mu u}{K} + \frac{\rho u^2}{C} \tag{68}$$

Here, μ is the liquid viscosity, u is the superficial velocity, K is the permeability of porous media, ρ is the fluid density, and C is the inertial coefficient. For higher Reynolds numbers ($\mathrm{Re} > 10$), the second term in Equation 68, referred to as the Forchheimer term, accounts for additional pressure drop due to inertial effects. However, for low Reynolds numbers ($\mathrm{Re} < 1$), the Forchheimer inertial term can be neglected and the generalized Darcy's law becomes linear. For the case of liquid transpiration with evaporation at the surface, the Reynolds number is very low ($\mathrm{Re} < 1$) and the required flow rate is small since the heat of vaporization is typically very high. Hence, we focus our study on the linear form of Darcy's law and neglect the high Reynolds number inertial effects.

While the permeability of porous media is typically measured experimentally, advancements in computational methods have facilitated and expedited the numerical determination of flow fields through such architectures. This is accomplished by obtaining a three-dimensional geometry of porous media through X-ray tomography and numerically solving the Navier-Stokes equation using the Finite Element Method (FEM) or Finite Volume Method (FVM). Such techniques have been implemented in several studies, some of which have been compared to experimentally-obtained results [131, 132, 133].

In this work, we numerically predict the permeability of our reticulated foams using digitally reconstructed three-dimensional CAD models. Porous media renderings are garnered from a series of X-ray tomography images of 65 PPI, 5% volume fraction (0.95 porosity)

Reticulated Vitreous Carbon (RVC) foam. Given the complex geometry of reticulated structures, X-ray tomography helps with visualization and analysis by scanning high-resolution slices of the specimen and combining them to create a three-dimensional rendering [134]. The images were stacked and filtered to generate a three-dimensional array of binary voxels where a value of “1” corresponds to material (ligament) and “0” corresponds to space (pore). An isosurface routine is used to convert the voxel model to a mesh model composed of small triangular surface elements. To manipulate porosity, a rasterized scan of the array identifies space voxels adjacent to surface material voxels. A fractional voxel is dropped at that location with the fractional value determined by the space voxel’s connectivity to the surface voxel (face, edge, or corner), ensuring that ligament growth occurs isotropically. The model is then filtered to create a binary bitmap again and the process is repeated until the desired porosity is reached. This method was first described and implemented in [135]. Finally, quadric collapse edge decimation (QCED) is used in Meshlab to coarsen the mesh to an element count suitable for numerical simulations, which in this case was about 30,000 surfaces. The initial surface mesh models of the foams have exceptionally high element counts due to the single digit micron resolution of the X-ray tomographs from which they were generated. Potentially exceeding a million surface elements for the foam sizes investigated, these preliminary models are too large and unwieldy for simulations. QECD is a mesh simplification algorithm that reduces the element count of the model to a workable size. We simulated five geometries (0.9-0.5 porosity in increments of 0.1) for which the 0.9, 0.7, and 0.5 porosities are shown in Fig. 36. To create foam geometries with different porosities, we added successive layers of material voxels to the ligaments until a target porosity was reached [136]. Figure 35 visually describes the digital reconstruction procedure.

Numerical simulations of fluid flow were performed using the commercial software ANSYS Fluent. We assumed steady, incompressible flow with constant properties in the laminar regime. A constant inlet velocity was assigned and symmetry boundary conditions were prescribed to the exterior surfaces perpendicular to the flow direction. Grid independence was achieved by increasing the number of elements until the relative error in pressure drop across the foam fell below 1%.

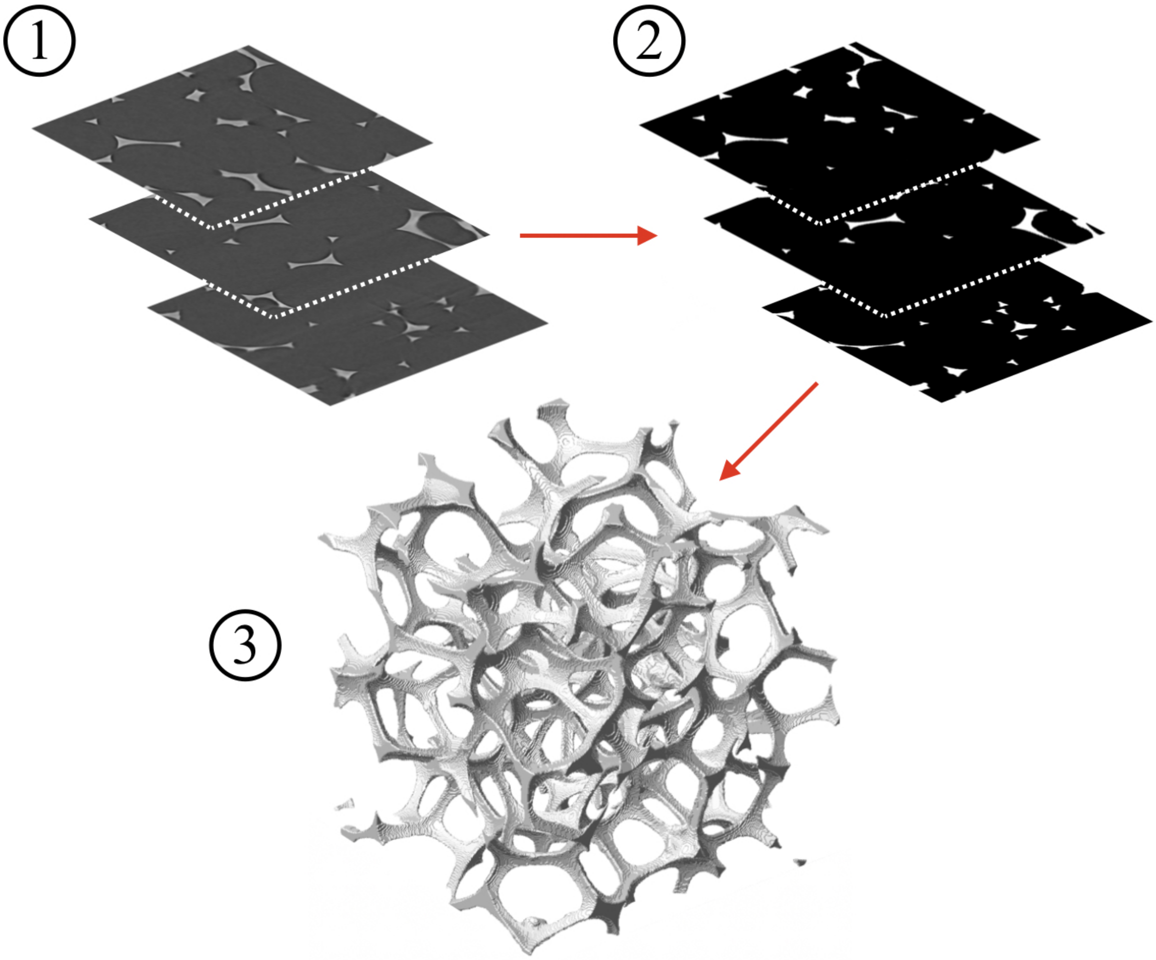

Figure 35: Computational foam reconstruction procedure: X-ray tomography scans (top left), filtered scans (top right), and final three-dimensional rendering (bottom).

From the numerical solution of the flow field shown in Fig. 36, the permeability was calculated using the difference between area-averaged pressures at the inlet and the outlet using Equation 68. The permeability values for all five foams of different porosities are listed in Table 6. Permeability of porous media is specific to the characteristics of geometry in consideration. However, it can be described as a function of porosity and pore diameter [137, 138]. A correlation for the permeability as a function of the average pore size and porosity was obtained using least squares regression as the following

$$K = 0.028\, d_p^2\, \epsilon^{\frac{5}{2}} \tag{69}$$

d_p is the average pore diameter, ϵ is the porosity, and the coefficient 0.028 and exponent

Table 6: Obtained permeability results as a function of porosity

Case	Porosity [-]	Pore diameter [μm]	Permeability [m^2]
1	0.9	347	2.5×10^{-9}
2	0.8	313	1.6×10^{-9}
3	0.7	269	7.2×10^{-10}
4	0.6	238	5.2×10^{-10}
5	0.5	191	1.7×10^{-10}

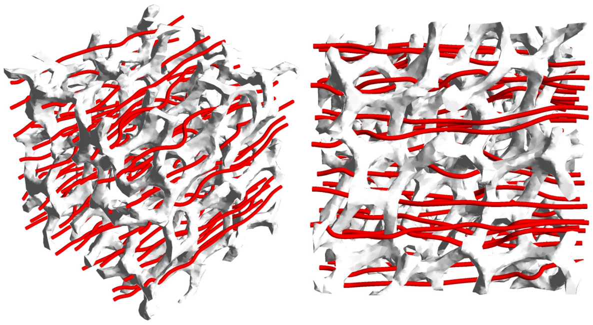

(a) 0.9 Porosity

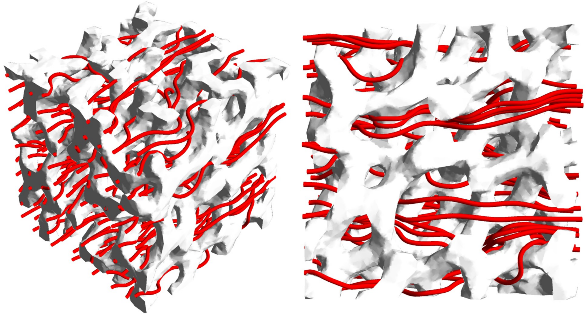

(b) 0.7 Porosity

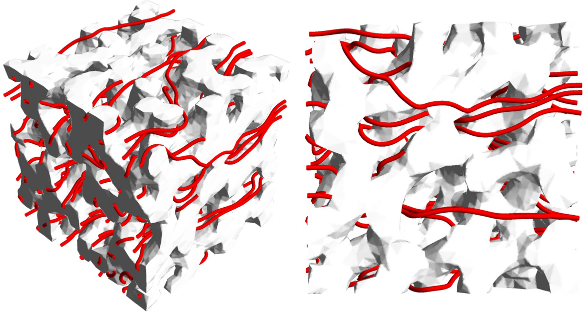

(c) 0.5 Porosity

Figure 36: Velocity streamlines for the flow field in foams with varying porosity.

2.5 are fitted constants. We used the five simulated cases provided in Table 6 to obtain the correlation. The permeability values for the simulated cases did not deviate more than 10% from the best fit curve. Simulation and correlation results are summarized in Fig. 37. The permeability prediction is done to provide the range of possible values that could be used to optimize the fluid flow in the geometrically complex LE. We derived correlations acknowledging that the non-dimensional permeability is only a function of the porosity [137].

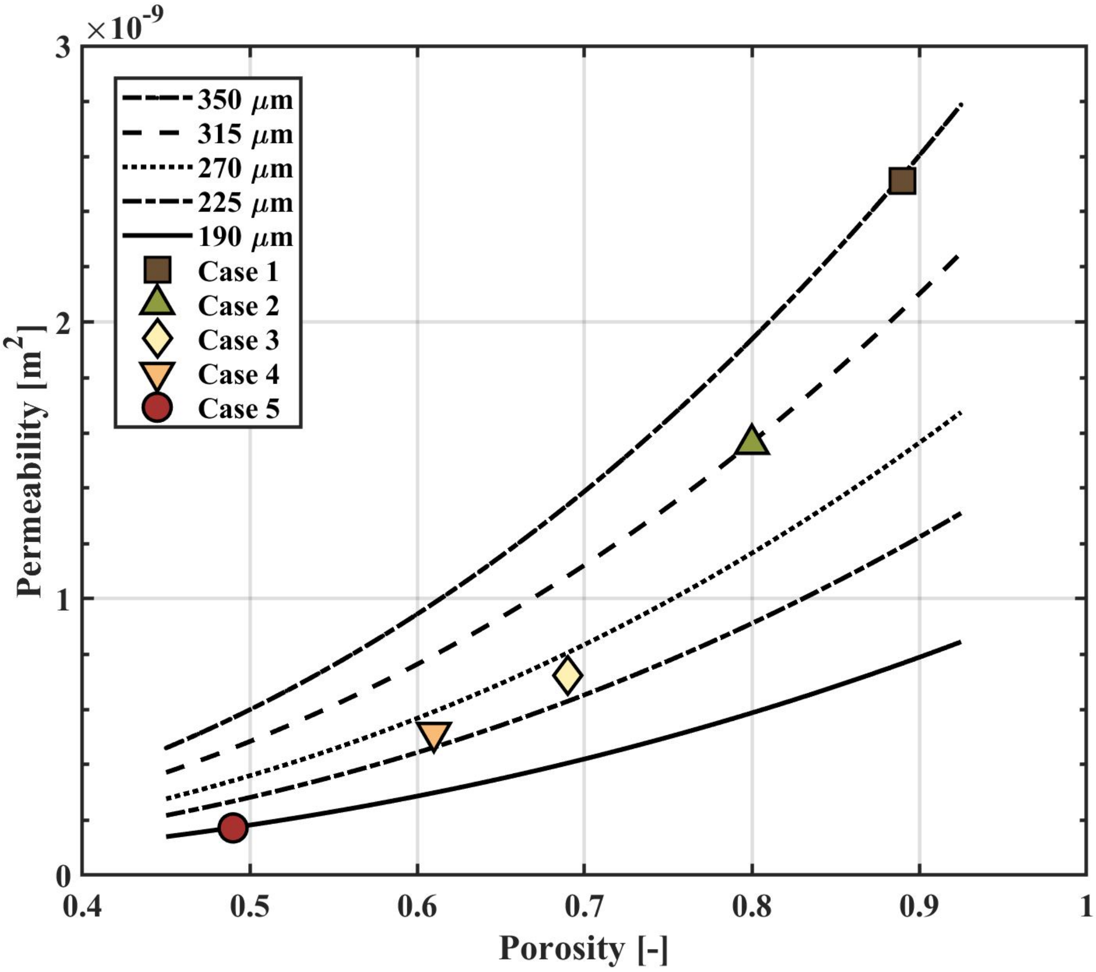

Figure 37: Permeability as a function of porosity for chosen pore diameters. Lines denote the correlation obtained using least squares regression (Equation 69), and symbols represent simulated cases (Table 6).

4.5 Optimization of the Spatial Distribution of Pores in the LE

4.5.1 Methodology

Now that we have determined the spatial distribution of the surface heat flux on the LE and the relationship between the porosity, average pore size, and the permeability, we will turn our attention to the question of optimal pore size distribution for a given heat flux profile. Since the heat flux is not spread evenly across the LE, but rather peaks at the stagnation point, it follows that a greater quantity of transpirant should be focused there. For a specified mass flow rate at the inlet, it is thus reasonable to expect a more porous (lower volume fraction) foam to have a greater impact on cooling the LE material. Considering the structural integrity of the vehicle, one can also impose a range of acceptable porosities that can withstand thermomechanical loads. Additionally, one can specify an average porosity within that range so the effective strength of the LE is maintained. This idea of varying the porosity within the LE in consonance with its heat flux suggests that an ideal geometry exists.

A three-dimensional CAD model of the LE was created to find the optimal porosity distribution. As shown in Fig. 33, the internal portion through which the coolant can travel was divided into 16 equal volume regions. Symmetry was imposed since we are only considering angles of attack equal to zero. Thus there are eight independent variables, each representing one of the eight volumes in the symmetric LE section. The Complex method of constrained optimization [139, 140] was implemented in COMSOL LiveLink for MATLAB. The Complex method is an extended version of the derivative-free Nelder-Mead method (or Simplex method) used for constrained minimization problems [141]. It relies on the use of a geometric figure called a *complex*, and is formed by a set of $k \geq n+1$ points in an n-dimensional space where n is the number of design variables. According to the studies carried out by Box et al. [139, 140], the best performance is obtained when $k = 2n$. The leading idea in the Complex method is to compare the values of the objective function at the k vertices of a general complex and incrementally move said values toward the optimum point (i.e. a global minimum or maximum of the objective function) during an iterative process.

The movement of the complex is achieved by using an operation known as *reflection*.

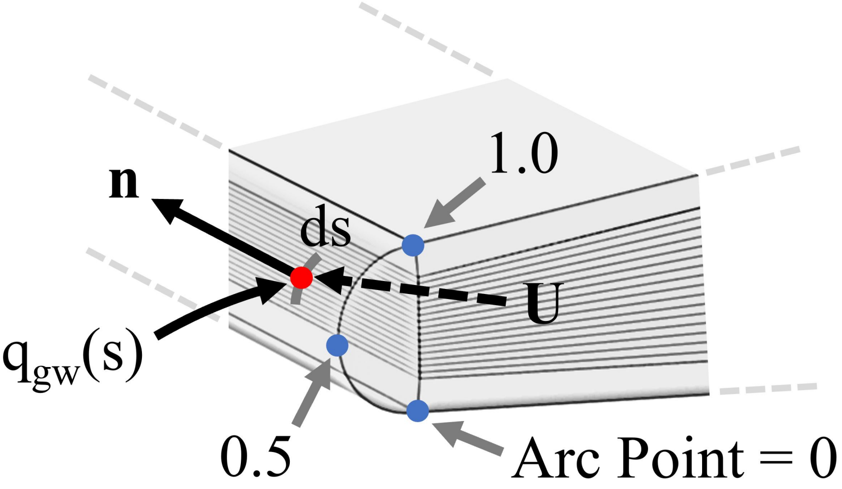

Figure 38: Schematic of the leading edge with annotations relevant to the optimization study objective function. Arc point ranges referenced as arc segments in Table 7.

The objective function is taken as the integrated evaporative energy flux over the leading edge surface at the curved portion of the LE, weighted by the incident heat flux. This is the dot product of the velocity vector, **U**, the surface normal along the LE's semicircular arc, **n**, multiplied by the heat of vaporization, H (chosen to be 3×10^6 J/kg as representative of energy-dense refractory ceramics). Figure 38 illustrates the relevant terms. Writing the summation of incident heat flux along the LE as $q_{\text{tot}} = \int_s q_{\text{gw}}(s)\ ds$, and the weight function as $w(s) = q_{\text{gw}}(s)/q_{\text{tot}}$ with units m^{-1}, one can compose an expression for the objective function $\mathcal{F}$. This is written as

$$\mathcal{F} = \rho H \int_s w(s)(\mathbf{U} \cdot \mathbf{n}) ds \tag{70}$$

The model is constrained by requiring each evaluation to have an average permeability which corresponds with a porosity of 0.7 (volume fraction of 30%) and a 5% bilateral tolerance. This is done to compare directly against an isotropic case for which the entire transpirant flow region is assigned a porosity of 0.7. The range of acceptable volume fractions for any individual layer is 10% to 50%. Note that the outer foam structure (i.e. all sections besides the 16 strata) is kept at a 50% volume fraction to maintain structural integrity in the vehicle. Permeabilities for each volume fraction are linearly interpolated from the results in Table 6.

Properties typical of refractory ceramics with a high heat of vaporization are assigned to the transpirant. The coolant density was chosen to be 5,000 kg/m^3 [142] and the dynamic viscosity was set at 0.01 Pa-s [143]. Environmental conditions on the LE correspond to a velocity of Mach 6 at an altitude of 26.93 km and follow the standard atmospheric model. Thus, the dynamic pressure is 48 kPa at the transpirant outlet. The inlet boundary condition is chosen to be a transpirant mass flow rate of 1×10^{-4} kg/s. We estimate from an energy balance that this mass flow rate could provide significant cooling for the given LE. It is also on the same order as the mass flow rate examined by van Foreest *et al.* [98] A no-slip condition is specified along the walls and backflow is suppressed at the outlet. The equation solved in each evaluation is the conservation of momentum using the Brinkman model. The momentum equation of this model is written as

$$\nabla \cdot \left[-p\mathbf{I} + \frac{\mu}{\epsilon} \left(\nabla \mathbf{U} + (\nabla \mathbf{U})^{\intercal} \right) \right] - \frac{\mu \mathbf{U}}{K} + \rho \mathbf{g} = 0 \tag{71}$$

where $\mathbf{I}$ is the identity matrix and $\mathbf{g}$ is the acceleration vector. Additionally, continuity is satisfied by the homogeneous condition $\rho \nabla \cdot (\mathbf{U}) = 0$. Moreover, the fluid is modeled as incompressible and a Stokes flow condition is satisfied due to the Reynolds number being sufficiently less than unity. The highest Reynolds number cases are those with the highest velocities and the largest pore diameters. The values for these are approximately 5 mm/s and 350 μm, respectively. Taking the coolant density to be 5,000 kg/m^3 and the dynamic viscosity to be 0.01 Pa-s, we get a peak Reynolds number of less than 1 inside the LE. The majority of the flows are slower than this case and most pore diameters in the model are smaller as well, so the Reynolds numbers are generally far less than 1.

Fluid flow in the porous medium is presented in two situations: 1) the internal foam structure is isotropic such that all eight independent permeability variables for the symmetrically-paired layers are held constant. This gives a single permeability value for all 16 slices; 2) the eight permeability variables are subject to the objective function and constraints defined for the Complex method to optimize. The average permeability for the 16 layers is held constant within the bilateral tolerance such that the improvement from the optimized permeability model can be readily compared against the isotropic case.

4.5.2 Results for Isotropic Permeability

With the permeability of the internal section maintained at 7.2×10^{-10} m^2 to correspond with a 30% volume fraction, the transpirant wicks about evenly along each layer of the LE. Figure 39 illustrates this uniformity in the velocity profile. The transpirant at the layers nearest the centerline and the outer walls of the flow all travel approximately 1-2 mm/s. Note that the flow speed along each layer is not perfectly equal because of the reduction in cross-sectional area as the coolant traverses the wedge shape. The objective function for this simulation is found to be 8.163 MW/m^2 for the entire curved section of the leading edge and 4.798 MW/m^2 for the region ± 5% the length of curve s centered at the stagnation point. These values along with those for intermediate length arc segments are shown in Table 7. Since the objective function weights the transpirant mass flow rate by the incident heat flux at the corresponding points along the nose tip, the values are effective heat fluxes. For reference, the expected heat flux removed via evaporative transpiration cooling (ETC) can be found using Equation 72. With s defined as the length of the curved section of the nose tip, the expression is written as

$$q_{\mathrm{ETC}} = \frac{\rho H}{s} \int_s (\mathbf{U} \cdot \mathbf{n}) ds \tag{72}$$

The magnitude is shown to be 4.522 MW/m^2 for the entire flow exiting through the nose tip. By investigating the velocity profile for the isotropic permeability leading edge case, a baseline is determined from which the optimized permeability results can be compared.

4.5.3 Results for Optimized Permeability

Allowing the discrete strata in the transpiration flow path to have different permeabilities makes it possible for the LE to prioritize coolant in the regions bombarded by the highest heat flux. This is evident from the increased velocity, and thus mass flow rate, nearest the stagnation point in the optimized case. Figure 34 quantifies the heat flux distribution and

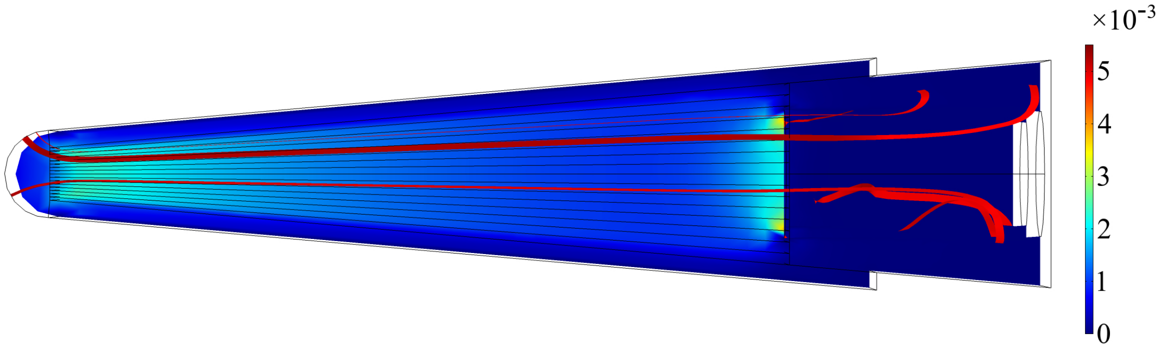

Figure 39: Flow velocity distribution in a porous LE with isotropic permeability. Velocities shown in m/s. Select streamlines are shown in red for flow visualization.

Table 7: Effective heat flux comparison for isotropic and optimized cases. Stagnation point is located at arc point of 0.5. See Fig. 38 for arc segment schematic.

Arc Segment →	0.45-0.55	0.40-0.60	0.30-0.70	0.20-0.80	0.10-0.90	0-1.0
$\mathcal{F}_{\text{isotropic}}$ [MW/m^2]	4.798	4.850	5.055	5.438	6.290	8.163
$\mathcal{F}_{\text{optimized}}$ [MW/m^2]	5.082	5.127	5.307	5.643	6.415	8.179
$\mathcal{F}$ Change [%]	5.92	5.71	4.99	3.77	1.99	0.20

intuitively q_{gw} peaks at the stagnation point. It follows that the plurality of the mass flow rate should wick through the layers nearest the centerline followed by those which flank them.

Figure 40 illustrates the convergence of the optimization study. The initial standard deviation threshold was reached after 84 evaluations, but we continued to run the simulation until the objective function was clearly unchanging. The total run time was 43 hours on a 40 CPU workstation. Note that the objective function is global, and thus corresponds with the arc segment 0-1.0 shown in Table 7. However, it is worth emphasizing that the greatest benefit from the optimization study is realized in the regions nearest the stagnation point.

Figure 41 displays the velocity profile for the optimal case. By inspection, the greatest speeds are along the centerline of the model and peak about 6 mm/s. This differs sharply from coolant in the outermost layers which progresses at approximately 1 mm/s. As in Fig. 39, select streamlines are included for flow visualization. Note that any apparent asymmetry

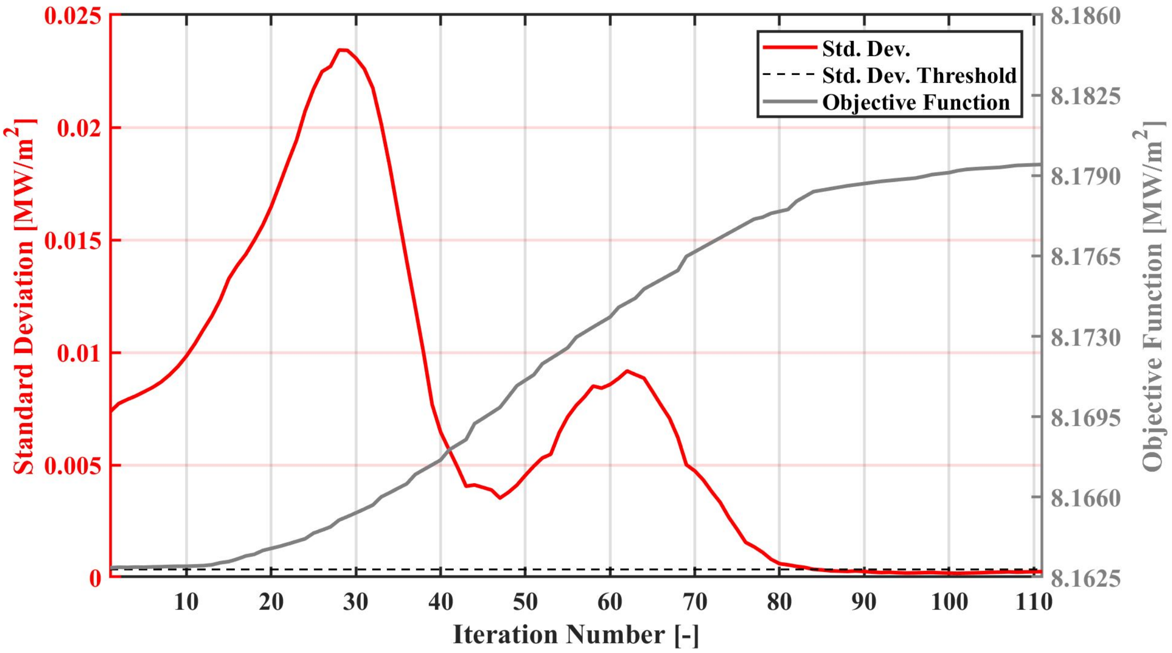

Figure 40: Convergence progression for the optimization study.

in the flow above and below the stagnation point is simply due to the streamlines originating from asymmetric points. The objective function for this simulation, $\mathcal{F}_{\text{optimized}}$, is found to be 8.179 MW/m^2 for the entire curved section of the leading edge and 5.082 MW/m^2 for the region ±5% the length of curve s centered at the stagnation point. As done with the isotropic permeability cases, these values along with those for intermediate length arc segments are catalogued in Table 7. The table also displays the percent difference for $\mathcal{F}$ between the two cases.

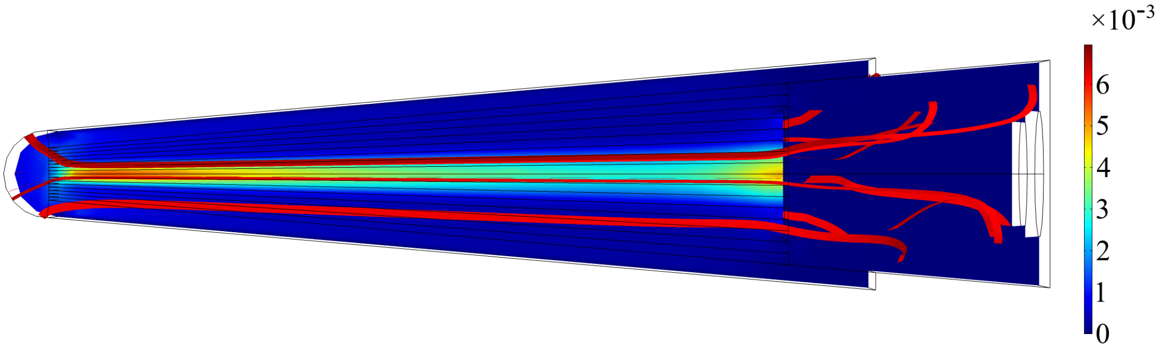

Figure 41: Fluid velocity field in a porous LE with optimized permeability. Velocities shown in m/s. Select streamlines are shown in red for flow visualization.

The optimization study increases the evaporative heat flux by 5.92% over the isotropic permeability case for the surface region close to the stagnation point and the percent change decreases for regions farther away. This suggests that about 6% less transpirant is required to attain the same amount of cooling in the region nearest the stagnation point. While this may be a modest improvement in cooling the tip of the LE, it is valuable in that it improves the LE reliability and ameliorates temperatures experienced by the vehicle. While determining flight limitations is outside the scope of the present work, the results can be used to estimate improvements in peak flight duration and speed. Additionally, the computational procedure can be used in other applications [89].

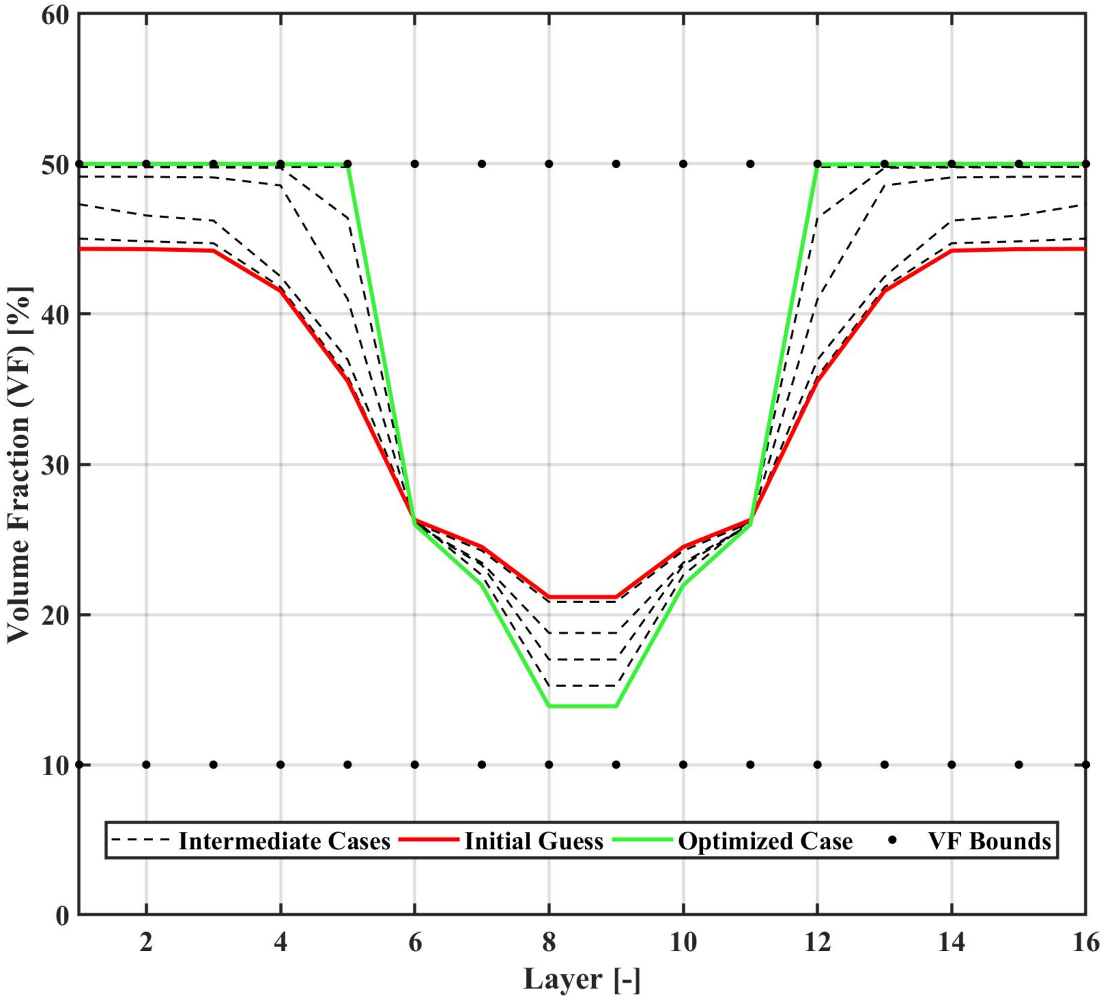

Figure 42: Volume fraction of each layer throughout optimization study.

Further discussing the process of obtaining the optimized solution, an initial guess for the permeability of each layer is specified in the Complex method model. Figure 42 displays this guess in red, the results of successive iterations toward the optimized complex as dashed black lines, and the final solution in green. The objective function converged to a global maximum after just over 100 iterations, a few of which are shown as the intermediate cases. The bounds (10% and 50%) are denoted as well. To satisfy the constraint of an average permeability corresponding with a volume fraction of 30%, the model is forced to be strategic about how it allocates porosity, especially for magnitudes near the prescribed permeability limits.

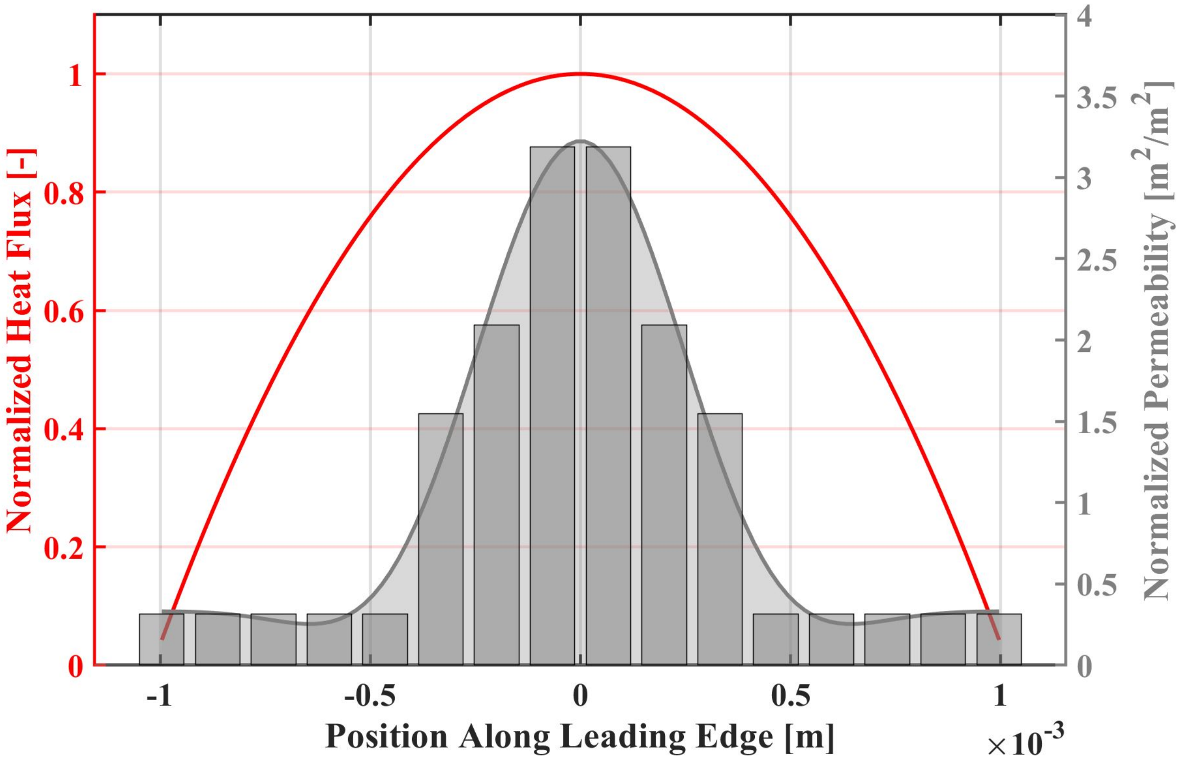

Figure 43: Optimized permeability for each layer (bar chart) compared with corresponding incident heat flux (red curve), and optimized permeability infinite layer fit (gray curve). Unity on the right vertical axis represents 7.2×10^{-10} m^2, or the permeability of 0.7 porosity. Heat fluxes are normalized by the stagnation point heat flux for the Mach 6 case.

This strategy is best illustrated in Fig. 43 which overlays the optimized permeability by stratum (bar chart) with the imparted heat flux along the LE (red line). The plot also includes a fitting curve which represents an extension of the 16 layer study to that of infinite layers. The optimal permeability for the first five independent variables is the lower limit of 1.7×10^{-10} m^2. By contrast, the center layer has an optimal permeability nearly at the upper permeability limit. This is only made possible by the outer layers reserving their permeability for regions with a greater need for transpirant. Additionally, the synchronization of the permeability distribution with that of the heat flux provides strong evidence that the objective function worked as intended. Note that the magnitudes on the graph are normalized to the permeability of 0.7 porosity (30% volume fraction). For instance, the isotropic case would contain a bar chart with every layer at 1.0 or 7.2×10^{-10} m^2. In the context of LEs which programmatically benefit from small performance improvements, a 6% increase in cooling effectiveness in the vicinity of the stagnation point relative to that of the isotropic permeability model has significant implications.

While eight independent variables gives a compelling result, it is worth considering an optimization study with a greater number of layers. One can fit the optimized solution for 16 layers to a continuous curve. This new set of permeabilities must still satisfy the constraint (average permeability across all layers must be $7.2 \times 10^{-10} \pm 5\%$ m^2) to be valid. Note that the propagation of this 5% tolerance causes a difference in the objective function that is orders of magnitude less than the difference exhibited between the isotropic and optimized cases. The sharp change in permeability from the fifth to sixth outermost layer is not conducive to a polynomial fit or a Gaussian curve. However, the fit behaves well with the generalized Fourier series $\left(f(x) = \frac{1}{2}a_0 + \sum_{n=1}^{\infty} a_n \cos(nx) + \sum_{n=1}^{\infty} b_n \sin(nx)\right)$. The residual sum of squares is minimized and the permeability constraint is satisfied for $n = 3$. The corresponding constants are $a_0 = 2.196$, $a_n = [1.300,\ 0.681,\ 0.149]$, and $b_n = [0.397,\ 0.278,\ 0.329] \times 10^{-15}$. In Fig. 43 this infinite layer curve is overlaid with the 16 layer bar chart for comparison.

It is worth highlighting that an infinite layer foam architecture is no longer a stratified structure, but rather a graded one. The permeability would vary continuously along the LE and the concept of strata would not apply. A key result is how the objective function magnitudes compare. To approximate this value, the equivalent study is rerun with four independent variables. The intention is to find the limit by fitting the three cases (isotropic, four independent variables, and eight independent variables). What is found is that to three decimal places the cooling effectiveness is identical for the four and eight independent variable cases. This suggests that 16 strata has a negligible improvement over eight. And furthermore, infinite strata, or a graded porosity, would exhibit a negligible improvement over a LE with eight optimal layers. This is a satisfying result for manufacturing purposes since any preexisting preference for fabricating graded or stratifed foams does not influence transpirant performance so long as enough strata are used.

4.5.4 Passive Pumping

Once the ideal foam topology is found for maximum cooling effectiveness, it is valuable to know other performance details such as the foam's ability to undergo acceleration without adverse effects on fluid flow and evaporative cooling. In addressing this, the computational model is parametrized to solve for the required pressure to achieve the same mass flow rate while the vehicle undergoes a specified acceleration. A forward acceleration would most negatively counteract the capillary pressure produced by the surface tension inside the pores. It is therefore interesting to find out if there is a critical acceleration value above which the capillary pressure does not provide adequate pumping. In this instance, any ability to pump transpirant passively would become infeasible. Only active pumping would allow the coolant to flow to the front of the LE given the specified mass flow rate at the inlet. The model generalizes the problem to consider acceleration with a vector pointing forward (positive x-direction), backward (negative x-direction), upward (positive y-direction), and downward (negative y-direction) as well as any combination of the x- and y-directions. With the optimized permeability for the 16 layers now known, we next consider the extent to which this topography is beneficial in other aspects. Hypersonic vehicles not only endure extreme heat fluxes, but also particularly high accelerations. Using the permeability profile shown in the bar chart of Fig. 43 and parametrizing an acceleration magnitude in the forward direction, one can obtain the acceleration required to nullify pumping benefits of capillary action in the porous media. This condition can be defined as the critical acceleration for passive pumping, or a_c. In calculating this, one must start by determining the capillary pressure. With γ defined as the interfacial tension, θ_c as the contact angle, and d_p as the pore diameter in the foam, the capillary pressure can be estimated as

$$p_{\text{cap}} = \frac{4\gamma \; \cos\theta_c}{d_p} \tag{73}$$

Since the contact angle and average pore diameter have significant impacts on the capillary pressure, a range of plausible combinations are considered. Maintaining the use of properties of typical refractory ceramics with a high heat of vaporization for the transpirant and assigning the foam as tungsten, γ is chosen to be 700×10^{-3} N/m [144]. Wettability can vary greatly with molten high-temperature transpirants, so θ_c is varied from 0° to 80° to capture optimistic and conservative cases. Pore diameters are kept consistent with Table 6.

The critical acceleration occurs when the gauge pressure in the LE is zero. This is when the external dynamic pressure, p_{dyn}, equals the internal pressure, $p + p_{\text{cap}}$. Recall that the Brinkman equations in Equation 71 give the resultant pressure after removing viscous pressure losses as simply p. It is also worth noting that care was taken to present pore diameters for which capillary pressures well exceed viscous losses. Viscous losses are calculated to be significant relative to p_{cap} for d_p less than about 50 μm given that $\theta_c \leq 80°$. At 190 μm, the minimum d_p analyzed is well above this approximate threshold. The solution for a_c is found when $p + p_{\text{cap}} - p_{\text{dyn}} = 0$. Six contact angle and pore diameter combinations are plotted for these pressures as a function of forward acceleration in Fig. 44.

The red dot in each subplot highlights the intersection point and the rounded value of each a_c is called out nearby. The subplots support the notion that critical angle and pore diameter have strong impacts on the critical acceleration. Since capillary pressure is inversely proportional to pore diameter it is reasonable that the smaller d_p would allow passive pumping at higher forward acceleration magnitudes. The linearity of the black lines is partly due to the geometry of the leading edge with the remaining rationale being attributed to the position of the acceleration vector, $\mathbf{g}$ in Equation 71.

Since a forward acceleration forces the fluid backward in the vehicle and the wedge is symmetric about the plane above and below the stagnation point, an increase in acceleration has a proportional increase in required pressure. Note that Fig. 45 shows a similar result with backward acceleration since the vehicle would experience a like geometric effect. The

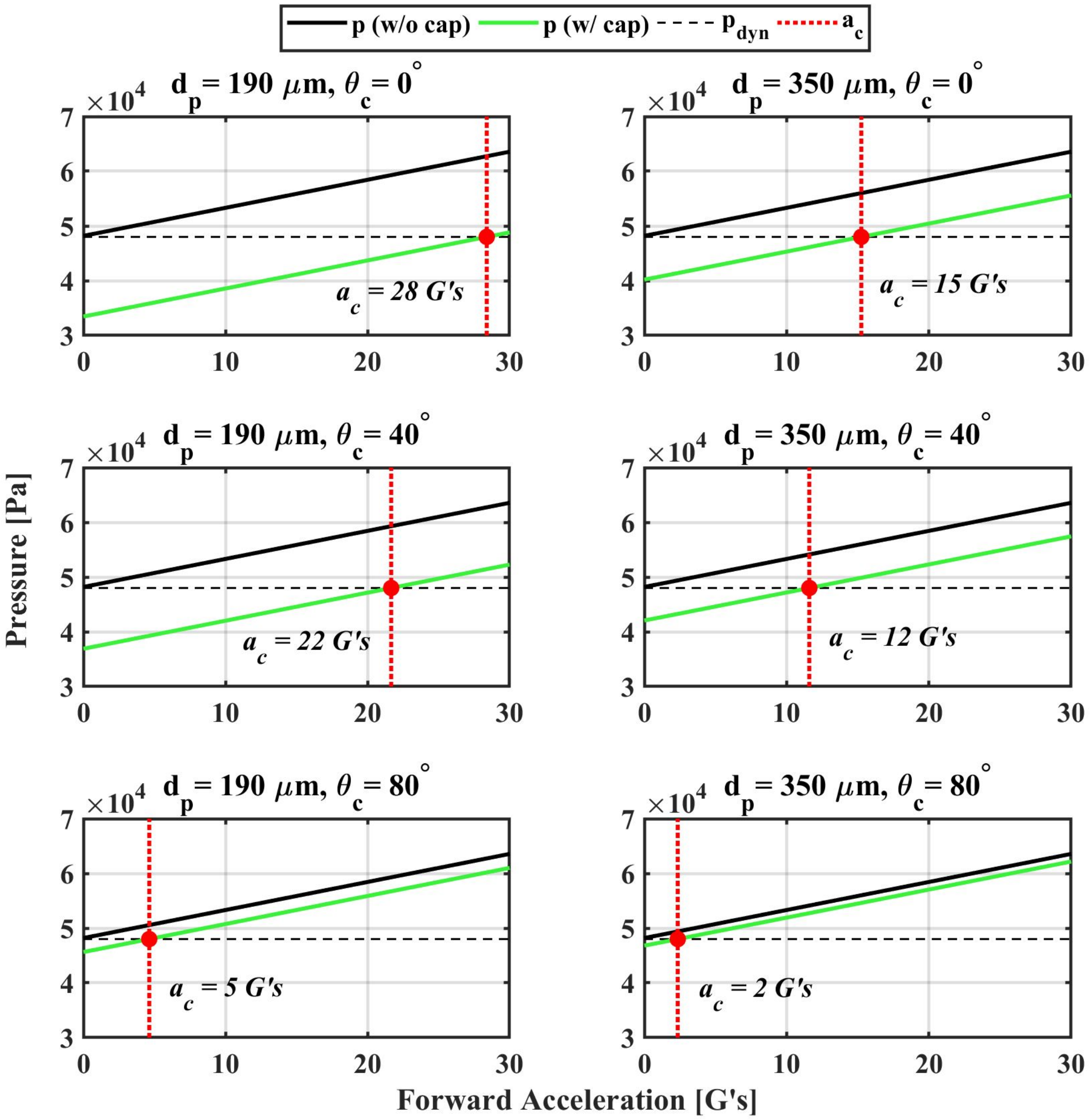

Figure 44: Dependence of the fluid pressure, with and without capillary effects, on the vehicle acceleration. Critical acceleration values for various contact angle and pore diameter combinations are shown in the red vertical dashed line. “w/o cap” is short for “without capillary pressure” and “w/ cap” refers to “with capillary pressure”.

required pressure reduces proportionally with increased backward acceleration, but with a different slope than the forward direction acceleration. Considering the outcomes for different amounts of wettability, it is clear that the results for higher θ_c perform worse than situations for which the contact angle is small. This is also reasonable since capillary pressure is directly proportional to the cosine of the contact angle. These conclusions are both academically valuable and practically useful. The volume fraction throughout the LE is provided in Fig. 43. Based on the wettability of the porous media/transpirant combination, an acceptable pore diameter, and thus pore density and mean ligament thickness can be estimated from the plots in Fig. 44.

While forward acceleration is the most critical single direction since it directly opposes the flow trajectory, it is worthwhile to generalize the study to a comprehensive sweep of acceleration vectors. To extend the results shown in Fig. 44, pressure terms p and p_{cap} were explicitly found for accelerations in the forward (positive x), backward (negative x), upward (positive y), and downward (negative y) directions and a general Fourier series fit helped complete the vector combinations of x and y. The best and worst pore diameter and contact angle combinations from Fig. 44 were chosen to model and the results are displayed in Fig. 45. The information for each case is illustrated using a three-dimensional plot and a corresponding contour plot. Given that the number of dimensions has increased by one, it follows that the passive pumping critical acceleration is not a point but rather a line. We note that this third dimension is most applicable for the idealized case whereby the velocity is parallel to the relative wind and accelerations are instantaneous.

Since the LE model is symmetric along the y-axis and centered at the origin, it is logical that this symmetry is seen in the critical acceleration plots as well. The x-direction is certainly the dominant one, but acceleration in the y-direction slightly aids the capillary pressure, especially when there is a (negative x)-component. An example of this situation could be an atmospheric reentry. The vehicle would slow down in the forward direction but gain speed in the downward direction. Transpirant would flow forward more easily due to the vehicle accelerating backward and the additional y-component would aid the coolant's forward momentum.

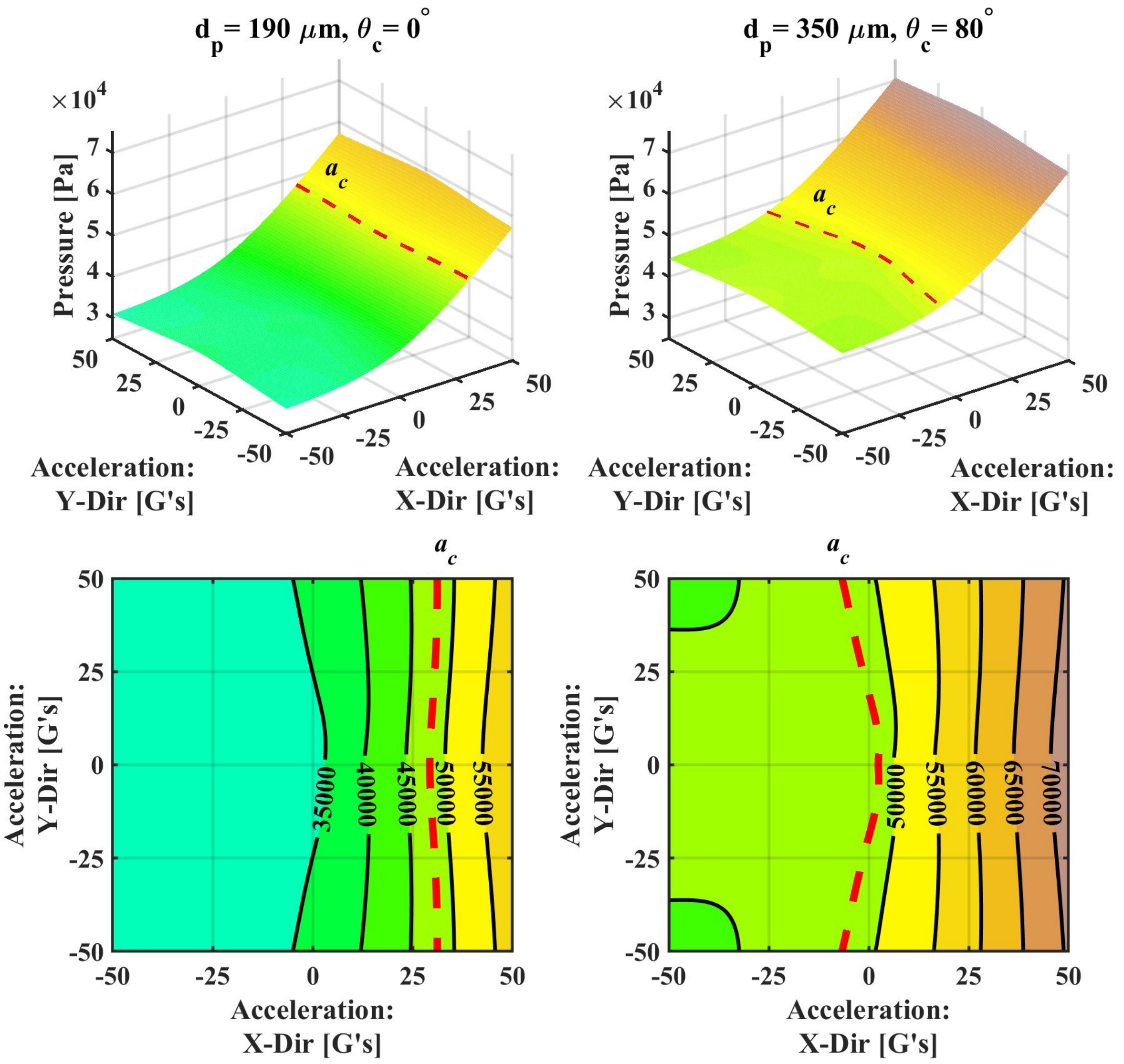

Figure 45: Critical acceleration three-dimensional plots for best (most optimistic) case and worst (most conservative) case in Fig. 44 with their respective contour plot. Positive x-direction is forward acceleration and positive y-direction is upward acceleration.

Comparing the most optimistic case with the most conservative case, it is apparent that a d_p of 190 μm with strong wettability performs far better than a pore diameter of 350 μm with poor wettability. While the former can passively handle up to about 28 G's in the forward direction and nearly any upward/downward acceleration, the latter can only passively pump while forward accelerations are below 2 G's with a y-component magnitude under roughly 5 G's. We thus conclude the feasibility of passive pumping in the optimized LE given that the pore diameter and contact angle are relatively small and the acceleration vector in the hypersonic LE's flight profile remains below a_c.

4.6 Summary & Conclusions

Hypersonic LEs are designed to protect the vehicle from extreme heat fluxes, especially at the stagnation point and in its vicinity where q_{gw} is greatest. While optimization of LE geometries have been discussed in the literature [107, 108, 109, 110, 111, 112] and porous LEs have been previously proposed [99, 100, 101, 102, 84, 103, 104, 105], little has been presented regarding the optimization of permeability for transpiration cooling effectiveness. This work provided incident heat fluxes along the LE for various Mach numbers from 5 to 8 and a permeability model for reticulated structures of volume fractions from 10% to 50%. These are 2.5×10^{-9} m^2 and 1.7×10^{-10} m^2, respectively.

Results in these studies were combined with the Complex method of constrained optimization to maximize the cooling effectiveness in a 16 layer stratified permeability LE model. We identify the main conclusions as follows: 1) The optimization study concluded that the greatest cooling efficiency corresponds with the incident heat flux distribution, but strategically allocates the highest permeabilities to the stagnation point and its adjacent regions. 2) The stratified model and the continuously graded LE (infinite layer case) benefit from a 6% increase in cooling effectiveness over the isotropic permeability case. This result illustrates the advantage of stratified permeability in a transpiration-cooled hypersonic LE. 3) It has also been found that the optimized foam can pump passively for forward accelerations as high as 28 G's given that d_p is 190 μm and the wettability is ideal ($\theta_c = 0°$).

Ultimately, the heat flux along the LE is determined for various Mach numbers, the permeability of different volume fraction foams has been found, the reticulated topography optimization study identified its solution, velocities have been compared for the isotropic and optimized cases, and the passive pumping critical acceleration has been discovered. Thus, all research objectives have been addressed and satisfied. It is clear that permeability plays a significant role in transpirant effectiveness and optimizing such a parameter in a reticulated structure in relation to its incident heat flux could make all the difference for the course of hypersonic spaceflight.

CHAPTER 5

Thermal Modeling of Foam-Infilterated Leading Edge of Hypersonic Aircraft

Efficient flights tend to emphasize a combination of minimum trip duration and fuel consumption. Given that habitable celestial bodies tend to have a relatively dense atmosphere, accomplishing these flight goals require vehicles to impact atmospheric particles at high speed. These contacts collectively impart a high heat flux on the fast-moving object. Since the structural integrity of the vehicle relies on its load-bearing components to operate at an acceptable temperature, there is an inherent need for hypersonic vehicles to cool a high incident heat flux. Reentry vehicles have a similar fate. Orbital mechanics and aerodynamics together suggest the infeasibility of returning from space to an object with great mass without reaching hypersonic speeds. The alternative of expending tanks of propellant is deemed unnecessary so long as the structure can remain functional. Vehicles traveling faster than Mach 5 will have to solve this physical phenomenon in every vehicle designed to travel in this manner. In terms of space exploration, venturing farther into the solar system, with particular emphasis on the unprecedented feat of landing humans on planets beyond our own, requires an improved understanding of novel materials, geometries, and design architectures.

A fiduciary impetus exists as well. The Pentagon has proposed \$2.6 billion USD to hypersonic funding in FY2020 [145]. Part of these funds are held by DARPA, which has voiced its desires to focus on two distinct technical areas. The first is to develop mature fully integrated passive thermal managements systems to cool leading edges based on scalable net-shape manufacturing and advanced thermal design. The second is the development of high-fidelity computational models for passive and active thermal management concepts, coatings, and materials for leading edge applications.

Knowledge gaps remain for how to model competing thermal processes while simultaneously considering the evolving geometry of microengineered materials. This chapter sets out to satisfy the following objectives as it illustrates novel approaches and uncovers significant findings: (a) Model passive heat transfer at hypersonic conditions; (b) Analytically determine incident heat flux along a leading edge; (c) Determine enthalpy change for each thermionic emission and thermosiphon cycle; (d) Qualify the feasibility of thermionic emission as a cooling mechanism for hypersonic vehicles.

In parallel with objectives a-d, the present investigation aims to determine the accuracy of the following hypotheses: (a) Metal foam materials will result in a greater outgoing heat flux than equivalent nonporous materials; (b) Heat transfer from a solid phase tungsten surface is less significant than the heat flux carried by thermionic emission and radiation; (c) Thermionic emission will increase heat transfer rates at the stagnation points with free stream velocities exceeding Mach 5 for all solid phase refractory materials with work functions less than 4 eV.

5.1 Geometric Modeling of the LE

Rigorous treatment of the boundary layer is key to accurately predicting the heat flux imparted on the walls of hypersonic vehicles. Equations derived in Chapter 2 are used extensively to evaluate the heat flux at each segment of a wedge-shaped leading edge (LE). SOLIDWORKS is used to build CAD models, MATLAB is used to evaluate equations and plot results, and models are proven in COMSOL.

A simulation-based approach to mitigating heat flux incident upon the leading edge of a hypersonic vehicle is investigated. A CAD model with a 2.3 mm leading edge and a 12° half-angle is designed. A half section isometric view and an annotated side view are provided in Figure 46. Intended for speeds in excess of Mach 5, this leading edge is designed to maximize heat mitigation for millimeter-scale leading edge radii. An overarching goal of the project is to uncover techniques that will makes small-scale leading edges feasible. The root of the issue is the inverse square-root proportionality between stagnation point heat flux and leading edge radius. This is written as

$$q_{stag} \propto \sqrt{\frac{\rho_\infty}{R}} u_\infty^3 \tag{74}$$

where ρ_∞ and u_∞ are the freestream density and freestream velocity, respectively. It follows that as organizations such as DARPA request proposals for increasingly small leading edges, then the required heat mitigation becomes immensely large. The solution we propose has three cooling methods: heat pipe vaporization and condensation cycle, thermionic emission whereby heat is exchanged for electrons, and mass vaporization.

Two variations were developed and are displayed in Figure 46 and Figure 47, respectively. The rationale for each major design choice is discussed in turn. For the first leading edge, the heat exchanger is comprised of a tungsten foam and the working fluid is liquid sodium working. Sodium is chosen for its high melting point, great creep strength, and elevated dynamic viscosity, μ. The fluid density and viscosity at 1,000 K for candidates sodium, potassium, and caesium are displayed in Table 8. Heated tungsten and barium oxide nearest

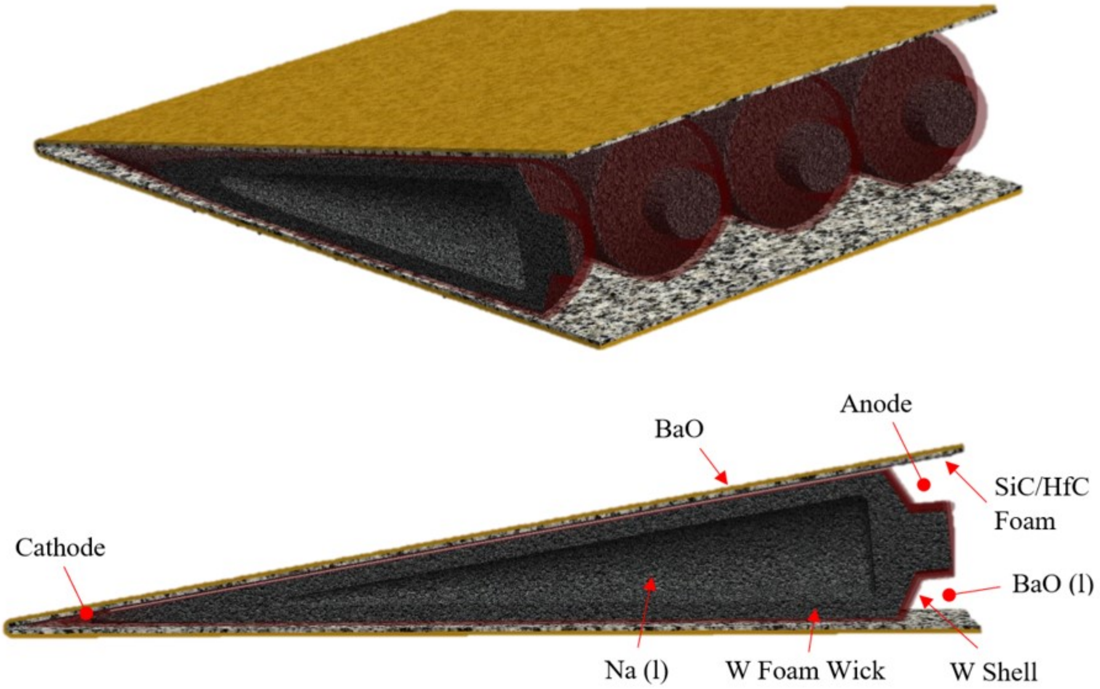

Figure 46: Half section isometric view of leading edge CAD model (top) and annotated side view (bottom).

Fluid	$\rho\ \left(\frac{kg}{m^3}\right)$	$\mu\ \left(\frac{kg}{m\cdot s}\right)$
Sodium (Na)	781	1.81E-4
Potassium (K)	680	1.3E-4
Caseium (Cs)	1,400	1.6E-4

Table 8: Properties of candidate heat pipe working fluids.

the stagnation point passively cool via thermionic emission. The electron transpiration cooling cycle is completed between the cathode and anode on the diagram. Liquid barium oxide is pumped around the inner wall and vaporizes as it becomes sufficiently hot. This compound is chosen for its high melting point and large heat capacity. Moreover, the chosen materials exhibit high strength and are chemically compatible.

The second version alters the internal structure and involves wicking through the leading edge in addition to that in the heat pipes. The black portion of the leading edge is tungsten foam. The pores in the reticulated structure allow liquid to flow through it. Moreover, the pore diameters are on the order of microns, so capillary action aids an upstream pump in pushing the working fluid forward. The tubes deliver barium oxide powder to the stagnation point where the heat flux is greatest. The powder passively turns molten from conduction. Heat flows from the outside through the tubes and ultimately to the metal powder. Previously, heat pipes were large and centrally located. Now they sit inside the primary wall. For additional structural support, internal ribbing has also been added. Manufacturing for

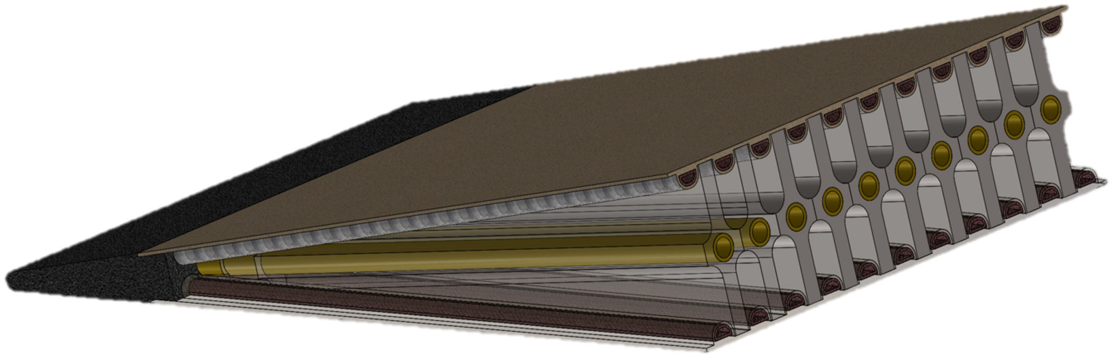

Figure 47: Half section view of the second version leading edge CAD model.

design is another consideration that is better executed in this iteration. The vehicle has substantial symmetry and repetition of parts. Moreover, access to the internal components is preferred with the second design. The heat pipes can be installed and secured more easily and the porous tungsten nose can be installed last to maximize access to the heat pipes and powdery delivery tubes from the front. It is worth noting that the reticulated structure facing the ram-direction needs a sufficiently high flow rate of working fluid such that few pores are directly exposed to the hypersonic flow. In a way, the molten barium oxide becomes part of the leading edge structure by providing a thin film which minimizes local vorticity at the pore ligaments.

5.2 LE Cooling Mechanisms

Finding the overall heat flux for a hypersonic leading edge involves the shared contributions from radiative, convective, and thermionic heat modes. Effects due to radiation are classically understood to be prevalent in hypersonic regimes since the extremely high temperatures at the leading edge greatly effect the roughly fourth-order dependence. By comparison, convective heat transfer has a nearly first-order relationship with temperature. Thermionic emission has a roughly T^2e^T correlation, so its effects become increasingly substantial at elevated temperatures.

5.2.1 Thermionic Emission

Much like how evaporation is an exothermic process, the release of sufficiently energized electrons via thermionic emission gives way to ones with lower kinetic energy, and ultimately cools the material. This release of high-energy electrons can be evaluated over a unit length to give a heat flux. Since the barrier to emission is the work function, W, it follows that materials with higher W, and thus a greater barrier to emission, relieve less heat. Equation 36 is evaluated for various W at typical hypersonic vehicle operating temperatures. Figure 48 plots these results and compares them with the heat flux magnitudes from radiative heat transfer.

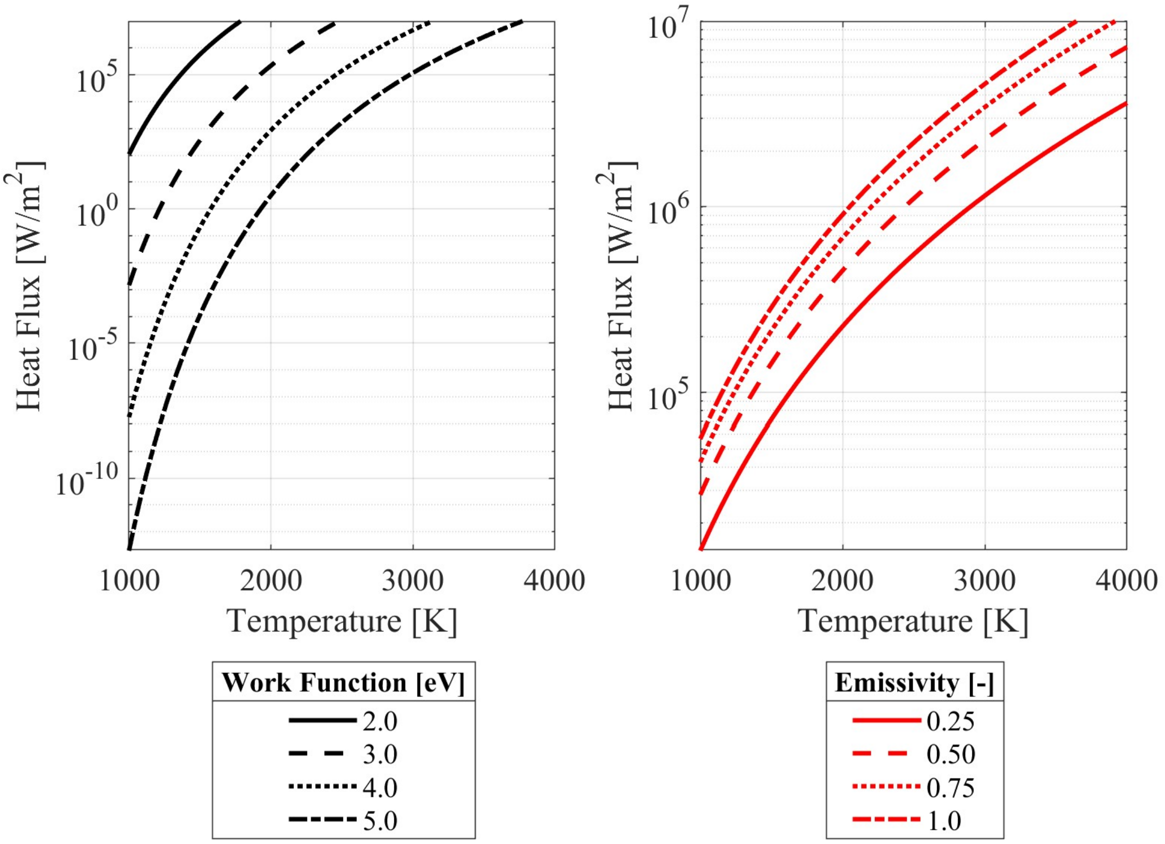

Figure 48: Heat flux from thermionic emission (left) and radiative heat transfer (right).

Various emissivity, ϵ, values are plotted to illustrate a more holistic picture of heat flux magnitudes from this mode. Comparing the two, it is important to recognize the ordinate is logarithmic. Imagining the two plots as overlapped, one might recognize that thermionic emission is generally less effective than radiation at temperatures below 2,000 K, but overall more influential at temperatures above 3,000 K. It is also worth identifying that a two-fold change to work function has a drastically greater impact on heat flux magnitudes than the same percent change to emissivity.

5.2.2 Evaporation and Condensation

The greatest advantage to using heat pipes for cooling is its ability to cycle passively. Where the temperature is the greatest, shown on the left side of Figure 49, the working fluid is sufficiently hot to exist as a gas. The vapor naturally moves toward the cooler section to equilibrate. As the vapor changes phase back to a liquid, it is forced toward the walls and remains there due to adhesion with the wicking surface. The liquid phase working fluid then naturally flows to the left to balance density. This completes the cycle and it repeats while a temperature gradient exists.

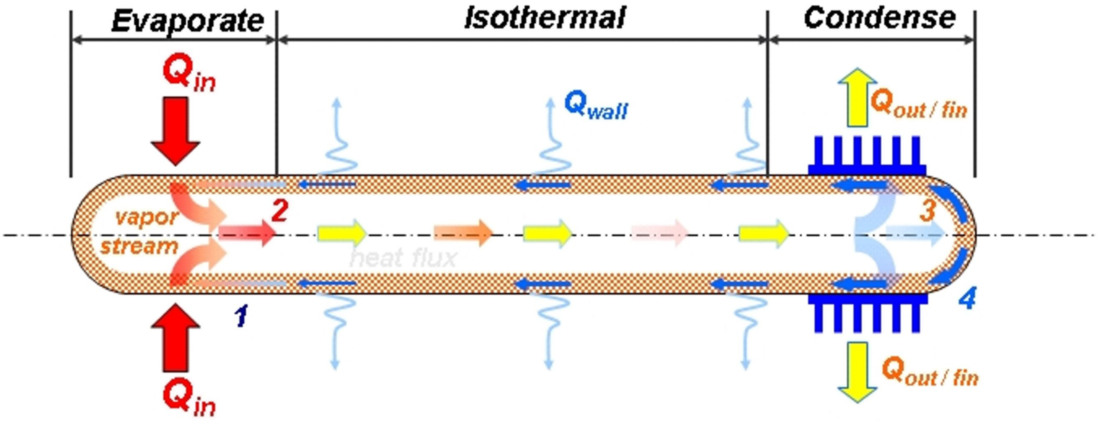

Figure 49: Heat pipe schematic with hot section shown in red and the cooler region in blue.

With sodium chosen as the working fluid, one can readily find the change in enthalpy per cycle. The reaction occurring inside of the heat pipe can be expressed simply as

$$Na(l) \to Na(g) \to Na(l)$$

which is the the succession of sodium evaporation and sodium condensation. The former is written as $Na(l) \to Na(g)$ for which $\Delta H = 107.74$ kJ/mol. The latter is the reverse, so the enthalpy change is identical in magnitude and opposite in sign. Thus, the total enthalpy change per cycle in the heat pipe is $\Delta H_{tot} = 215.78$ kJ/mol.

5.2.3 Mass Vaporization

It is clear that a material requires energy to go up a phase. This fundamental concept, however, can be exploited to cool hypersonic leading edges. By letting the imparted heat flux from the gas to the wall be the source of heat, materials near the walls can passively change from a solid to a liquid, liquid to gas, or gas to a plasma, and expend energy in doing so. Heat is lost to the environment as vaporized gas exudes from the vehicle, which in turn causes the vehicle to cool. Given that the chosen working fluid for this heat mode is liquid barium oxide, a Born-Haber cycle can be used. This is the method of calculating the total change in enthalpy by considering the effect of each step in the reaction. The vaporization of barium oxide is represented by the chemical equation

$$BaO(l) \rightarrow Ba(g) + \frac{1}{2}O_2(g)$$

Transitioning from the product to the reactants takes four discrete steps. These include the vaporization of BaO, $BaO(l) \rightarrow Ba^{2+}(g) + O^{2-}(g)$, electron dissociation of oxygen, $O^{2-}(g) \rightarrow O(g) + 2e^{-}$, association of oxygen atoms into molecules, $O(g) \rightarrow \frac{1}{2}O_2(g)$, and the deonization of barium gas, $Ba^{2+}(g)$. Each respective step has the following enthalpy change: $\Delta H_1 = 2,999$ kJ/mol, $\Delta H_2 = -603$ kJ/mol , $\Delta H_3 = -249.17$ kJ/mol, and $\Delta H_4 = -1468.1$ kJ/mol. Summing these reaction steps, one gets a total enthalpy of $\Delta H_{tot} = 678.73$ kJ/mol.

5.2.4 Cooling Effectiveness

While discussion in terms of heat flux and enthalpy change is prudent for heat transfer equations and chemical reactions, the extent to which cooling methods are effective is more valuably discussed with respect to temperature. For load-bearing structures, the melting point is a clear upper bound for operation. For aerospace applications, ASTM and NASA standards often suggest a factor of safety of 1.25 relative to the maximum design conditions. The specific safety factor and performance knockdowns depend on other criteria including fault-tolerance and flight criticality, but we shall use this value for the sake of argument. Given that the melting point of tungsten is 3,700 K, it follows that a tungsten component of an aerospace flight assembly shall not exceed 75% of the absolute melting point temperature, or 2,960 K.

5.3 Temperature Distributions in the LE

The leading edge CAD model is imported into COMSOL to solve for the temperature experienced at each element. As before, a 48 kPa dynamic pressure is maintained and Mach

6, 7, and 8 are the vehicle speeds being tested. Figure 50 illustrates the altitude and subsequent cold wall heat flux that are nominally associated with the specified dynamic pressures and speeds. Note that the vertical dotted line in the rightmost figure corresponds with the model's 2.3 mm leading edge radius.

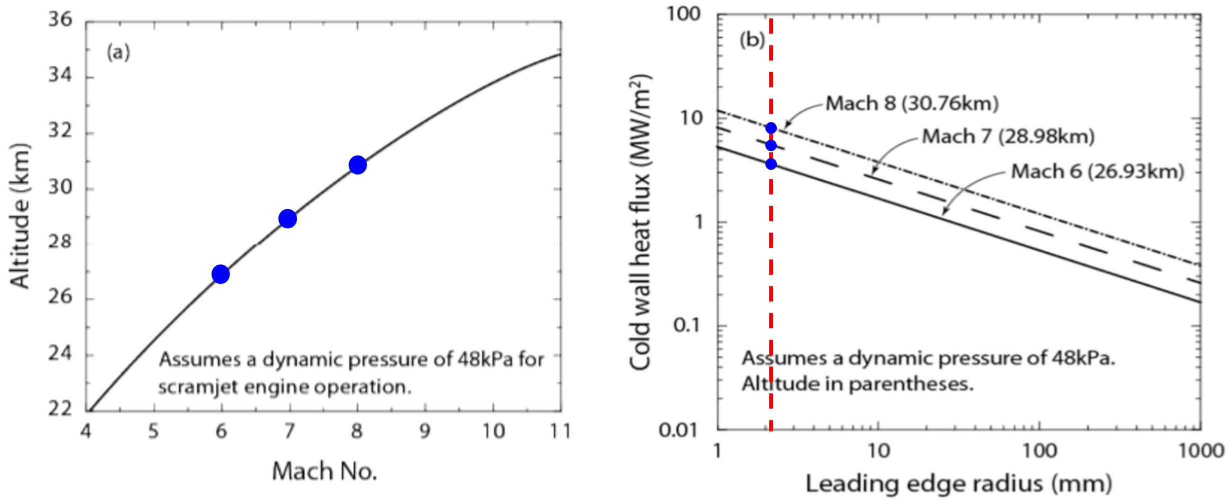

Figure 50: Select hypersonic vehicle ambient conditions (left) and associated cold wall heat flux magnitudes for varied leading edge radii (right). Adapted from [35].

A symmetric boundary condition is applied along the cut section. All external surfaces are capable of radiating heat to the the environment and internal components can radiate to each other as well. The vehicle can conduct to itself and convection occurs on all external walls. The greatest difference is that the magnitude of convection from the gas to the walls, as shown earlier in this chapter, greatly depends on its position along the leading edge and its normal vector relative to the ram-direction. Heat flux magnitudes typical of Mach 8 hypersonic speeds are assigned to the vehicle. Figure 51 directly compares the vehicle temperatures while convection and radiation are the sole modes of heat transfer with the case of added evaporation and thermionic emission.

The case of radiative cooling alone would be marginally impassable since it exceeds the 75% of absolute scale melting point threshold. Any higher speeds would likely melt the areas nearest the stagnation point. Note that the cooler regions of the simulation are aided by the

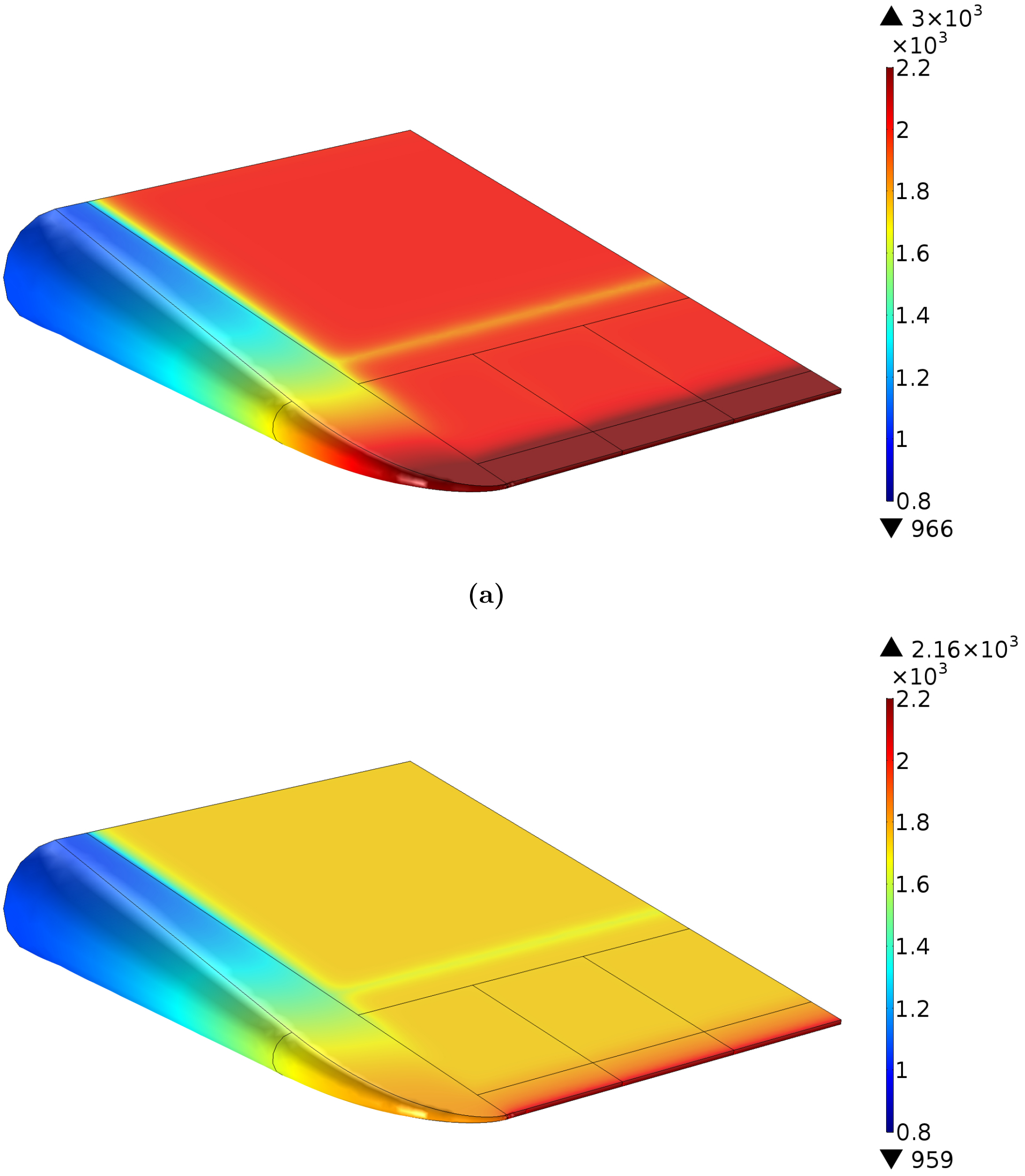

(a)

(b)

Figure 51: COMSOL model of leading edge for tungsten vehicle traveling at Mach 8 (a) without evaporation or thermionic emission and (b) with evaporation and thermionic emission.

thick tungsten piece in the model. The large scale component is able to disperse heat more easily than the relatively thin sections elsewhere in the CAD. This helps to explain the temperature gradient seen in both runs. The case which considers evaporation and thermionic emission peaks at 2,160 K which is well below the melting point. A reduction of nearly 850 K separates the stagnation point temperatures between the two runs. This substantial temperature change is partially due to the fact that thermionic emission is increasingly effective at high temperatures. A graphical representation of this is illustrated in Figure 52. Note that the model is given a 10 s period of hypersonic heat flux and begins from ambient conditions that would otherwise satisfy the 48 kPa dynamic pressure at Mach 8 flight speeds. The red set of data saturates in about four seconds whereas the blue set of data reaches its plateau in under three seconds. The red lines, also designated with the subscript "hot" in the legend, are from the radiatively cooled case. Locations of points A, B, and C are highlighted in the image to its right.

The evaporatively and thermionically cooled run has a narrower band of temperatures for the three points. This aligns with the previous argument that especially high temperatures are most greatly assuaged by thermionic emission. The graph also matches intuition in that temperatures drop as the distance from the virtual tip increases. Thermionic emission and evaporation are clearly effective in reducing the magnitude of heat flux relative to radiation alone.

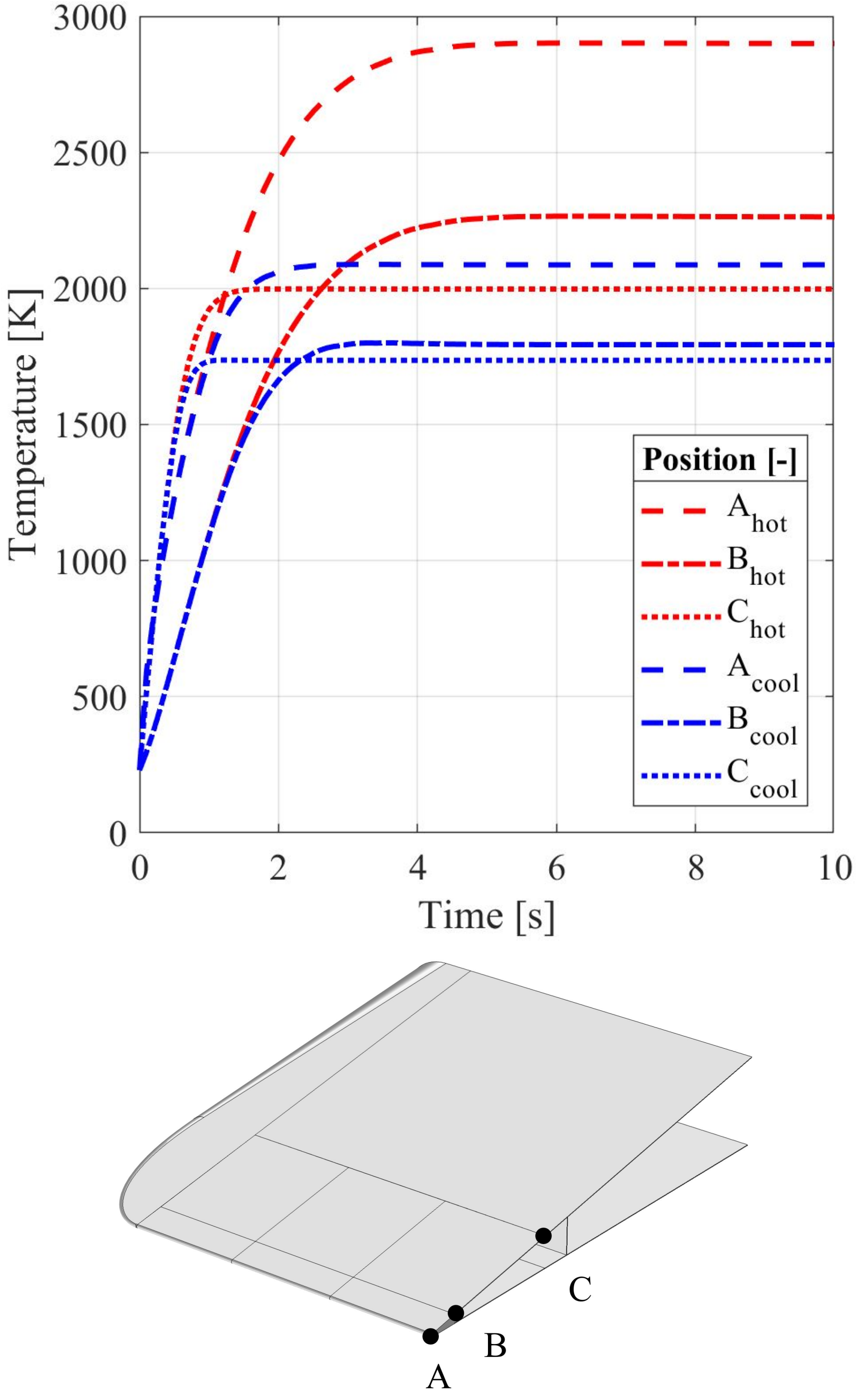

Figure 52: Temperature comparison for specified points on leading edge. Vehicle exposed to Mach 8 flow with 48 kPa dynamic pressure and corresponding standard atmosphere conditions for 10 s.

CHAPTER 6

Mass Loss, Sublimation, and Surface Damage of Lanthanum Hexaboride in an Arc Jet Plasma

6.1 Introduction & Background

Lanthanum hexaboride (LaB_6) is an excellent high-temperature material that is distinguished by its high thermionic current capability. It is extensively used as a cathode material in many applications that require an electron current. For this reason, mass evaporation in vacuum has been studied in the past [146, 147, 148]. However, the mechanisms of mass loss and surface damage in a severe heat flux environment are not fully understood. LaB_6 has recently gained the interest of the hypersonics community as a potential material for the leading edge (LE) because of its operability at extreme temperatures and the possibility of cooling via thermionic emission. Since vehicles flying in the hypersonic regime endure extreme heating, especially at LEs, LaB_6 is presently considered for incorporation into semi-structural and non-structural components or in other regions of local hot-spots [149]. We plan to also explore its merits as a candidate for transpiration cooling in a hypersonic LE.

The purple-colored material can be manufactured using solid-state reactions, electrolysis and flux techniques, vapor deposition or metal-gas reactions, and combustion or self-propagation [150]. Its high hardness and melting point are largely due to the strong covalent bonding between the boron atoms. Since the lanthanum cation is La^{3+}, LaB_6 is a trivalent hexaboride compound and this results in the La ions being organized in parallel rows on the surface to minimize the surface energy. This uncommon structure contributes to the material's particularly low work function. It follows that LaB_6 also has applications in vacuum electron beam welding, transmission and scanning electron microscopes (SEMs), and thermionic emission devices. A list of key LaB_6 properties is provided in Table 9.

Evaporative transpiration cooling is a method of cooling a body by moving a fluid through it to absorb heat. This can involve raising the temperature of a fluid within a specific phase or across multiple phases. One method is to deliver solid powder to a sufficiently hot region such that the material melts, vaporizes, or sublimates and then wicks out. Regardless of phase, delivery of the transpirant can be accomplished using porous media. This can be advantageous for such reasons as capillary action and the transpirant delivery channel doubling as a structural component [151]. A major factor in determining the ideal transpirant for an application is the operating temperature of the body. For reasons including the shock boundary layer and aerodynamic friction, the regions nearest the stagnation point of hypersonic LEs can operate above 2,000 K [152, 153, 105] depending on the particular conditions. Clearly, a transpirant intended to melt, vaporize, or sublimate must undergo one or multiple phase changes just below this temperature for the heat to be fully absorbed. The operating temperatures associated with this application suggest that certain refractory ceramics could provide a viable solution.

Surface recession of LaB_6 at high temperatures was measured by Storms [154], Davis [155], and Futamoto [156] in the 1970s and 1980s. The temperature range in these experiments was well below the melting point of the material. These studies showed fairly good agreement with each other and with the Lafferty [157] and Fesenko [158] evaporation models. Nevertheless, extrapolating recession rates for significantly higher temperatures is dubious because of the onset of other potential transport mechanisms; these include subsurface pore formation, dissociation, oxidation, melting, fluid flow, splashing, and droplet ejection. Recent relevant works have discussed such topics as the influence of carbonaceous species [159] on gas phase LaB_6 and the role of plasma parameters on the morphology of LaB_6 nanocrystalline powders [160].

The most pertinent recent work is an experimental and computational study of the ablation characteristics of LEs made from LaB_6 compounds [161]. LaB_6 was doped into a coating and applied to a 1.5 mm radius of curvature LE. The test article was then exposed to an oxyacetylene flame for 60 s and temperatures peaked just above 2,000 °C. SEM images showed microscale fractures, pores, and evidence of melting. This investigation concluded that excess boron content may be responsible for initiating micropores at elevated temperatures which reduces the compactness of the coating. Additionally, the results of their ablation experiments included multiple samples which gained mass. It was suggested that certain compounds can achieve a net mass gain if the conditions result in a greater mass increase from oxidation than a mass loss from vaporization. A shortcoming of the work is its omission of experiments or simulations at vaporization temperatures. Thus, it follows that there is no discussion of surface recession rates near the melting point.

We attempt here to clarify the dominant mass loss and surface damage mechanisms of LaB_6 under the severe conditions of an extreme plasma heat flux. Simulations are also developed to connect the results with applications for a sharp LE. The findings will allow us to assess the feasibility of LaB_6 and like refractory ceramics as potential hypersonic vehicle transpirants. The objective of the present work is to utilize computational and experimental methods to investigate the mechanisms of mass loss, surface oxidation, and surface damage in an arc jet environment that mimics some of the conditions encountered by the LE of hypersonic aircraft. To achieve this goal, we address the following: 1) conduct material characterization pre- and post-exposure to the arc jet plasma; 2) model heat transfer in samples exposed to the plasma arc jet so as to explain our experimental results; 3) quantify the surface recession rate of LaB_6 samples at temperatures exceeding its melting point; 4) discuss the feasibility of LaB_6 and similar refractory ceramics as potential hypersonic vehicle transpirant coolants.

The manuscript is organized as follows. First, the research background is provided in Section 4.2. Subsequently, in Section 6.3, we detail the experimental methods and the corresponding results. LaB_6 material properties are also tabulated here. Then we present the simulation conditions and outcomes in Section 6.4. Discussion of differences between the experimental and simulated results are also included. Section 6.6 takes the experimental and computational results from Sections 6.3 and 6.4 and orients the discussion toward cooling hypersonic vehicles. Finally, conclusions of the present work are summarized in Section 6.7.

6.2 Temperature & Pressure Effects on $\mathrm{LaB_6}$

6.2.1 Phase Transitions in $\mathrm{LaB_6}$

Prior to discussing vaporization theory, we provide a brief review of phase change concepts and a discussion about phase change as it relates to $\mathrm{LaB_6}$ in particular. The review is pertained to first-order phase transitions since the materials being considered are those which include a latent heat. To change a substance from a solid to a liquid, the latent heat of fusion (H_{fus}) must be added. Similarly, the latent heat of vaporization, H_{vap}, is the energy per unit mass needed to change a material from its liquid state to its gaseous state. Figure 53 helps illustrate these phase transitions. Sublimation, or the process by which a material changes from a solid to a gas directly, and deposition (the reverse process) can occur at temperatures below a material's triple point temperature, T_{tp}. By inspection, one can tell from Fig. 53 that an isothermal pressure drop for $T < T_{tp}$ can result in sublimation. Similarly, a material can undergo deposition if it isobarically reduces in temperature from below the triple point pressure, P_{tp}. For completeness, a "supercritical fluid" is a phase whereby a material takes on liquid and gaseous properties. In this phase, a material can move through solids like a gas and dissolve materials in a manner that is more akin to a liquid. Taking the generic phase diagram displayed in Fig. 53, one can see that a fluid is supercritical if it has a temperature above the critical point and a pressure which ranges from the critical point to the quantity which would cause the substance to transition into a solid.

To avoid ambiguity, we also clarify a few like terms. "Vaporization" is the general word for the process by which a material undergoes a phase change from liquid to gas. What makes the term broad is that it applies to evaporation, boiling, and some forms of ablation. The term "boiling" is more specific in that the phase change must come about by way of convection. This contrasts with "evaporation" which is a liquid to gas phase change, but takes place at a temperature below the boiling the point. It is a surface phenomenon whereby bubbles cannot form as the vapor pressure is less than the atmospheric pressure. Finally, "ablation" is the removal or destruction of material by an erosive process such as burning, charring, or vaporization, and often with the intention of cooling or protecting the underlying

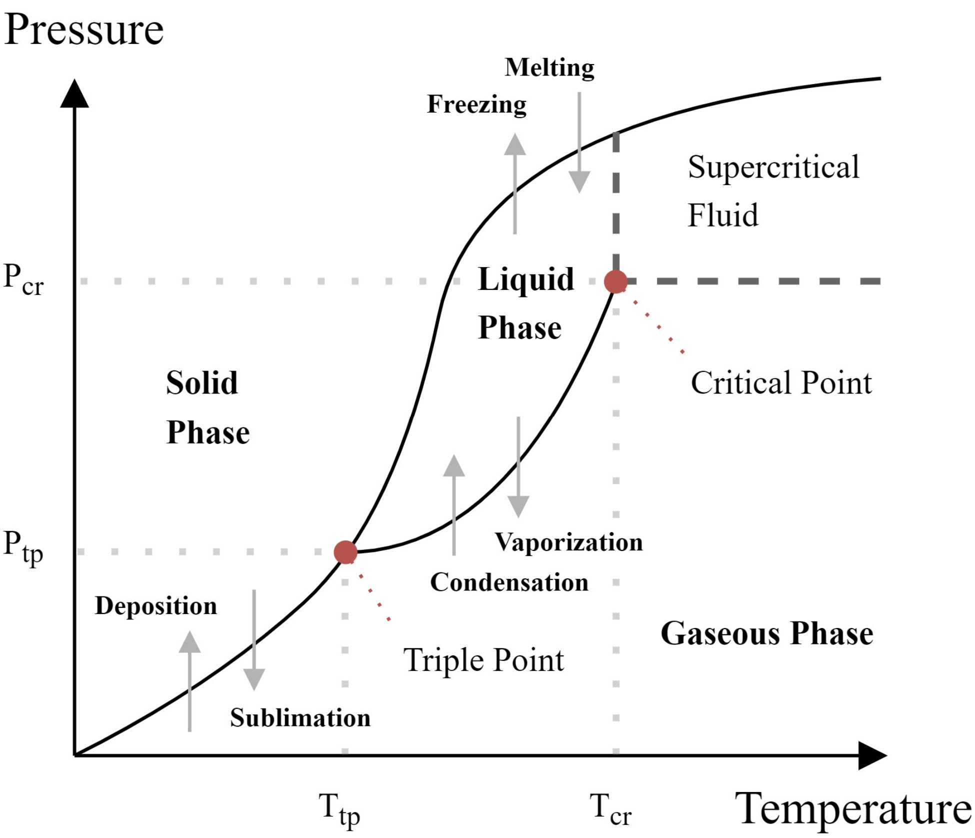

Figure 53: General pressure-temperature phase diagram. The triple point (tp) and critical point (cr) values for each axis are annotated.

structure. Since the transition from a gas to a plasma (i.e., ionization) and the changeover from plasma to gas (i.e., neutralization) happens gradually with increasing and decreasing temperatures, respectively, some argue that this is not a phase transition [162]. Others focus on the plasma-phase transition and characterize it as the shift of a neutral or weakly ionized plasma to a fully ionized fluid with an electrical conductivity similar to a metal as well as an increase in density [163].

Since LaB_6 is a binary compound, sections in phase diagrams are typically shown in relation to the atomic or weight percent of one of the two molecules as well as the range of temperatures for which the substance is solid, liquid, or both. Figure 54 shows the stable phases which exist at different temperatures for the spectrum of atomic percent lanthanum. Depending on the temperature, LaB_6 has an atomic percent lanthanum in the range of 10.0

to 14.3. Given the exceptionally high melting point of LaB_6, it is unsurprising that it has among the highest melting points in the B-La binary phase diagram. The peak melting point can be identified by the apex of the uppermost partially solid phases and the fully liquid phase. It is worth noting that the dotted lines represent regions where phases may be metastable. Phases γLa and βLa are allotropes which have the cubic crystal structures body-centered cubic and face-centered cubic, respectively. The αLa phase has the related structure known as double hexagonal close-packed [164, 165].

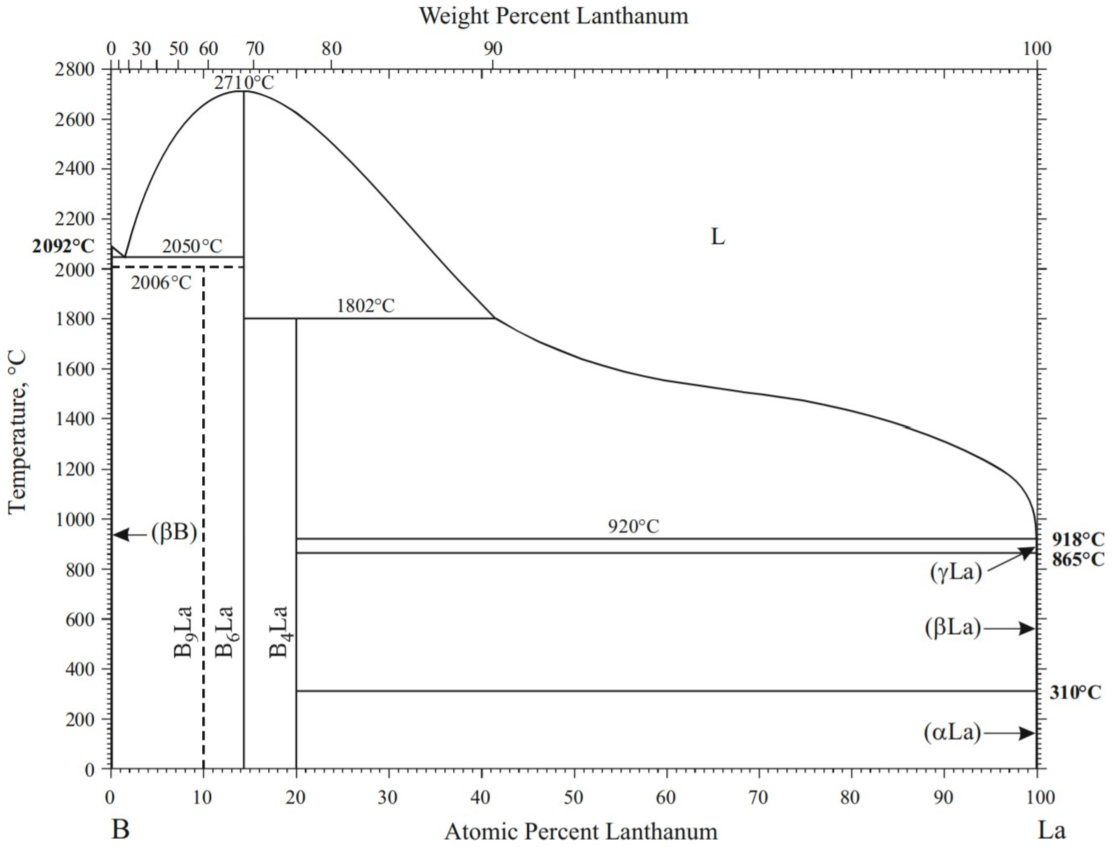

Figure 54: LaB_6 phase diagram for varying atomic percentages of lanthanum. Borrowed from [166].

Each phase has its own microstructure, but those for LaB_6 at elevated temperatures have only been sparsely documented. One of the few studies which includes this type of analysis was performed by Koblov *et al.* [167] Figure 55 displays a few micrographs from the cited work. The call-outs with annotations "M1" refer to lanthanum, "1" and "2" identify plateshaped phases of lanthanum borates of angular form, “3” points to an intermetallic compound of rounded form, and “4” labels lanthanum oxide. We note that the darkest regions are pores in the solid. One can observe clear differences between the four images despite the relatively subtle changes in sintering temperature. As the temperature is increased, the material densifies significantly, but maintains a nearly constant grain size. Lanthanum borates also appear to be more numerous in the sample sintered at 1,850 °C.

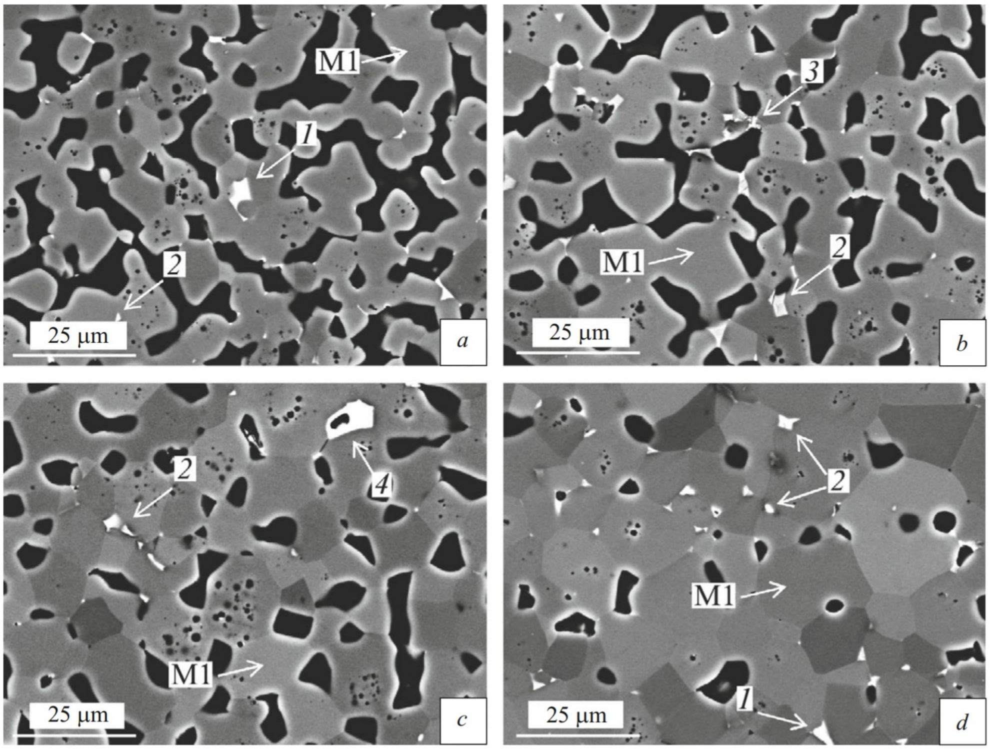

Figure 55: Experimental data of LaB_6 microstructure for the following sintering temperatures: a) 1,700 °C; b) 1,750 °C; c) 1,800 °C; d) 1,850 °C. Borrowed from [167].

6.2.2 Vaporization

Determining the vaporization rate of a material can be found by using the kinetic theory of gases. If we consider a liquid-gas interface whereby liquid is able to vaporize and gas is able to condense, then there should exist some amount of flux in either direction. For a system that is losing material, the rate of vaporization is therefore the difference in the flux of liquid particles becoming a gas, Φ_v and the flux of gas particles becoming liquid, Φ_c. This is simply

$$\Phi_{net} = \Phi_v - \Phi_c \tag{75}$$

Our scenario is a form of effusion as the particles undergoing phase change have a non-isotropic angular distribution, or directional component, into and out of a sample material. We can derive an equation for fluxes Φ_v and Φ_c by considering molecules coming in contact with a differential area dA. Figure 56 provides a schematic to guide the derivation. With $\mathbf{v}$ defined as the molecular velocity, the vector components can be written as $\mathbf{v} = v\left(\sin\theta\cos\phi,\ \sin\theta\sin\phi,\ \cos\theta\right)$. Since we are only interested in the molecules that could contact the differential surface element, our discussion pertains to velocities between $\mathbf{v}$ and $\mathbf{v} + d\mathbf{v}$, inclusive. It follows that we are only concerned with angles $[\theta,\ \theta + d\theta]$ and $[\phi,\ \phi + d\phi]$. We will also consider the particle movement over some differential time, dt. The resulting region is an infinitesimal cylinder within a spherical domain. Any molecule inside the cylinder will hit the elemental surface and molecules outside of it will not. The volume of the cylinder is $dA\ v\cos\theta\ dt$. Per unit volume, the quantity of molecules in the velocity range is $f\left(\mathbf{v}\right) d^3\mathbf{v}$. The product of this term and the volume of the cylinder gives the number of molecules that hit the elemental surface in the differential time. This is simply $\left[f\left(\mathbf{v}\right) d^3\mathbf{v}\right]\left(dA\ v\cos\theta\ dt\right)$. Dividing by the differential area and the time interval, we obtain the number of molecules in the prescribed velocity range that strike a surface element of unit area per unit time. We thus define $\Phi\left(\mathbf{v}\right) d^3\mathbf{v} = f\left(\mathbf{v}\right) v\cos\theta\ d^3\mathbf{v}$.

We can denote the flux per unit time as Φ_0 and obtain it by summing $\Phi\left(\mathbf{v}\right) d^3\mathbf{v}$ over all applicable velocities, namely $0 < v < \infty$. In our spherical coordinates, we also sum over azimuthal angles $0 < \phi < 2\pi$ and polar angles $0 < \theta < \pi/2$. Note than the hemisphere for which $\pi/2 < \theta < \pi$ entirely contains molecules headed in the directions away from the surface element, and thus are not relevant. As can be seen from Figure 56, the velocity component in the z-direction is simply $v_z = v\cos\theta$. Now we can write

$$\Phi_0 = \int_{v_z>0} f\left(\mathbf{v}\right) v\cos\theta\ d^3\mathbf{v} \tag{76}$$

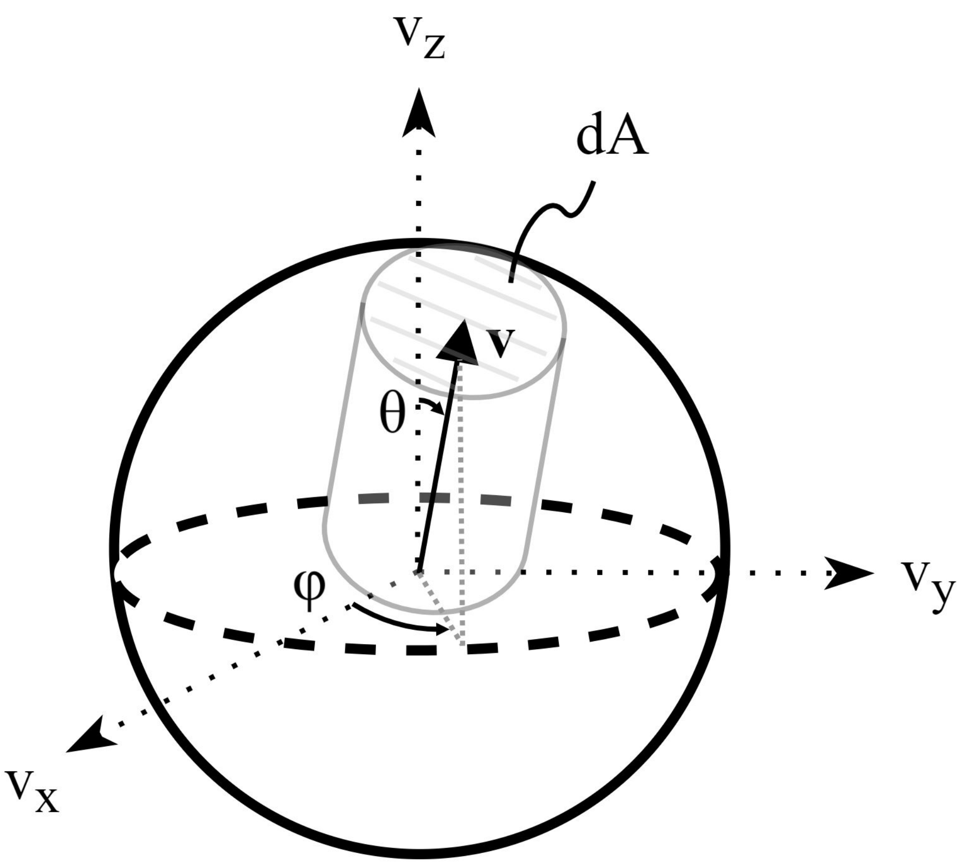

Figure 56: Infinitesimal cylinder inside the spherical domain. Represents the range of velocities and angles possible for a given vaporizing or condensing molecule.

In spherical coordinates the differential volume element in velocity space is $d^3\mathbf{v} = v^2 dv\,(\sin\theta\ d\theta\ d\phi)$. Also, in thermal equilibrium the function $f(\mathbf{v}) = f(v)$ because there are no special directions in the system and it is only a function of $|\mathbf{v}|$. This allows us to rewrite the equation as

$$\Phi_0 = \int_{v_z > 0} f(v)\, v \cos\theta \left(v^2 dv \sin\theta\ d\theta\ d\phi\right) = \pi \int_0^\infty f(v)\, v^3 dv \tag{77}$$

With n used to denote the number density of the molecules, the mean molecular speed is written as

$$\bar{v} = \frac{1}{n} \int f(v)\, v\ d^3\mathbf{v} = \frac{4\pi}{n} \int_0^\infty f(v)\, v^3\ dv \tag{78}$$

Recall from the famous Maxwell distribution of molecular speeds that also $\bar{v} = \sqrt{\frac{8k_B T}{\pi m}}$ where m is the mass of each molecule. Noting the similarities in these results for Φ_0 and $\bar{v}$, we can equate their latest forms and get

$$\Phi_0 = \frac{1}{4} n\bar{v} \tag{79}$$

Assuming ideal gas conditions and defining $\bar{p}$ as the average pressure, k_B as the Boltzmann constant, and T as the temperature, we can use the equation $\bar{p} = nk_BT$ and the Maxwell distribution form of $\bar{v}$ to write the final version of the flux per unit time as

$$\Phi_0 = \frac{\bar{p}}{\sqrt{2\pi m k_B T}} \tag{80}$$

As previously discussed, there is a flux of condensing molecules and a flux of vaporizing ones. If we call the pressure of the vaporized environment p and the pressure of the condensed environment p^*, then plugging into Equation 75 gives

$$\Phi_{net} = \frac{p^*}{\sqrt{2\pi m k_B T}} - \frac{p}{\sqrt{2\pi m k_B T}} \tag{81}$$

For many applications, the vaporized environment is some form of vacuum such that the term $p << p^*$, so the term on the right side can often be taken as negligible. An important note is that some of the evaporated vapor molecules colliding with the liquid-gas interface may be reflected back. Thus, we append the scalar term, α_v which is the sticking coefficient for vapor molecules onto the surface. Simplifying slightly, we retrieve the general Hertz-Knudsen equation

$$\Phi_{net} = \alpha_v \frac{1}{\sqrt{2\pi m k_B T}} \left(p^* - p\right) \tag{82}$$

To define p^* in a more useful manner, we consider the pressure-volume plot showing a change in phase for the material. During this phase transition, the temperature and pressure remain constant. The molar or specific values of the extensive thermodynamic properties change abruptly during a phase transition. Specific volume, entropy, enthalpy, and internal energy change drastically during the same process. The only exception is the Gibb's free energy, which remains constant. Thus, in a transition from phase α to phase β, we have: $dG^\alpha = dG^\beta$. Substituting for dG^α and dG^β, we get: $V^\alpha dP^{sat} - S^\alpha dT = V^\beta dP^{sat} - S^\beta dT$, where dP^{sat} is the "saturation pressure" during the phase transition. Upon rearrangement of the last equation, we obtain:

$$\frac{dP^{sat}}{dT} = \frac{S^\beta - S^\alpha}{V^\beta - V^\alpha} = \frac{\Delta S^{\alpha\beta}}{\Delta V^{\alpha\beta}} \tag{83}$$

However, since P and T are constant across a phase transition we have: $\Delta H^{\alpha\beta} = T\Delta S^{\alpha\beta}$, and the following form of the Clausius-Clapeyron equation is obtained:

$$\frac{dP^{sat}}{dT} = \frac{\Delta H^{\alpha\beta}}{T\Delta V^{\alpha\beta}} \tag{84}$$

Regarding the liquid-gas phase transition itself, the heat of vaporization, $\Delta H^{\alpha\beta} = L_v$. The subscripts c and g will be used to represent the wholly compressed and completely gaseous phases, respectively. The heat of vaporization can be written as $L_v = T\left(S_g - S_c\right)$. This allows the change in pressure with respect to temperature to be rewritten as

$$\begin{aligned} \frac{dp^*}{dT} &= \frac{S_g - S_c}{V_g - V_c} \\ &= \frac{L_v}{T\left(V_g - V_c\right)} \end{aligned} \tag{85}$$

which is a form of the Clapeyron Equation. Since the volume of the condensed phase is negligible compared to that of the gaseous phase, we can say $V_g - V_c \approx V_g$. Using the ideal gas law, which includes the gas constant R, we can also write $V_g \approx NRT/p*$. Rearranging, we get

$$\frac{dp^*}{p^*} = \frac{L_v \, dT}{NRT^2} \tag{86}$$

which is a form of the Clausius-Clapeyron Equation. Integrating the differential equation as a definite integral from the boiling point, denoted with the subscript b, to an arbitrary point gives the Arrhenius relation

$$p^* = p_b \exp\left[\frac{L_v}{NR}\left(\frac{1}{T_b} - \frac{1}{T}\right)\right] \tag{87}$$

Inserting Equation 87 into Equation 82 and noting that $1/NR$ is equivalent to m/k_B, we get the general flux equation

$$\Phi_{net} = \alpha_v \frac{1}{\sqrt{2\pi m k_B T}}\left(p_b \exp\left[\frac{mL_v}{k_B}\left(\frac{1}{T_b} - \frac{1}{T}\right)\right] - p\right) \tag{88}$$

This is the total number of molecules that vaporize from the material per unit area and per unit time or dimensionally $1/(\mathrm{L}^2{\cdot}\mathrm{T})$. The mass evaporation rate with dimensions $\mathrm{M}/(\mathrm{L}^2{\cdot}\mathrm{T})$ is obtained by simply multiplying Equation 88 by the mass of the material. Finally, a familiar form is given in terms of dimensions L/T and represents a sort of erosion or ablation rate.

Recall that dimensions length, mass, and time are written as L, M, and T, respectively. This form is achieved by taking the mass evaporation rate and dividing by the density of the material, ρ. This final form of the net vaporization flux equation is

$$\Phi_{net} V = \alpha_v \sqrt{\frac{m}{2\pi k_B T}} \left(\frac{p_b}{\rho} \exp\left[\frac{m L_v}{k_B} \left(\frac{1}{T_b} - \frac{1}{T} \right) \right] - \frac{p}{\rho} \right) \tag{89}$$

6.3 Experimental Conditions and Results

6.3.1 Experimental Setup

To address the objectives of the study on mass loss, sublimation, and surface damage, we have devised a testing regimen which involves taking LaB_6 discs and exposing each specimen to an argon plasma torch inside of a low vacuum chamber. The distance between the jet's outlet and the surface of each LaB_6 sample is specified for the experiment to produce a particular heat flux severity. Select heat flux conditions are also examined at a few test durations. After a sample is exposed, it is given a thorough material characterization comprised of scanning electron microscopy (SEM), energy-dispersive X-ray spectroscopy (EDS), optical microscopy, X-ray diffraction (XRD), and optical profilometry.

Experiments are performed at the High Energy Flux Test facilitY (HEFTY) at UCLA. Figure 57 provides a couple of visuals of the setup. Argon is supplied at a flow rate of 80 L/min and, depending on where we are in the standard operating procedure, is delivered to either the Praxair SG-100 plasma spray torch to become ionized and accelerated through the outlet or to the chamber for promoting a non-oxidizing testing environment. The torch is rated up to 80 kW of power and ionizes the argon gas. Prior to beginning a test, the chamber is brought to a low vacuum using a roughing pump and then 5 psi of argon is pumped and held inside to mitigate potential oxidation. Power is supplied by two direct current arc welding power sources rated to 80 kW each and the arc is maintained by a high frequency arc starter. Room-temperature water impinges on the sample backplate at a rate of approximately 2 gal/min. Water is also flowed through a heat exchanger in the chamber to prevent the most thermally sensitive internal components (e.g. linear actuator motor and insulation on electrical wiring) from overheating.

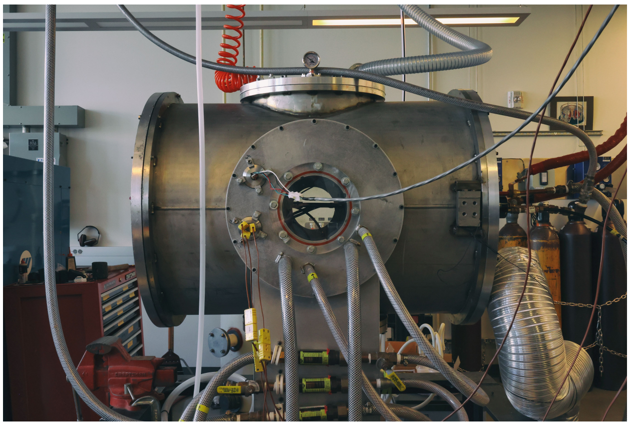

(a) Right side view.

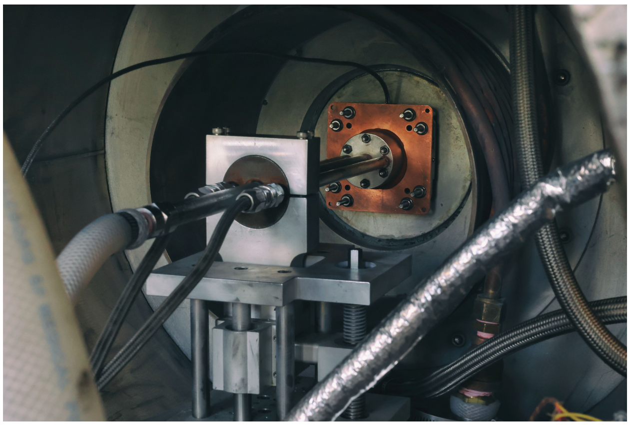

(b) Internal view. Sample positioned at 2.5 cm from jet outlet.

Figure 57: Images of HEFTY chamber with LaB_6 mounted in sample holder.

Key components inside of the HEFTY chamber have been annotated in Fig. 58. The sample is mounted to the sample fixture and is normal to the arc jet outlet. The sample fixture is connected to the sample dolly by way of pipes which provide water to the backplate. This set of components is mounted to the sample dolly, of which is connected to a pair of rails. A linear actuator motor is commanded to position the sample dolly at a distance, d, from the arc jet outlet. Water is also flowed above the sample dolly via the heat exchanger and around the heat shield to further counteract any potential of the chamber becoming too hot for the internal support equipment.

We now concentrate the discussion on the plasma, and more specifically, its distribution

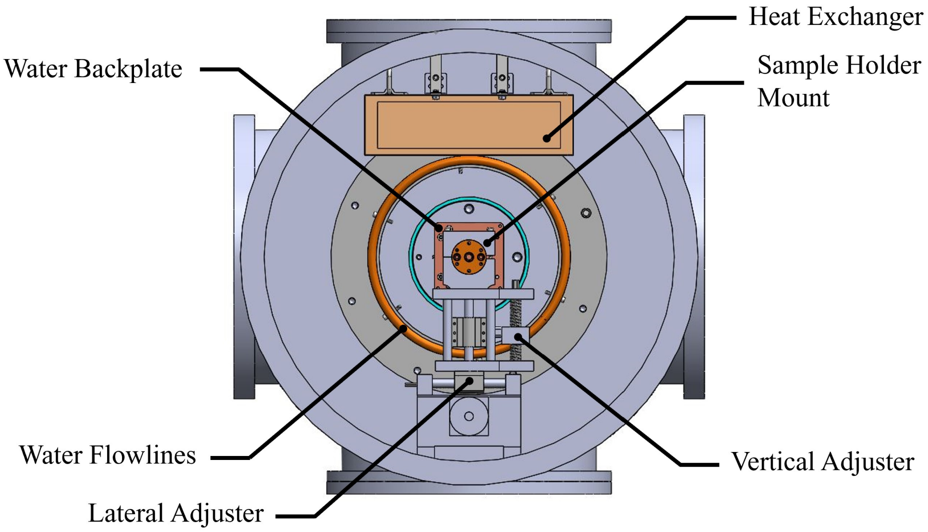

(a) Front view.

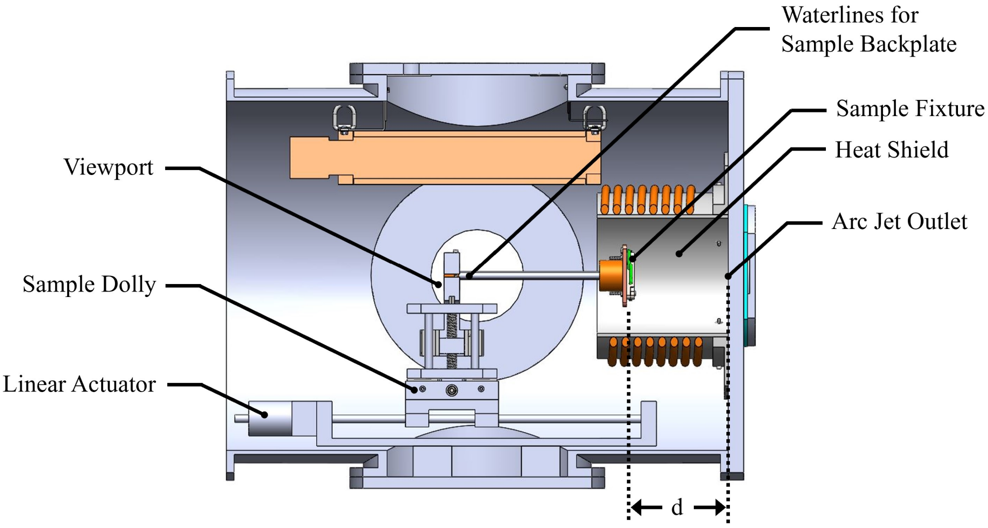

(b) Right side section view.

Figure 58: CAD model of HEFTY chamber with LaB_6 mounted in sample holder. Door is removed for visualization.

over the surface of the sample. At the outlet of the plasma spray torch, the beam is only the width of the outlet itself. For distances of $d > 0$, however, the beam naturally spreads out and the emitted energy becomes more diffuse. This has a significant impact on the heat flux profile at the surface of the sample, so it is important to carefully model this geometric effect. We define the distance from the jet centerline to be r for radius. Note that we assume the beam to be axially symmetric about the centerline. We also define the distance from the centerline to the edge of the beam to be the half width, or HW. Moreover, the angle that the half width occupies is defined as θ. Figure 59 illustrates the beam spreading effect and qualitatively what it does to the heat flux profile. We can now define the half width as

$$HW = d \tan\theta \tag{90}$$

We make a few additional assumptions. The first is that the heat flux profile follows a Gaussian curve and the second is that the standard deviation is effectively the summation of the standard deviation of the heat flux profile upon exiting the torch and the length of the half width as a function of d. We write the initial standard deviation as σ_0. We also assume that the peak heat flux occurs at the torch exit and decreases monotonically as the distance, d, increases. Letting the exponential function be normalized to unity, we write the expression for the heat flux as a function of the radius and the distance from the torch outlet as

$$q\left(r, d\right) = q\Big|_{d=0} \cdot q_{exp}\left(r, d\right) \tag{91}$$

Expanding the exponential function, we write the final form of the heat flux equation as

$$q\left(r, d\right) = \frac{q\Big|_{d=0} \exp\left[-\frac{1}{2}\left(\frac{r}{\sigma_0 + HW(d)}\right)^2\right]}{\left[\sigma_0 + HW\left(d\right)\right]\sqrt{2\pi}} \tag{92}$$

Now we have a way to represent the heat flux incident on the surface of a sample as a function of the distance from the torch as well as radially along the material's surface. The unknowns in Equation 92 are the angle, θ, the initial standard deviation, σ_0, and the heat flux at the torch outlet, $q\Big|_{d=0}$. Note that the coefficients for these variables are unique to the experimental conditions. For instance, using a gas other than argon, altering the mass flow rate, or supplying a different amount of power to the torch would produce a new set of values.

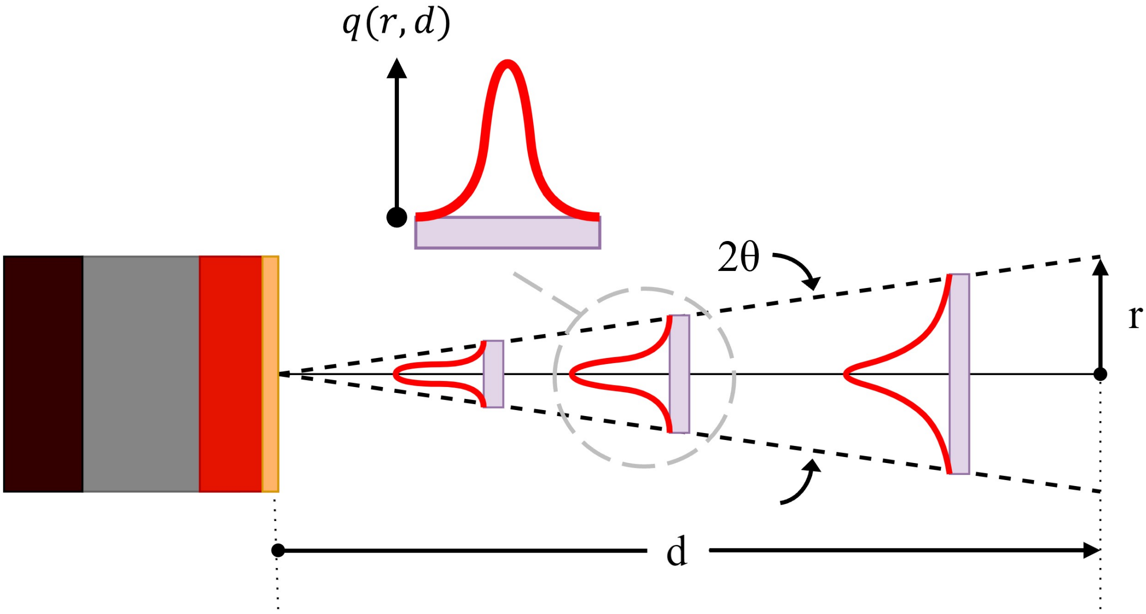

Figure 59: Plasma torch beam spreading and resultant heat flux profile illustration.

In the case of HEFTY, a few previous works have used similar conditions as the present study, so we have a range of values by which these variables should be bounded [168, 169, 170]. The half width beam angle varies from approximately 10° to 20°. Secondly, the maximum heat flux produced by the plasma torch ranges from about 32 $\mathrm{MW/m^2}$ to 38 $\mathrm{MW/m^2}$. Using Equation 92 and plotting these ranges, the initial standard deviation that best aligns with previous data is $\sigma_0 = 0.1^{1/2}$, and thus a variance of 0.1. Figure 60 illustrates the resultant plots when looking at the neighborhood values for the expected ranges. The subplot located in the center boasts values of $\theta = 15°$ and $q\Big|_{d=0} = 35\ \mathrm{MW/m^2}$ and is the best estimation of the heat flux produced by the argon plasma torch for the aforementioned conditions prior to calibrating the simulations with the experimental data. The calibrated heat flux profile will be presented in Section 6.4.2. As expected, when the surface of the experimental material is closer to the torch outlet, the heat flux profile becomes sharper and has a higher peak incident heat flux. Increased values of θ, however, have a broadening effect on the profile. The most important regions in each plot are the horizontal gray portions as they represent the width of the 0.75 in. diameter samples. These heat fluxes are those that impact the sample directly. We note that the white regions adjacent to the gray sections are incident on the sample holder.

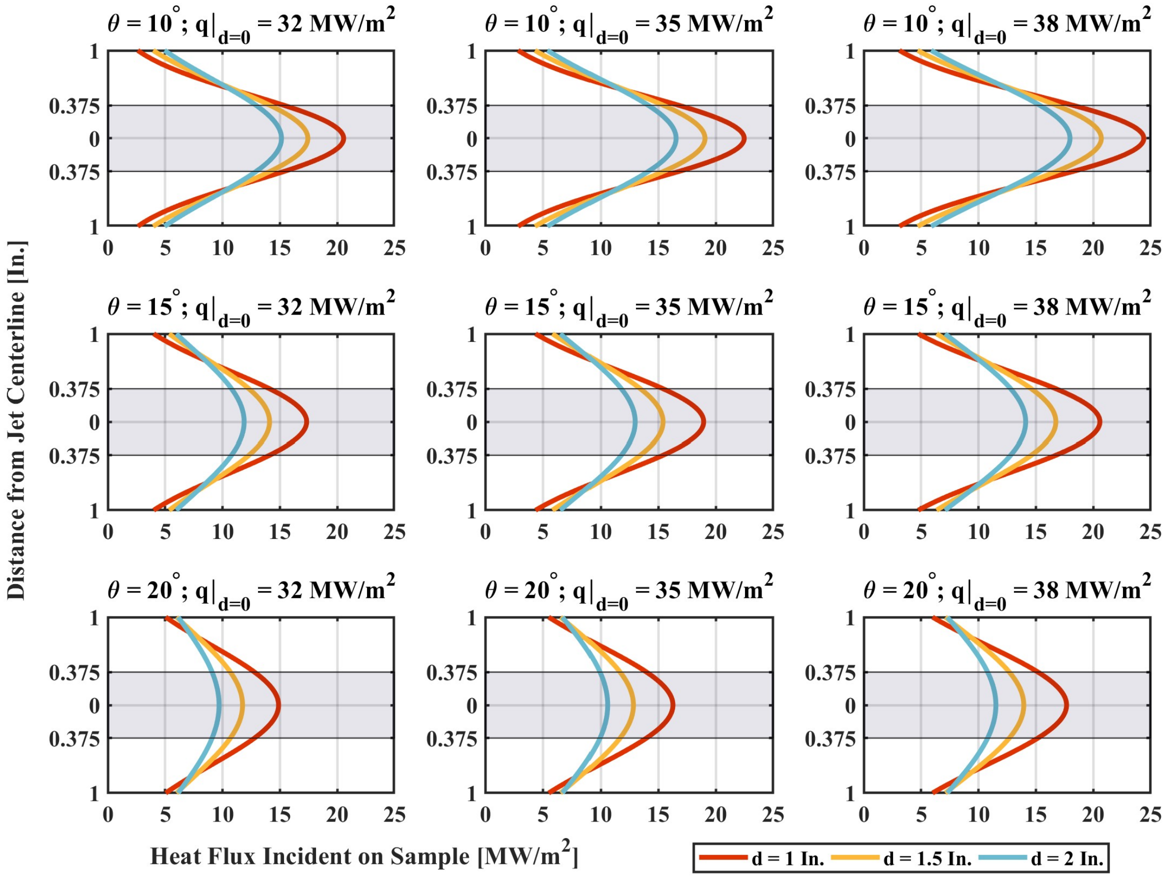

Figure 60: Heat flux sensitivity on LaB$_6$ surface (gray region) to plasma jet geometric and strength parameters. The statistical variance is set to 0.1 in. at $d = 0$.

As shown in Fig. 60, the three distances of interest are $d = [2.0, 1.5, 1.0]$ in. or [5.1, 3.8, 2.5] cm. Preliminary tests have shown us that the farthest distance in this vector is capable of achieving microscopic vaporization of the LaB$_6$ surface, the middle distance can cause some discernible macroscopic melting, and the nearest distance causes overt damage to the material's surface. Two test series are devised to obtain the desired experimental data. Series 1 is a fixed transient duration with varying heat flux profiles. Series 2 is a fixed heat flux profile with varying transient-length durations. The first series aims to produce snapshots of LaB$_6$ undergoing increasingly extreme heat flux conditions whereas a purpose

Table 9: $\mathrm{LaB_6}$ material properties

Material Property	Symbol	Magnitude	Unit	Reference	Temperature Dependence (*From Reference, **Derived)
Density	ρ	4.71	$\mathrm{g/cm^3}$	[171]	-
Melting Point	T_m	2,988	K	[172]	-
Heat of Formation	H_f° (298.15 K)	(-400.4 ±11.9) × 10^3	J/mol	[173]	-
Heat of Vaporization	L_v	530.7 ×10^3	J/mol	[174]	-
Standard Entropy	S° (298.15 K)	83.14	J/(mol · K)	[154]	$\mathrm{S}^{\circ **} = 2.711 \times 10^{-8}\ T^3$ $- 1.471\ \times 10^{-4}\ T^2 + 0.3818T - 16.34$ $298.15\ \mathrm{K} \leq T \leq 2,200\ \mathrm{K}$
Gibbs Free Energy	G° (298.15 K)	3.756 × 10^5	J/mol	[154]	$\mathrm{G}^{\circ **} = -0.0764T^2 - 84.02T + 4.127 \times 10^5$ $298.15\ \mathrm{K} \leq T \leq 2,200\ \mathrm{K}$
Thermal Conductivity	k (2,000 K)	0.40	J/(cm · s · K)	[175]	-
Specific Heat Capacity	C_p (298.15 K)	96.90	J/(mol · K)	[154]	$\mathrm{C}_p^{**} = -1.965 \times 10^{-11}\ T^4 + 1.291 \times 10^{-7}\ T^3$ $-2.881\ \times 10^{-4}\ T^2 + 0.3181T + 26.56$ $298.15\ \mathrm{K} \leq T \leq 2,200\ \mathrm{K}$
Emissivity	ϵ (2,000 K)	0.72	-	[176]	$\epsilon^* = 1.2144 - 2.467 \times 10^{-4}\ T$ $1,600\ \mathrm{K} \leq T \leq 2,100\ \mathrm{K}$
Elastic Modulus	E	376	GPa	[177]	-
Fracture Toughness	K_{Ic}	3.42	MPa · $\mathrm{m^{1/2}}$	[178]	-
Poisson's Ratio	ν	0.0386	-	[177]	-
Coefficient of Thermal Expansion	α_t	6.4	1/K × 10^{-6}	[177]	-
Work Function	Φ	2.76	eV	[179]	-
Electrical Resistivity	ρ_e (1,500 K)	100	Ω · cm × 10^{-6}	[175]	-

of the second series is to help us quantify the mass loss of $\mathrm{LaB_6}$ at elevated temperatures.

Ahead of presenting the experimental results, it is necessary to provide a comprehensive list of material properties for $\mathrm{LaB_6}$. Table 9 includes parameters which relate primarily to thermophysics, but some relevant strength and electrical properties have been included as well. Various temperature-dependent data in previous works have remained disconnected from any quantifiable trends. With the purpose of modeling the material properties for the experiments performed in the present study, polynomial fitting functions have been created for such data and these expressions are shown in the the same table. We will periodically reference Table 9 as the results and analyses are conveyed.

6.3.2 Experimental Results

Two test series have been performed in HEFTY to determine the rate of surface recession for temperatures which exceed the melting point of $\mathrm{LaB_6}$ and to obtain snapshots of the material enduring increasingly extreme heat fluxes. These test series and their experimental

Table 10: Experimental conditions by sample

Sample ID	d [cm] (in)	Duration [s]
1A	5.1 (2.0)	20
1B	3.8 (1.5)	20
1C/2A	2.5 (1.0)	20
2B	2.5 (1.0)	15
2C	2.5 (1.0)	25

conditions are detailed in Table 10. Samples 1A, 1B, and 1C/2A are exposed to the argon plasma torch for 20 s at 5.1 cm, 3.8 cm, and 2.5 cm from the arc jet outlet, respectively. Imperial units are included in the table as well. Recalling Fig. 60, we note that the variety of heat fluxes endured in Series 1 are represented by each subplot. That is, Sample 1A experiences the heat flux displayed in the gray region for the black curves. Similarly, Sample 2A undergoes the heat flux shown by the blue curves and that of Sample 3A by the red curves. Series 2, however, solely experiences the heat flux represented by the red curves, but for varying durations.

After exposing each sample in HEFTY at its prescribed distance from the jet outlet and for the given test duration, we put the 0.25 in. tall and 0.75 in. diameter LaB_6 discs through a gamut of material characterization tools. Additionally, each sample has been photographed from an isometric and a top view. These images are provided in Fig. 61. By inspection, the pre-exposed sample is a matte purple color, typical of LaB_6, and has a uniform machined finish. Sample 1A, which was exposed to the lowest severity conditions, became a shade of purple-gray and gained faint streaks which appear to diverge from the center. This sample has little macroscopic evidence of melting. Sample 1B appears to be incrementally more impacted by the high heat flux as some macroscopic evidence of melting is visible. This can be observed by the smoothed region nearest the center of the disc. The discoloration compared with the pre-exposed sample, however, is similar to that of Sample 1A. Despite the change in distance from the jet outlet being equal among Sample 1A and 1B and from 1B to 1C/2A, damage on the latter sample is far more extensive.

(a) Pre-exposed sample

(b) Sample 1A; d = 5.1 cm; 20 s

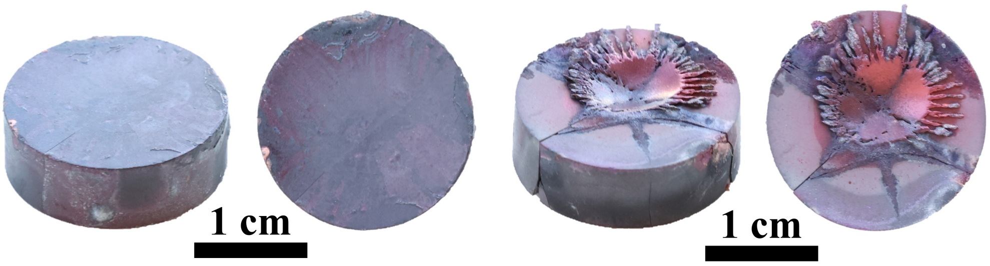

(c) Sample 1B; d = 3.8 cm; 20 s

(d) Sample 1C/2A; d = 2.5 cm; 20 s

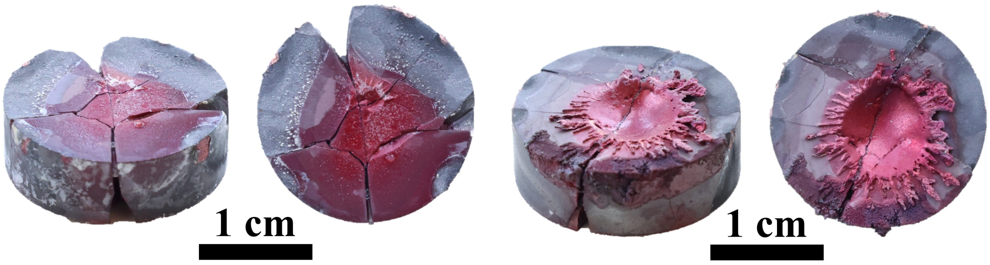

(e) Sample 2B; d = 2.5 cm; 15 s

(f) Sample 2C; d = 2.5 cm; 25 s

Figure 61: Photographs of the LaB_6 specimens. Each subfigure includes an isometric view (left) and a top view (right).

Sample 1C/2A has several notable features at the macroscopic level. Firstly, a portion of the sample contains a crater where a sort of corona splash took place. It is apparent that melting occurred in this region and the pressure from the plasma impinging on the surface of the sample was sufficient to blow the majority of the liquid-pool out of this highest heat flux area. That liquid then created a corona-like rim as it spread away from the center and interacted with lower heat fluxes before solidifying. Another feature is the set of fractures that extends along large portions of the sample. Two cracks are nearly perpendicular to each other and are centered at the point of the highest heat flux. Other small fractures appear to have developed from these two initial breaks for additional thermal stress relief. Finally, the color at the base of the melt pool is magenta and the finish is smooth and relatively reflective. Samples 2B and 2C exhibit similar features to Sample 1C/2A with the primary difference being the size of the melt pool. Sample 2B has a significantly smaller melt pool than Sample 1C/2A and that of Sample 2C is somewhat larger. There is clearly a direct correlation between exposure time at 2.5 cm from the jet outlet and the size of the melt pool.

Optical microscopy was performed on each characteristically unique sample using the Phenom proX at 20x magnification. Figure 62 displays the images captured on this tool. The optical micrographs inform a similar story to the one told by the photographs shown in Fig. 61, but they provide additional detail, especially regarding the damage mechanisms. The progression from Sample 1A to Sample 1B is clearer at this scale. The surface of Sample 1A is pockmarked with the same lighter magenta color that is consistent across the region shown for the higher severity Sample 1B. As detailed in a later discussion on the SEM images for these samples, these markings are regions where melt flows have covered the underlying solid surface. Sample 1A is predominately a darker purple color which shows that melting was not pervasive, but rather localized to said pockmarks. This is evidence that Sample 1A reached the LaB_6 melting point of 2,988 K near the center of the sample, but likely did not well-exceed this temperature. This observation helps guide the simulations presented in Section 6.4. The optical micrograph for Sample 1C/2A is also provided, and it is representative of Samples 2B and 2C since the Series 2 tests have a similar visual presentation. The principal difference between the Series 2 samples is the scale of the cratered region and the amount of ejected material on the periphery of the cavity.

By magnifying these images one, two, and three orders of magnitude and using secondary electrons to reflect resolute images of the samples, the ZEISS Supra 40VP SEM in the California NanoSystems Institute at UCLA can help qualify the extent to which each experimental condition in HEFTY is melting, vaporizing, and damaging the samples. Figure 63 displays SEM images of the pre-exposed sample, Fig. 64 of Sample 1A, Fig. 65 of Sample 1B, and Fig. 66 of representative images for Series 2 samples at three length scales. The pre-

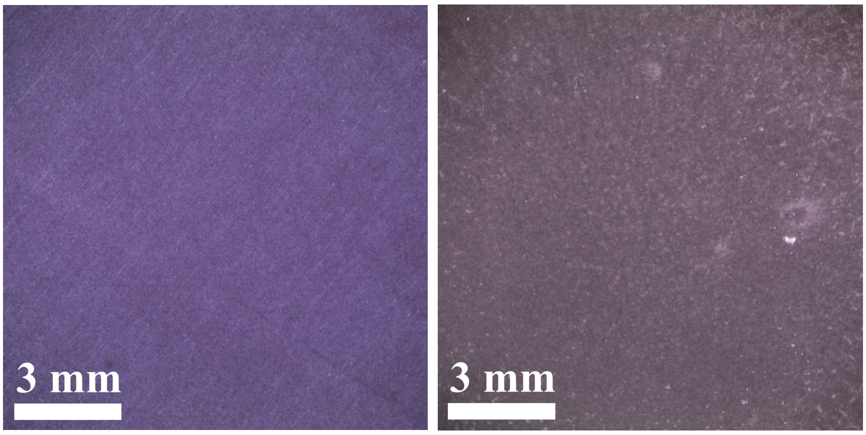

(a) Pre-exposed sample **(b)** Sample 1A; d = 5.1 cm; 20 s

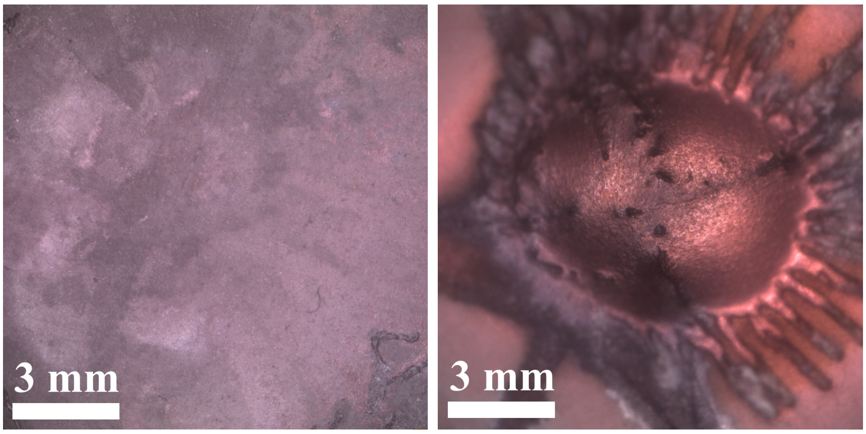

(c) Sample 1B; d = 3.8 cm; 20 s **(d)** Sample 1C/2A; d = 2.5 cm; 20 s

Figure 62: Optical micrographs of the LaB_6 samples from Series 1 and a representative sample from Series 2. Each image is centered at the location of highest heat flux.

exposed sample is clearly a machined sample as evidenced by the diagonal and parallel lines seen at the 250x magnification. Additionally, there are occasional pores of roughly 20-50 μm diameter. To this point, the relative density has been measured for the pre-exposed samples and they are all 94.0±1.0% dense for which the theoretical LaB_6 density of 4.71 g/cm^3 is considered 100%. In other words, the original samples are approximately 6.0% porous and this is corroborated by the various pores seen in Fig. 63a. Increasing the magnification by an order of magnitude shows the surface is fairly rough, but also quite uniform. Finally, the 25,000x magnification image shows the surface is jagged, polycrystalline, and void of obvious contamination.

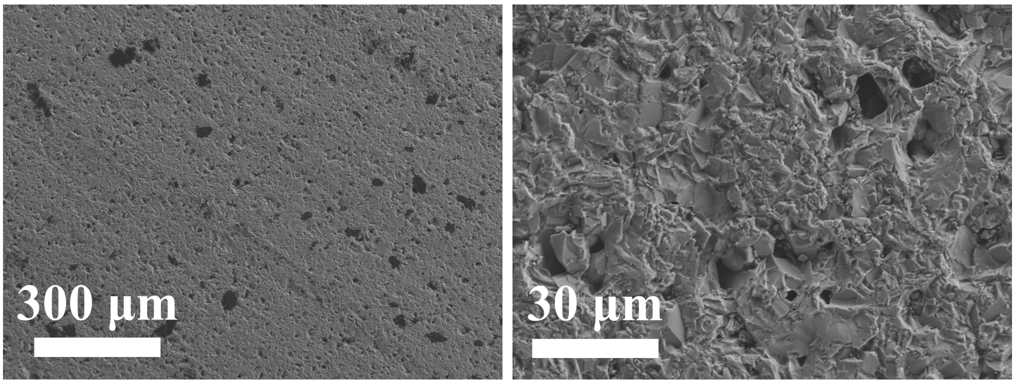

(a) Pre-exposed sample (250x mag.) **(b)** Pre-exposed sample (2,500x mag.)

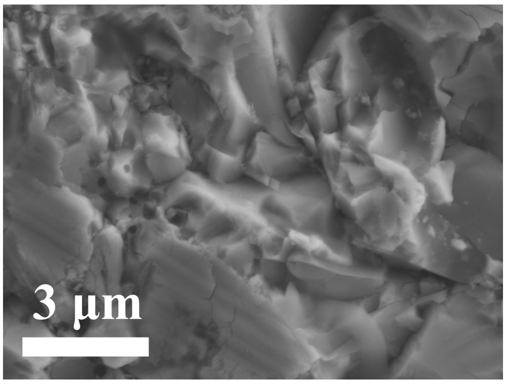

(c) Pre-exposed sample (25,000x mag.)

Figure 63: Scanning electron micrographs of the pre-exposed sample. All images are centered at the location of highest heat flux.

We know from the optical micrographs that all exposed samples have at least some evidence of undergoing phase change, but the mechanistic details are unclear. Fortunately, viewing the region of each specimen that was impacted by the highest heat flux through SEM aids in clarifying the melting process. After exposing the LaB_6 disc to the plasma torch for 20 s at a distance of 5.1 cm from the jet outlet, the surface gained microfractures and the jagged exterior became somewhat dulled. EDS shows us that the crack which is highlighted in Figures 64a and 64b occurred during the cool down portion of the experiment. This is evidenced by the existence of trace amounts of tungsten on the sample except for in the fracture itself. The grips which maintain the position of the LaB_6 on the sample holder are made of tungsten and particles from these grips get swirled around the sample during the experiments. Had the tungsten been identified inside of the crack, this would suggest that the crack formed during the portion of the test when the ionized argon is flowing. Rather, the fracture formed while the plasma torch was off. During cool down, the sample contracts quickly in the region where the temperature was highest. Similarly, the radial temperature gradient is greatest at the center of the plasma and reduces gradually at greater r. These combined factors were enough to cause a microfracture to form in the sample.

From a phase change standpoint, however, the features in Fig. 64c are particularly important. While another microfracture is visible in this SEM image, it is the pore and the smooth texture on the grains that are especially telling. The substance most likely experienced melting in this region and upon cool down the material nucleated, grew, and fused into grains. Furthermore, the hole suggests that gases were released during the exposure to the high heat flux. So, not only did the material locally undergo the solid to liquid phase change, but a portion of the LaB_6 vaporized as well. Another type of feature in this image is the faint and light gray web-like structure that is most prominent around the borders of the grain boundaries. These are clusters of lanthanum borate ($LaBO_3$) and they have managed to form despite being grown in a low vacuum environment.

While Sample 1A does not have conspicuous signs of melting until the smallest length scale shown, Sample 1B appears to have melted. Figure 65b has a partially smooth and reflective surface compared with the pre-exposed sample and Sample 1A. This suggests that prominent melt pools developed during the test, but the heat flux was not sufficiently high to create an uninterrupted layer of melted material. We also note that the regions of the image which do not contain a resolidifed melt pool do have an evenly distributed popcorn-like structure which will be discussed momentarily. As expected, vaporization pores can be seen at the 2,500x magnification and are more frequent and larger in Sample 1B than in Sample 1A. These same pores are seen in the 25,000x magnification image and are approximately 500-800 nm in diameter. At this length scale the popcorn-like structures are clearly visible and contrast significantly from the smooth gray regions which are part of the resolidified LaB_6 grains. These are more organized versions of the $LaBO_3$ clusters seen in Fig. 64c. Since oxides are more likely to form in higher temperature environments, it is reasonable that the $LaBO_3$ identified in Sample 1A would be more widespread in Sample 1B.

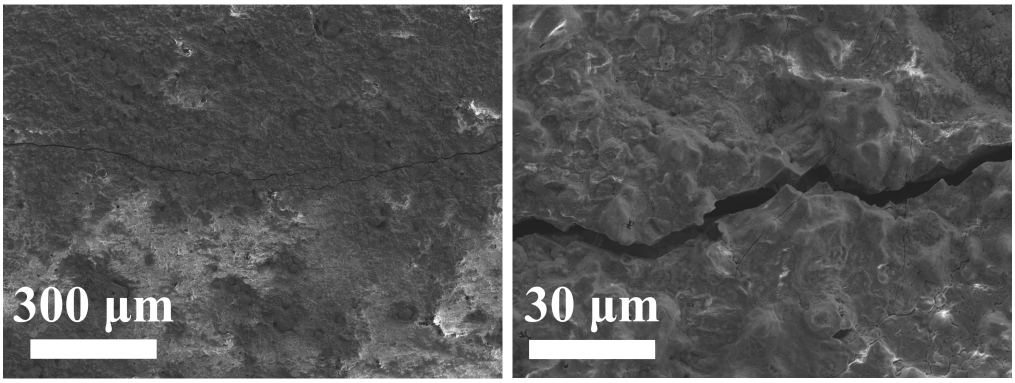

(a) Sample 1A (250x mag.) **(b)** Sample 1A (2,500x mag.)

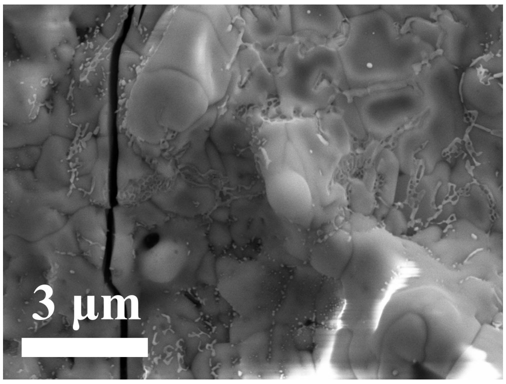

(c) Sample 1A (25,000x mag.)

Figure 64: Scanning electron micrographs of Sample 1A. All images are centered at the location of highest heat flux.

SEM images of the highest severity conditions, for which we anticipate extensive melting and significant vaporization, are useful in that they show what features are contained in resolidified LaB_6 melt pools and the extent to which the surface is disfigured from its pre-exposed counterpart. We note that the SEM and EDS results for Sample 1C/2A reflect those for 2B and 2C, and thus we present one set of images to encompass the Series 2 tests. Each of the samples in Series 2 was exposed to the plasma torch in HEFTY at 2.5 cm from the jet outlet. Recalling the estimated heat fluxes provided in Fig. 60, the center of these samples endured a heat flux of 20 ± 5 MW/m^2. It is clear that this heat flux causes the temperature of the surface to exceed the T_m of 2,988 K. Still, a more thorough discussion of the corresponding temperature is warranted and is provided in Section 6.4.

Relative to Sample 1A and 2A, the SEM images for 1C/2A show a consistent underlying

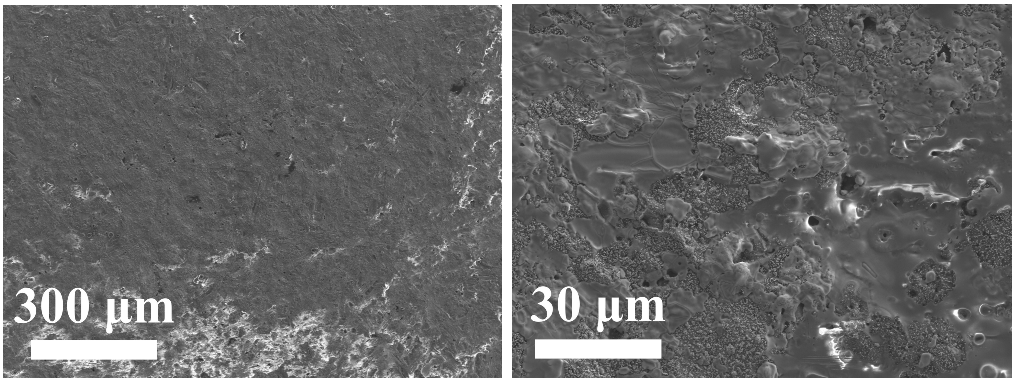

(a) Sample 1B (250x mag.) **(b)** Sample 1B (2,500x mag.)

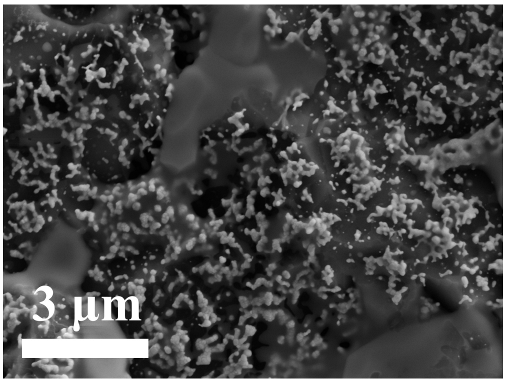

(c) Sample 1B (25,000x mag.)

Figure 65: Scanning electron micrographs of Sample 1B. All images are centered at the location of highest heat flux.

smooth and reflective surface which has been blemished by numerous microfractures and pores. Also, we observe an absence of oxides in Sample 1C/2A. Since the temperatures seen by this specimen were higher that Sample 1A and 1B, one could expect the continued progression of the oxide development. However, we note that the smooth and reflective regions of Sample 1B appear to be void of these oxides as well. Thus, we conclude that melt pools flow over top the existing oxides and simply cover them or, if sufficiently hot, melt them such that they combine with the liquid flow.

As with the cracks seen in Sample 1A, EDS results for Sample 1C/2A suggest that these fractures are created upon cool down of the material as a sort of stress relief. Mechanistically, these images show that LaB_6 exposed to temperatures well above its melting point will produce a melt pool which evenly wets the affected surface, but this liquid layer creates a sort of resistance to active vaporization. It appears that the way in which the material adjusts for this obstruction is to create through-holes that allow gas to exit. We note that the raised surfaces seen in the 2,500x magnification image (Fig. 66b) are attempted holes which failed to rupture. This is especially important for the surface recession rate at temperatures near to and exceeding the melting point. Further analysis of surface damage is presented in Section 6.5.

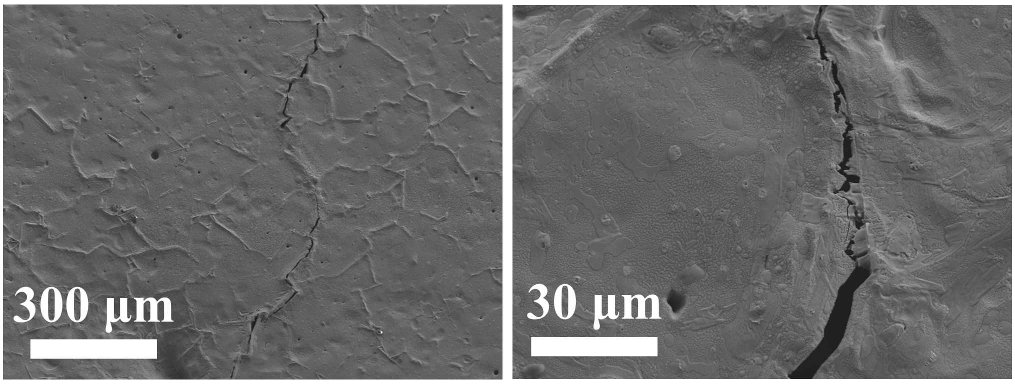

(a) Sample 1C/2A (250x mag.) **(b)** Sample 1C/2A (2,500x mag.)

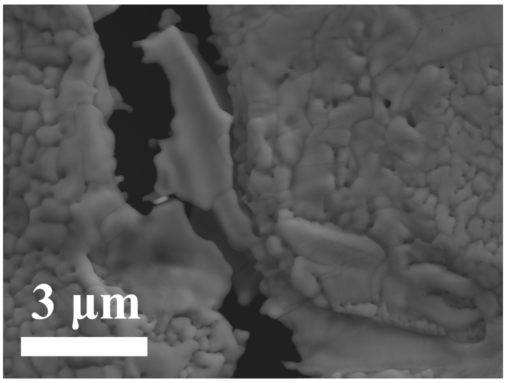

(c) Sample 1C/2A (25,000x mag.)

Figure 66: Scanning electron micrographs of a representative sample from Series 2. All images are centered at the location of highest heat flux.

A theme among the discs in test Series 2 is the existence of a crater and ejecta. The plasma torch primarily provides heat, but it also supplies a blowing coefficient as well. That is, the ionized argon molecules flow with a particular velocity and those molecules collide with the LaB_6 surface and spread out radially. This is why the ejecta takes the form of a corona splash. Typically a splash event involves a liquid volume initially in motion interacting with a relatively static substance (e.g., a liquid droplet falling onto a hard surface), but in this case we have a relatively static liquid volume being disturbed by a gas in motion. Regardless, what results is molten LaB_6 being forced away from the evolving crater and solidifying as tendrils which point radially away from the peak incident heat flux on the sample's surface. Figure 67 annotates three regions around the splash and helps illustrate the impact of the blowing coefficient on the molten material. Region "1" is the heated surface near the edge of the disc which experiences a significantly lower heat flux than the center does. This is the reason its surface is rough, but vaporization holes are abundant. Region "2" contains the tendrils themselves and region "3" is the center of the sample which endures the highest heat flux. "3" is best represented by Fig. 66a.

Looking closely at region "2", one may notice what appears to be fuzz or debris on the tendrils. The enlarged section helps illuminate these features. What are seemingly debris are in fact off-scourings. The expanded region presents two LaB_6 fragments which solidified onto part of the corona. This was most likely molten material which was not part of the main wave of splashed melt pool, but unstable sections of the corona-like rim and tendrils which were ejected while the pieces were still molten. These microscale particles landed on the farthest radial sections of the tendrils and started resolidifying. Finally, as this ejecta was cooling on its new substrate, the continued blowing from the plasma torch bent the ejecta in the direction radially away from the impinged surface. This is why the two fragments are bent toward the left side of the image as though trees in straight line winds.

Another type of material characterization we involved to better understand mechanisms of heat flux-induced mass loss in LaB_6 is XRD. The method provides phase identification of crystalline materials and lattice strain. The tool used is the BEDE D1 and it contains a 2.2 kW sealed tube X-ray generator, a goniometer with 0.16 in. resolution in θ and ω, and a high dynamic range scintillation detector. Similar to EDS, XRD plots show peaks of highest intensity according to characteristic energies. These energies, though, satisfy the Bragg Equation for which constructive interference achieves a local maximum. An X-ray diffractometer rotates the sample such that 2θ symbolizes the angle between incident rays and the detector. This differs from ω which is the angle between incident rays and the

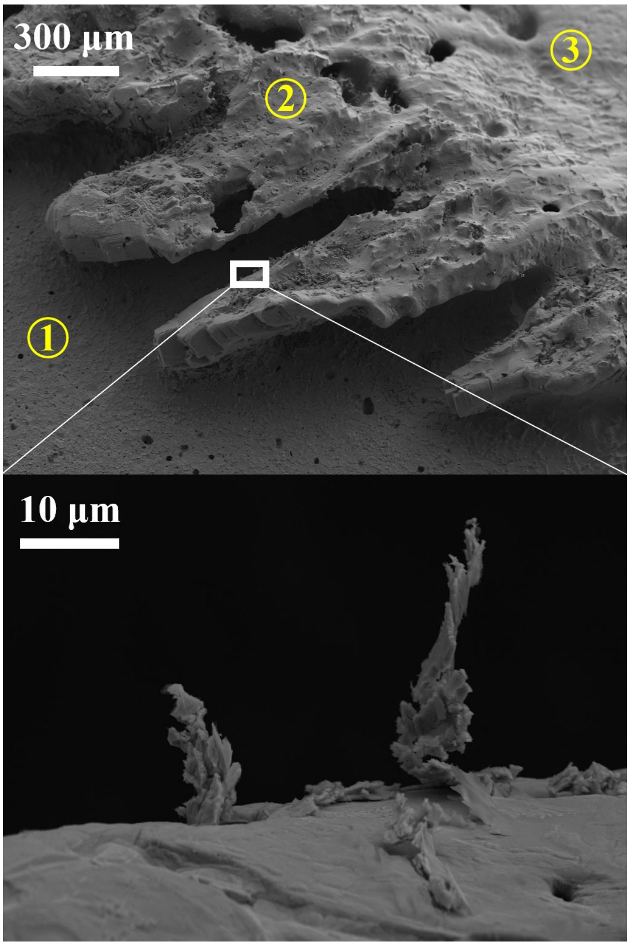

Figure 67: Solidified ejecta on Sample 1C/2A.

sample surface [134]. Figure 68 includes the scans for each type of high-energy plasma exposure discussed throughout the present work. The outcome aligns well with the EDS and SEM results in that the pre-exposed sample is uncontaminated LaB_6 and exposed samples develop some $LaBO_3$, especially those which do not develop a melt pool. A trifle amount of tungsten from the sample holder apparatus is also found in the XRD scans. We note that $LaBO_3$ exhibits over a hundred peaks in the 2θ range sampled, so select planes have been annotated.

The final type of material characterization tool we used to analyze the samples is optical profilometry. The purpose of these scans is to determine the precise depths of the melt pool cavities at all positions in the crater. Each sample in the Series 2 test campaign was scanned with the Bruker ContourGT-X. The machine is calibrated with a laser, collects images with

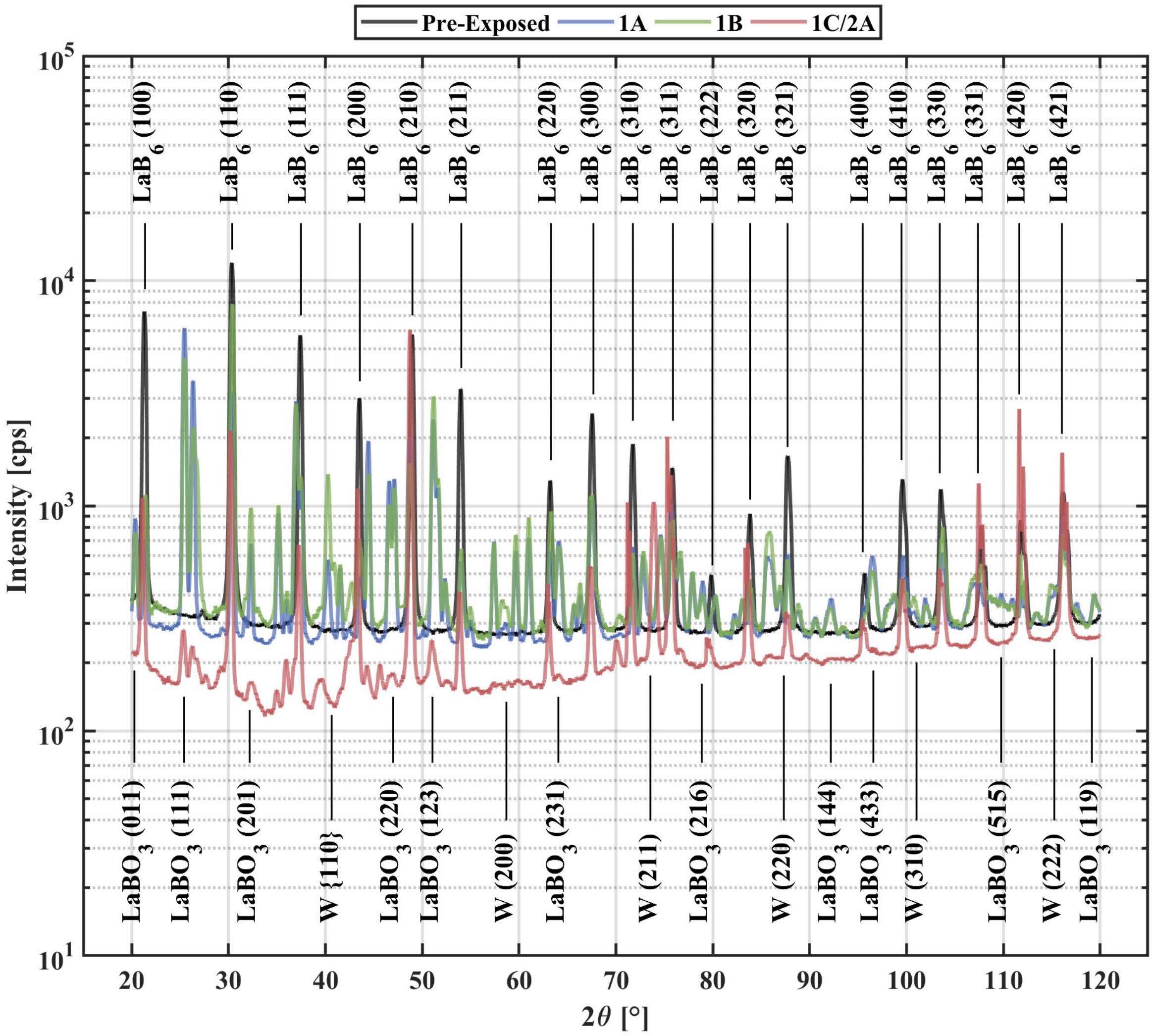

Figure 68: XRD 2θ-ω scan for each LaB_6 specimen from Series 1 and a representative sample from Series 2.

a microscope, and obtains height information with a vertical scanning interferometer. A 5x objective lens and a 0.55x zoom lens were used to capture the data. Figure 69 displays the three scans in a descending, top, and side view. The height data is tilt-adjusted and zeroed at the pre-exposed height or neutral plane. We recall that these three samples endured the same heat flux profile, but for different lengths of time. Sample 2B was exposed for 15 s, Sample 1C/2A for 20 s, and Sample 2C for 25 s. Sample 2B contains a small, but noticeable melt pool cavity and features a disorganized corona splash. The solidified ejecta rises approximately 0.25 mm above the neutral plane and has a trough at about 0.15 mm below the original height. Both Samples 1C/2A and 2C have well-developed corona splashes which rise just over 0.6 and 0.8 mm, respectively. Their deepest points are about 1.0 and 1.2 mm below their neutral planes. Thus, the data aligns with expectations in that the maximum depth is positively correlated with the test duration. A more precise and detailed quantification of the optical profilometry data is provided in Section 6.5.

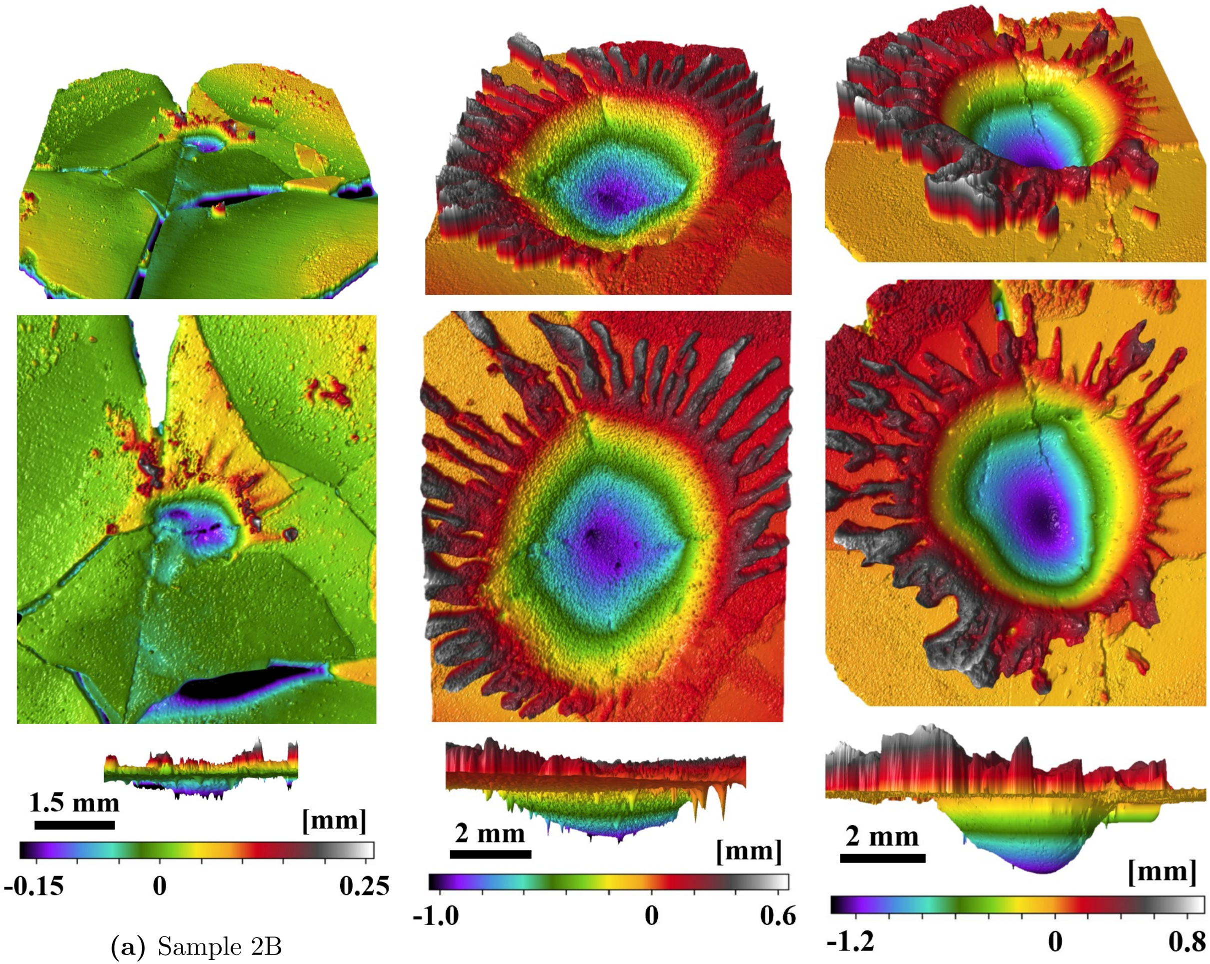

(a) Sample 2B

(b) Sample 1C/2A

(c) Sample 2C

Figure 69: Optical profilometry data for each melt pool cavity. Color scales apply to descending, top, and side views and length scales pertain to top and side views only.

6.4 Modeling Heat Transfer in LaB_6 Samples

6.4.1 Model Setup

In parallel with the experimental efforts, a simulation of the LaB_6 disc testing in HEFTY was developed to provide greater insight into the temperatures experienced by the samples throughout the argon plasma torch exposures. The sample and the neighboring sample holder components were included in the simulation to capture the thermal conductivity between the components as well as the surface-to-ambient radiation from all heated surfaces. Moreover, since the standard deviation of the beam at the jet outlet spreading is approximately $\sigma_0 = 0.1^{1/2}$, and the beam spreads out with a half angle of about $\theta = 15°$, there is a portion of the Gaussian curves' tails which provide significant incident flux to the sample holder components. Thus, such components as the spring-loaded tungsten grips which maintain the centering of the sample without applying significant stress on the specimen, the high temperature steel housing which helps secure the tungsten grips and any thermocouples used in select tests, and the copper chromium zirconium backplate which allows for cooling of the sample's backside and fixes the supporting structure in place, are integral to the accuracy of the simulation. The location of each component as well as the boundary conditions applied to them have been illustrated in Fig. 70.

Initial conditions include the temperature of the water impinging on the backplate and the temperature of the argon gas in the chamber. Both are kept at room temperature in the model, but it is worth noting that the simulation is insensitive to realistic perturbations in these temperatures. The boundary conditions are the incident heat flux from the plasma torch, convective heat transfer done by the water, and heat radiated from the surfaces to the ambient chamber. The previously detailed Equation 92 gives the incident heat flux as a function of the distance from the jet outlet along the torch centerline, d, and the radial distance away from the jet centerline, r. The forced convection by the water has been estimated to have a heat transfer coefficient of h=10,000 $W/(m^2 \cdot K)$. We also note that the simulations are somewhat insensitive to realistic perturbations of h. The most severe heating conditions that were simulated saw a fluctuation of no greater than 200 °C when the heat transfer coefficient was altered to 1,000 W/(m^2·K). The thermal conductivity is taken to be 36.7 W/(m·K) which is gathered from [175] at 2,000 K and accounts for the average volume fraction of the discs being 94%. We recognize that in practice thermal conductivity is marginally lower at cooler temperatures and slightly higher nearer to the melting point. At 0.25 in. thick, each sample is much thinner than the diffusion length for the 15 to 25 s transient test durations. Thus, the temperature gradient across the thickness is expected to be nearly linear by the end of each test. The latent heats corresponding with the melting and vaporization processes are not accounted for, and thus the simulation is most accurate for temperatures up to incipient melting. Finally, a sensitivity study performed on the mesh showed that the 70,100 element configuration used in the model allowed for less than a 1.5% difference in the temperature profile than the greater element count meshes which proved to be overly expensive computationally.

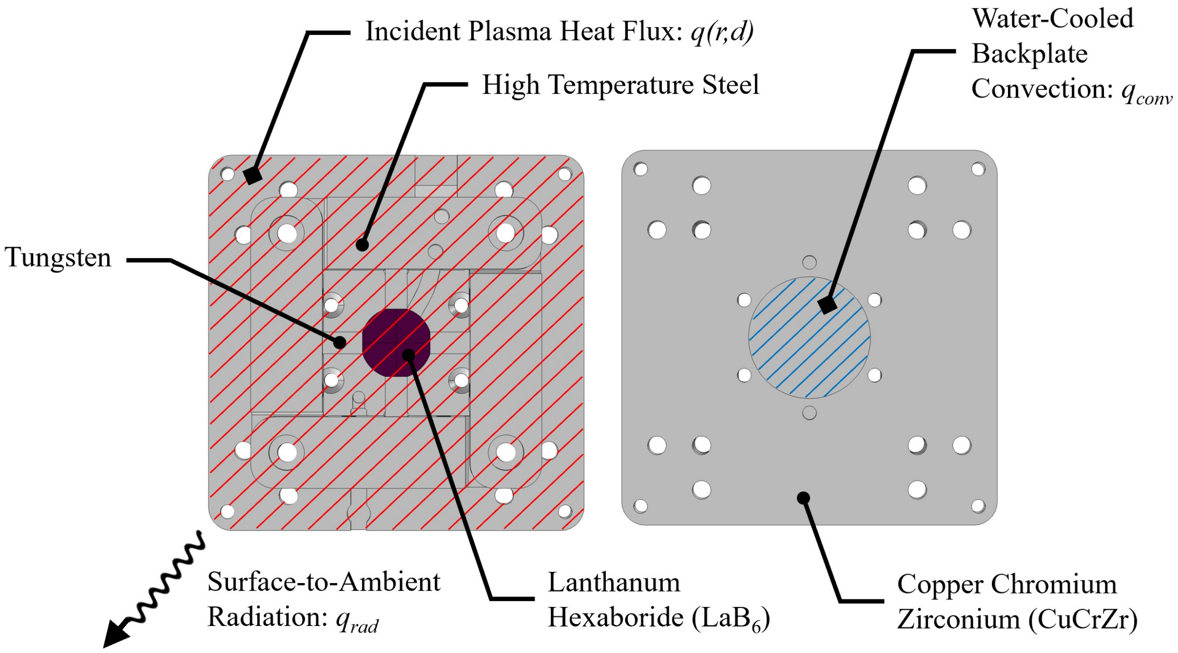

Figure 70: Schematic of simulated conditions on sample holder and LaB_6 sample.

Two methods are used to validate the accuracy of the model. The first technique is to compare the initial simulation results with the extent of melting and vaporization seen in the exposed samples. For instance, if one sample had no observable evidence of melting, but the simulation reported a peak temperature above the melting point, then there is clearly more calibration needed. The second method involves a thermocouple. As alluded to earlier, the sample holder has the capability of securing K-type thermocouples. This type is chosen for its high-temperature performance combined with its fast sampling rate. For the lowest severity tests (i.e., those which are unlikely to melt the measurement device), we secure a thermocouple to the back center of the sample. This allows us to apply the transient temperature results as a boundary condition in the model. This acts a handshake between the experiments and the simulations whereby the model is incorporating measured results. Once the lowest severity tests are calibrated with the experimental data, then the model is expandable to all anticipated testing conditions in HEFTY for that setup.

6.4.2 Modeling Results

Initial testing using HEFTY on the LaB_6 discs as well as previous works at the facility [168, 169, 170, 180] helped inform the model and allowed for efficient calibration of the heat flux profiles. Recall that the span of heat flux profiles the plasma torch could reasonably produce at the jet outlet was presented in Fig. 60. To hone in on the heat flux and beam half angle combination which best represents the argon plasma, we inspect the experimental results from the lowest severity condition tests. As mentioned previously, the tests with the lower incident heat fluxes allow for a thermocouple to accurately measure the transient temperature of the back center of a LaB_6 disc. A relevant specimen which gave a useful signature was Sample 1A. This test's severity was sufficiently low such that a thermocouple could record properly throughout the exposure. More critically, however, this sample showed microscopic evidence of melting in the center half of the radius, or $r \leq \frac{0.75}{4}$ in. Thus, we have the condition needed to begin the calibration process.

We prescribe the transient temperature data from the experiment for Sample 1A as a boundary condition in the simulation and iterate through combinations of θ and $q\Big|_{d=0}$ centered around $\theta = 15°$ and $q\Big|_{d=0} = 35\ \mathrm{MW/m^2}$. Only a few iterations were needed before a calibrated solution was found. A half angle of $\theta = 15°$ and a peak heat flux at the jet outlet of $36\ \mathrm{MW/m^2}$ results in a simulated temperature profile which best fits the experimental outcome. The corresponding calibrated heat flux curves are provided in Fig. 71. The plot shows that the peak heat flux at 1 in. (2.5 cm) from the jet outlet is 19.5 MW/m^2. Similarly, distances of 1.5 in. (3.8 cm) and 2.0 in. (5.1 cm) result in maximum incident heat fluxes of 15.9 and 13.4 MW/m^2, respectively. One can also glean from the figure that the edges of the sample (same as the upper and lower limits of the gray region), receive a significantly lower heat flux than at the center of the plasma torch. In fact, at $d = 1$ in., the reduction is approximately 40%. This is a natural byproduct of the plasma torch outputting an ionized gas that can be modeled as a Gaussian curve in conjunction with the varying extent of beam spreading at different distances from the jet outlet.

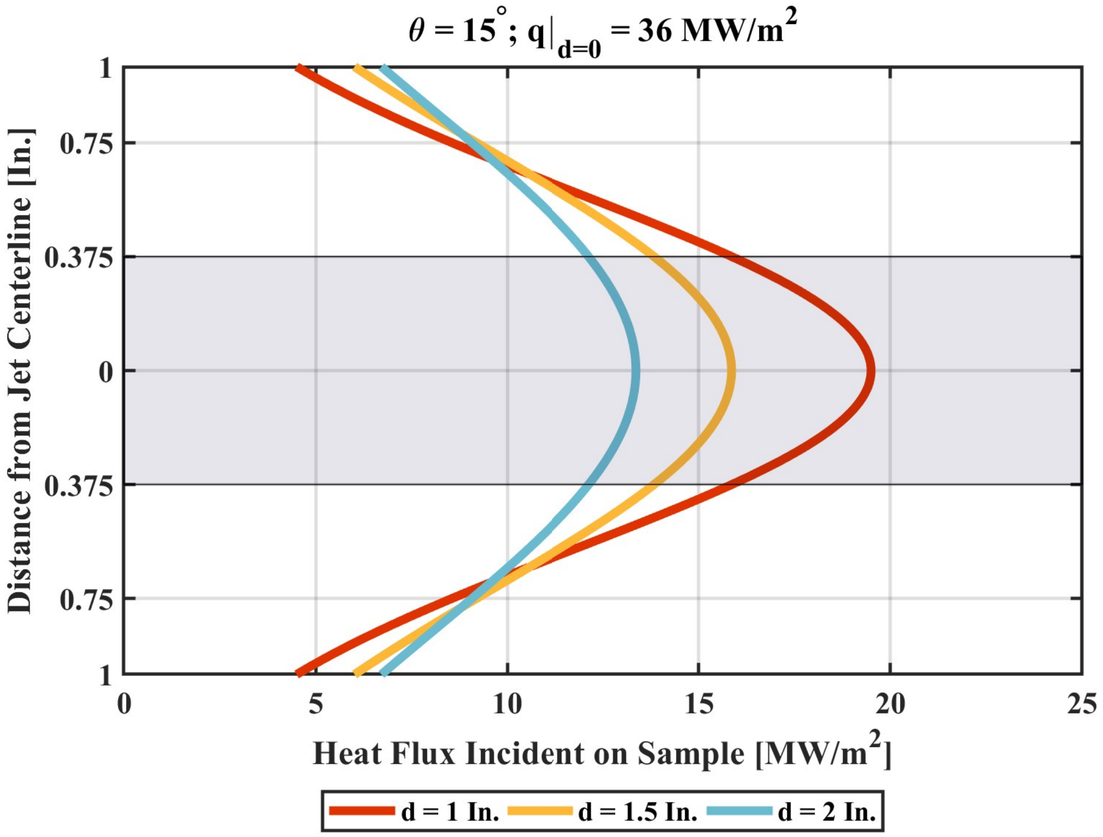

Figure 71: Calibrated heat flux incident on each sample as a function of its distance from the jet outlet and the radial distance from the jet centerline. The gray section represents the LaB$_6$ sample.

The corresponding temperature profile for Sample 1A on the LaB$_6$ specimen and adjacent components is illustrated in Fig. 72. Select times during the 20 s test duration have been included for visualization. It is clear that the specimen heats up more quickly than the surrounding support equipment does. Moreover, the surface of the sample is approximately 2,200 K after 5 s which suggests the average temperature ramp rate is about 400 K/s during this period. Since the experimental Sample 1A had evidence of melting only in the center half of the radius and exhibits no sign of far exceeding the melting point, it is reasonable that the simulation indicates that the test completed just above the melting point in the most central part of the sample only. While each of the five samples has a similar transient temperature progression, their ramp rates and final temperatures are higher since their distances from the jet outlet are less. Even Sample 2B, which has a shorter duration by 5 s, ends its test at a significantly more elevated temperature than Sample 1A.

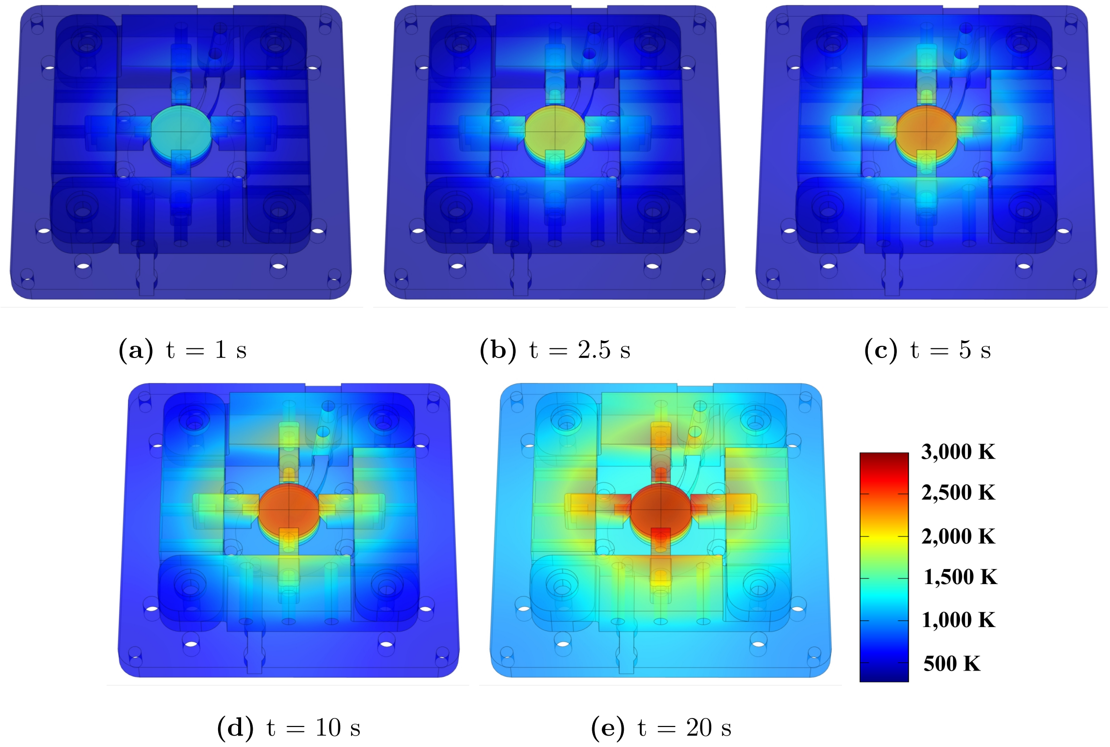

(a) t = 1 s **(b)** t = 2.5 s **(c)** t = 5 s

(d) t = 10 s **(e)** t = 20 s

Figure 72: Transient temperature profile simulation for Sample 1A and sample holder at select times during the exposure.

Delving further into the transient temperature profiles of each sample, there is a clear trend among the samples in the same test series and apparent differences between the Series 1 and Series 2 samples. Figure 73 displays the temperatures as a function of time for each sample at the position on the surface where the incident heat is the greatest. The melting point, T_m, is included to bifurcate the temperatures into those for which the material is solid and those which are molten or vaporized. By inspection, we recognize that the Series 1 samples are vertically oriented in the chart to one another and the Series 2 tests are nearly horizontal to each other. While the test durations chosen for Series 2 are not intended to be overly long such that the temperatures would saturate or become sustained, we did aim for the exposures to well exceed the period of highest ramp rate. The figure clearly shows that after about 6 s, all samples experience a significant reduction in their ramp rate. From the optical images presented earlier, we know that the Series 2 samples all produced a melt pool. It is evident that by quantifying the amount of molten material and relating it to the temperature results in the corresponding model, we can determine the temperature-dependent rate of surface recession and compare it with existing works. A thorough discussion on this topic is provided in Section 6.5.

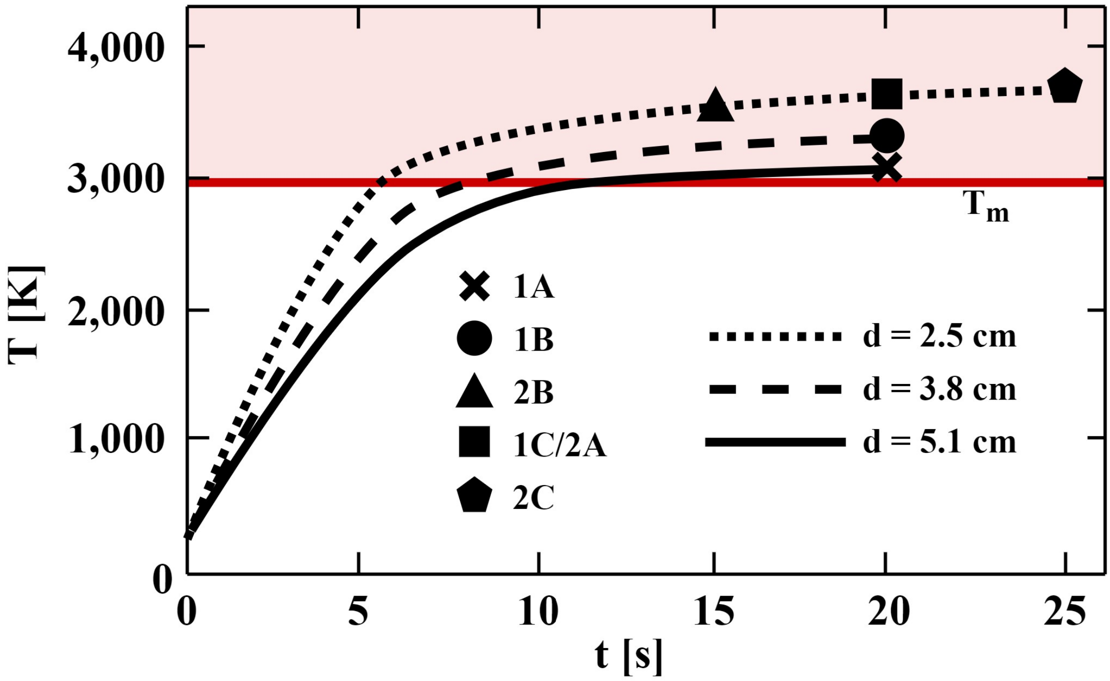

Figure 73: Temperature at top center of each sample as a function of time. $T > T_m$ correspond with molten and vaporized LaB_6.

Figure 74 provides a clear comparison between the final temperature profiles across the surface of each sample. We note that the horizontal scale bar applies for both the line graph and the top view of the LaB_6 surfaces. The samples are arranged left to right in order of least to greatest final temperature. The curves at the top of the figure show the temperatures for each sample along the diameter. This provides another visual of Sample 1A which helped calibrate the heat flux profile in the model. We recall the boundary condition $T = T_m$ for $r = \frac{0.75}{4}$ in. The dashed line indicates the melting point and intersects this threshold at the radial positions of interest. Furthermore, the temperature hovers just above the melting point for $r < \frac{0.75}{4}$ in. which represents the experimental observations well. Since the samples in Series 1 have varying distances from the jet outlet, it is expected that the temperatures across the diameter would vary less at the farthest distance and the most at the shortest distance.

The samples in Series 2, however, are all at the closest distance to the jet outlet. Thus, the radial temperature gradient is nearly the same among Samples 1C/2A, 2B, and 2C. Another commonality among these models is they report temperatures above the the melting point of LaB_6 for all points along the discs' diameter. We also recall that all Series 2 experiments contained a melt pool at the region of highest heat flux. Interestingly, the melt pool contained in the shortest duration Series 2 test, Sample 2B, included a particularly small pool. This suggests that a 15 s exposure at 2.5 cm from the jet provides sufficient energy to cause the onset of a LaB_6 melt pool. Furthermore, we can infer that a significantly shorter duration test at the same distance would not impart adequate energy to erode the surface in this way. Finally, this reveals the minimum temperature required to produce a melt pool. The small, but conspicuous melt pool in Sample 2B developed as the temperature reached about 3,400 K. Further evidence that a temperature of 3,400 K may be a barrier to creating molten LaB_6 is the fact that the widths of the melt pools in Sample 1C/2A and Sample 2C are approximately the widths of the regions which the simulations show as exceeding this threshold.

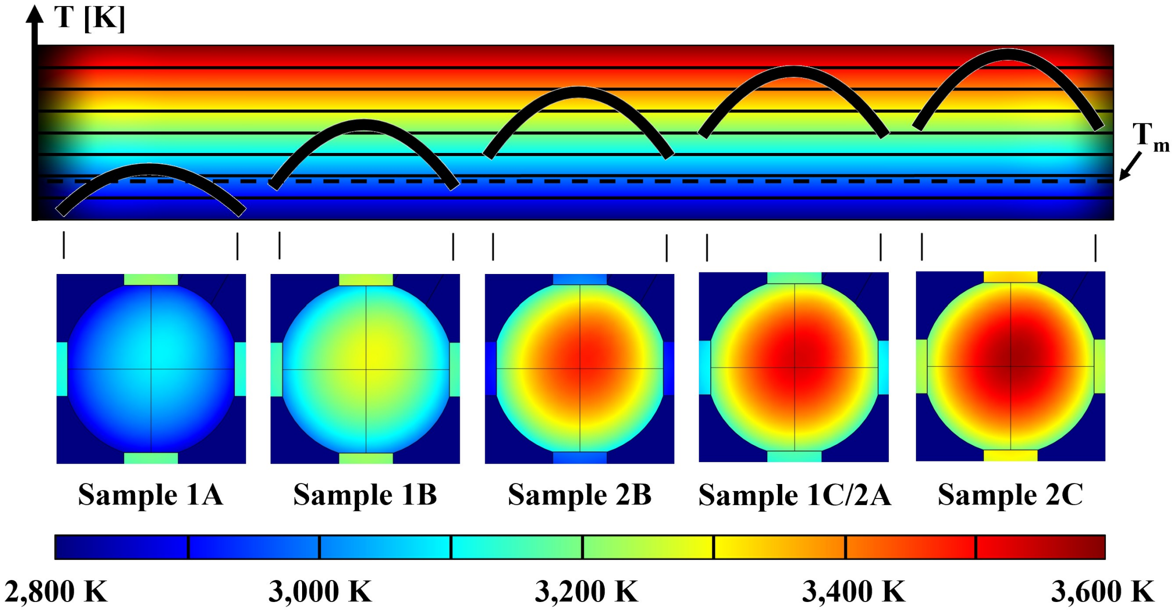

Figure 74: Temperature profile across diameter of top surface for each sample at full duration. Colors in graph correspond with temperatures shown for horizontal scale.

6.5 Data Analysis

By analyzing the melt pool cavity of each sample in Series 2, we can determine the LaB_6 surface recession rate at temperatures above the melting point. Since each specimen in Series 2 endured the same heat flux profile and we obtained spatial-dependent depth data from the optical profilometer (previously shown in Fig. 69), we can readily plot the incident heat flux with relation to the recessed depth and the radial distance from the jet centerline. Since each cavity has non-zero eccentricity at the rim and asymmetric depth for a given radius, we average the depths, Z_n, along the circumference of radii, r_n, for incremental heat fluxes. Most importantly, the two extremes (i.e., the outer edge of the cavity where $r = r_{max}$ and $Z = 0$ and the deepest point where $r = 0$ and $Z = Z_{max}$) are included in these measurements. A schematic of the generalized procedure is provided in Fig. 75. We note that all melted and vaporized material formerly in the cavity is estimated to be fully removed by the pressure impinging on the sample by the arc jet plasma. This assumption is supported by a test sample which was halved after enduring the same conditions. When viewed from the side, the cavity section had an insignificant thickness of remaining solidified material.

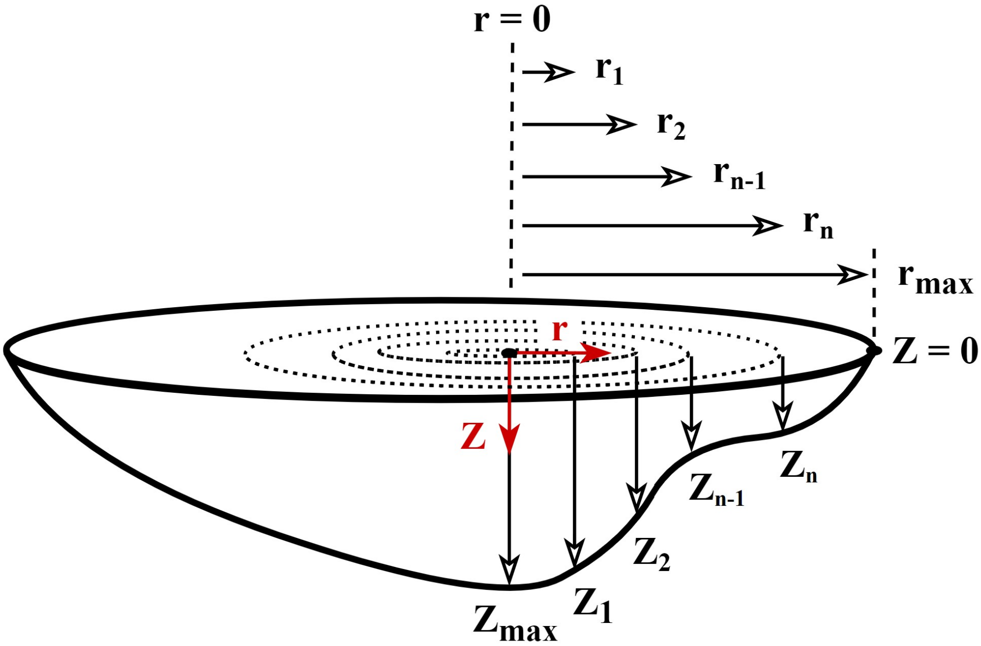

Figure 75: Generalized procedure for determining surface recession depth from optical profilometry data.

It was found that the range of heat fluxes for which the cavities exist is approximately 19 to 19.5 MW/m^2. Depths are calculated in 0.1 MW/m^2 steps as this gives sufficient resolution without overcrowding the graph. This plot which quantifies the surface recession depth results is provided in Fig. 76. The dotted line illustrates the incident heat flux on the sample in the radial range for which a melt pool cavity formed. By inspection, the greatest depths are achieved at the higher heat fluxes. Furthermore, the greatest depth occurs approximately at the point of the highest heat flux. The maximum surface recession depths for Samples 2B, 1C/2A, and 2C are 0.18, 1.02, and 1.29 mm, respectively. Similarly, the lowest heat fluxes where a melt pool developed in these same samples were 19.48, 19.14, and 19.03 MW/m^2.

A logical next step is to study these results with respect to time to estimate the speed at which the material was removed. By plotting the total exposure time for each sample in Series 2 against its maximum depth, Z_{max}, we get a glimpse into how the material's depth changed during the high-severity test. It follows that the slope of each line would be the instantaneous surface recession rate, $\dot{Z}$. These results are provided in Fig. 77. The surface

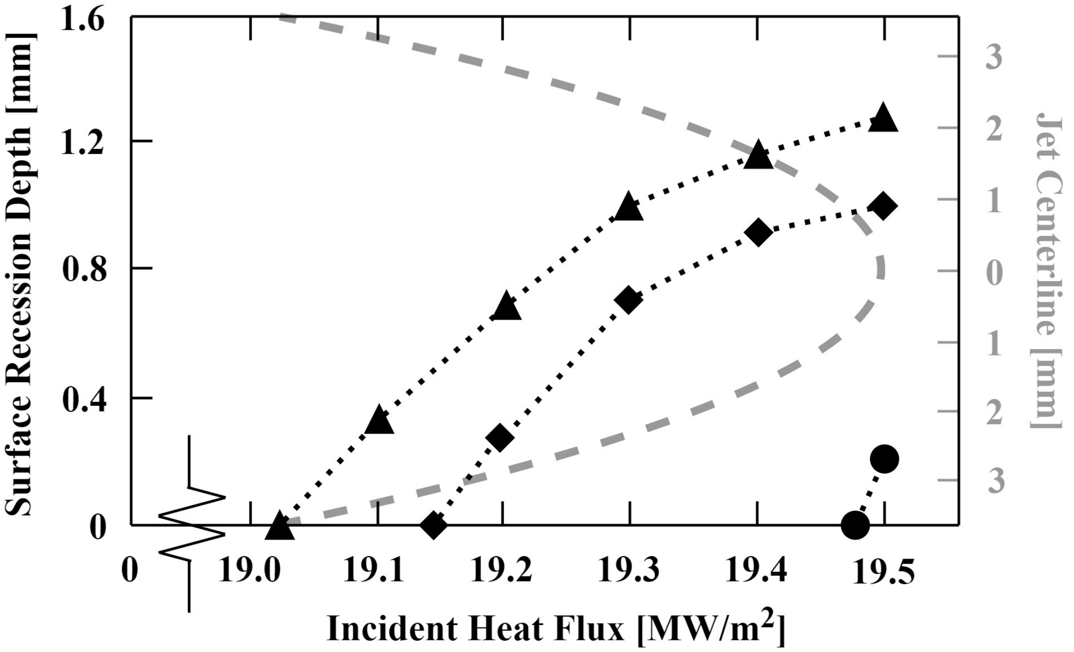

Figure 76: Surface recession depth as a function of heat flux for each sample in Series 2. Corresponding heat flux profile is overlaid for visualization as a dashed line. Sample 2C (▲); Sample 1C/2A (◆); Sample 2B (●).

recession rate between the 15 and 20 s exposure times is found to be 0.17 mm/s whereas the 20 to 25 s segment gives a rate of 0.05 mm/s. The dotted horizontal line displays the mean recession rate, $\dot{Z}_m$, of 0.11 mm/s. The energy fluence is included as the secondary abscissa. We observe that the Series 2 tests ranged from about 300 to 500 MJ/m^2 of energy per unit area. We can also estimate that the energy fluence required to initiate a melt pool is between 200 and 300 MJ/m^2.

While we provided the instantaneous surface recession rates and have shown interpolated recession depth data for LaB$_6$, it is worth discussing theoretically what an extrapolation of the data could look like. For exposure times less than 15 s, it is clear that the small melt pool was previously an incipient melt pool and prior to that a sample which had no such cavity. One of the main considerations is whether the slope of the recession depth line would be shallow, steeper, or roughly the same as the segment from 10 to 15 s. Since an incipient melt pool has the smallest possible surface area, the ionized argon is incident only on the top surface whereas a cratered geometry allows for plasma to directly heat additional surface

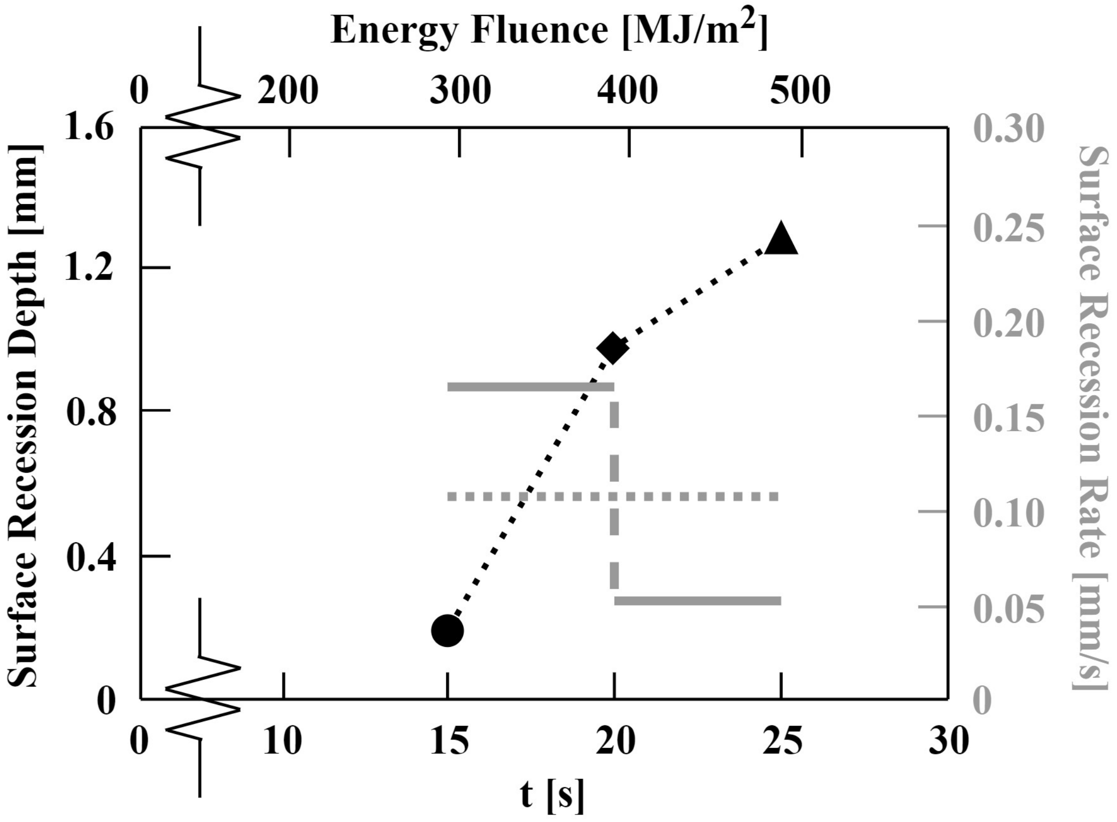

Figure 77: Surface recession depth and recession rate as a function of time. Depth is obtained by measuring the deepest point in each Series 2 sample's cavity. Solid and dashed lines are instantaneous recession rates, $\dot{Z}$, and dotted line is mean recession rate, $\dot{Z}_m$. Sample 2B (●); Sample 1C/2A (◆); Sample 2C (▲).

area. This suggests that the slope should be shallower from the time the melt pool initiates to the measured depth at 15 s. A main opposing argument is the top center of the sample is expected to rise by about 100 K from 10 to 15 s. From this standpoint, there is a greater efficacy for a melt pool to develop at 15 s than at 10 s. Regarding exposure times which exceed 25 s, the percent difference in surface area from one moment to the next would be less significant and the temperatures are nearly saturated by this point. Thus, we would expect the surface recession rate to be nearly constant after about 25 s of exposure.

In the context of previously performed experiments on the surface recession rates of LaB_6, the present work quantifies rates at far higher temperatures than what exists in the literature. This is best illustrated in Fig. 78 which plots data by Storms [154], Davis [155], and Futamoto [156] and connects the present work with a logarithmic regression curve. What results is a smooth and plausible interpolation across a wide range of temperatures. We can glean from the downward concavity that the surface recession rate is subject to diminishing returns. That is, at more elevated temperatures the rate changes by a smaller amount for the same step size. A point of interest in the figure is the melting point. While we expect this region to have local variability due to the latent heat involved in the material undergoing a phase change, the regression curve suggests that the recession rate at the melting point is roughly 0.01 mm/s. Furthermore, a recession rate in excess of 1 mm/s should not be expected for temperatures that do not well exceed 4,000 K.

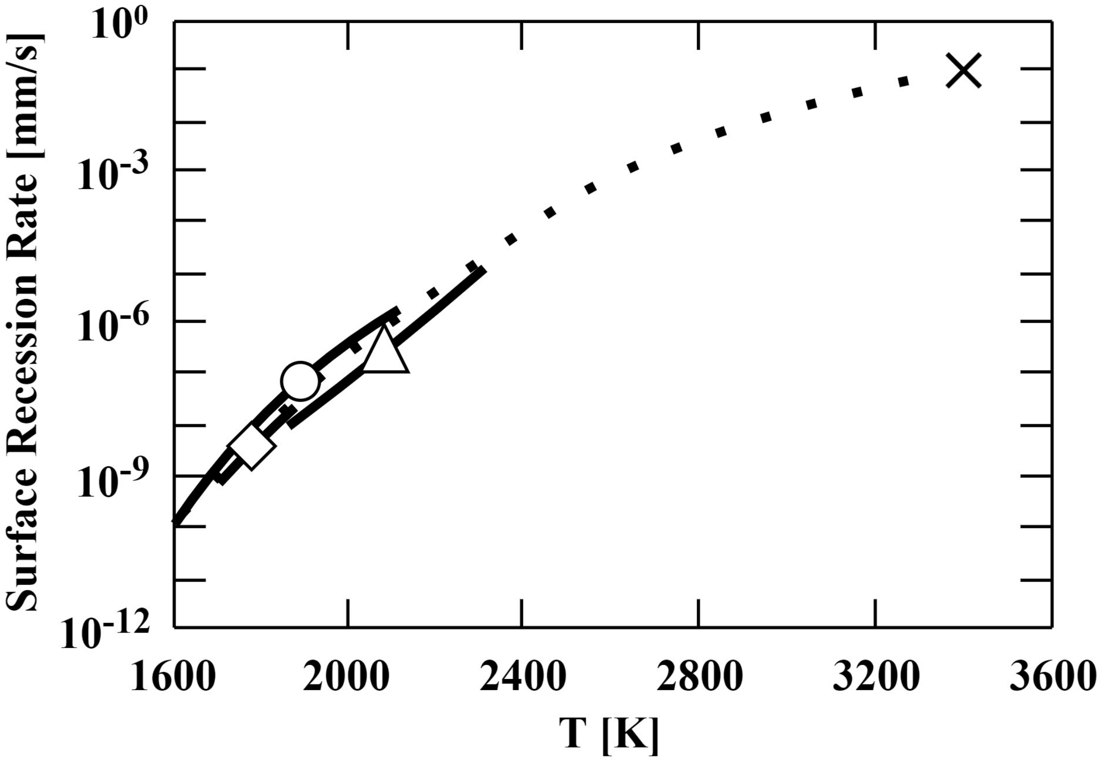

Figure 78: Comparison of surface recession rate data from the present work with previous efforts. Logarithmic regression curve connecting all data shown as dotted line. Davis [155] (◇); Storms [154] (○); Futamoto [156] (△); Present work (×).

6.6 Leading Edge Applications

With our newly found knowledge on the surface recession rate of LaB_6 near to and beyond its melting point, we are able to discuss this material's relevance in the context of hypersonic vehicles and its feasibility as a transpirant. Two of the main criteria for an acceptable transpirant include the ability to remove a significant quantity of heat per unit volume and to maintain a molten consistency during the evaporative process. Other criteria worth mentioning, but are beyond the scope of the present work, account for such design risks as chemical compatibility, viscous drag, and capillary action.

The present work on LaB_6 has shown that while the melting point may be at 2,988 K, the material does not develop a melt pool until approximately 3,400 K. The melt pool is crucial in the context of a transpirant since it is a proxy for a molten material which is capable of flowing. Hypersonic vehicles frequently endure temperatures around 3,000 K, but to maintain operating temperatures in excess of 3,400 K the vehicle would most likely need to be an exceptionally sharp leading edge wedge operating at a high Mach number while simultaneously flying at a low altitude. Thus, LaB_6 would be most appropriate as a transpirant at the highest severity flight conditions. Otherwise, the material would be unlikely to flow. Moreover, the lower temperatures would also be associated with reduced surface recession rates and thus a smaller amount of heat would be removed per unit time.

While the molten phase for LaB_6 phase allows the material to flow, it does provide an additional risk that a sublimating material would otherwise circumvent. A hypersonic leading edge wedge which relies on wicking transpirant to cool the regions with the highest incident heat flux cannot experience an extensive blockage without losing significant functionality. If the temperature in the leading edge falls below an expected operating lower bound, any remaining molten LaB_6 in the passageway would solidify and prevent further wicking. A refractory ceramic which changes phase from a solid to a gas directly, without becoming a liquid first, would be less likely to create such a blockage. A design which frequently clears passageways of remnant LaB_6 would minimize this concern and help enable such refractory ceramics to be feasible options as transpirants in hypersonic leading edges.

6.7 Summary & Conclusions

Lanthanum hexaboride (LaB_6) is a refractory ceramic material that has been previously characterized at temperatures up to approximately 2,300 K, but data relating to surface damage at temperatures in the vicinity of and well exceeding its melting point are incredibly sparse. By performing arc jet experiments on LaB_6 discs in the High Energy Flux Test Facility (HEFTY) as well as corroborating computer simulations of the setup and involving a breadth of material characterization tools, we have come across useful and somewhat controversial results. We summarize the main conclusions of the present study as follows: 1) While LaB_6 melts and vaporizes at nearly the same temperature, the material does not sublimate at the pressures tested. A portion of the relevant literature suggests that LaB_6 changes phase from a solid to a gas directly, but the melt pool cavities presented in the current approach clearly illustrate that the material exhibits a liquid phase. 2) LaB_6 becomes a consistent melt pool if exposed to an energy fluence of at least 200-300 MJ/m^2. This amount of energy per unit area is the lower limit for the creation of melt pool cavities which are entirely molten. 3) A 19.5 MW/m^2 incident heat flux on a LaB_6 surface causes a melt pool cavity to recess at a rate of 0.11 mm/s. Furthermore, for energy fluence magnitudes above about 400 MJ/m^2, the surface recession rate can be estimated as a constant value.

Material characterization pre- and post-exposure suggested that lanthanum borate ($LaBO_3$) was the only oxide which formed and survived in the argon arc jet environment with a significant quantity. We also saw strong agreement between the experimental results and the calibrated simulations. Finally, we provided a short discussion on the feasibility of LaB_6 as a potential transpirant in hypersonic leading edges. It was determined that the material could potentially be feasible in the highest severity hypersonic conditions so long as the wedge region remains above 3,400 K until remnant transpirant is cleared from the passageways. It was already understood that LaB_6 is a highly capable material in the realm of electronics, but now it is apparent that the material could also have success in hypersonics given the right vehicle architectures and operating conditions.

CHAPTER 7

Thesis Conclusions

In this investigation on the fundamentals and applications of aerospace “metamaterials”, the work set out to quantify the impact of reticulated foam geometry on secondary electron yield (SEY), determine the optimal foam porosity distribution to maximize evaporative cooling in a hypersonic leading edge (LE), and characterize and evaluate the effects of an arc jet on a material with hypersonic vehicle design potential. SEY experiments were performed at The Aerospace Corporation on copper and the arc plasma experiments at the High Energy Flux Test Facility (HEFTY) on lanthanum hexaboride (LaB_6). In parallel, ray-tracing Monte Carlo simulations were created to model SEY on reticulated copper and an optimization study was built and run to determine whether an internally porous hypersonic LE could benefit from a non-isotropic distribution of volume fraction foam and to what extent that would improve cooling. Finally, an arsenal of material characterization tools were deployed to capture the macroscopic and microscopic changes in the specimens. These tools helped illustrate how the physical forms of “metamaterials” relate to their functions.

While the fully detailed conclusions for each segment of the dissertation are provided locally in Sections 3.6, 4.6, and 6.7, it is worthwhile to review the conclusions gained from each topic. Our discussion on SEY concluded that a reticulated geometry suppresses secondary electrons significantly. Both the experiments and Monte Carlo simulations agree that porous materials entrap primary electrons. Furthermore, it was found that foams are less sensitive to changes in electron energy than flat surfaces are, especially for $E_0 > E_0\left(\delta_m\right)$. Regarding the study on optimized permeability in a hypersonic LE, we found that higher permeability foams, and thus lower volume fraction ones, allow transpirant to flow with a higher speed. When this transpirant is channeled toward regions with the highest q, the vehicle experiences a greater amount of cooling than if the foam permeability is isotropic. Also, the pore diameter and wettability of the foam/fluid pair is found to greatly influence an LE's ability to wick transpirant without needing to actively pump the molten material. Small d_p and low θ_c allow the vehicle to accelerate faster while only relying on capillary action to accomplish the wicking. We even delved into a potential LE design and modeled the reduction in temperature at the stagnation point with the aid of evaporative transpiration cooling and thermionic emission cooling. When excluding space charge and allowing molten barium oxide transpirant to fully evaporate upon exiting the vehicle, a tungsten foam LE at Mach 8 is about 800 K lower in temperature at the stagnation point than a model with identical parameters except the only cooling mechanism considered is radiative heat transfer. The investigation on the surface damage of LaB_6 showed that the purple refractory ceramic indeed melts for the pressures and temperatures studied rather than sublimates and causes high-energy particles to change from a solid to a vapor directly. Also, the minimum energy fluence required for LaB_6 to become molten was found to be 200-300 MJ/m^2.

Finally, we can use our new perspective to present the global conclusions for the thesis. These overarching conclusions are as follows:

1. 4.6% volume fraction (VF) copper foam suppresses secondary electron yield (SEY) by approximately 20%. Furthermore, the SEY suppression is found to be inversely proportional to foam volume fraction. That is, SEY suppression $\propto \frac{1}{VF}$.
2. Optimizing permeability in a hypersonic LE wedge results in a 6% increase in cooling effectiveness over the isotropic permeability case by focusing transpirant on regions with the highest incident heat flux, q. This can also be written as $VF \propto \frac{1}{q}$.
3. Arc jet plasma environments with an incident heat flux, q, of 19.5 MW/m^2 cause LaB_6 to exhibit a surface recession rate, $\dot{Z}$, of 0.11 mm/s. Also, $\dot{Z}$ is determined to be nearly constant for energy fluence magnitudes exceeding about 400 MJ/m^2.

Together, these three results neatly summarize the body of work presented in this dissertation.

REFERENCES

[1] Gurwinder Singh and Anupma Marwaha. A Review of Metamaterials and its Applications. 2015.

[2] Michael F. Ashby, Tony Evans, N. A. Fleck, J. W. Hutchinson, H. N. G. Wadley, and L. J. Gibson. *Metal Foams: A Design Guide.* Elsevier, July 2000. Google-Books-ID: C0daIBo6LjgC.

[3] Experimental Investigation of Hydrodynamics in SiSiC Foam Packed Reactors - Helmholtz-Zentrum Dresden-Rossendorf, HZDR.

[4] Jason Dawes, Robert Bowerman, and Ross Trepleton. Introduction to the Additive Manufacturing Powder Metallurgy Supply Chain. *Johnson Matthey Technology Review*, 59(3):243–256, July 2015.

[5] John B. Hudson. *Surface Science: An Introduction.* John Wiley & Sons, March 1998.

[6] Raseong Kim, Changwook Jeong, and Mark S. Lundstrom. On Momentum Conservation and Thermionic Emission Cooling. *Journal of Applied Physics*, 107(5):054502, March 2010.

[7] Florent Houdellier, Aurélien Masseboeuf, Marc Monthioux, and Martin J. Hÿtch. New Carbon Cone Nanotip for Use in a Highly Coherent Cold Field Emission Electron Microscope. *Carbon*, 50(5):2037–2044, April 2012.

[8] Jai Singh. *Organic Light Emitting Devices.* BoD – Books on Demand, November 2012.

[9] K. L. Jensen. Improved Fowler–Nordheim Equation for Field Emission from Semiconductors. *Journal of Vacuum Science & Technology B: Microelectronics and Nanometer Structures Processing, Measurement, and Phenomena*, 13(2):516–521, March 1995. Publisher: American Institute of Physics.

[10] Otto Buck and William J. Pardee. Mechanistic Basis for Exo-Electron Spectroscopy. In *Electron and Positron Spectroscopies in Materials Science and Engineering*, Materials Science and Technology. Academic Press.

[11] Different Types of SEM Imaging – BSE and Secondary Electron Imaging, August 2017. Section: Materials Article.

[12] Minoru Iwata, Arifur R. Khan, Hideyuki Igawa, Kazuhiro Toyoda, Mengu Cho, and Tatsuhito Fujita. Development of Electron-Emitting Film for Spacecraft Charging Mitigation. *Journal of Spacecraft and Rockets*, 49(3):546–552, May 2012.

[13] Aerospaceweb.org | Hypersonic Waveriders - Flow Characteristics. http://www.aerospaceweb.org/design/waverider/flow.shtml.

[14] Andrew J. Lofthouse, Iain D. Boyd, and Michael J. Wright. Effects of Continuum Breakdown on Hypersonic Aerothermodynamics. *Physics of Fluids*, 19(2):027105, February 2007. Publisher: American Institute of Physics.

[15] Swarajya Staff. DRDO Tests Made In India Hypersonic Technology Capable Of Reaching Mach 6 Speed Via Scram-Jet Engine.

[16] John Antczak and Associated Press. DARPA Releases Video of HTV-2 Hypersonic Glider Flight.

[17] Orion – Spacecraft & Satellites. https://spaceflight101.com/spacecraft/orion/.

[18] Michael J. Wright, Chun Y. Tang, Karl T. Edquist, Brian R. Hollis, and Paul Krasa. A Review of Aerothermal Modeling for Mars Entry Missions. Orlando, FL, December 2009. NTRS Author Affiliations: NASA Ames Research Center, NASA Langley Research Center NTRS Report/Patent Number: ARC-E-DAA-TN1069 NTRS Document ID: 20100021401 NTRS Research Center: Ames Research Center (ARC).

[19] Kevin Dirscherl, Michael Riechers, and Jonathan Sanders. Hypersonic Speed Through Scramjet Technology. page 12.

[20] Oriana Pawlyk. Air Force Doubles Down on Hypersonic Weapons Development with 2nd Contract, August 2018. Section: Defense Tech.

[21] Hans Pettersson. Cosmic Spherules And Meteoric Dust. *Scientific American*, 202(2):123–135, 1960. Publisher: Scientific American, a division of Nature America, Inc.

[22] Lilith Grassi, Francesca Tiboldo, Roberto Destefanis, Thérèse Donath, Arne Winterboer, Leanne Evans, Rolf Janovsky, Scott Kempf, Martin Rudolph, Frank Schäfer, et al. Satellite Vulnerability to Space Debris–an Improved 3D Risk Assessment Methodology. *Acta Astronautica*, 99:283–291, 2014.

[23] C. R. Francis. Electrostatic Charging Problems of Spacecraft. *Journal of Electrostatics*, 11(3):265–280, February 1982.

[24] John Linsley. Evidence for a Primary Cosmic-Ray Particle with Energy 10^{20} eV. *Physical Review Letters*, 10(4):146, 1963.

[25] MA Lawrence, RJO Reid, and AA Watson. The Cosmic Ray Energy Spectrum Above $4*10^{17}$ eV as Measured by the Haverah Park Array. *Journal of Physics G: nuclear and particle physics*, 17(5):733, 1991.

[26] Richard A. Kerr. Radiation Will Make Astronauts' Trip to Mars Even Riskier. *Science*, 340(6136):1031–1031, May 2013. Publisher: American Association for the Advancement of Science.

[27] David G Fearn. The Ultimate Performance of Gridded Ion Thrusters for Interstellar Missions. *AIP Conference Proceedings*, 504(1):941–946, January 2000. Publisher: American Institute of Physics.

[28] Scott J. Hall, Benjamin A. Jorns, Sarah E. Cusson, Alec D. Gallimore, Hani Kamhawi, Peter Y. Peterson, Thomas W. Haag, Jonathan A. Mackey, Matthew J. Baird, and James H. Gilland. Performance and High-Speed Characterization of a 100-kW Nested Hall Thruster. *Journal of Propulsion and Power*, 38(1):40–50, 2022. Publisher: American Institute of Aeronautics and Astronautics, https://doi.org/10.2514/1.B38080.

[29] Käthe Dannenmayer and Stéphane Mazouffre. Elementary Scaling Relations for Hall Effect Thrusters. *Journal of Propulsion and Power*, 27(1):236–245, January 2011.

[30] M. Auweter-Kurtz, B. Glocker, T. Golz, H. L. Kurtz, E. W. Messerschmid, M. Riehle, and D. M. Zube. Arcjet Thruster Development. *Journal of Propulsion and Power*, 12(6):1077–1083, November 1996.

[31] H. Eichhorn, K. H. Schoenbach, and T. Tessnow. Paschen's Law for a Hollow Cathode Discharge. *Applied Physics Letters*, 63(18):2481–2483, November 1993. Publisher: American Institute of Physics.

[32] Pierre-Yves Camille Regis Taunay. *Scaling Laws in Orificed Thermionic Hollow Cathodes.* Ph.D., Princeton University, United States – New Jersey. ISBN: 9798684653674.

[33] A Ottaviano, GZ Li, CE Huerta, A Thuppul, Z Chen, CA Dodson, and RE Wirz. Plasma-Material Interactions for Electric Propulsion: Challenges, Approaches and Future. In *The 36th International Electric Propulsion Conference, Austria*, 2019.

[34] N. M. Uchizono, A. L. Collins, C. Marrese-Reading, S. M. Arestie, J. K. Ziemer, and R. E. Wirz. The role of Secondary Species Emission in Vacuum Facility Effects for Electrospray Thrusters. *Journal of Applied Physics*, 130(14):143301, October 2021.

[35] Scott Kasen. *Thermal Management at Hypersonic Leading Edges.* PhD thesis, University of Virginia, April 2013.

[36] Saul Dushman. Thermionic Emission. *Reviews of Modern Physics*, 2(4):381–476, October 1930. Publisher: American Physical Society.

[37] Shigehiko Yamamoto, Kenzo Susa, and Ushio Kawabe. Work Functions of Binary Compounds. *The Journal of Chemical Physics*, 60(10):4076–4080, May 1974.

[38] Bernhard Wolf. *Handbook of Ion Sources.* CRC Press, August 1995. Google-Books-ID: qoQHMSBNFsAC.

[39] Kyle M. Hanquist and Iain D. Boyd. Plasma Assisted Cooling of Hot Surfaces on Hypersonic Vehicles. *Frontiers in Physics*, 7, 2019.

[40] Mehul Bambhania. *CFD Analysis for Laplace Pressure Drop in Vertical Y-Junction Mini-Channel with Gasliquid Flow.* October 2015.

[41] T. Koshikawa and R. Shimizu. Secondary Electron and Backscattering Measurements for Polycrystalline Copper With a Spherical Retarding-Field Analyser. *Journal of Physics D: Applied Physics*, 6(11):1369–1380, July 1973. Publisher: IOP Publishing.

[42] A. Shih and C. Hor. Secondary Emission Properties as a Function of the Electron Incidence Angle. *IEEE Transactions on Electron Devices*, 40(4):824–829, April 1993.

[43] J. J Scholtz, D Dijkkamp, and R. W. A Schmitz. Secondary Electron Emission Properties. *Philips Journal of Research*, 50(3):375–389, January 1996.

[44] R. E. Davies and J. R. Dennison. Evolution of Secondary Electron Emission Characteristics of Spacecraft Surfaces. *Journal of Spacecraft and Rockets*, 34(4):571–574, July 1997.

[45] M. A. Furman and M. T. F. Pivi. Probabilistic Model for the Simulation of Secondary Electron Emission. *Physical Review Special Topics - Accelerators and Beams*, 5(12):124404, December 2002.

[46] Charles Swanson and Igor D. Kaganovich. Modeling of Reduced Secondary Electron Emission Yield From a Foam or Fuzz Surface. *Journal of Applied Physics*, 123(2):023302, January 2018.

[47] L. Austin and H. Starke. Ueber die Reflexion der Kathodenstrahlen und Eine Damit Verbundene Neue Erscheinung Secundarer Emission. *Annalen der Physik*, 314(10):271–292, 1902.

[48] N. Balcon, D. Payan, M. Belhaj, T. Tondu, and V. Inguimbert. Secondary Electron Emission on Space Materials: Evaluation of the Total Secondary Electron Yield From Surface Potential Measurements. *IEEE Transactions on Plasma Science*, 40(2):282–290, February 2012.

[49] T. J. Vink, A. R. Balkenende, R. G. F. A. Verbeek, H. a. M. van Hal, and S. T. de Zwart. Materials With a High Secondary-Electron Yield for use in Plasma Displays. *Applied Physics Letters*, 80(12):2216–2218, March 2002.

[50] Chenggang Jin, Angelica Ottaviano, and Yevgeny Raitses. Secondary Electron Emission Yield From High Aspect Ratio Carbon Velvet Surfaces. *Journal of Applied Physics*, 122(17):173301, November 2017.

[51] P. M. Shikhaliev. Mechanism of Field-Enhanced Self-Sustaining Secondary Electron Emission in Porous Dielectrics. *Technical Physics Letters*, 24(10):752–754, October 1998.

[52] Charles Swanson and Igor D. Kaganovich. Modeling of Reduced Effective Secondary Electron Emission Yield From a Velvet Surface. *Journal of Applied Physics*, 120(21):213302, December 2016.

[53] C. Li, S. F. Mao, and Z. J. Ding. Time-Dependent Characteristics of Secondary Electron Emission. *Journal of Applied Physics*, 125(2):024902, January 2019.

[54] T Koshikawa and R Shimizu. A Monte Carlo Calculation of Low-Energy Secondary Electron Emission From Metals. *Journal of Physics D: Applied Physics*, 7(9):1303–1315, June 1974.

[55] M Baltruschat and H Starke. Über Sekundäre Kathodenstrahlung. *Physikalische Zeitschrift*, 23:403, 1922.

[56] H. E. Farnsworth. Energy Distribution of Secondary Electrons From Copper, Iron, Nickel and Silver. *Physical Review*, 31(3):405, 1928.

[57] Carl Tingwaldt. Über den Einfluß der Entgasung Einer von Kathodenstrahlen Getroffenen Metallplatte auf die Ausgelöste Elektronenstrahlung. *Zeitschrift für Physik*, 34(1):280–284, 1925.

[58] R. E. Davies and J. R. Dennison. Evolution of Secondary Electron Emission Characteristics of Spacecraft Surfaces. *Journal of Spacecraft and Rockets*, May 2012.

[59] M Pivi, F. K. King, R. E. Kirby, T. O. Raubenheimer, G Stupakov, and F Le Pimpec. Sharp Reduction of the Secondary Electron Emission Yield From Grooved Surfaces. *Journal of Applied Physics*, 104(10):104904, 2008.

[60] M. Ye, Y. N. He, S. G. Hu, R. Wang, T. C. Hu, J. Yang, and W. Z. Cui. Suppression of Secondary Electron Yield by Micro-Porous Array Structure. *Journal of Applied Physics*, 113(7):074904, February 2013.

[61] M. Patino, Y. Raitses, and R. Wirz. Secondary Electron Emission From Plasma-Generated Nanostructured Tungsten Fuzz. *Applied Physics Letters*, 109(20):201602, November 2016. Publisher: American Institute of Physics.

[62] C. E. Huerta, M. I. Patino, and R. E. Wirz. Secondary Electron Emission From Textured Surfaces. *Journal of Physics D: Applied Physics*, 51(14):145202, April 2018.

[63] N. Bundaleski, M. Belhaj, T. Gineste, and O. M. N. D. Teodoro. Calculation of the Angular Dependence of the Total Electron Yield. *Vacuum*, 122:255 – 259, 2015.

[64] Andrew Alvarado, Hsing-Yin Chang, Warren Nadvornick, Nasr Ghoniem, and Jaime Marian. Monte carlo Raytracing Method for Calculating Secondary Electron Emission From Micro-Architected Surfaces. *Applied Surface Science*, 478:142–149, 2019.

[65] Hsing-Yin Chang, Andrew Alvarado, Trey Weber, and Jaime Marian. Monte Carlo Modeling of Low-Energy Electron-Induced Secondary Electron Emission Yields in Micro-Architected Boron Nitride Surfaces. February 2019.

[66] E. M. Baroody. A Theory of Secondary Electron Emission from Metals. *Physical Review*, 78(6):780–787, June 1950.

[67] A. E. Kadyschewitsch. Theorie der Sekundärelektronenemission aus Metallen. *Journal of Physics-USSR*, 2:115–129, 1940.

[68] H Bruining. Secondary Electron Emission: Part II. Absorption of Secondary Electrons. *Physica*, 5(10):901–912, 1938.

[69] Robert G. Lye and A. J. Dekker. Theory of Secondary Emission. *Physical Review*, 107(4):977–981, August 1957.

[70] Hsing-Yin Chang, Andrew Alvarado, and Jaime Marian. Calculation of Secondary Electron Emission Yields From Low-Energy Electron Deposition in Tungsten Surfaces. *Applied Surface Science*, 450:190–199, 2018.

[71] Nevill Francis Mott. The Scattering of Fast Electrons by Atomic Nuclei. *Proceedings of the Royal Society of London. Series A, Containing Papers of a Mathematical and Physical Character*, 124(794):425–442, 1929.

[72] Cedric J. Powell, Aleksander Jablonski, Francesc Salvat, and Angela Y. Lee. NIST Electron Elastic-Scattering Cross-Section Database, Version 4.0. Technical Report NIST NSRDS 64, National Institute of Standards and Technology, September 2016.

[73] R. H. Ritchie and A Howie. Electron Excitation and the Optical Potential in Electron Microscopy. *Philosophical Magazine*, 36(2):463–481, 1977.

[74] P. Prieto, C. Quiros, E. Elizalde, and J. M. Sanz. Electron Inelastic Mean Free Path and Dielectric Properties of a-Boron, a-Carbon, and Their Nitrides as Determined by Quantitative Analysis of Reflection Electron Energy Loss Spectroscopy. *Journal of Vacuum Science & Technology A*, 24(3):396–407, April 2006.

[75] Yang Sun, Huan Xu, Bo Da, Shi-feng Mao, and Ze-jun Ding. Calculations of Energy-Loss Function for 26 Materials. *Chinese Journal of Chemical Physics*, 29(6):663–670, December 2016.

[76] J. C. Ashley. Interaction of Low-Energy Electrons With Condensed Matter: Stopping Powers and Inelastic Mean Free Paths From Optical Data. *Journal of Electron Spectroscopy and Related Phenomena*, 46(1):199–214, January 1988.

[77] R. K. Islamgaliev, K. Pekala, M. Pekala, and R. Z. Valiev. The Determination of the Grain Boundary Width of Ultrafine Grained Copper and Nickel from Electrical Resistivity Measurements. *physica status solidi (a)*, 162(2):559–566, 1997.

[78] V. Baglin, G. Vorlaufer, Noël Hilleret, I. Collins, and Bernard Henrist. A Summary of Main Experimental Results Concerning the Secondary Electron Emission of Copper, August 2001.

[79] Meng Cao, Xiu-Sheng Zhang, Wei-Hua Liu, Hong-Guang Wang, and Yong-Dong Li. Secondary Electron Emission of Graphene-Coated Copper. *Diamond and Related Materials*, 73:199–203, March 2017.

[80] Hai-Bo Zhang, Xiao-Chuan Hu, Rui Wang, Meng Cao, Na Zhang, and Wan-Zhao Cui. Note: Measuring Effects of Ar-Ion Cleaning on the Secondary Electron Yield of Copper Due to Electron Impact. *Review of Scientific Instruments*, 83(6):066105, June 2012.

[81] J. J. Scholtz and Roger A. Schmitz. Secondary Electron Emission Properties by J.J. Scholtz, D. Dijkkamp and R.W.A. Schmitz. 2003.

[82] Robert L Kosson and Herbert J Schneider. Injection-Cooled Hypersonic Leading Edge Construction and Method, April 5 1994. US Patent 5,299,762.

[83] Hao Su, Jianhua Wang, Fei He, Liang Chen, and Bangcheng Ai. Numerical Investigation on Transpiration Cooling With Coolant Phase Change Under Hypersonic Conditions. *International Journal of Heat and Mass Transfer*, 129:480–490, 2019.

[84] A. Brune, S. Hosder, S. Gulli, and L. Maddalena. Variable Transpiration Cooling Effectiveness in Laminar and Turbulent Flows for Hypersonic Vehicles. *AIAA Journal*, 53(1):176–189, 2015. Publisher: American Institute of Aeronautics and Astronautics: https://doi.org/10.2514/1.J053053.

[85] Robert L Brown, Kaushik Das, Paul G. A. Cizmas, and John D Whitcomb. Numerical Investigation of Actively Cooled Structures in Hypersonic Flow. *Journal of Aircraft*, 51(5):1522–1531, 2014.

[86] Hicham Alkandry, Kyle Hanquist, and Iain D Boyd. Conceptual Analysis of Electron Transpiration Cooling for the Leading Edges of Hypersonic Vehicles. In *11th AIAA/ASME Joint Thermophysics and Heat Transfer Conference*, page 2674, 2014.

[87] Simon Drieschner, Michael Weber, Jörg Wohlketzetter, Josua Vieten, Evangelos Makrygiannis, Benno M. Blaschke, Vittorio Morandi, Luigi Colombo, Francesco Bonaccorso, and Jose A. Garrido. High Surface Area Graphene Foams by Chemical Vapor Deposition. *2D Materials*, 3(4):045013, October 2016. Publisher: IOP Publishing.

[88] Ali Gülhan, Sebastian Willems, and Dominik Neeb. Shock Interaction Induced Heat Flux Augmentation in Hypersonic Flows. *Experiments in Fluids*, 62(12):242, November 2021.

[89] Shen Du, Tian Xia, Ya-Ling He, Zeng-Yao Li, Dong Li, and Xiang-Qian Xie. Experiment and Optimization Study on the Radial Graded Porous Volumetric Solar Receiver Matching Non-Uniform Solar Flux Distribution. *Applied Energy*, 275:115343, October 2020.

[90] Zhiyong Li, Tingting Tang, Yu Liu, Elias J. G. Arcondoulis, and Yannian Yang. Numerical Study of Aerodynamic and Aeroacoustic Characteristics of Flow Over Porous Coated Cylinders: Effects of Porous Properties. *Aerospace Science and Technology*, 105:106042, October 2020.

[91] Stephen Whitaker. Flow in Porous Media I: A Theoretical Derivation of Darcy's Law. *Transport in Porous Media*, 1(1):3–25, 1986.

[92] Yakov Pachepsky, Dennis Timlin, and Walter Rawls. Generalized Richards' Equation to Simulate Water Transport in Unsaturated Soils. *Journal of Hydrology*, 272(1-4):3–13, 2003.

[93] L Durlofsky and J. F. Brady. Analysis of the Brinkman Equation as a Model for Flow in Porous Media. *The Physics of Fluids*, 30(11):3329–3341, 1987.

[94] Craig A. Steeves, Ming Y. He, Scott D. Kasen, Lorenzo Valdevit, Haydn N. G. Wadley, and Anthony G. Evans. Feasibility of Metallic Structural Heat Pipes as Sharp Leading Edges for Hypersonic Vehicles. *Journal of Applied Mechanics*, 76(3), May 2009. Publisher: American Society of Mechanical Engineers Digital Collection.

[95] Scott D. Kasen, Doug T. Queheillalt, Craig A. Steeves, Anthony G. Evans, and Haydn N. G. Wadley. A Heat Plate Leading Edge for Hypersonic Vehicles. pages 175–181. American Society of Mechanical Engineers Digital Collection, August 2009.

[96] M. Yakushin, I. Pershin, and Anatoly Kolesnikov. An Experimental Study of Stagnation Point Heat Transfer from High-Enthalpy Reacting Gas Flow to Surface with Catalysis and Gas Injection. *European Space Agency-Publications*, 487:473–480, January 2002.

[97] Benjamin Meyer, H. F. Nelson, and David W. Riggins. Hypersonic Drag and Heat-Transfer Reduction Using a Forward-Facing Jet. *Journal of Aircraft*, 38(4):680–686, July 2001.

[98] Arnold van Foreest, Martin Sippel, Ali Gülhan, Burkard Esser, B. A. C. Ambrosius, and K. Sudmeijer. Transpiration Cooling Using Liquid Water. *Journal of Thermophysics and Heat Transfer*, 23(4):693–702, October 2009.

[99] S. Gulli, L. Maddalena, and S. Hosder. Variable Transpiration Cooling for the Thermal Management of Reusable Hypersonic Vehicles. *Aerospace Science and Technology*, 29(1):434–444, August 2013.

[100] Christian Dittert, Markus Selzer, and Hannah Böhrk. Flowfield and Pressure Decay Analysis of Porous Cones. *AIAA Journal*, 55(3):874–882, 2017. Publisher: American Institute of Aeronautics and Astronautics: https://doi.org/10.2514/1.J055298.

[101] Daniel Prokein, Christian Dittert, Hannah Böhrk, and Jens von Wolfersdorf. Numerical Simulation of Transpiration Cooling Experiments in Supersonic Flow Using OpenFOAM. *CEAS Space Journal*, 12(2):247–265, June 2020.

[102] Zheng Min, Gan Huang, Sarwesh Narayan Parbat, Li Yang, and Minking K. Chyu. Experimental Investigation on Additively Manufactured Transpiration and Film Cooling Structures. *Journal of Turbomachinery*, 141(3), March 2019. Publisher: American Society of Mechanical Engineers Digital Collection.

[103] Scott D. Kasen and Haydn N. G. Wadley. Heat Pipe Thermal Management at Hypersonic Vehicle Leading Edges: A Low-Temperature Model Study. *Journal of Thermal Science and Engineering Applications*, 11(6), December 2019. Publisher: American Society of Mechanical Engineers Digital Collection.

[104] Simone Di Giorgio, Domenico Quagliarella, Giuseppe Pezzella, and Sergio Pirozzoli. An Aerothermodynamic Design Optimization Framework for Hypersonic Vehicles. *Aerospace Science and Technology*, 84:339–347, January 2019.

[105] Fei He, Nan Wu, Fangyuan Ran, and Jianhua Wang. Numerical Investigation on the Transpiration Cooling of Three-Dimensional Hypersonic Inlet. *Aerospace Science and Technology*, 106:106152, November 2020.

[106] Xinhai Zhao, Shihe Yi, and Feng Zhang. Experimental Study on the Cooling Film Effectiveness of a Hypersonic Blunt Body. *Journal of Thermophysics and Heat Transfer*, 35(3):623–626, 2021. Publisher: American Institute of Aeronautics and Astronautics, https://doi.org/10.2514/1.T6194.

[107] Christopher Seager and Ramesh K. Agarwal. Hypersonic Blunt-Body Shape Optimization for Reducing Drag and Heat Transfer. *Journal of Thermophysics and Heat Transfer*, 31(1):48–55, 2017. Publisher: American Institute of Aeronautics and Astronautics: https://doi.org/10.2514/1.T4650.

[108] W. Schuyler Hinman, Craig T. Johansen, and Patrick E. Rodi. Optimization and Analysis of Hypersonic Leading Edge Geometries. *Aerospace Science and Technology*, 70:549–558, November 2017.

[109] Jie Huang and Wei-Xing Yao. Multi-Objective Design Optimization of Blunt Body With Spike and Aerodisk in Hypersonic Flow. *Aerospace Science and Technology*, 93:105122, October 2019.

[110] Shengjun Ju, Zhenxu Sun, Guowei Yang, Prasert Prapamonthon, and Junyuan Zhang. Multi-Objective Design Optimization of the Combinational Configuration of the Upstream Energy Deposition and Opposing Jet for Drag Reduction in Supersonic Flows. *Aerospace Science and Technology*, 105:105941, October 2020.

[111] Di Zhou, Zhiliang Lu, Tongqing Guo, Ennan Shen, Jiangpeng Wu, and Guoping Chen. Fluid-thermal Modeling of Hypersonic Vehicles Via a Gas-Kinetic BGK Scheme-Based Integrated Algorithm. *Aerospace Science and Technology*, 99:105748, April 2020.

[112] Jian-Jun Gou, Zheng-Wei Yan, Jia-Xin Hu, Ge Gao, and Chun-Lin Gong. The Heat Dissipation, Transport and Reuse Management for Hypersonic Vehicles Based on Regenerative Cooling and Thermoelectric Conversion. *Aerospace Science and Technology*, 108:106373, January 2021.

[113] Michael E. Holloway, Kyle M. Hanquist, and Iain D. Boyd. Assessment of Thermochemistry Modeling for Hypersonic Flow over a Double Cone. *Journal of Thermophysics and Heat Transfer*, 34(3):538–547, 2020. Publisher: American Institute of Aeronautics and Astronautics, https://doi.org/10.2514/1.T5792.

[114] Oğuz K. Onay and Sinan Eyi. Ablation Analyses of Optimized Nose Tips for Hypersonic Vehicles. *Journal of Thermophysics and Heat Transfer*, 34(1):78–89, 2020. Publisher: American Institute of Aeronautics and Astronautics, https://doi.org/10.2514/1.T5644.

[115] Sinan Eyi, Kyle M. Hanquist, and Iain D. Boyd. Aerothermodynamic Design Optimization of Hypersonic Vehicles. *Journal of Thermophysics and Heat Transfer*,

33(2):392–406, 2019. Publisher: American Institute of Aeronautics and Astronautics, https://doi.org/10.2514/1.T5523.

[116] Yazhong Jiang, Zhenxun Gao, Chongwen Jiang, and Chun-Hian Lee. Hypersonic Aeroheating Characteristics of Leading Edges with Different Nose Radii. *Journal of Thermophysics and Heat Transfer*, 31(3):538–548, 2017. Publisher: American Institute of Aeronautics and Astronautics, https://doi.org/10.2514/1.T4950.

[117] Lin Shen and Jianhua Wang. Numerical Investigation on the Optimization of Local Transpiration Cooling Effectiveness. *Applied Thermal Engineering*, 127:58–69, December 2017.

[118] J. Grzelak, P. Doerffer, and T. Lewandowski. The Efficiency of Transpiration Flow Through Perforated Plate. *Aerospace Science and Technology*, 110:106494, March 2021.

[119] Tobias Hermann, Matthew McGilvray, Hassan Saad Ifti, Fabian Hufgard, and Stefan Löhle. Thermal Impulse Response in Porous Media for Transpiration-Cooling Systems. *Journal of Thermophysics and Heat Transfer*, 34(2):447–456, 2020. Publisher: American Institute of Aeronautics and Astronautics, https://doi.org/10.2514/1.T5841.

[120] Lin Shen, Jianhua Wang, Wenjie Dong, Jian Pu, Jinlong Peng, Dejun Qu, and Lianzhong Chen. An Experimental Investigation on Transpiration Cooling With Phase Change Under Supersonic Condition. *Applied Thermal Engineering*, 105:549–556, July 2016.

[121] Gan Huang, Zhiyuan Liao, Ruina Xu, Yinhai Zhu, and Pei-Xue Jiang. Self-Pumping Transpiration Cooling With a Protective Porous Armor. *Applied Thermal Engineering*, 164:114485, January 2020.

[122] John D. Anderson Jr. *Hypersonic and High-Temperature Gas Dynamics, Second Edition*. American Institute of Aeronautics and Astronautics, Reston, VA, 2006. https://arc.aiaa.org/doi/pdf/10.2514/4.861956.

[123] E Reginald Van Driest. *The Problem of Aerodynamic Heating*. Institute of the Aeronautical Sciences, 1956.

[124] COESA. U.S. Standard Atmosphere, 1976. *U.S. Government Printing Office, Washington, D.C.*, 1976.

[125] Lester Lees. Laminar Heat Transfer Over Blunt-Nosed Bodies at Hypersonic Flight Speeds. *Journal of Jet Propulsion*, 26(4):259–269, 1956. Publisher: American Institute of Aeronautics and Astronautics: https://doi.org/10.2514/8.6977.

[126] Fengshou Xiao, Zhufei Li, Zhiyu Zhang, Yujian Zhu, and Jiming Yang. Hypersonic Shock Wave Interactions on a V-Shaped Blunt Leading Edge. *AIAA Journal*, 56(1):356–367, January 2018.

[127] Shripad P. Mahulikar. Theoretical Aerothermal Concepts for Configuration Design of Hypersonic Vehicles. *Aerospace Science and Technology*, 9(8):681–685, November 2005.

[128] Tobias Hermann, Matthew McGilvray, and Imran Naved. Performance of Transpiration-Cooled Heat Shields for Reentry Vehicles. *AIAA Journal*, 58(2):830–841, 2020.

[129] Randolph Lillard, Brandon Oliver, Michael Olsen, Gregory Blaisdell, and Anastasios Lyrintzis. The lagRST Model: A Turbulence Model for Non-Equilibrium Flows. In *50th AIAA Aerospace Sciences Meeting Including the New Horizons Forum and Aerospace Exposition*, page 444, 2011.

[130] J. M. Jones, P. E. Mason, and A. Williams. A Compilation of Data on the Radiant Emissivity of Some Materials at High Temperatures. *Journal of the Energy Institute*, 92(3):523–534, June 2019.

[131] Karthik K. Bodla, Jayathi Y. Murthy, and Suresh V. Garimella. Microtomography-Based Simulation of Transport Through Open-Cell Metal Foams. *Numerical Heat Transfer, Part A: Applications*, 58(7):527–544, October 2010. Publisher: Taylor & Francis: https://doi.org/10.1080/10407782.2010.511987.

[132] Andrea Diani, Karthik K. Bodla, Luisa Rossetto, and Suresh V. Garimella. Numerical Investigation of Pressure Drop and Heat Transfer Through Reconstructed Metal Foams and Comparison Against Experiments. *International Journal of Heat and Mass Transfer*, 88:508–515, September 2015.

[133] Paola Ranut, Enrico Nobile, and Lucia Mancini. High Resolution X-Ray Microtomography-Based CFD Simulation for the Characterization of Flow Permeability and Effective Thermal Conductivity of Aluminum Metal Foams. *Experimental Thermal and Fluid Science*, 67:30–36, October 2015.

[134] Dylan Dickstein, Hsing-Yin Chang, Jaime Marian, Matthew Feldman, Aimee Hubble, Rostislav Spektor, and Nasr Ghoniem. Secondary Electron Emission from Reticulated Cellular Copper Surfaces. *Journal of Applied Physics*, 128(12):123302, 2020.

[135] Warren Nadvornick, Hsing-Yin Chang, Andrew Alvarado, Pablo Molina, Jaime Marian, and Nasr Ghoniem. A Linked-Scale Coupled Model of Mass Erosion and Redistribution in Plasma-Exposed Micro-Foam Surfaces. *Journal of Nuclear Materials*, 553:153010, 2021.

[136] Yue Huang, Warren Nadvornick, Arian Ghazari, and Nasr M. Ghoniem. Multiphysics-Multiscale Modeling of Plasma-Facing Structures in Extreme Heat and Radiation Environments. *International Journal for Multiscale Computational Engineering*, 18(2), 2020. Publisher: Begel House Inc.

[137] Prieur Du Plessis, Agnes Montillet, Jacques Comiti, and Jack Legrand. Pressure Drop Prediction for Flow Through High Porosity Metallic Foams. *Chemical Engineering Science*, 49(21):3545–3553, January 1994.

[138] A. Bhattacharya, V. V. Calmidi, and R. L. Mahajan. Thermophysical Properties of High Porosity Metal Foams. *International Journal of Heat and Mass Transfer*, 45(5):1017–1031, February 2002.

[139] M. J. Box. A New Method of Constrained Optimization and a Comparison With Other Methods. *The Computer Journal*, 8(1):42–52, April 1965. Publisher: Oxford Academic.

[140] J. A. Guin. Modification of the Complex Method of Constrained Optimization. *The Computer Journal*, 10(4):416–417, February 1968. Publisher: Oxford Academic.

[141] Saša Singer and John Nelder. Nelder-Mead Algorithm. *Scholarpedia*, 4(7):2928, 2009.

[142] James P Kelly, Raghunath Kanakala, and Olivia A Graeve. A Solvothermal Approach for the Preparation of Nanostructured Carbide and Boride Ultra-High-Temperature Ceramics. *Journal of the American Ceramic Society*, 93(10):3035–3038, 2010.

[143] J. L. Bates, C. E. McNeilly, and J. J. Rasmussen. Properties of Molten Ceramics. In *Ceramics in Severe Environments*, pages 11–26. Springer, 1971.

[144] B. J. Keene. Review of Data for the Surface Tension of Pure Metals. *International Materials Reviews*, 38(4):157–192, January 1993. Publisher: Taylor & Francis, https://doi.org/10.1179/imr.1993.38.4.157.

[145] Report to Congress on Hypersonic Weapons, July 2019. Section: Aviation.

[146] L. W. Swanson and T Dickinson. Single-Crystal Work-Function and Evaporation Measurements of LaB6. *Applied Physics Letters*, 28(10):578–580, 1976.

[147] Ryo Iiyoshi, Hiroshi Shimoyama, and Susumu Maruse. A Comparison of Thermionic Emission Current Density and Brightness Against Evaporation Loss for LaB6 and Tungsten. *Microscopy*, 45(6):514–517, 1996.

[148] Haruto Nagata, Ken Harada, and Ryuichi Shimizu. Thermal Field Emission Observation of Single-Crystal LaB6. *Journal of Applied Physics*, 68(7):3614–3618, 1990.

[149] John M. Nowak. Refractory Nonmetals for Use in Hypersonic Aircraft. *SAE Transactions*, 68:571–577, 1960. Publisher: SAE International.

[150] James T. Cahill and Olivia A. Graeve. Hexaborides: A Review of Structure, Synthesis and Processing. *Journal of Materials Research and Technology*, 8(6):6321–6335, November 2019.

[151] Dylan Dickstein, Danny Donghyun Ko, Warren Nadvornick, Karan Jain, Saurin Holdheim, Yongho Sungtaek Ju, and Nasr Ghoniem. Optimized Permeability of Microporous Foam for Transpiration Cooling in Hypersonic Leading Edge. *Journal of Thermophysics and Heat Transfer*, pages 1–13, 2022.

[152] Triplicane A. Parthasarathy, Melvin D. Petry, Michael K Cinibulk, Tarun Mathur, and Mark R. Gruber. Thermal and Oxidation Response of UHTC Leading Edge Samples Exposed to Simulated Hypersonic Flight Conditions. *Journal of the American Ceramic Society*, 96(3):907–915, 2013. https://onlinelibrary.wiley.com/doi/pdf/10.1111/jace.12180.

[153] R. Prakash, S. Gai, and S. O'Byrne. A Direct Simulation Monte Carlo Study of Hypersonic Leading-Edge Separation With Rarefaction Effects. *Physics of Fluids*, 30(6):063602, June 2018. Publisher: American Institute of Physics.

[154] Edmund Storms and Barbara Mueller. Phase Relationship, Vaporization, and Thermodynamic Properties of the Lanthanum-Boron System. *The Journal of Physical Chemistry*, 82(1):51–59, January 1978. Publisher: American Chemical Society.

[155] Paul R. Davis, Mark A. Gesley, Gregory A. Schwind, Lynwood W. Swanson, and Joseph J. Hutta. Comparison of Thermionic Cathode Parameters of Low Index Single Crystal Faces of LaB6, CeB6 and PrB6. *Applied Surface Science*, 37(4):381–394, August 1989.

[156] M. Futamoto, M. Nakazawa, K. Usami, S. Hosoki, and U. Kawabe. Thermionic Emission Properties of a Single-Crystal LaB6 Cathode. *Journal of Applied Physics*, 51(7):3869–3876, July 1980. Publisher: American Institute of Physics.

[157] J. M. Lafferty. Boride Cathodes. *Journal of Applied Physics*, 22(3):299–309, March 1951. Publisher: American Institute of Physics.

[158] V. V. Fesenko and A. S. Bolgar. Evaporation Rate and Vapor Pressure of Carbides, Silicides, Nitrides, and Borides. *Soviet Powder Metallurgy and Metal Ceramics*, 2(1):11–17, January 1964.

[159] S. A. Kamble, D. M. Phase, S. Ghorui, D. Bhattacharjee, S. V. Bhoraskar, and V. L. Mathe. Influence of Carbonaceous Species Entered During Arc Plasma Synthesis on the Stoichiometry of LaB6. *Physica B: Condensed Matter*, 626:413289, February 2022.

[160] Shalaka A. Kamble, Somnath R. Bhopale, Srikumar Ghorui, Dhurva Bhattacharjee, Amiya Kumar Nandi, S. V. Bhoraskar, Mahendra A. More, and Vikas L. Mathe. Development of Nanocrystalline LaB Electron Emitters Processed Using Arc Thermal Plasma Route. *IEEE Transactions on Plasma Science*, 49(8):2440–2451, August 2021. Conference Name: IEEE Transactions on Plasma Science.

[161] Bo Li, Hejun Li, Xiyuan Yao, Yigao Chen, Xu Hu, Guanghui Feng, and Jinhua Lu. Ablation Behavior of Sharp Leading Edge Parts Made of Rare Earth La-Compound Modified ZrB2 Coated C/C Composites. *Corrosion Science*, 175:108895, October 2020.

[162] C. Lettieri, D. Yang, and Z. Spakovszky. An Investigation of Condensation Effects in Supercritical Carbon Dioxide Compressors. *Journal of Engineering for Gas Turbines and Power*, 137(8), August 2015.

[163] H. Hess. An Estimation of Plasma-Phase-Transition (PPT) Critical Values. *High Pressure Research*, 1(3):203–211, May 1989. Publisher: Taylor & Francis, https://doi.org/10.1080/08957958908201686.

[164] Ying Tang, Biao Hu, Jiong Wang, Qiannan Gao, Yong Du, Xiaoming Yuan, and Dragana Živković. Thermodynamic Modeling of the La-B and La-Bi Systems Supported by First-Principles Calculations. *Journal of Phase Equilibria and Diffusion*, 34(4):297–306, August 2013.

[165] M. E. Schlesinger, P. K. Liao, and K. E. Spear. The B-La (Boron-Lanthanum) System. *Journal of Phase Equilibria*, 20(1):73, January 1999.

[166] H. Okamoto. Supplemental Literature Review of Binary Phase Diagrams: Al-Mg, Bi-Sr, Ce-Cu, Co-Nd, Cu-Nd, Dy-Pb, Fe-Nb, Nd-Pb, Pb-Pr, Pb-Tb, Pd-Sb, and Si-W. *Journal of Phase Equilibria and Diffusion*, 36(2):183–195, April 2015.

[167] E. N. Kablov, D. A. Movenko, E. A. Lukina, P. N. Medvedev, and N. E. Shchegoleva. Investigation of the Structural-Phase State of Lanthanum Hexaboride Based Ceramic Material. *Glass and Ceramics*, 76(11):410–414, March 2020.

[168] David Rivera, Tamer Crosby, Andrew Sheng, and Nasr M Ghoniem. Characterization of Thermomechanical Damage on Tungsten Surfaces During Long-Duration Plasma Transients. *Journal of Nuclear Materials*, 455(1-3):500–506, 2014.

[169] David Rivera, Richard E Wirz, and Nasr M Ghoniem. Experimental Measurements of Surface Damage and Residual Stresses in Micro-Engineered Plasma Facing Materials. *Journal of Nuclear Materials*, 486:111–121, 2017.

[170] Arian Ghazari, Cameron McElfresh, Dylan Dickstein, Jaime Marian, and Nasr Ghoniem. Effects of Cyclic Plasma Heating on Surface Damage of Micro-Porous Tungsten. *Physica Scripta*, 96(12):124033, 2021.

[171] V. Craciun and D. Craciun. Pulsed Laser Deposition of Crystalline LaB6 Thin Films. *Applied Surface Science*, 247(1-4):384–389, July 2005.

[172] Masaki Kuno, Takeo Oku, and Katsuaki Suganuma. Synthesis of Boron Nitride Nanotubes and Nanocapsules With LaB6. *Diamond and Related Materials*, 10(3):1231–1234, March 2001.

[173] Letitia Topor and O. J Kleppa. Standard Molar Enthalpy of Formation of LaB6 by High-Temperature Calorimetry. *The Journal of Chemical Thermodynamics*, 16(10):993–1002, October 1984.

[174] Bernard Goldstein and D. J. Szostak. Characterization of Clean and Oxidized (100) LaB6. *Surface Science*, 74(2):461–478, 1978.

[175] T. Tanaka. The Thermal and Electrical Conductivities of LaB6 at High Temperatures. *Journal of Physics C: Solid State Physics*, 7(9):L177–L180, May 1974. Publisher: IOP Publishing.

[176] Edmund K. Storms. The Emissivity of LaB6 at 650 nm. *Journal of Applied Physics*, 50(6):4450–4450, June 1979. Publisher: American Institute of Physics.

[177] I. Bogomol, T. Nishimura, Yu. Nesterenko, O. Vasylkiv, Y. Sakka, and P. Loboda. The Bending Strength Temperature Dependence of the Directionally Solidified Eutectic LaB6–ZrB2 Composite. *Journal of Alloys and Compounds*, 509(20):6123–6129, May 2011.

[178] P. I. Loboda, H. P. Kysla, S. M. Dub, and O. P. Karasevs'ka. Mechanical Properties of the Monocrystals of Lanthanum Hexaboride. *Materials Science*, 45(1):108–113, January 2009. Num Pages: 108-113 Place: New York, Netherlands Publisher: Springer Nature B.V.

[179] G. I. Kuznetsov and E. A. Sokolovsky. Dependence of Effective Work Function for LaB6 on Surface Conditions. *Physica Scripta*, T71:130–133, January 1997. Publisher: IOP Publishing.

[180] Arian Ghazari, Cameron McElfresh, Dylan Dickstein, Warren Nadvornick, Gerald Pintsuk, Egbert Wessel, Marius Wirtz, Don Hughes, Brian Williams, Jaime Marian, et al. Intense Cyclic Heating Effects on Thermo-Fracture and Thermal Shock of Solid Tungsten and Open-Cell Tungsten Foam. *Journal of Nuclear Materials*, 565:153730, 2022.